



Universitat de Girona

SIMULATION OF INTERLAMINAR AND INTRALAMINAR DAMAGE IN POLYMER-BASED COMPOSITES FOR AERONAUTICAL APPLICATIONS UNDER IMPACT LOADING

Emilio Vicente GONZÁLEZ JUAN

ISBN: 978-84-694-4282-1

Dipòsit legal: GI-695-2011

<http://hdl.handle.net/10803/22834>

ADVERTIMENT. La consulta d'aquesta tesi queda condicionada a l'acceptació de les següents condicions d'ús: La difusió d'aquesta tesi per mitjà del servei [TDX](#) ha estat autoritzada pels titulars dels drets de propietat intel·lectual únicament per a usos privats emmarcats en activitats d'investigació i docència. No s'autoritza la seva reproducció amb finalitats de lucre ni la seva difusió i posada a disposició des d'un lloc aliè al servei TDX. No s'autoritza la presentació del seu contingut en una finestra o marc aliè a TDX (framing). Aquesta reserva de drets afecta tant al resum de presentació de la tesi com als seus continguts. En la utilització o cita de parts de la tesi és obligat indicar el nom de la persona autora.

ADVERTENCIA. La consulta de esta tesis queda condicionada a la aceptación de las siguientes condiciones de uso: La difusión de esta tesis por medio del servicio [TDR](#) ha sido autorizada por los titulares de los derechos de propiedad intelectual únicamente para usos privados enmarcados en actividades de investigación y docencia. No se autoriza su reproducción con finalidades de lucro ni su difusión y puesta a disposición desde un sitio ajeno al servicio TDR. No se autoriza la presentación de su contenido en una ventana o marco ajeno a TDR (framing). Esta reserva de derechos afecta tanto al resumen de presentación de la tesis como a sus contenidos. En la utilización o cita de partes de la tesis es obligado indicar el nombre de la persona autora.

WARNING. On having consulted this thesis you're accepting the following use conditions: Spreading this thesis by the [TDX](#) service has been authorized by the titular of the intellectual property rights only for private uses placed in investigation and teaching activities. Reproduction with lucrative aims is not authorized neither its spreading and availability from a site foreign to the TDX service. Introducing its content in a window or frame foreign to the TDX service is not authorized (framing). This rights affect to the presentation summary of the thesis as well as to its contents. In the using or citation of parts of the thesis it's obliged to indicate the name of the author.



UNIVERSITAT DE GIRONA

PHD THESIS

SIMULATION OF INTERLAMINAR AND
INTRALAMINAR DAMAGE IN
POLYMER-BASED COMPOSITES FOR
AERONAUTICAL APPLICATIONS UNDER
IMPACT LOADING

EMILIO VICENTE GONZÁLEZ JUAN

2010



UNIVERSITAT DE GIRONA

PHD THESIS

SIMULATION OF INTERLAMINAR AND
INTRALAMINAR DAMAGE IN POLYMER-BASED
COMPOSITES FOR AERONAUTICAL
APPLICATIONS UNDER IMPACT LOADING

EMILIO VICENTE GONZÁLEZ JUAN

2010

TECHNOLOGY DOCTORATE PROGRAM

ADVISORS

DR. PERE MAIMÍ VERT DR. PEDRO P. CAMANHO
Universitat de Girona, Spain *Universidade do Porto, Portugal*

A thesis submitted for the degree of Doctor of Philosophy by the
University of Girona

To whom it might concern,

Dr. Pere Maimí Vert, Associate Professor at the *Universitat de Girona* of the Department of *Enginyeria Mecànica i de la Construcció Industrial*, and Dr. Pedro Manuel Ponces Rodrigues de Castro Camanho, Associate Professor at the *Universidade do Porto* of the Department of *Engenharia Mecânica*,

CERTIFY that the study entitled *Simulation of interlaminar and intralaminar damage in polymer-based composites for aeronautical applications under impact loading* has been carried out under their supervision by Emilio Vicente González Juan to apply the doctoral degree with the European Mention,

Girona, October 2010,

Dr. Pere Maimí Vert
Universitat de Girona, Spain

Dr. Pedro P. Camanho
Universidade do Porto, Portugal

*A mis padres,
Angel y Tere*

Acknowledgements - Agraïments - Agradecimientos

I would like to express my most sincerely gratitude to my advisors, Pere Maimí and Pedro P. Camanho, for the indefatigable help and for the key contributions that have allowed the development of the present thesis. I feel very fortunate to have worked with them. The treatment that I have received since the first day has been close and friendly, and this good relationship has grown day by day yielding to a nice friendship and allowing to enjoy a lot with the work.

I want to thank also the help received from Joan Andreu Mayugo, Josep Costa and Norbert Blanco, who have spent a lot of time making the work easy and clarifying a lot of things, not only related to composite materials, also in many other things which are required to continue forward. This help has existed always, since the first day that I started to work with the research group AMADE in July of 2003. Also, I have to remember that they are the guilty of encouraged me to start the thesis.

I have to do a special mention of my friends G. Catalanotti, C.S. Lopes, and H. Koerber, with the ones that I have shared great moments and I have learned a lot of them during my research stages at the University of Porto. In addition, I would like to express my gratitude to Carlos Dávila who offered me the possibility to visit NASA - Langley Research Center in Hampton, during the summer of 2008.

Of course, I am grateful to all members of the research group AMADE of the University of Girona for the help and nice moments that I have received from each one: A. Turon, J. Renart, D. Trias, M. Baena, M. Gascons, P. Vicens, E. Pajares, R. Cruz, J. Bonilla, C. Mias, Ll. Ripoll, L. Zubillaga, N. Isart, S. Ortiz, C. Barris, I. Vilanova, D. Sans, J. Bofill, P. Badalló, T. Kanzaki, N. Gascons, J. Torres, Ll. Torres, J. Vives and M. Compte. In addition, I want to thank to: Grup de Recerca en Enginyeria de Producte, Procés i Producció (GREP), of the University of Girona, in special to Jordi Delgado, for the dent-depth measurements; Instituto Nacional de Técnica Aeroespacial (INTA), for the help in the specimen manufacturing; Mechanic Engineering Laboratory of the University of Porto for the manufacturing of the test rigs; and the Computer Science team of INEGI (University of Porto) for the well working of the cluster for the computation of the simulations.

No vull oblidar els meus amics, Aniceto, Auguet, Blai, Calli, Manel·la, Palacios, i Terri, pels bons moments de desconnexió que m'heu donat, encara que no han pogut ser molts, però que han estat intensos i divertits.

Finalmente, quiero dar un especial agradecimiento a mi hermana Bego, mi cuñado Joan, y a mis padres, Angel y Tere, por la confianza, apoyo y ánimos que me habéis dado, no sólo en este proyecto, sino a lo largo de mi vida para todas las dificultades que se me han presentado. Estoy en deuda con vosotros.

Funds

The period of doctorate studies comprised between July of 2006 and June of 2007 has been supported by the University of Girona through the research grant *BR06/07*. The period of research has been funded by the Comissionat per a Universitats i Recerca del Departament d'Innovació, Universitats i Empresa de la Generalitat de Catalunya, and by European Social Funds, under a research grant *FI - Formació de Personal Investigador*, started in July of 2007 and finished in June of 2010.

Also, the present work has been partially funded by the Spanish Government through the contracts MAT2006-14159-C02-01 and TRA2006-15718-C02-01/TAIR, and by the Portuguese Foundation for Science and Technology under the project PDCT/EMEPME/64984/2006.

Part of the work has been carried out during three stages at the University of Porto, under the grants for mobility: *VUDG-2007* (of the University of Girona), and *BE-2008* and *BE-2009* (of the Comissionat per a Universitats i Recerca del Departament d'Innovació, Universitats i Empresa de la Generalitat de Catalunya). Also, the analysis of some topics were performed during the research stage at NASA - Langley Research Center in Hampton (Virginia, USA), that was supported by the National Institute of Aerospace (NIA), in the summer of 2008.

Finally, I want to thank the award received in May of 2009 for the best thesis project, announced by the Associació d'Enginyers Industrials de Catalunya, and supported by the Agrupació Socio-Cultural dels Enginyers Industrials de Catalunya.

Resumen

La aplicación de materiales compuestos de matriz polimérica reforzados mediante fibras largas (FRP, "*Fiber Reinforced Plastic*"), está en gradual crecimiento debido a las buenas propiedades específicas y a la flexibilidad en el diseño. Uno de los mayores consumidores es la industria aeroespacial, dado que la aplicación de estos materiales tiene claros beneficios económicos y medioambientales.

Cuando los materiales compuestos se aplican en componentes estructurales, se inicia un programa de diseño donde se combinan ensayos reales y técnicas de análisis. El desarrollo de herramientas de análisis fiables que permiten comprender el comportamiento mecánico de la estructura, así como reemplazar muchos, pero no todos, los ensayos reales, es de claro interés.

Susceptibilidad al daño debido a cargas de impacto fuera del plano es uno de los aspectos de más importancia que se tienen en cuenta durante el proceso de diseño de estructuras de material compuesto. La falta de conocimiento de los efectos del impacto en estas estructuras es un factor que limita el uso de estos materiales.

Por lo tanto, el desarrollo de modelos de ensayo virtual mecánico para analizar la resistencia a impacto de una estructura es de gran interés, pero aún más, la predicción de la resistencia residual después del impacto.

En este sentido, el presente trabajo abarca un amplio rango de análisis de eventos de impacto a baja velocidad en placas laminadas de material compuesto, monolíticas, planas, rectangulares, y con secuencias de apilamiento convencionales. Teniendo en cuenta que el principal objetivo del presente trabajo es la predicción de la resistencia residual a compresión, diferentes tareas se llevan a cabo para favorecer el adecuado análisis del problema. Los temas que se desarrollan son: la descripción analítica del impacto, el diseño y la realización de un plan de ensayos experimentales, la formulación e implementación de modelos constitutivos para la descripción del com-

portamiento del material, y el desarrollo de ensayos virtuales basados en modelos de elementos finitos en los que se usan los modelos constitutivos implementados.

Summary

The application of polymer-based composites reinforced by long fibers, called advanced Fiber Reinforced Plastic (FRP), is gradually increasing as a result of their good specific mechanical properties and increased flexibility of design. One of the largest consumers is the aerospace industry, since the application of these materials has clear economic and environmental benefits.

When composites are to be used in structural components, a design development program is initiated, where a combination of testing and analysis techniques is typically performed. The development of reliable analysis tools that enable to understand the structure mechanical behavior, as well as to replace most, but not all, the real experimental tests, is of clear interest.

Susceptibility to damage from concentrated out-of-plane impact forces is one of the major design concerns of structures made of advanced FRPs used in the aerospace industry. Lack of knowledge of the impact effects on these structures is a factor in limiting the use of composite materials.

Therefore, the development of virtual mechanical testing models to analyze the impact damage resistance of a structure is of great interest, but even more, the prediction of the post-impact residual strength.

In this sense, the present thesis covers a wide range of analysis of the low-velocity and large mass impact events on monolithic, flat, rectangular, polymer-based laminated composite plates with conventional stacking sequences. Keeping in mind that the main goal of this work is the prediction of the residual compressive strength of an impacted specimen coupon, a set of different tasks are performed in order to provide suitable tools to analyze the problem. Accordingly, the topics which are addressed in this thesis are: the analytical description of the impact, the design and the realization of an experimental test plan, the formulation and implementation

of constitutive models for the description of the composite material behavior, and the assessment of the performance of virtual tests based on finite element models where the constitutive models are used.

Contents

Resumen	xi
Summary	xiii
List de Figures	xxvii
List de Tables	xxx
List of Symbols	xxxii
List of Acronyms	xlvii
1 Introduction and objectives	1
1.1 Introduction	1
1.2 Motivation	4
1.3 Objectives	5
1.4 Thesis lay-out	6
2 Analytical description of the impact event	9
2.1 Introduction	9
2.2 Impact behavior	10
2.3 Local deflection	13
2.3.1 Hertz contact law adapted for laminated composite plates	16
2.3.2 Unloading and reloading contact process	18
2.3.3 Elastic-plastic contact models	20
2.3.4 Linearized contact laws	22
2.4 Analytical impact models	22

2.4.1	Complete analytical models	24
2.4.2	Infinite plate impact models	29
2.4.3	Half-space impact models	35
2.4.4	Quasi-static impact models	36
2.5	Approaches for impact behavior description	38
2.5.1	Christoforou and Yigit characterization diagram	38
2.5.2	Olsson mass criterion	42
2.6	Impact damage and analytical thresholds	45
2.6.1	Matrix cracking	45
2.6.2	Delamination	51
2.6.3	Permanent indentation	57
2.6.4	Fiber failure	58
2.6.5	Perforation	58
3	Test configurations	61
3.1	Introduction	61
3.2	Impact tests	62
3.2.1	Benchmark: ASTM drop-weight impact test	63
3.2.2	Selected studies: fixed and variable parameters	67
3.3	Compression after impact tests (CAI)	78
3.3.1	Benchmark: ASTM compression after impact test	79
3.3.2	Resources used and specimen instrumentation	81
4	Experimental results	83
4.1	Introduction	83
4.2	Effect of ply thickness (clustering)	84
4.2.1	Impact tests	84
4.2.2	NDI: C-scan after impact	91
4.2.3	Dent-depth measurements	96
4.2.4	CAI tests	97
4.3	Effect of ply mismatch angle at interfaces	103
4.3.1	Impact tests	103
4.3.2	NDI: C-scan after impact	108
4.3.3	Dent-depth measurements	110

4.3.4	CAI tests	111
4.4	Effect of the laminate thickness	113
4.4.1	Impact tests	113
4.4.2	NDI: C-scan after impact	123
4.4.3	Dent-depth measurements	127
4.4.4	CAI tests	128
4.5	Summary of conclusions	133
5	Interlaminar damage model	137
5.1	Introduction	137
5.2	Damage model formulation	141
5.2.1	Norm of the relative displacement vector	143
5.2.2	Surface of damage activation and law for damage evolution	144
5.2.3	Criterion for damage propagation	145
5.2.4	Criterion for damage onset	147
5.3	Formulation adaptations	148
5.3.1	Relation between relative displacements and strains	148
5.3.2	Penalty stiffness	149
5.3.3	Redefined onset and propagation damage criteria	150
5.4	Model implementation	153
5.4.1	Strategy of implementation	153
5.4.2	Input variables to define the model	154
5.4.3	Algorithm	156
5.5	Size of cohesive elements	159
5.5.1	Maximum thickness of volumetric cohesive elements	159
5.5.2	In-plane dimensions of the cohesive elements	161
5.6	Simulations	162
5.6.1	Considerations for quasi-static explicit simulations	163
5.6.2	MMB and ENF fracture toughness tests	164
5.6.3	TCT tests	171
5.7	Conclusions	174
6	Intralaminar damage model	177
6.1	Introduction	177

6.2	Continuum damage model	178
6.2.1	Constitutive model	178
6.2.2	Damage activation functions	180
6.2.3	Damage evolution laws	183
6.2.4	Maximum in-plane finite element size	185
6.2.5	Material properties	186
6.2.6	In-situ strengths	187
6.3	Limitations of continuum damage models	188
7	Virtual testing	195
7.1	Introduction	195
7.2	Description of the FE models	195
7.2.1	Explicit FE code	195
7.2.2	Plate modeling	197
7.2.3	Virtual test set-up	204
7.2.4	Energy balance	207
7.3	Virtual results and comparison with experiments	208
8	Conclusions and future work	223
8.1	Conclusions	223
8.1.1	Analytical impact description	223
8.1.2	Experimental test plan	224
8.1.3	Constitutive models for FE simulations	228
8.1.4	Virtual tests: drop-weight impact and CAI	229
8.2	Future works	231
8.2.1	Analytical impact description	231
8.2.2	Experimental tests	232
8.2.3	Constitutive models for FE simulations	232
8.2.4	Virtual tests	234
8.3	Publications	235
	Bibliography	236

A	Governing equations of the plate	255
A.1	Ingredients for the development of the equations	256
A.1.1	Strain-displacement relations	257
A.1.2	Lamina constitutive equation	258
A.1.3	Laminate resultants	261
A.1.4	Frameworks to develop the governing equations	263
A.2	Plate theories and governing equations	268
A.2.1	Classical laminated plate theory	268
A.2.2	First-order shear plate theory	276

List of Figures

2.1	Impact responses.	12
2.2	Extreme plate responses under impact loading.	14
2.3	Coordinate systems.	16
2.4	Detail of the contact law phases.	22
2.5	Boundary conditions of a simply supported plate.	24
2.6	Lumped-mass models for infinite plate behavior.	32
2.7	Spring-mass model for half-space impact behavior.	35
2.8	Complete and simplified spring-mass models for quasi-static impact behavior.	37
2.9	Impact characterization diagram.	41
2.10	Type of matrix cracks in a cross-ply laminated composite plate.	46
2.11	Projected damage patterns.	47
2.12	Example of peanut shaped delaminations.	52
2.13	Maximum delamination size as a function of the impact force for plates with different thickness.	53
2.14	Representative impact force versus time history.	53
3.1	Impact support fixture.	64
3.2	Impact test fixture.	68
3.3	Analytical threshold load trend in function of h_p	71
3.4	Analytical threshold trends for all laminates.	77
3.5	Buckling modes of delaminated plates in compression.	78
3.6	CAI support fixture.	79
3.7	CAI test fixture.	81
3.8	Instrumentation of CAI tests.	82

4.1	Impact force histories of laminate L02 (repeatability).	84
4.2	Impact force histories of laminate L04 (repeatability).	85
4.3	Impact force histories of laminate L02 for each impact energy.	85
4.4	Impact force histories of laminate L03 for each impact energy.	86
4.5	Impact force histories of laminate L04 for each impact energy.	86
4.6	Experimental and analytical impact force histories of laminate L02.	87
4.7	Impact force histories for 38.6J (ply clustering).	88
4.8	Impact force histories for 28.6J (ply clustering).	88
4.9	Impact force histories for 19.3J (ply clustering).	89
4.10	Experimental points and analytical predictions of F_d (ply clustering).	90
4.11	Impactor displacements and velocities of all laminates for 28.6J (ply clustering).	91
4.12	Evolution of the absorbed energy and the impact force versus impactor displacement of each laminate for 38.6J (ply clustering).	92
4.13	Evolution of the absorbed energy and the impact force versus impactor displacement of each laminate for 28.6J (ply clustering).	92
4.14	Evolution of the absorbed energy and the impact force versus impactor displacement of each laminate for 19.3J (ply clustering).	93
4.15	Sample of C-scan inspections (ply clustering).	94
4.16	Projected delamination areas in function of the impact energy (ply clustering).	96
4.17	Dent-depth inspections (ply clustering).	98
4.18	Displacement transducer lectures for 29.6J (ply clustering).	100
4.19	Strain gage lectures for 29.6J (ply clustering).	101
4.20	DIC lectures of the specimen L04-S04, impacted at 29.6J.	102
4.21	Impact force histories of laminate L06 for each impact energy.	103
4.22	Experimental and analytical impact force histories of laminate L06.	104
4.23	Impact force histories for 38.6J (ply mismatch angle).	104
4.24	Impact force histories for 28.6J (ply mismatch angle).	105
4.25	Impact force histories for 19.3J (ply mismatch angle).	105
4.26	Experimental points and analytical predictions of F_d (ply mismatch angle).	106

4.27	Impactor displacements and velocities of laminates L02 and L06 for 28.6J (ply mismatch angle).	107
4.28	Evolution of the absorbed energy and the impact force versus impactor displacement of laminates L02 and L06 for 38.6J (ply mismatch angle).	108
4.29	Evolution of the absorbed energy and the impact force versus impactor displacement of laminates L02 and L06 for 28.6J (ply mismatch angle).	108
4.30	Evolution of the absorbed energy and the impact force versus impactor displacement of laminates L02 and L06 for 19.3J (ply mismatch angle).	109
4.31	Sample of C-scan inspections of laminates L02 and L06 (ply mismatch angle).	109
4.32	Dent-depth inspections of laminates L02 and L06 (ply mismatch angle).	110
4.33	Displacement transducer lectures (ply mismatch angle).	112
4.34	Strain gage lectures (ply mismatch angle).	113
4.35	Impact force histories of laminate L01 for each impact configuration.	114
4.36	Impact force histories of laminate L05 for each impact configuration.	115
4.37	Impact force histories of laminate L01 and laminate L05 (impactor mass effect).	116
4.38	Experimental and analytical impact force histories of laminate L01 (impactor mass effect).	117
4.39	Experimental and analytical impact force histories of laminate L05 (impactor mass effect).	118
4.40	Impact force histories of laminates (laminate thickness).	118
4.41	Experimental and analytical threshold loads F_d of all laminates.	119
4.42	Impactor displacement and velocity of laminate L01 (impactor mass effect).	120
4.43	Impactor displacement and velocity of laminate L05 (impactor mass effect).	120
4.44	Evolution of the absorbed energy and the impact force versus impactor displacement of laminate L01 (impactor mass effect).	121

4.45	Evolution of the absorbed energy and the impact force versus impactor displacement of laminate L05 (impactor mass effect).	121
4.46	Impactor displacement and velocity of laminates L01 and L02 (laminate thickness).	122
4.47	Impactor displacement and velocity of laminates L01, L02 and L05 (laminate thickness).	123
4.48	Evolution of the absorbed energy and the impact force versus impactor displacement of laminates L01 and L02 for 19.3J (laminate thickness).	124
4.49	Evolution of the absorbed energy and the impact force versus impactor displacement of laminates L01, L02 and L05 for 38.6J (laminate thickness).	124
4.50	Sample of C-scan inspections of laminate L01 (impactor mass effect).	125
4.51	Sample of C-scan inspections of laminate L05 (impactor mass effect).	125
4.52	Sample of C-scan inspections of laminates L01 and L02 for 19.3J (laminate thickness).	125
4.53	Sample of C-scan inspections of laminates L02 and L05 for 38.6J (laminate thickness).	126
4.54	C-scan inspection of specimen L01-S06.	126
4.55	Dent-depth inspections of laminate L01 (impactor mass effect).	127
4.56	Dent-depth inspections of laminate L05 (impactor mass effect).	127
4.57	Dent-depth inspections of laminates L01 and L02 for 19.3J (laminate thickness).	128
4.58	Dent-depth inspections of laminates L02 and L05 for 38.6J (laminate thickness).	128
4.59	Displacement transducer and strain gage lectures of laminate L05 (impactor mass effect).	130
4.60	Displacement transducer and strain gage lectures of laminates L01 and L02 for 19.3J (laminate thickness).	131
4.61	Displacement transducer and strain gage lectures of laminates L02 and L05 for 38.6J (laminate thickness).	132
5.1	Bilinear constitutive law.	141
5.2	Propagation modes.	142

5.3	Parameters of the bilinear constitutive equation.	145
5.4	Constitutive charts defined by stresses and relative displacements, or by stresses and strains.	149
5.5	Transformations from strains to relative displacements for each prop- agation mode.	153
5.6	Evolution of the maximum element thickness in function of the mixed- mode ratio.	160
5.7	Constitutive equation charts defined by relative displacements and by strains in function of the element thickness.	161
5.8	Sketches of the MMB test and the ENF test configurations.	165
5.9	Experimental and numerical force-displacement relation of the MMB test $B = 0.0$ (pure mode I).	168
5.10	Experimental and numerical force-displacement relation of the MMB test $B = 0.2$	168
5.11	Experimental and numerical force-displacement relation of the MMB test $B = 0.5$	169
5.12	Experimental and numerical force-displacement relation of the MMB test $B = 0.8$	169
5.13	Experimental and numerical force-displacement relation of the ENF test (pure mode II).	170
5.14	TCT specimen.	171
5.15	Detail of the location of the cohesive elements for the TCT test sim- ulations.	173
5.16	Numerical load-displacement relations for the TCT specimens.	175
6.1	Fracture surfaces and corresponding internal variables for four differ- ent modes.	180
6.2	Details of the off-axis ply subjected to tensile loading.	190
6.3	Predictions of the matrix cracks in an off-axis ply subjected to tensile loading (using non-structured mesh).	190
6.4	Predictions of the matrix cracks in an off-axis ply subjected to tensile loading (using a structured mesh).	191
6.5	Ultimate tensile strengths versus off-axis angle.	192
6.6	Schematic of pull-out failure of a laminate with no fiber fracture.	192

6.7	Prediction of the matrix crack bands of laminate $[45/-45]_S$ subjected to tensile loading.	193
7.1	Superposition of the finite element discretization with an image of a laminated composite material.	198
7.2	Strategies for modeling a laminated composite plate.	198
7.3	In-plane mesh size of the plate.	201
7.4	Set-up of the virtual impact tests.	205
7.5	Boundary conditions of the CAI test.	207
7.6	Experimental and numerical impact force histories of the laminate L04 for 38.6J.	209
7.7	Experimental and numerical impact force histories of the laminate L04 for 29.6J.	210
7.8	Experimental and numerical impact force histories of the laminate L04 for 19.3J.	210
7.9	Experimental and numerical evolutions of the absorbed energy, and numerical evolutions of the impact force and the energy dissipated due to delamination (case: L04 for 19.3J).	211
7.10	Projected delamination area for different impact times of the laminate L04 for 19.3J.	212
7.11	Example of back face delaminations.	213
7.12	Projected delamination areas of the laminate L04 for each impact energy.	214
7.13	Through-the-thickness plane views of matrix cracking of the laminate L04.	215
7.14	Numerical prediction of the absorbed energies and the compressive load as a function of the compression displacement, of the laminate L04 for 19.3J.	216
7.15	Predicted displacement fields of the laminate L04 for 19.3J.	217
7.16	Experimental and numerical impact force histories of the laminate L03 for 29.6J.	218
7.17	Experimental and numerical impact force histories of the laminate L03 for 19.3J.	218

7.18 Experimental and numerical evolutions of the absorbed energy, and numerical evolutions of the impact force and the energy dissipated due to delamination (case: L03 for 19.3J). 219

7.19 Projected delamination areas of the laminate L03 for each impact energy. 219

7.20 Numerical prediction of the absorbed energies and the compressive load as a function of the compression displacement, of the laminate L03 for 19.3J. 220

7.21 Predicted displacement fields of the laminate L03 for 19.3J. 221

A.1 Laminated composite plate and coordinate systems. 256

A.2 Transverse isotropic lamina. 260

A.3 Lamina coordinate systems. 261

A.4 Force and moment resultants on a lamina (or laminate). 262

A.5 Lamina location in a laminate. 263

A.6 Behavior of transverse section in classical plate theory. 269

A.7 Stress resultants on an arbitrary edge of a laminate. 273

A.8 Behavior of transverse section in first-order shear plate theory. 278

List of Tables

2.1	Energy release rates for unequal size delaminations.	56
3.1	ASTM D7136 / D7136M specifications for the specimen.	65
3.2	ASTM D7136 / D7136M specifications for the impactor.	66
3.3	Damage thresholds for AS4/8552 carbon-epoxy composite material. . .	67
3.4	Impact configurations for laminates: L02, L03 and L04.	69
3.5	Damage thresholds for laminates: L02, L03 and L04.	70
3.6	Damage thresholds for laminate L06.	73
3.7	Impact configurations for laminate type L01.	74
3.8	Impact configurations for laminate type L05.	74
3.9	Maximum elastic impact force predictions for laminate type L01. . . .	75
3.10	Maximum elastic impact force predictions for laminate type L05. . . .	75
3.11	Damage thresholds for laminates: L01 and L05.	76
3.12	Selected laminates.	78
4.1	Experimental threshold loads F_d and peak loads F_{max}	89
4.2	Absorbed energies of all laminates for each impact energy.	93
4.3	Projected delamination areas given by C-scan inspections.	96
4.4	Failure compressive loads F_{fc} of laminates L02, L03 and L04.	99
4.5	Maximum lectures of the displacement transducers of laminates L02, L03 and L04.	99
4.6	Experimental threshold loads F_d and peak loads F_{max} of laminates L02 and L06.	106
4.7	Absorbed energies of laminates L02 and L06 for each impact energy. .	107
4.8	Failure compressive loads F_{fc} of laminates L02 and L06.	111
4.9	Residual compressive strengths σ_{fc} of laminates L02 and L06. . . .	111

4.10	Maximum lectures of the displacement transducers of laminates L02 and L06.	112
4.11	Experimental threshold loads F_d and peak loads F_{max} for laminate L01.	114
4.12	Experimental threshold loads F_d and peak loads F_{max} for laminate L05.	115
4.13	Residual compressive strengths σ_{fc} of laminates L01, L02 and L06. . .	129
4.14	Summary of analytical and experimental thresholds.	136
5.1	AS4/PEEK properties.	166
5.2	Interface properties (MMB and ENF tests).	167
5.3	Fracture toughnesses of the interface for different mixed-mode ratios.	167
5.4	Analytical equations of MMB test with $B = 0.0$, and ENF test ($B = 1.0$).	167
5.5	T300/914C properties.	174
5.6	Interface properties (TCT tests).	174
5.7	Experimental and numerical results (TCT tests).	175
7.1	Hexply AS4/8552 properties.	203
7.2	Interface properties.	204
7.3	Values of the threshold to generate n_d^* sub-laminates counted from the back face of the plate.	214
7.4	Predictions of the post-impact residual compressive load and the compressive displacement of the laminate L04.	215
7.5	Predictions of the post-impact residual compressive load and the compressive displacement of the laminate L03.	220
A.1	Stress notations.	256
A.2	Strain notations.	257

List of Symbols

Symbol	Description
a and b	Effective in-plane dimensions of the plate in x and y axis.
a_t and b_t	In-plane dimensions of the plate in x and y axis.
a_{c0}	Initial crack length (MMB and ENF tests).
a_c	Delamination radius or crack size.
A_{crack}	Area of a crack.
$A_{ij}, \quad i = 1, 2, 6$	Extensional stiffness components of a laminate.
$A_{ij}, \quad i = 4, 5$	Transverse shear stiffness components of a laminate.
$A_M, \quad M = 1+, 1-, 2+, 2-, 6$	Parameters to ensure independency on the finite element size.
b	Width of a TCT specimen.
B	Ratio of shear energy release rate versus total energy release rate.
$B_{ij}, \quad i = 1, 2, 6$	Bending-extensional coupling stiffness components of a laminate.
c	Length of the loading arm (MMB tests).
$c_{bend,i}, \quad i = x, y$	Flexural wave velocities.
C_{ijkl}	Fourth-order stiffness tensor.

Symbol	Description
c_m	Wave speed of a material.
c_z	Speed of sound in the through-the-thickness direction.
C_E	Ratio of the impact energy to the specimen thickness.
C_i	Mobility of the impactor.
$C_{ij}, \quad i = 1, 2, 6; j = 1, 2, 3, 6$	Constitutive stiffness components of a ply or laminate.
C_p	Mobility of the plate.
d	Isotropic damage variable (interlaminar damage model).
d_{1-}	Longitudinal compression (fiber) damage variable.
d_{1+}	Longitudinal tensile (fiber) damage variable.
d_{2-}	Transverse compression (matrix) damage variable.
d_{2+}	Transverse tensile (matrix) damage variable.
d_1	Longitudinal (fiber) damage variable.
d_2	Transverse (matrix) damage variable due to in-plane loads.
d_3	Transverse (matrix) damage variable due to out-of-plane loads.
d_4	Shear damage variable at plane 23.
d_5	Shear damage variable at plane 13.
d_6	Shear damage variable at plane 12.
d_s	Maximum delamination size.
D	Isotropic bending stiffness.

Symbol

D^*
 $D_{ij}, \quad i = 1, 2, 6$
 D_{ij}^o
 $D_r(\theta)$

 E
 E_a
 E_{DC}
 E_{Dd}
 E_{Df}
 E_{Dm}
 E_E
 E_F
 E_H
 E_i
 E_I
 $E_j, \quad j = 1, 2, 3 \text{ or } j = r, \theta, z$
 E_K
 E_T
 E_V

 E_m
 $f_N(r_N), \quad N = 1+, 1-, 2+, 2-$

 \mathbf{f}
 $F(\Delta, d)$
 F
 F_{bend}

Description

Effective bending stiffness.
 Bending stiffness components of a laminate.
 Undamaged stiffness tensor of an interface.
 Radial plate bending stiffness in direction θ .

 Isotropic or homogenized Young modulus.
 Energy absorbed by the specimen.
 Energy dissipated by distortion control.
 Energy dissipated by delamination.
 Energy dissipated by fiber damage.
 Energy dissipated by matrix damage.
 Recoverable strain energy.
 Frictional dissipation energy.
 Energy generated to prevent hourglassing.
 Impact energy.
 Internal energy.
 Young modulus.
 Kinetic energy.
 Total energy of the system.
 Energy dissipated by bulk viscosity damping.

 Interface Young modulus.
 Parameters to force softening of a constitutive relation.

 Body forces per unit of mass.
 Surface of damage activation.
 Impact force.
 Force due to plate bending.

Symbol	Description
F_c	Contact load.
$F_{d,e}$	Experimental impact threshold load.
$F_{d,n}$	Numerical impact threshold load.
F_d	Impact threshold load.
F_{d1}^{dyn}	Threshold load for a mid-plane delamination with dynamic effects.
F_{d1}^{stat}	Threshold load for a mid-plane delamination.
F_{dbf}^{stat}	Threshold load to generate n_d^* sublaminates or delaminations counted from the back face of the plate.
$F_{dn_d}^{dyn}$	Threshold load for n_d delaminations with dynamic effects.
$F_{dn_d}^{stat}$	Threshold load for n_d delaminations.
F_{fc}	Residual compressive load in a CAI test.
F_{ind}	Threshold load for permanent indentation.
F_m	Contact load at the start of the unloading process.
F_{max}	Maximum impact load.
F_{mc}^{sh}	Threshold load for shear matrix cracking.
F_{mc}^{ten}	Threshold load for tensile matrix cracking at the back face of the plate.
$F_N, \quad N = 1+, 1-, 2+, 2-$	Damage activation functions.
F_{per}^{sh}	Threshold load for perforation due to laminate shear failure.
F_{per}^{ten}	Threshold load for perforation due to tensile fiber failure.
\bar{F}_b	Boundary of the quasi-static response.

Symbol	Description
$\bar{F}_{hs,max}$	Maximum normalized impact force for half-space behavior.
\bar{F}_{hs}	Normalized impact force for half-space behavior.
\bar{F}_{max}	Maximum normalized impact force.
$\bar{F}_{q,max}$	Maximum normalized impact force for quasi-static behavior.
\bar{F}_q	Normalized impact force for quasi-static behavior.
$\bar{F}_{w,max}$	Maximum normalized impact force for infinite plate behavior.
\bar{F}_w	Normalized impact force for infinite plate behavior.
g	Acceleration due to the gravity.
g	Pure mode fracture toughness ratio.
$g_M, \quad M = 1+, 1-, 2+, 2-, 6$	Dissipated energy by unit of volume at an integration point (intralaminar damage model).
g_e	Dissipated energy by unit of volume at an integration point (interlaminar damage model).
G	Complementary free energy density.
G	Isotropic shear elastic modulus.
$G(\Delta)$	Monotonic loading function.
$G_{ij}, \quad i, j = 1, 2, 3 \text{ or } i, j = r, \theta, z$	Shear elastic modulus.
G_m	Interface shear elastic modulus.
$\mathcal{G}^o(\beta)$	Delamination onset criterion defined by elastic terms.

Symbol	Description
\mathcal{G}_{1+}^E	Fracture toughness in the exponential softening branch for longitudinal tensile.
\mathcal{G}_{1+}^L	Fracture toughness in the linear softening branch for longitudinal tensile.
\mathcal{G}_I	Energy release rate in mode I.
\mathcal{G}_{Ic}	Fracture toughness in pure mode I.
\mathcal{G}_{II}	Energy release rate in mode II.
\mathcal{G}_{IIc}	Fracture toughness in pure mode II.
$\mathcal{G}_M, \quad M = 1+, 1-, 2+, 2-, 6$	Fracture toughnesses.
\mathcal{G}_{shear_c}	Fracture toughness in pure mode II.
\mathcal{G}_{shear}	Shear energy release rate.
\mathcal{G}_T	Total energy release rate.
\mathcal{G}_c	Critical energy release rate.
h	Plate thickness.
h_a	Laminate thickness.
h_c	Thickness of the central cut laminate (TCT tests).
h_e	FE thickness.
$(h_e)_{max}$	Maximum finite element thickness.
h_p	Clustering thickness (ply thickness).
h_{pp}	Thickness of a single pre-preg ply.
H	Lamina compliance tensor for intralaminar damage model.
H₀	Undamaged compliance tensor.
I_1	Mass by in-plane surface unit.
I_2	Mass by length unit.
I_3	Rotatory inertia term.
k_α	Contact stiffness.

Symbol	Description
k_α^*	Linearized contact stiffness.
k_Σ	Lumped stiffness of the plate and of the contact law.
k_b	Bending stiffness of the plate.
k_{bsm}	Lumped shearing, bending and membrane stiffness of the plate.
$k_i, \quad i = x, y$	Wave numbers.
k_m	Membrane stiffness of the plate.
k_m^*	Linearized membrane stiffness of the plate.
k_s	Shearing stiffness of the plate.
k_y	Linearized contact stiffness with plasticity.
k_H	Hertz contact stiffness.
K	Kinetic energy.
K	Penalty stiffness of an interface.
K_1	Penalty stiffness of an interface in pure mode I.
K_2	Penalty stiffness of an interface in pure shear mode.
K_{ij}	Dimensionless shear correction factors.
l_{cz}	Length of the cohesive zone.
l_e	In-plane element size.
ℓ^*	Characteristic finite element length.
ℓ_{max}^*	Maximum characteristic element length.
ℓ_{min}	Minimum dimension of an element.
ℓ_x	Finite element length at x direction.
ℓ_y	Finite element length at y direction.
L	Half specimen length (MMB or ENF tests).
L	Lagrangian function.

Symbol	Description
L	Length of a TCT specimen.
M_i	Impactor mass.
$M_j, \quad j = 1, 2$	Bending moments respect x ($i = 1$) and y ($i = 2$) axis.
M_L	Mismatch bending stiffness parameter for two-layer plates.
M_M	Mismatch bending stiffness parameter.
$M_{p,max}$	Largest plate mass which can remain unaffected by the boundaries.
$M_{p,wave}$	Mass of the plate area affected by the first wave.
M_p	Lumped mass of the structure.
M_p^*	Equivalent lumped mass of the structure.
M_x, M_y, M_{xy}	In-plane laminate moments.
n	Number of same thickness plate regions.
$n_j, \quad j = 1, 2, 3$	Unitary normal vector to a delamination plane.
n_d	Number of interfaces for delamination.
n_d^*	Number of delaminations.
N_e	Number of elements in a cohesive zone.
N_x, N_y, N_{xy}	In-plane laminate forces.
$\mathcal{N}(u_o, v_o, w_o)$	Non-linear terms of the plate governing equations.
$p(r)$	Normal contact pressure of the Hertz contact theory.
p_0	Maximum normal contact pressure.
P	Normal contact pressure.
P_B	Percent of bending in CAI test.

Symbol	Description
P_c	Critical load for crack propagation (MMB, ENF and TCT tests).
q	Power parameter of the contact law.
$q(x, y, t)$	Concentrated impact force.
Q_α	Effective contact modulus.
Q_x, Q_y	Through-the-thickness shear forces.
Q_{zi}	Effective contact modulus along the loading axis z of the impactor.
Q_{zp}	Effective contact modulus along the loading axis z of the plate.
r_c	Radial position of an arbitrary point in the contact zone.
$r_n(\theta)$	Position of the leading edge of the n -th wave mode.
$r_N, \quad N = 1+, 1-, 2+, 2-$	Elastic domain thresholds.
r_p	Plate radius.
R	Impactor tip radius.
R_c	Contact radius of the Hertz contact theory.
s	Unloading rigidity.
S_L	Longitudinal shear strength of a ply.
S_L^{is}	In-situ longitudinal shear strength of a ply.
S_T	Transverse shear strength (transverse compressive fracture).
S_u	Fiber shear strength.
t	Time.
t_i	Impact time.
\bar{t}_{hs}	Normalized impact time at the maximum impact force for half-space behavior.

Symbol	Description
\bar{t}_q	Normalized impact time at the maximum impact force for quasi-static behavior.
\bar{t}_w	Normalized impact time at the maximum impact force for finite plate behavior.
T	Surface tractions per unit area.
u_{fc}	Compressive displacement at failure.
U	Elastic energy or internal work.
v_L	Loading velocity.
V	External work.
$V(t)$	Impactor velocity.
V_0	Initial impactor velocity.
V_{ind}	Impact velocity for permanent indentation.
V_{per}^{com}	Impact velocity for perforation due to laminate compressive failure.
V_{per}^{sh}	Impact velocity for perforation due to laminate shear failure.
w_b	Displacement of the back face of the plate at the impact point.
w_i	Displacement of the impactor.
w_o	Displacement of the mid-plane of the plate at the impact point.
W	Total length of a TCT specimen.
W	Total work.
W_C	Work done by contact penalties.
W_E	External work.
W_I	Internal work.
$W_{mn}(t)$, $X_{mn}(t)$ and $Y_{mn}(t)$	Coefficients of Fourier series (complete analytical impact models).

Symbol	Description
W_{MS}	Work done in propelling mass added in mass scaling.
X_{PO}	Pull-out strength.
X_C	Longitudinal (fiber) compression strength.
X_T	Longitudinal (fiber) tensile strength.
Y	Thermodynamic force.
Y_C	Transverse compressive strength of a ply.
Y_T	Transverse tensile strength.
Y_T^{is}	In-situ transverse tensile strength.
α	Indentation.
α_0	Fracture angle.
α_0	Permanent indentation.
α_{cr}	Critical indentation as from of it permanent indentation starts.
$\alpha_{ii}, \quad i = 1, 2$	Coefficients of thermal expansion.
α_{max}	Maximum indentation.
β	Characteristic impact parameter.
β	Mixed-mode ratio.
$\beta_{ii}, \quad i = 1, 2$	Coefficients of hygroscopic expansion.
$\gamma_{ij}, \quad i, j = x, y, z \text{ or } i, j = 1, 2, 3$	Shear strains.
δt	Increment of time.
δt_{stable}	Stable time increment (FE explicit algorithm).
δ	Variational operator.
$\delta(\cdot)$	Dirac delta function.
$\delta_{ij}, \quad i, j = 1, 2, 3$	Kronecker delta operator.

Symbol	Description
δ_{LP}	Displacement at LP point (MMB tests).
δ_M	Displacement at M point (MMB and ENF tests).
ΔM	Difference of moisture content respect to the corresponding reference value.
ΔT	Difference of temperature respect to the corresponding reference value.
Δ^f	Propagation criterion for delamination.
Δ^o	Onset criterion for delamination.
Δ_{shear}	Euclidian norm of the relative displacements in mode II and mode III.
Δ_{shear}^f	Relative displacement for damage propagation in shear mode.
Δ_{shear}^o	Relative displacement for damage onset in shear mode.
Δ_3^f	Relative displacement for damage propagation in pure mode I.
Δ_3^o	Relative displacement for damage onset in pure mode I.
$\Delta_i, \quad i = 1, 2, 3$	Relative displacements.
Δ	Relative displacement vector.
$\varepsilon_i^o, \quad i = q, r$	Transverse shear strains.
$\varepsilon_i^o, \quad i = x, y, s$	In-plane stretching and shearing of the mid-plane (membrane strains).
$\varepsilon_i, \quad i = x, y, z, q, r, s$ or $i = 1, \dots, 6$	Contracted notation of the strain.
$\varepsilon_{ij}, \quad i, j = x, y, z$ or $i, j = 1, 2, 3$	Tensorial strain notation.
ε_{SG1}	Strain lecture from a gage located on the top face of a plate (CAI test).

Symbol	Description
ε_{SG3}	Strain lecture from a gage located on the bottom face of a plate (CAI test).
ε_c	Through-the-thickness compressive failure strain.
ζ , (or $\zeta_w = \zeta/2$)	Relative plate mobility, inelastic parameter, or loss factor.
η	Least-square fitting parameter of interlaminar fracture toughnesses.
η^L	Longitudinal friction coefficient.
η^T	Coefficient of transverse influence (transverse compressive fracture).
θ	Off-axis loading axis or orientation of a ply.
θ_s	Sliding angle (transverse compressive fracture).
κ_i , $i = x, y, s$	Curvatures.
λ	Norm of the relative displacement components.
λ	Relative stiffness.
λ_i , $i = x, y$	Wavelengths.
μ	Effective mass ratio.
μ	Friction coefficient.
ν	Isotropic Poisson ratio.
ν_{ij} , $i, j = 1, 2, 3$ or $i, j = r, \theta, z$	Poisson coefficients.
ν_m	Interface Poisson ratio.
Ξ	Computed energy dissipated by delamination.
Π	Total potential energy.
ρ	Density.

Symbol	Description
ρ_m	Density of the interface material.
σ_{fc}	Residual compressive strength in a CAI test.
$\sigma_i, \quad i = x, y, z, q, r, s$ or $i = 1, \dots, 6$	Contracted notation of the stress.
$\sigma_{ij}, \quad i, j = x, y, z$ or $i, j = 1, 2, 3$	Tensorial stress notation.
σ_{yc}	Compressive elastic limit of the plate in the through-the-thickness direction.
$(\sigma_1, \sigma_2, \sigma_6)_p$	Stress components on the back outer ply of the laminate.
$(\sigma_x)_{max}$ and $(\sigma_y)_{max}$	Maximum values of the in-plane tensile stresses due to the flexural deformation.
$\tilde{\sigma}^{(m)}$	Components of the stress tensor defined in a coordinate system (m) representing the fiber misalignment.
$\tilde{\sigma}$	Effective stress tensor.
τ	Mixed-mode interface stress.
τ^o	Mixed-mode interface strength.
τ_1^o	Shear pure mode interface strength.
τ_3^o	Pure mode I interface strength.
$\tau_{ij}, \quad i, j = x, y, z$ or $i, j = 1, 2, 3$	Shear stresses.
τ_{max}	Maximum allowable frictional shear stress.
$\tau_i, \quad i = 1, 2, 3$	Interface stresses.
$\tilde{\tau}_{\text{eff}}^T$ and $\tilde{\tau}_{\text{eff}}^L$	Effective stresses (transverse compressive fracture).
$\phi_i, \quad i = 1, 2$	Rotations of a transverse normal about the y ($i = 1$) and x ($i = 2$) axis.
$\phi_N, \quad N = 1+, 1-, 2+, 2-$	Loading functions.
φ^C	Fiber misalignment angle.

Symbol	Description
Ψ	Helmholtz free energy.
$\Psi^o(\beta)$	Elastic energy of the interlaminar constitutive equation.
Ψ^o	Function of the relative displacement space.
ω_{mn}	Natural frequencies of a plate.
(r, θ, z)	Cylindrical coordinates of the plate.
(u, v, w)	Displacements of the plate at (x, y, z) .
(u_1, u_2, u_3)	Displacements of the plate at (x_1, x_2, x_3) .
(u_o, v_o, w_o)	Mid-plane displacements of the plate at (x, y, z) .
(x, y, z)	Cartesian coordinates of the plate.
(x_1, x_2, x_3)	Cartesian coordinates of the ply.
$[C]_p$	Constitutive matrix of the back outer ply in the ply coordinate system.
$[S]$	Compliance matrix of the plate in the plate coordinate system.
$[T]_\gamma$	Rotation matrix of the engineering strains from the plate coordinate system to the ply coordinate system.

List of Acronyms

Acronym	Description
AFP	Automated Fiber Placement.
AITM	AIrbus Test Method.
ASTM	American Society for Testing Materials.
BVID	Barely Visible Impact Damage.
CAI	Compression After Impact.
CFRP	Carbon Fiber Reinforced Plastic.
CMC	Ceramic Matrix Composite.
CPU	Central Processing Unit.
DIC	Digital Image Correlation.
ENF	End-Notched Flexure test.
FE	Finite Element.
GB	Giga-Byte.
GFRP	Glass Fiber Reinforced Plastic.
GLARE	GLAss REinforced fiber metal laminate.
LaRC	Langley Research Center (failure criteria).
LEFM	Linear Elastic Fracture Mechanics.
LVDT	Linear Variable Differential Transformer.
MMB	Mixed-Mode Bending test.
MMC	Metal Matrix Composite.
MPI	Message Passing Interface mode.

Acronym	Description
NDI	Non-Destructive Inspection methods.
PMC	Polymeric Matrix Composite.
RAM	Random-Access Memory.
SG	Strain Gage.
TCT	Transverse Crack Tension test.
UEL	User ELe ment subroutine (Abaqus/Implicit code).
VCCT	Virtual Crack Closure Technique.
VUEL	User ELe ment subroutine (Abaqus/Explicit code).
VUINTER	User INTERaction subroutine (Abaqus/Explicit code).
VUMAT	User MATerial subroutine (Abaqus/Explicit code).

Chapter 1

Introduction and objectives

1.1 Introduction

A composite material is defined as the combination of two or more phases on the macroscopic scale. The mechanical performance and properties of the composite are superior to those of the individual constituent materials.

Typically, composite materials are classified in function of the reinforcement geometry, or in function of the matrix material. Related to the geometry of the reinforcement, it can be composed by long fibers, short fibers, or particles. The fibers can be presented randomly distributed, following an established direction in the composite, or even as a fabric. Related to the matrix material, the most typical are Polymeric Matrix Composite (PMC), Metal Matrix Composite (MMC), and Ceramic Matrix Composite (CMC).

When the PMC is reinforced by long fibers, it is called advanced Fiber Reinforced Plastic (FRP), using for example glass (GFRP) or carbon (CFRP). Advanced FRPs are often fabricated in the form of laminates. A laminate consists of one or more thin layers (laminae or ply) stacked together, where each one has the reinforcement oriented at one given direction, in the form of unidirectional plies. The orientation of each ply is changed suitably in order to stand the mechanical design requests. Nowadays, there are manufacturing systems completely automatized, Automated Fiber Placement machine (AFP), that stack each ply according to the final geometry of the structure and with the desired fiber orientation, or even with orientations that change point to point (curved fibers).

The application of advanced FRPs is gradually increasing as a result of their good specific mechanical properties and increased flexibility of design. Composites are used in a wide spectrum of industrial components and customers, where the aerospace industry, including military and commercial aircraft, is the largest consumer [1].

At present, the advanced FRPs are included in the set of materials that improve and advance the aviation industry. In this field, it is well known that the main issues of concern are the greenhouse gas emissions and the fuel costs, which are the largest operating expense for airlines. The development of technologies to address these issues has clear economic and environmental benefits. As documented by King et al. [2], the reduction of the amount of fuel burnt can be achieved by "*reducing both aircraft weight and its parasitic drag (drag due to the non-lift component, i.e. the fuselage)*". In this sense, the application of advanced FRPs in primary and secondary structures is taking part in the improvement of the whole weight due to the good combination of light weight, and high stiffness and strength.

When composites are to be used in structural components, a design development program is generally initiated during which the performance of the structure is assessed prior to its use. Typically, the process of design starts with the analysis of a large set of simple small specimens and, when sufficient knowledge is acquired at this level, it is changed over to a more complex structure but carrying out fewer tests. This process is repeated until to reach the complete full scale product, at which one or two very expensive tests are performed. This process is commonly known as the Building Block approach [3]. At each step of this approach, a combination of testing and analysis techniques is typically performed, because testing alone can be prohibitively expensive due to the large number of specimens needed to verify every geometry, loading, environment, and failure mode [4].

As reported Davies and Ankersen [5], design time is expensive and structural testing is also expensive, of the order of \$40 million for a new aircraft variant. Therefore, the development of reliable analysis tools that enable to understand the structure mechanical behavior, as well as to replace most, but not all, the real experimental tests, is clear interest. Recent advances in simulation by means of computers, known as Virtual Mechanical Testing, have given realistic models for the prediction of the complicated physical processes involved in the behavior of

composite materials. These models are of special interest in configurations that are too complex to certify by purely empirical methods.

During all the stages of the certification process for aeronautic structures, two key concepts are permanently addressed: damage resistance (or durability), and damage tolerance. As reported by Bailie et al. [6], *"the damage resistance is the ability of the structure to resist damage initiation and/or growth for a specified length of time. How durable the structure should be designed to be is an economic issue. A highly durable structure requires fewer inspections and repairs"*. On the other hand, *"the damage tolerance is the ability of the structure to resist catastrophic failure in the presence of cracks or other damage without being repaired, for a specified number of operations (flights) or length of time in service. Damage tolerance is usually demonstrated by residual strength tests conducted on a component that has been previously damaged in a well defined manner. Residual strength must be greater than a limit value, defined by the certifying authority, that depends on the ability to detect the damage during an inspection"*.

It is well known that laminated composite structures have excellent fatigue lives compared to metallic structures. However, they are specially weak to environment changes and impact loadings.

An impact is a dynamic event where the contact of the collided bodies generates forces that act in a very short interval of time, and initiate stress waves which travel away from the region of contact. Impacts by foreign objects can be expected during all the stages of the life of the composite structure (manufacturing, service and maintenance). The design of impact damage resistant and damage tolerant composite components is a conceptually difficult task. Unlike metallic components, which can yield and dissipate energy via plasticity, composites dissipate energy by a variety of interacting damage modes. The damage created often cannot be detected by simple visual inspection, can grow under load, and can cause severe reductions in the stiffness and the strength. Lack of knowledge of the impact effects on composite structures is a factor in limiting the use of composite materials [7].

1.2 Motivation

Susceptibility to damage from concentrated out-of-plane impact forces is one of the major design concerns of structures made of advanced FRPs used in the aeronautical industry. The development of virtual mechanical testing models to analyze the impact damage resistance of a structure is of great interest for reducing certification costs. But even more, the prediction of the residual strength of the impacted structure is the most valuable data. However, it is a difficult task.

When an impact is given on a composite structure, the description of the problem is quite complex. Laminated composites are heterogeneous materials due to presence of local flaws, such as air micro-gaps, resin-rich zones, discontinuities of the fibers, loss of fiber lineup, changes of fiber density, etc. Accordingly, composite structures degrade in a large variety of failure mechanisms (matrix cracking, fiber-matrix interface debonding, delamination, and fiber breakage) which interact in a complicated way, especially when the structure is subjected to impact loading. Moreover, the onset and the evolution of these failure mechanisms depend on a large set of impact parameters, that are the physical parameters and properties of the projectile, the structural configuration, and the environmental conditions. Due to all these facts, the development of a reliable tool for the prediction of the impact damage resistance and the corresponding damage tolerance is a challenging task, which at present, it is not available.

Analytical impact models representing the physical system must be considerably idealized to render them amenable for a possible theoretical treatment. Consequently, the solutions obtained often are valid for a narrow range of impact configurations, or even they are not suitable because the predictions are too far from the reality.

Using the major recent advances in computational methods and the conceptual representation of the composite failure mechanisms, the virtual testing of the impact event by means of numerical simulations of finite element (FE) codes seems to be reachable. The proposal of modeling impact in a FE code is in part possible due to the advances in Computer Sciences which allow enough detailed description of the event with acceptable analysis runtime. This is succeeded by means of the parallelization of the FE model in multiple CPUs, i.e. using a cluster.

In contrast to the analytical models, FE methods are capable of modeling large number of impact configurations and several related phenomena, such as dynamic modeling, contact analysis, and progressive degradation of the material. The material behavior can be described by the implementation of constitutive models formulated in the framework of Continuum Damage Mechanics. One of the main keys for the realistic prediction of the virtual testing is the suitable formulation of the constitutive models.

1.3 Objectives

The main goal of the present thesis is the development of a FE tool for the simulation of two sequenced and standardized tests, drop-weight impact and Compression After Impact (CAI), on specimen coupons manufactured with polymer-based composite materials reinforced with continuum fibers. Drop-weight impact is categorized as a low-velocity and large mass impact test. Under this loading, the delamination is the major damage mechanism as it reduces considerably the compressive strength of the structure. On that account, the CAI test is performed to assess the effect of the impact damage on the compressive strength. Therefore, the purpose of the simulations is the prediction of the residual compressive strength of the corresponding impacted specimen; to achieve this goal, the previous simulation of the impact should be accurately performed.

The reliability of the predictions depends mainly on the constitutive model for the description of the composite material behavior. That is the description of the onset and the growth of the different damage mechanisms. The strategy used here is based on modeling the laminate failure, where a laminate consists of homogeneous plies, each with orthotropic properties that depend on the fiber orientation. Accordingly, two separated constitutive models are formulated using a rigorous thermodynamic framework: one for the description of the debonding between the plies of the laminate (i.e. delamination), and another for the description of the damage mechanisms that can occur in each ply (i.e. intralaminar damage mechanisms: matrix cracking, fiber-matrix interface debonding, and fiber breakage). The formulation and implementation of both constitutive models are performed separately, but the interaction of the damage mechanisms is ensured since both damage models

are used in the same FE model. The proposed delamination model and intralaminar model are respectively based on previous thesis and papers presented by Turon et al. [8–13] and Maimí et al. [14–17].

Other aims of the present project, that are as relevant as the FE predictions, are the analytical description of the impact event and the realization of an experimental test plan. The FE simulations need an appropriate experimental program to assess the validity of the numerical predictions.

Also, due to the simplicity of the structure considered (monolithic, flat and rectangular laminated composite plates with conventional stacking sequences), the analytical description of the impact event is feasible. This analytical description comprises the prediction of the elastic response and the proposals of new thresholds at which significant damage starts. The analytical description is suitable for preliminary design analysis, as it enables the fast assessment of the role that each parameter plays in the impact event. Accordingly, the analytical description is useful for the definition of impact experimental plans. Although the analytical tools studied herein are focused on laboratory coupons, the concepts acquired often can be applied for more complex impact configurations.

Since the experimental drop-weight impact and CAI tests are performed with the goal of having real data to validate the results obtained by means of the FE simulations, the impact configurations considered should assure the damage occurrence. Because of that, the design of the experimental plan is carried out by means of the analytical impact models.

1.4 Thesis lay-out

According to the objectives described previously, the thesis is structured as follows:

In Chapter 2 and in the related Appendix A, a detailed review of the analytical impact models available in the bibliography is given. This review includes the models for the prediction of the elastic impact response, as well as the description of available and new proposals for damage thresholds. By means of this analysis, the experimental plan and set-ups of the drop-weight impact and CAI tests are defined in Chapter 3.

In Chapter 4, the significant experimental results of the drop-weight impact

tests, the non-destructive inspections, and the CAI tests are shown and discussed. Additionally, comparisons with analytical predictions are also carried out.

Related to the development of FE simulations, an interlaminar damage model for the simulation of the delamination onset and growth under variable mixed-mode conditions is developed in Chapter 5. The formulation and implementation presented is a modified proposal of the model originally developed by Turon et al. [8–13]. The model is validated by simulating quasi-static standard delamination toughness tests and by comparing the results with experimental data.

In Chapter 6, the formulation of a continuum damage model for the prediction of the onset and accumulation of intralaminar damage mechanisms in laminated composites is described. The model presented is based on the work developed by Maimí et al. [14–17]. In this chapter, simulations of different tests in order to illustrate the limitations of using a constitutive damage model formulated in the Continuum Damage Mechanics framework are presented.

Using the damage models developed, some of the impact and CAI tests which are tested experimentally are also simulated. The considerations for the proper simulation of the tests are detailed in Chapter 7, as well as the virtual results and their comparison with the experimental data presented previously in Chapter 4.

Finally, the thesis is concluded in Chapter 8 with an overall assessment of its achievements and a discussion of possible future research developments.

Chapter 2

Analytical description of the impact event

2.1 Introduction

The prediction of damage in laminated composite structures induced by the impact of an external object is a complex task. Damage results from the interaction between different failure mechanisms (matrix cracking, fiber-matrix interface debonding, delamination, and fiber breakage), and it depends on the governing parameters of the impact event. These parameters include the physical parameters and properties of the projectile, the structural configuration, and the environmental conditions.

Experimental evidence shows that impact damage is directly related to the nature of the impact behavior which, in turn, is controlled by the governing parameters. Therefore, it is useful to know the effects of each governing parameter on the impact behavior, and thus to have a qualitative understanding of the possible damage mechanisms that can occur. For example, under constant energy impact conditions, a quasi-static type of impact behavior will result mostly in delamination damage whereas in a dilatational wave-controlled type of impact behavior will result mostly in permanent indentation and fiber breakage at the impact site [18]. There are approaches in the literature, based on analytical models, which predict the type of the impact response for a determined configuration, such as impact on flat and rectangular laminated composite plates [19, 20]. The initial knowledge of the impact behavior not only helps in assessing the possible type of damage induced,

but it is also useful for the development of efficient numerical models, for planning test programs, and for selecting a proper simplified analytical model to describe the impact event.

The analytical models are a suitable and powerful tool to obtain fast predictive results for a given impact configuration. Generally, these analytical models are limited to simple geometries of the structure and rely on stepwise solution of nonlinear differential equations or integral equations which describe the transitory response of the system until damage onset, i.e. in the elastic regime. The results given by these analytical models are suitable to compare different impact cases with different values of the governing parameters.

The framework and the ingredients used for the impact dynamics description on rectangular, flat, and monolithic laminated composite plates are presented in this chapter. Therefore, a literature survey of the analytical impact models available is presented. On the other hand, an overview of the main approaches used to identify quickly the nature of the impact behavior is done. Finally, a review of the analytical damage thresholds available in the literature, as well as the development of new proposals for some damage mechanisms are presented.

The issues analyzed in this chapter and in the related Appendix A are used to define a suitable set of low-velocity impact tests in order to capture different damage phenomena which can occur. The details of this task are described in Chapter 3.

2.2 Impact behavior

Experimental evidence shows that the nature of the impact behavior and the resulting damage are related. Since the impact behavior is defined by the governing parameters of the impact event, the damage created also depends on these parameters. For impacts on rectangular, flat, and monolithic laminated composite plates, the governing parameters are typically grouped in three sets: plate parameters (thickness, in-plane size, lamina type, elastic and fracture properties, density, stacking sequence, and boundary conditions), impactor parameters (shape, size, elastic properties, mass, velocity, and incidence angle), and the environmental conditions.

The impact behavior can be predicted easily in the elastic regime by means of

approaches based on analytical models of the impact event. Thus, the information obtained can be used to know the possible related damage which can occur. Damage starts when a suitable parameter of the elastic response, typically the impact force, is greater than the corresponding damage threshold (see Section 2.6).

Before to describe the models for the prediction of the impact response, it is useful to review the different types of impact responses for plates (impact behaviors), as the response type is crucial to have a qualitative insight of the resulting possible damage, and for the selection of a simplified model for impact description. Detailed descriptions of the impact behaviors are given by Olsson [20–25], by Christoforou and Yigit [18, 19, 26, 27], by Abrate [7, 28], and by Lin and Fatt [29].

According to Olsson [22], an impact event initiates stress waves propagating from the impact point, where the influence of the waves gradually fade away due to material damping and wave scattering. For impact times t_i close to the time required for the waves to propagate through-the-thickness direction (i.e. $t_i \leq \frac{h}{c_z}$, where h is the plate thickness, and c_z the speed of sound in the through-the-thickness direction), the response is dominated by three-dimensional wave propagation (see Figure 2.1.a). For longer impact times, flexural and shear waves govern the response (see Figure 2.1.b). For times much longer than the time needed by these waves to reach the plate boundaries, the lowest vibration mode of the impactor-plate system predominates (see Figure 2.1.c). Eventually, the deformation mode approaches a purely static deformation.

The response dominated by through-the-thickness waves is typically associated with ballistic impact, which in most cases, causes localized and easily detectable damage. Related to the impacts that can have an aircraft, the response in Figure 2.1.b is typical for impacts by hail and runway debris, whereas the response in Figure 2.1.c is typical for dropping of heavy tools. The in-plane plate size and the boundary conditions affect the response shown in Figure 2.1.c, but not the responses shown in Figures 2.1.a and 2.1.b, because in these cases, the impact event is over before the stress waves have reached the edges of the structure. The load and the deflection are out of phase during a small mass impact while they are more or less in phase during a large mass impact. Furthermore, due to the more localized deflection, small mass impactors cause higher impact loads and earlier damage initiation than large mass impactors with the same kinetic energy.

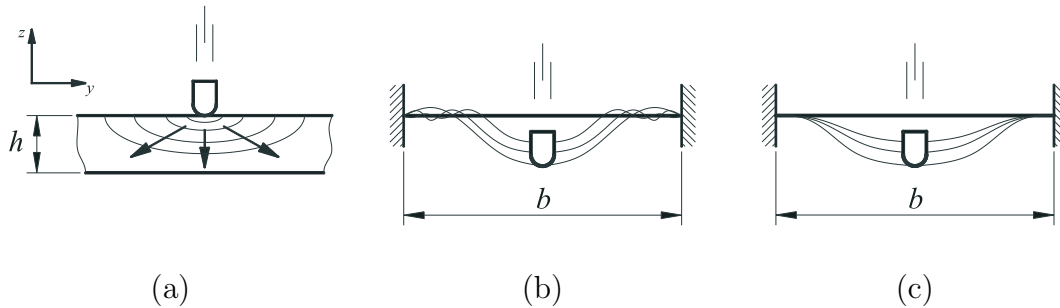


Figure 2.1: Impact responses (after Olsson [22]): (a) dominated by dilatational waves, (b) dominated by flexural and shear waves, and (c) quasi-static response.

Summarizing, the impact behaviors can be classified into three extreme categories that are referenced in the literature as: (a) *three-dimensional wave-controlled, through-the-thickness wave-controlled* or *ballistic impact*; (b) *global behavior with no size effects, flexural and shear wave-controlled*, or *impact on an infinite plate*; (c) *fully-global* or *quasi-static impact behavior*. If the global response of the plate can be neglected (extreme case of (b)), this impact behavior is typically called *half-space impact*.

Clear Visible Impact Damage is associated with the response shown in Figure 2.1.a. In addition, *Barely Visible Impact Damage* (BVID) is associated with the response types shown in Figures 2.1.b and 2.1.c [6], where delamination is the main damage mechanism. Delaminations are a major threat because they are hidden and reduce significantly the compressive strength of the impacted structure.

Impacts are often categorized in the literature as *low-* or *high-velocity*, but there is not a clear transition between categories and authors disagree on its definition [30]. Some authors refer, improperly, to the response type under small mass of the impactor as high-velocity impact and under large mass impact as low-velocity impact. Olsson [20], and Christoforou and Yigit [19] demonstrate that the response type under elastic conditions depends on the impactor mass, the mass of the surface of the plate affected by the impact and the structural stiffness. Increasing the velocity, the impact force increases and induces a large damage extension or even a change in the main damage mechanism type, but the velocity does not affect the impact behavior. The classification by means of the velocity may be motivated from a practical point of view for damage creation, since large mass impactors

usually cause damage at a lower velocity than small mass impactors with the same kinetic energy. When an impact is categorized as low-velocity impact, the material properties are assumed to be rate independent [31].

A physically based criterion to distinguish low- or high-velocity impact categories was suggested in Davies and Godwin [32], which defined high-velocity impact as cases where the ratio of the impactor velocity V_0 versus the speed of sound in the plate thickness direction c_z , exceeds the through-the-thickness compressive failure strain ε_c . That is:

$$\varepsilon_c = \frac{V_0}{c_z} \quad (2.1)$$

The assumed failure mode implies a response governed by through-the-thickness waves (i.e. ballistic impact). For typical composite materials, the corresponding impactor velocity ranges from 10 to 20m/s [33]. However, the large strains associated with contact stresses are highly localized and the resulting failure may often not affect the general response of the plate. Thus, response governed by flexural and shear waves has been experimentally demonstrated in carbon/epoxy laminates at velocities of 45m/s. Thus, the use of velocity for classifying impact events is highly debatable [20].

Finally it should be noted that the term *hyper-velocity* has come to be applied to satellites and spacecraft which may be struck by micro-meteorites where the impact duration is measured in nanoseconds, and both the meteorite and impacted structure will vaporize [21].

2.3 Local deflection

Impact on monolithic plates involves local and global deflection. Therefore, impact damage may be caused due to local contact stresses and/or stresses resulting from the structural response. Figure 2.2 shows two extreme responses of a plate under impact loading. Only local deflection is shown in Figure 2.2.a, which can result from small-mass and high-velocity impact on thick laminate plates. However, only global deflection is shown in Figure 2.2.b, which can occur from large-mass and low-velocity impact on thin laminate plates.

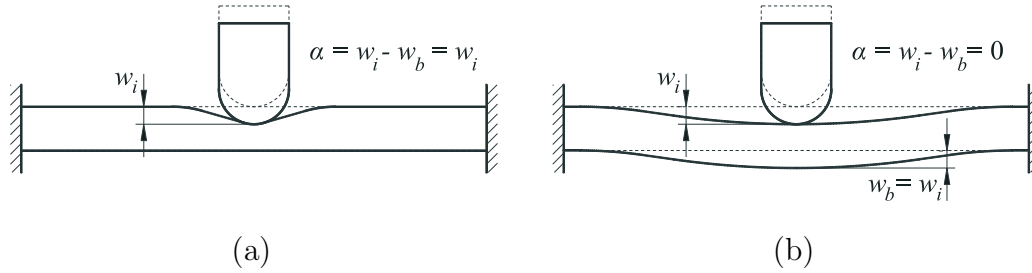


Figure 2.2: Extreme plate responses under impact loading, (a) pure local deflection and (b) pure global deflection.

The local deflection typically is described by means of a proper contact law, which relates the concentrated contact load F_c and the indentation α as:

$$F_c = k_\alpha \alpha^q \quad (2.2)$$

where k_α is the contact stiffness, q is a power parameter, and α is the indentation defined as the difference between the displacement of the impactor w_i and the displacement of the back face w_b [7], or mid-plane w_o [22], of the plate at the impact point. That is:

$$\alpha = w_i - w_o \quad (2.3)$$

As it will be shown in next sections, the contact law is a required ingredient for the development of analytical models of the impact event. Alternative models, such as spring-dashpot and the momentum balance methods, use the coefficient of restitution to characterize the local energy loss due to impact [27]. The contact law can be obtained experimentally or by analytical methods, and depends on the material properties of the bodies, the stacking sequence, and the size and shape of the impactor.

For composite materials it is accepted that local deflection can be modeled using a statically determined contact law for moderate strain rates [34, 35], as happens in low-velocity impact events. The static contact load between two linear elastic bodies is described by the *Hertz contact law*, which is based on the following assumptions: infinite plate thickness (i.e. impact on a half-space plate), the bodies in contact are isotropic, frictionless contact between the impactor and the plate, and negligible

curvature of the plate surface during contact (i.e. the wrapping effect is neglected). The Hertz contact law has been applied in a wide range of cases even when if all assumptions are not satisfied (e.g. indentation on laminated composite plates), because usually it fits quite well the experimental data obtained from indentation tests.

In the literature there are advanced developments for the contact description which take into account the anisotropy of laminated composite materials. These models are not often simple as the Hertz contact law, because the resulting laws require the numerical solution of differential or integral equations. Some examples for transversely isotropic materials are the work presented by Dahan and Zarka [36], and Turner [37]. For orthotropic materials, the work of Wu and Yen [38], Chao and Tu [39], and Swanson [40] should be mentioned.

A comprehensive justification of the Hertz contact law agreement for local deflection modeling of laminated composite plates in contact with a hemispherical indenter, and a collection of some developments available in the literature to get over some of the Hertz assumptions are given by Abrate [7], and Davies and Olsson [21]. In [21], the descriptions are given in function of the static indentation tests which can be performed:

- **Measuring differences between front and back face deflections on plates with an unsupported back face.** This test is suitable for local deflection analysis in flexible plates. Under low contact loads, the load-indentation behavior is in agreement with the Hertz contact law [41, 42]. Under high contact loads, the plate may result in a large flexural curvature, which increases the contact area (i.e. the wrapping effect). Also, matrix cracking and delamination reduces the flexural stiffness which contributes to a large flexural curvature. Due to this increase of the contact area, the pressure distribution changes from a bell-shaped (Hertzian-type distribution) to a saddle-shaped. As a result of this redistribution, the indentation decreases as the force keeps increasing [7]. However, this effect has a small influence on the response, which is then dominated by global plate deflections.
- **Placing the plate on a flat rigid support.** This test is suitable for the local deflection analysis in rigid plates. Under low contact loads, the load-

indentation behavior is in agreement with the Hertz contact law. However, under moderate loads the behavior results in a softening response caused by the fiber damage and plasticity of the matrix. There are some simple models which take into account this effect and they yield more realistic results, such as the work of Cairns [43], Christoforou [44], and Yigit and Christoforou [45]. On the other hand, if the thickness of the plate is small enough there is a stiffening effect on the load-indentation behavior which depends on the ratio between the indentation depth and plate thickness [46]. This effect is included in the contact models of Suemasu et al. [47] and Chen et al. [48].

2.3.1 Hertz contact law adapted for laminated composite plates

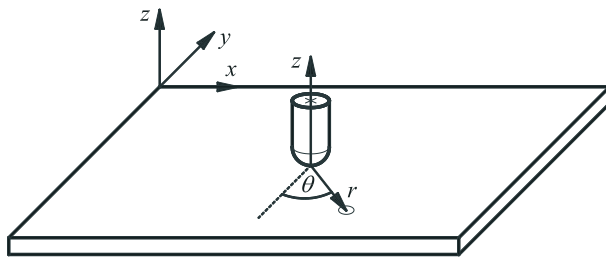
Considering Equation (2.2) and the case of a hemispherical impactor indenting a plate (see Figure 2.3), the Hertz contact law is defined by equaling the power q to $3/2$, and the contact stiffness k_α to k_H which is given by:

$$k_H = \frac{4}{3}Q_\alpha\sqrt{R} \quad (2.4)$$

where:

$$Q_\alpha = \left(\frac{1}{Q_{zi}} + \frac{1}{Q_{zp}} \right)^{-1} \quad (2.5)$$

The parameters Q_{zi} and Q_{zp} are the effective contact modulus along the loading axis z of the impactor and the plate, respectively. R is the impactor tip radius.



Cartesian coordinates: (x, y, z)
Cylindrical coordinates: (r, θ, z)

Figure 2.3: Coordinate systems.

The normal contact pressure $p(r)$ of the Hertz theory varies within the contact radius R_c as:

$$p(r) = p_0 \sqrt{1 - \frac{r_c^2}{R_c^2}}, \quad 0 \leq r_c \leq R_c \quad (2.6)$$

$$R_c = \left(\frac{3 F_c R}{4 Q_\alpha} \right)^{\frac{1}{3}} = \sqrt{R\alpha} \quad (2.7)$$

where r_c is the radial position of an arbitrary point in the contact zone, and p_0 is the maximum pressure located at $r_c = 0$ given by:

$$p_0 = \frac{3F_c}{2\pi R_c^2} \quad (2.8)$$

For isotropic materials (e.g. a steel impactor), the effective contact modulus is defined by:

$$Q_z = \frac{E}{(1 - \nu^2)} \quad (2.9)$$

where E and ν are the Young modulus and the Poisson ratio, respectively. For the case where the indenter is much stiffer than the plate, Equation (2.5) simplifies to $Q_\alpha \approx Q_{zp}$.

The extension of Equation (2.9) for materials with transverse isotropy (along the loading axis z) is [22]:

$$Q_{zp} = \frac{E_z}{(1 - \nu_{rz}\nu_{zr})} \quad (2.10)$$

where ν_{rz} and ν_{zr} are the through-the-thickness Poisson ratios. In most laminate plates $\nu_{rz}\nu_{zr} \approx 0$, and Equation (2.10) can be simplified to $Q_{zp} = E_z$ [41, 46]. The through-the-thickness Young modulus of the laminate E_z is common to set equal to the transversal Young modulus of a single ply (i.e. $E_z = E_2$).

It is important to remark that Equation (2.10) is an approximation of the effective modulus of transversally isotropic plates which underestimates the contact modulus of typical composite plates by 10-20% [23, 40].

More advanced expressions of Q_{zp} for transversally isotropic materials are available in the literature: Turner [37, 40, 49], or that of Greszczuk [23, 50].

The expression of Q_{zp} proposed by Turner [37] is given as:

$$Q_{zp} = \frac{2}{\beta_1 \beta_3} \quad (2.11)$$

where:

$$\beta_1 = \left(\frac{\frac{E_r}{E_z} - \nu_{rz}^2}{1 - \nu_{rr}^2} \right)^{1/2}, \quad \beta_2 = \frac{1 + \left(\frac{E_r}{2G_{rz}} - 1 \right) - \nu_{rz}(1 + \nu_{rr})}{1 - \nu_{rr}^2} \quad (2.12)$$

$$\beta_3 = \left(\frac{\beta_1 + \beta_2}{2} \right)^{1/2} \left(\frac{1 - \nu_{rr}}{G_{rr}} \right)$$

The expression developed by Greszczuk [50] is given as:

$$Q_{zp} = \frac{2\sqrt{\frac{G_{rz}}{C_{rr}}} (C_{rr}C_{zz} - C_{rz}^2)}{\sqrt{(\sqrt{C_{rr}C_{zz}} + G_{zr})^2 - (C_{rz} + G_{zr})^2}} \quad (2.13)$$

where:

$$C_{rr} = \frac{E_r(1 - \nu_{rz}\nu_{zr})\Omega}{(1 + \nu_{rr})}, \quad C_{rz} = E_r\nu_{zr}\Omega \quad (2.14)$$

$$C_{zz} = E_z(1 - \nu_{rr})\Omega, \quad \Omega = \frac{1}{(1 - \nu_{rr} - 2\nu_{rz}\nu_{zr})}$$

In an orthotropic plate, the effective contact modulus Q_{zp} defined by Equation (2.10) becomes directionally dependent. Then, the shape of the indentation, which is circular in transverse isotropic plates along z axis, becomes elliptical in orthotropic plates. The effective contact modulus can be estimated by integrating $E_r(\theta)$ over 2π and taking the average [22]. However, since in most laminated plates $\nu_{rz}\nu_{zr} \approx 0$, the solution again simplifies to $Q_{zp} = E_z$.

2.3.2 Unloading and reloading contact process

Typically, in an impact event the contact force increases to a maximum value and then decreases back to zero. During the unloading phase, Yang and Sun [41] found

that the Hertzian contact law was not adequate. The unloading phase is significantly different from the loading phase due to permanent indentation. In order to account this effect, Crook [51] proposed the following equation:

$$F_c = F_m \left(\frac{\alpha - \alpha_0}{\alpha_{max} - \alpha_0} \right)^{5/2} \quad (2.15)$$

where F_m is the contact force at the start of the unloading, α_{max} is the indentation corresponding to F_m (i.e. maximum indentation) and α_0 is the permanent indentation. Equation (2.15) can be rewritten as:

$$F_c = s (\alpha - \alpha_0)^{5/2} \quad (2.16)$$

where:

$$s = \frac{F_m}{(\alpha_{max} - \alpha_0)^{5/2}} \quad (2.17)$$

is called unloading rigidity. Equating the Hertz contact law for loading with Equation (2.15), the permanent indentation α_0 and the critical indentation α_{cr} as from of it permanent indentation starts, are given as:

$$\alpha_0 = \begin{cases} \alpha_{max} \left(1 - \left(\frac{\alpha_{cr}}{\alpha_{max}} \right)^{2/5} \right) & \text{if } \alpha_{max} > \alpha_{cr} \\ 0 & \text{if } \alpha_{max} \leq \alpha_{cr} \end{cases} \quad (2.18)$$

$$\alpha_{cr} = \frac{k_H}{s} \quad (2.19)$$

The procedure in order to define α_{cr} starts by the selection of a proper value of α_0 by means of the unloading contact law (Equation (2.15)), so that the areas under the analytical unloading curves are equal to that calculated from the corresponding experimental curves. If these values of α_0 are substituted into Equation (2.17), a range of values of s is obtained. Using the average of s values, the value of α_{cr} is finally obtained.

If a subsequent reloading phase is done, the contact law is also distinct from the unloading curve but always returns to the point where unloading began [41]. The reloading curve is modeled by:

$$F_c = F_m \left(\frac{\alpha - \alpha_0}{\alpha_{max} - \alpha_0} \right)^{3/2} \quad (2.20)$$

In this case, there is no need to perform reloading experiments to find the parameters of the contact law.

2.3.3 Elastic-plastic contact models

Permanent deformations can be introduced in composite materials when the indentation exceeds a critical value because the material behavior is mainly governed by the properties of the matrix where a plastic behavior is expected. Under this circumstance, the Hertz contact law overestimates the maximum contact force and elastic-plastic contact laws can yield more realistic results. In these models, the critical indentation is taken into account during the loading process, unlike the previous approach where the critical indentation is accounted for using the unloading phase.

Elastic-plastic models assume that initially the material behaves elastically until a critical indentation is reached (see Figure 2.4). At this point, the contact area is divided into a plastic zone and an elastic zone as the loading increases and a new contact law is obtained [7]. Some elastic-plastic contact models are described below.

The elastic-plastic model developed by Christoforou [44] describes the contact loading and unloading between a rigid sphere and a thin laminated composite plate supported on a rigid substrate. Thus, the model is focused only on local deflections since the global response becomes negligible. The material is assumed to be transversely isotropic and follows an elastic-perfectly plastic behavior of the through-the-thickness normal stress-strain law. As yielding stress, a maximum shear failure criterion governed only by the fiber shear strength S_u is considered, although it is approached to the shear strength of the laminate S_L [19]. The development of Cairns [43] results in the same contact law for loading by assuming that the contact radius and the indentation are much smaller than the impactor radius.

Therefore, for the loading case, the contact law is defined by:

$$F_c = \begin{cases} \frac{\pi R E_z}{(1 - \nu_{rz} \nu_{zr}) h} \alpha^2 & \text{if } 0 \leq \alpha \leq \alpha_{cr} \\ 2\pi R S_u (2\alpha - \alpha_{cr}) & \text{if } \alpha_{cr} < \alpha \leq \alpha_{max} \end{cases} \quad (2.21)$$

and for the elastic unloading phase, the contact law is:

$$F_c = \frac{\pi R E_z}{(1 - \nu_{rz} \nu_{zr}) h} (\alpha^2 - \alpha_0^2) \quad (2.22)$$

where h is the specimen thickness. The critical indentation α_{cr} and the permanent indentation α_0 are given by:

$$\alpha_{cr} = \frac{2S_u h (1 - \nu_{rz} \nu_{zr})}{E_z} \quad (2.23)$$

$$\alpha_0 = \alpha_{max} - \alpha_{cr} \quad (2.24)$$

Another contact law is proposed by Yigit and Christoforou [45]. It is obtained by combining the classical Hertz contact theory and the elastic-plastic indentation theory given in Johnson [34]. In this case, the contact law for loading is given by:

$$F_c = \begin{cases} k_H \alpha^{3/2} & \text{if } 0 \leq \alpha \leq \alpha_{cr} \\ k_H \alpha_{cr}^{3/2} + k_y (\alpha - \alpha_{cr}) & \text{if } \alpha_{cr} < \alpha \leq \alpha_{max} \end{cases} \quad (2.25)$$

and for the elastic unloading phase, the contact law is:

$$F_c = k_H (\alpha^{3/2} - \alpha_m^{3/2} + \alpha_{cr}^{3/2}) + k_y (\alpha_{max} - \alpha_{cr}) \quad (2.26)$$

where k_y is the linear stiffness of the elastic-plastic loading phase which is equal to the slope of the elastic indentation curve at $\alpha = \alpha_{cr}$:

$$k_y = \frac{3}{2} k_H \sqrt{\alpha_{cr}} \quad (2.27)$$

The critical indentation α_{cr} can be obtained from the contact stress distribution using a maximum shear failure criterion [34]. Knowing that Y_C is the transverse compressive strength of the laminate, α_{cr} is approached to [26]:

$$\alpha_{cr} = \frac{0.68 (Y_C)^2 \pi^2 R}{Q_\alpha^2} \quad (2.28)$$

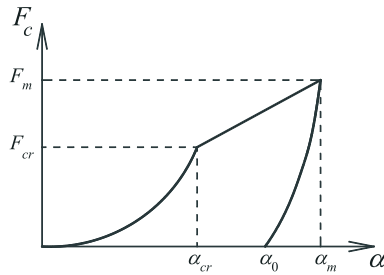


Figure 2.4: Detail of the contact law phases.

2.3.4 Linearized contact laws

In the analytical models of the impact event (see Section 2.4), the local deflections are simply described using a proper contact law. When the contact law is replaced in the governing equations of the plate and of the impactor, an exact solution of these equations generally are not available and a numerical solution is required. However, in some cases a closed-form solution can be obtained if the contact law is linearized (e.g. Christoforou and Swanson [52]; Olsson [35]). The resulting closed-form equations are more useful to gain a better understanding of the effects of the governing parameters on the behavior of the impact event.

Yigit and Christoforou [53] proposed a linearization of the elastic-plastic contact law of Christoforou [44]. Also, the loading contact law presented in [45] is linearized by Christoforou and Yigit [27], and used in [19, 26, 54]. In addition, Choi and Lim [55] developed a linearization of the Hertz contact law which allows to model low-velocity impact problems in a general-purpose finite element method software.

2.4 Analytical impact models

The analytical impact models are a powerful tool to get fast predictive results for a given impact configuration. These models are usually developed to predict the response of the system in the elastic regime, which is sufficient to compare different impact cases with different values of the governing parameters.

These models describe the motion of the impactor, the motion of the structure (e.g. laminated composite plates) and the local deflections in the area surrounding the impact point. To consider these local deflections, a contact law is commonly used.

Closed-form solutions can be obtained for some cases. Usually, these solutions are developed by means of *Duhamel integral* (i.e. *convolution integral*), *Laplace* and *Fourier transforms*. If a closed-form solution is not possible, then a numerical method is required, such as *Newmark step-by-step time integration method*.

It is essential to identify the effects of the large number of governing parameters on the impact behavior. In order to make the analysis more manageable, a dimensionless framework for the formulation of analytical models is recommended [56]. The goal is to reduce the number of governing parameters into a set of suitable governing dimensionless parameters that provide more insight into the impact problem, minimize the amount of computations required, and produce the output in particularly instructive forms [45]. The definition of these dimensionless parameters are usually given by means of *Buckingham Pi Theorem* [57], such as in Yigit and Christoforou [26].

The analytical models are often classified in function of how the plate is modeled [7, 28]. Davies and Olsson [21] classify the models in two main groups: *multi-degree-of-freedom models* and *one- or two-degree-of-freedom models*. The first group yields the typically so-called *complete analytical models*, and are based on numerical mode summation which rarely allows explicit expressions for the assessment of the influence of the different parameters. The second group includes *energy-balance models* and *spring-mass models*. These usually allow closed-form solutions which explicitly show the influence of the governing parameters, but have limited flexibility in handling complex geometries and different impact behaviors.

For the impact cases discussed in the present thesis, the inertia of the impactor is usually treated by considering its rigid motion described by Newton law. The inertia of the plate is more complicated, because during impact space deflections and transverse rotations are experienced. Typically, the weight load of the impactor is neglected, because it may be expected that the gravitational force is small relative to the contact force during the impact. On the other hand, the static properties of a material for low-velocity impacts are used without discussion of possible strain-rate effects [58].

2.4.1 Complete analytical models

The governing equations of a laminated composite plate (resulting from a selected plate theory) added with the governing equation of the impactor, a suitable contact law, and a proper approximation of the unknown variables yield to called *complete analytical models* of the impact event [19, 28]. The complete models fully describe the dynamic behavior of the plate and often are taken as a reference to validate analytical simplified models (e.g. Yigit and Christoforou [19]). The complete analytical models are valid in cases where dilatational waves are not important. In addition, from the complete models, it is possible to deduce simplified models which predicts the response for extreme behaviors (infinite plate and quasi-static impact behaviors).

The boundary conditions considered for the drop-weight test referenced in ASTM D7136 / D7136M [59] are approximated to simply supported boundary conditions [60]. Under this consideration, the displacement solutions are assumed by means of *Navier method* which gives, for some laminate configurations, the exact solution of the governing equations for both plate theories presented in Appendix A: *classical laminated plate theory* and *first-order shear deformation plate theory*. In practice, exact solutions for the dynamic response of plates generally are not available due to the boundary conditions or the laminate configuration. In these cases, classical variational methods are used, such as *Raleigh-Ritz* method [58, 61].

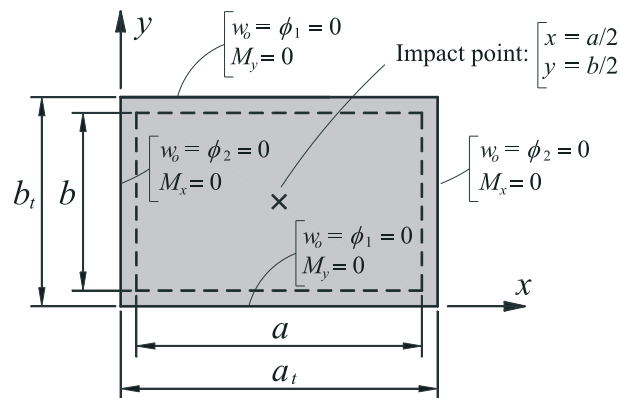


Figure 2.5: Boundary conditions of a simply supported plate.

The boundary conditions for simply supported and first-order shear deformation plate theory can be expressed as (see Figure 2.5):

$$\begin{aligned}
w_o(x, 0, t) = 0, \quad w_o(x, b_t, t) = 0, \quad w_o(0, y, t) = 0, \quad w_o(a_t, y, t) = 0 \\
\phi_1(x, 0, t) = 0, \quad \phi_1(x, b_t, t) = 0, \quad \phi_2(0, y, t) = 0, \quad \phi_2(a_t, y, t) = 0 \\
M_y(x, 0, t) = 0, \quad M_y(x, b_t, t) = 0, \quad M_x(0, y, t) = 0, \quad M_x(a_t, y, t) = 0
\end{aligned} \tag{2.29}$$

where t is the time, w_o is the mid-plane displacement in the normal direction z , ϕ_1 and ϕ_2 are respectively the rotations of a transverse normal about the y and x axis, and M_y and M_x are respectively the bending moments respect x and y axis (see Appendix A). In addition, a_t and b_t are the in-plane dimensions of the plate, and a and b are the effective in-plane dimensions of the plate.

The governing equations are solved by expansion of unknown displacements and rotations in Fourier series (i.e. mode summation) which satisfies the corresponding boundary conditions of the plate. For the plate theory considered, they are:

$$w_o(x, y, t) = \sum_{m=1}^{\infty} \sum_{n=1}^{\infty} W_{mn}(t) \sin \frac{m\pi x}{a} \sin \frac{n\pi y}{b} \tag{2.30}$$

$$\phi_1(x, y, t) = \sum_{m=1}^{\infty} \sum_{n=1}^{\infty} X_{mn}(t) \cos \frac{m\pi x}{a} \sin \frac{n\pi y}{b} \tag{2.31}$$

$$\phi_2(x, y, t) = \sum_{m=1}^{\infty} \sum_{n=1}^{\infty} Y_{mn}(t) \sin \frac{m\pi x}{a} \cos \frac{n\pi y}{b} \tag{2.32}$$

where $W_{mn}(t)$, $X_{mn}(t)$ and $Y_{mn}(t)$ are the coefficients to be determined such that corresponding governing equations are satisfied everywhere in the domain of the plate.

All laminates considered in the thesis are symmetrical and balanced. Therefore, the following simplifications for the governing equations may be used:

1. Symmetric plates: the bending-extensional coupling stiffness matrix $[B]$ is equal to zero. This simplification allows to decouple the equation which gives the flexural displacement w_o of the other two equations for displacements u_o and v_o for classical laminated plate theory. And for first-order shear deformation plate theory, the rotation equations are decoupled of the in-plane displacements.

2. Symmetric and balanced plates: the components A_{16} and A_{26} of the extensional stiffness matrix $[A]$ are equal to zero.
3. All lamina of the laminate is manufactured with the same material and the center of masses is located in the laminate centerline: the inertia term $I_2 = \int_{-h/2}^{h/2} z\rho dz$ is equal to zero.
4. All lamina is modeled as a transverse isotropic material: if first-order shear deformation plate theory is considered, the transverse shear stiffness component A_{45} is equal to zero.

In addition, geometric nonlinear effects are not considered in the development of the governing equations. These geometric nonlinearities are typically called membrane effects which are significant when the deflection of the plate reaches the order of the plate thickness. On the other hand, the nonlinear terms \mathcal{N} considered in the development of the governing equations are omitted (see Appendix A).

Classical laminated plate theory

The resulting simplified governing equation obtained from the classical laminated plate theory is:

$$\begin{aligned}
& \frac{\partial^2}{\partial x^2} \left[D_{11} \left(-\frac{\partial^2 w_o}{\partial x^2} \right) + D_{12} \left(-\frac{\partial^2 w_o}{\partial y^2} \right) + D_{16} \left(-2\frac{\partial^2 w_o}{\partial x \partial y} \right) \right] \\
& + 2\frac{\partial^2}{\partial x \partial y} \left[D_{16} \left(-\frac{\partial^2 w_o}{\partial x^2} \right) + D_{26} \left(-\frac{\partial^2 w_o}{\partial y^2} \right) + D_{66} \left(-2\frac{\partial^2 w_o}{\partial x \partial y} \right) \right] \\
& + \frac{\partial^2}{\partial y^2} \left[D_{12} \left(-\frac{\partial^2 w_o}{\partial x^2} \right) + D_{22} \left(-\frac{\partial^2 w_o}{\partial y^2} \right) + D_{26} \left(-2\frac{\partial^2 w_o}{\partial x \partial y} \right) \right] \\
& + q = I_1 \frac{\partial^2 w_o}{\partial t^2}
\end{aligned} \tag{2.33}$$

On the other hand, the load $q(x, y, t)$ is set as a concentrated impact force located at $x = a/2$ and $y = b/2$, and it is defined as [7]:

$$q(x, y, t) = F_c(t)\delta\left(x - \frac{a}{2}\right)\delta\left(y - \frac{b}{2}\right) \tag{2.34}$$

where $F_c(t)$ is the contact force described by a desired contact law (see Section 2.3). The function $\delta(\cdot)$ is the *Dirac delta function*, which has the following property:

$$\int_{-\infty}^{\infty} \mu(\xi) \delta(\xi - \xi_0) d\xi = \mu(\xi_0) \quad (2.35)$$

Replacing the Navier solution (Equation (2.30)) and their respective space derivatives into Equation (2.33), multiplying all equation terms by $\sin\left(\frac{m\pi x}{a}\right) \sin\left(\frac{n\pi y}{b}\right)$ and finally integrating the $x - y$ space, the governing equation at impact point (i.e. at $x = a/2$ and $y = b/2$) takes the form:

$$\ddot{W}_{mn} + \omega_{mn}^2 W_{mn} = \frac{4}{ab\chi} F_c(t) \sin \frac{m\pi}{2} \sin \frac{n\pi}{2} \quad (2.36)$$

If m and n vary respectively from 1 to p and 1 to q , the motion of the plate is then described by $N = p \cdot q$ equations. Note that due to the impact location, only odd numbered terms m and n are contributing to the solution. For the other plate material points, the right hand side of Equation (2.36) is equal to zero. The term χ is defined by Equation (2.37) and ω_{mn}^2 is the natural frequency defined by Equation (2.38).

$$\chi = I_1 + I_3 \left[\left(\frac{m\pi}{a} \right)^2 + \left(\frac{n\pi}{b} \right)^2 \right] \quad (2.37)$$

$$\omega_{mn}^2 = \frac{1}{\chi} \left[D_{11} \left(\frac{m\pi}{a} \right)^4 + 2(D_{12} + 2D_{66}) \left(\frac{m\pi}{a} \right)^2 \left(\frac{n\pi}{b} \right)^2 - 4D_{16} \left(\frac{m\pi}{a} \right)^3 \left(\frac{n\pi}{b} \right) - 4D_{26} \left(\frac{m\pi}{a} \right) \left(\frac{n\pi}{b} \right)^3 + D_{22} \left(\frac{n\pi}{b} \right)^4 \right] \quad (2.38)$$

The governing equation of the impactor is easily found by applying *D'Alembert Principle* [62]. By neglecting the gravitational force of the impactor, the resulting equation is:

$$F_c(t) + M_i \ddot{w}_i = 0 \quad (2.39)$$

If a closed-form solution is not possible, the dynamic response of the plate and the impactor can be obtained by time integration of set $N + 1$ second order ordinary differential equations with appropriate initial conditions (see Equation (2.40)) by

using a numerical solution procedure such as *Newmark step-by-step time integration method*.

$$W_{mn}(0) = 0, \quad \dot{W}_{mn}(0) = 0, \quad w_i = 0, \quad \dot{w}_i = V_0 \quad (2.40)$$

V_0 is the initial impact velocity of the impactor and M_i the impactor mass.

First-order shear deformation plate theory case

For the first-order shear deformation plate theory, the resulting simplified governing equations to predict the unknown variables w_o , ϕ_1 and ϕ_2 are:

$$A_{55} \left(\frac{\partial^2 w_o}{\partial x^2} + \frac{\partial \phi_1}{\partial x} \right) + A_{44} \left(\frac{\partial^2 w_o}{\partial y^2} + \frac{\partial \phi_2}{\partial y} \right) + q = I_1 \frac{\partial^2 w_o}{\partial t^2} \quad (2.41)$$

$$\begin{aligned} & \frac{\partial}{\partial x} \left[D_{11} \frac{\partial \phi_1}{\partial x} + D_{12} \left(\frac{\partial \phi_2}{\partial y} \right) + D_{16} \left(\frac{\partial \phi_1}{\partial y} + \frac{\partial \phi_2}{\partial x} \right) \right] \\ & + \frac{\partial}{\partial y} \left[D_{16} \frac{\partial \phi_1}{\partial x} + D_{26} \frac{\partial \phi_2}{\partial y} + D_{66} \left(\frac{\partial \phi_1}{\partial y} + \frac{\partial \phi_2}{\partial x} \right) \right] \\ & - A_{55} \left(\frac{\partial w_o}{\partial x} + \phi_1 \right) = I_3 \frac{\partial^2 \phi_1}{\partial t^2} \end{aligned} \quad (2.42)$$

$$\begin{aligned} & \frac{\partial}{\partial x} \left[D_{16} \frac{\partial \phi_1}{\partial x} + D_{26} \left(\frac{\partial \phi_2}{\partial y} \right) + D_{66} \left(\frac{\partial \phi_1}{\partial y} + \frac{\partial \phi_2}{\partial x} \right) \right] \\ & + \frac{\partial}{\partial y} \left[D_{12} \frac{\partial \phi_1}{\partial x} + D_{22} \frac{\partial \phi_2}{\partial y} + D_{26} \left(\frac{\partial \phi_1}{\partial y} + \frac{\partial \phi_2}{\partial x} \right) \right] \\ & - A_{44} \left(\frac{\partial w_o}{\partial y} + \phi_2 \right) = I_3 \frac{\partial^2 \phi_2}{\partial t^2} \end{aligned} \quad (2.43)$$

Following the same procedure as in classical laminated plate theory, the resulting system of equations which describe the dynamic response of the plate is:

$$\begin{bmatrix} s_{11} & s_{12} & s_{13} \\ s_{12} & s_{22} & s_{23} \\ s_{13} & s_{23} & s_{33} \end{bmatrix} \begin{Bmatrix} W_{mn} \\ X_{mn} \\ Y_{mn} \end{Bmatrix} + \begin{bmatrix} I_1 & 0 & 0 \\ 0 & I_3 & 0 \\ 0 & 0 & I_3 \end{bmatrix} \begin{Bmatrix} \ddot{W}_{mn} \\ \ddot{X}_{mn} \\ \ddot{Y}_{mn} \end{Bmatrix} = \begin{Bmatrix} q_{mn} \\ 0 \\ 0 \end{Bmatrix} \quad (2.44)$$

Defining $\alpha_m = \frac{m\pi}{a}$ and $\beta_n = \frac{n\pi}{b}$, the terms s_{ij} and q_{mn} are obtained by:

$$\begin{aligned}
s_{11} &= \beta_n^2 A_{44} + \alpha_m^2 A_{55}, & s_{12} &= \alpha_m A_{55}, & s_{13} &= \beta_n A_{44} \\
s_{22} &= \alpha_m^2 D_{11} + \beta_n^2 D_{66} + A_{55} - \left(\frac{1}{2ab}\right) D_{16} \\
s_{23} &= \alpha_m \beta_n (D_{12} + D_{66}) - \left(\frac{m}{4na^2}\right) D_{16} - \left(\frac{n}{4mb^2}\right) D_{26} \\
s_{33} &= \beta_n^2 D_{22} + \alpha_m^2 D_{66} + A_{44} - \left(\frac{1}{2ab}\right) D_{26}
\end{aligned} \tag{2.45}$$

$$q_{mn} = \frac{4F_c(t)}{ab} \sin\left(\alpha_m \frac{a}{2}\right) \sin\left(\beta_n \frac{b}{2}\right) \tag{2.46}$$

For each (m, n) combination, a system of three equations with three unknowns is solved for the coefficients $W_{mn}(t)$, $X_{mn}(t)$ and $Y_{mn}(t)$. The motion for the impactor is again governed by Equation (2.39). The initial conditions are defined by:

$$\begin{aligned}
W_{mn}(0) &= 0, & \dot{W}_{mn}(0) &= 0, & w_i &= 0, & \dot{w}_i &= V_0 \\
X_{mn}(0) &= 0, & \dot{X}_{mn}(0) &= 0, & Y_{mn}(0) &= 0, & \dot{Y}_{mn}(0) &= 0
\end{aligned} \tag{2.47}$$

where V_0 is the initial impact velocity of the impactor.

2.4.2 Infinite plate impact models

The response of a plate under impact is governed by flexural and shear waves when the major wave emanating from the impact point has not time to reach the boundaries of the plate (see Figure 2.1.b). This situation is similar to an impact on an infinite plate. Therefore, the in-plane plate size and the boundary conditions do not affect the response. In the literature this behavior is referenced by the descriptors: global behavior with no size effects, flexural and shear wave-controlled, or impact on an infinite plate.

There are some analytical models in the literature for the description of this response type. Olsson [35] developed a model for orthotropic plates without shear deformation and assuming a Hertzian contact law. Closed-form solutions for this problem with a linearized contact law are proposed in Yigit and Christoforou [26]. A solution for Hertzian contact law on quasi-isotropic plates with transverse shear deformation is given in Mittal [63]. An extension of the model to both linear and

Hertzian contact law on orthotropic plates was presented in Olsson [64]. A closed-form prediction of the peak load for small mass impact based on three asymptotic cases with purely deformation by indentation, bending or shear, is developed in Olsson [25].

The model described here was proposed by Olsson [20, 35], which in turn was based on the work of Zener [65]. This model is referenced in many publications and used in the development of approaches for predicting the response type for a determined impact configuration [19, 20, 25–28] (see Section 2.5). The solution was proposed for the description of the impact until the waves are reflected back from the boundaries in orthotropic plates impacted by an impactor with a hemispherical tip.

In orthotropic plates, waves propagate at different speeds in different directions and the flexural wavefront will have an almost elliptical shape centered at the impact point. The analysis assumes that the area affected by the major wave emanating from the impact point can be approximated by a rectangular simply supported plate with side lengths a and b . Thus, the development of the model can be performed by using the framework explained for the complete analytical models (see Section 2.4.1) assuming classical laminated plate theory for orthotropic plates, and equal contact law for loading and unloading process. Therefore, no account was made for transverse shear deformation waves. In applications, shear deformations are usually of minor importance for monolithic laminates, while the influence on sandwich panels may be substantial [20].

The governing equation for transverse displacement description in a simply supported orthotropic plate assuming classical laminated plate theory, neglecting the I_3 term (see Appendix A) and impacted in $x = a/2$ and $y = b/2$ (see Figure 2.5) is:

$$\ddot{W}_{mn} + \omega_{mn}^2 W_{mn} = \frac{4}{abI_1} F_c(t) \quad (2.48)$$

where the natural frequencies ω_{mn} are described by:

$$\omega_{mn}^2 = \frac{1}{I_1} \left[D_{11} \left(\frac{m\pi}{a} \right)^4 + 2(D_{12} + 2D_{66}) \left(\frac{m\pi}{a} \right)^2 \left(\frac{n\pi}{b} \right)^2 + D_{22} \left(\frac{n\pi}{b} \right)^4 \right] \quad (2.49)$$

The solution of the differential Equation (2.48) can be found by means of the Duhamel integral:

$$W_{mn} = \frac{4}{abI_1\omega_{mn}} \int_0^t F_c(\tau) \sin[\omega_{mn}(t - \tau)] d\tau \quad (2.50)$$

By inserting Equation (2.50) into Equation (2.30), the transverse displacement of the plate at the impact point, $x = a/2$ and $y = b/2$, is :

$$w_o(a/2, b/2, t) = \frac{4}{abI_1} \int_0^t F_c(\tau) \sum_{n=1}^{\infty} \sum_{m=1}^{\infty} \frac{1}{\omega_{mn}} \sin[\omega_{mn}(t - \tau)] d\tau \quad (2.51)$$

The double sum in Equation (2.51) can be approximated by a continuous integration over m and n . Since only odd values of m and n are used in the summations, only half of the continuous integrals should be retained:

$$w_o(a/2, b/2, t) = \frac{1}{abI_1} \int_0^t F_c(\tau) \int_0^{\infty} \int_0^{\infty} \frac{1}{\omega_{mn}} \sin[\omega_{mn}(t - \tau)] dm dn d\tau \quad (2.52)$$

The fact that the waves are closed ellipses implies $m \equiv n$, which allows to consider the ratio a/b equal to the ratio of wavelengths λ_x/λ_y . The wavelengths are the inverses of the wave numbers $k_i = \omega_{mn}/c_{bend,i}$ ($i = x, y$), where $c_{bend,i}$ are the flexural wave velocities. Knowing $c_{bend,x} = \sqrt{\omega_{mn}(D_{11}/I_1)^{1/4}}$ and $c_{bend,y} = \sqrt{\omega_{mn}(D_{22}/I_1)^{1/4}}$, the following relation is obtained:

$$\frac{a}{b} = \frac{c_{bend,x}}{c_{bend,y}} = \left(\frac{D_{11}}{D_{22}} \right)^{1/4} \quad (2.53)$$

Then, the natural frequencies can be expressed as:

$$\omega_{mn} = \frac{2\pi^2 mn}{ab} \sqrt{\frac{D^*}{I_1}} \quad (2.54)$$

where D^* is called *effective plate stiffness* [35] and is defined by fairly complicated expressions involving elliptic functions. A sufficient approximation is [20, 25]:

$$D^* \approx \sqrt{\left(\frac{A+1}{2} \right) D_{11} D_{22}}, \quad \text{where } A = \frac{D_{12} + 2D_{66}}{\sqrt{D_{11} D_{22}}} \quad (2.55)$$

Therefore, the plate displacement can be rewritten by:

$$w_o(a/2, b/2, t) = \frac{1}{8\sqrt{I_1 D^*}} \int_0^t F_c(\tau) d\tau \quad (2.56)$$

On the other hand, the governing equation of the impactor is described by Equation (2.39). After integrating twice, the displacement of the impactor can be expressed by:

$$w_i(t) = V_0 t - \frac{1}{M_i} \int_0^t \int_0^\tau F_c(\tau') d\tau' d\tau \quad (2.57)$$

The indentation of the plate was defined by Equation (2.3). Differentiating twice with respect the time and using Equations (2.56) and (2.57), and the contact law defined by Equation (2.2), the indentation is found to be governed by the nonlinear differential equation:

$$\ddot{\alpha} + \frac{1}{8\sqrt{I_1 D^*}} q k_\alpha \alpha^{q-1} \dot{\alpha} + \frac{k_\alpha}{M_i} \alpha^q = 0 \quad (2.58)$$

If a linear contact law is used, $q = 1$, Equation (2.58) yields to the well-known differential equation of a damped harmonic oscillator which has closed-form solutions. In Yigit and Christoforou [26] these closed-form solutions are developed. On the other hand, the model defined by the governing Equation (2.58) can be represented by a simplified lumped-mass model shown in Figure 2.6.a [20], which is equivalent to the single degree of freedom model shown in Figure 2.6.b.

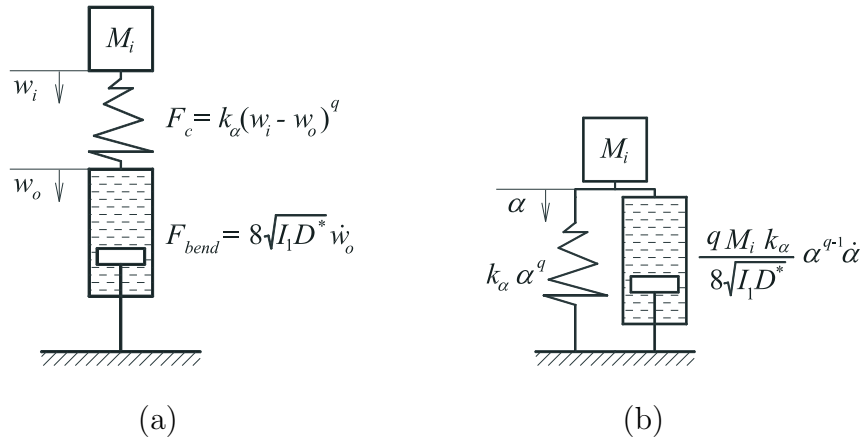


Figure 2.6: Lumped-mass models for infinite plate behavior.

The governing Equation (2.58) can be expressed in a dimensionless form, which is more effective in order to analyze the effects of the governing parameters on the impact behavior. That is because the governing parameters are set on key dimensionless parameters, yielding to less characterization parameters of the impact response. This framework can be developed by defining all the basic magnitudes of the problem (i.e. mass $[M]$, length $[L]$, and time $[T]$) by means of selected parameters of the impact problem [26, 57]. The chosen definitions are [65]: mass $[M] = M_i$, length $[L] = V_0[T]$, and time $[T]$ is extracted from the contact stiffness k_α which depends on the selected contact law. Therefore $[T] = (k_\alpha^{-1}[M][L]^{(1-q)})^{1/2} = (k_\alpha^{-1}M_iV_0^{(1-q)})^{1/(1+q)}$.

The explained definitions are equivalent to define the variable $[L]$ equal to α_{max} [19, 26, 54]. The α_{max} corresponds to the maximum indentation of the plate (i.e. when the global response of the plate is neglected, which is called *half-space* impact). The expression of α_{max} is simply found by equating all impact energy with the indentation energy. Consequently, the impact force is normalized with respect to the maximum impact force for a half-space behavior. Therefore, the equation of α_{max} for a general contact law yields to:

$$\alpha_{max} = \left(\frac{1+q}{2} \frac{M_i V_0^2}{k_\alpha} \right)^{1/(1+q)} \quad (2.59)$$

The resulting dimensionless differential equation is:

$$\ddot{\bar{\alpha}} + \zeta q \bar{\alpha}^{q-1} \dot{\bar{\alpha}} + \bar{\alpha}^q = 0 \quad (2.60)$$

where the over bar indicates dimensionless parameters and the initial conditions are $\bar{\alpha}(0) = 0$ and $\dot{\bar{\alpha}}(0) = 1$. All parameters that describe the impact behavior are now lumped in a single dimensionless parameter ζ . This parameter is defined by:

$$\zeta = \frac{1}{8\sqrt{I_1 D^*}} (k_\alpha M_i^q V_0^{q-1})^{1/(1+q)} \quad (2.61)$$

In the bibliography, the ζ parameter is called *relative plate mobility* [20], *inelastic parameter* [7, 28], or *loss factor* [19]. The highest contact force is obtained for $\zeta = 0$, in which case the plate is very rigid and the problem is reduced to that of an impact on a half-space impact behavior where the impactor will rebound with the

initial velocity V_0 [22]. As the impact parameter ζ increases, the contact force history becomes asymmetrical and the contact duration increases because the flexural deformation of the target becomes more significant (i.e. the behavior approaches to a quasi-static response type). Under high values of ζ the model is not appropriate since the model is affected by the boundary conditions and the global deformation of the structure.

In Olsson [20] the parameter ζ is defined by introducing the concept of *mobility*, C , which is defined as velocity per unit force applied to a component. The mobility of the plate, C_p , is given by:

$$C_p = \frac{\dot{w}_o}{F_{bend}} = \frac{1}{8\sqrt{I_1 D^*}} \quad (2.62)$$

The impactor mobility, C_i , may be defined from peak (initial) velocity, V_0 , per peak load, F_{max} for a complete immovable plate (i.e. $C_p = 0$ and the indentation is maximum α_{max}):

$$C_i = \frac{V_0}{F_{max}} = \frac{V_0}{k_\alpha \alpha_{max}^q} = \left(k_\alpha^{-1} V_0^{1-q} \left(\frac{1+q}{2} M_i \right)^{-q} \right)^{1/(1+q)} \quad (2.63)$$

By means of the mobility definitions, the ζ parameter can be redefined by the following expression:

$$\zeta = \left(\frac{2}{1+q} \right)^{q/(1+q)} \frac{C_p}{C_i} \quad (2.64)$$

The simplified model can be applied until the waves are reflected back from the boundaries. Equation (2.65) was proposed by Olsson [20], and it gives the position in polar coordinates r and θ for the leading edge of the n -th wave mode in an orthotropic plate. Therefore, the simplified model is not suitable if the value given by this equation is greater than the minimum distance from the impact point to the boundaries of the plate.

$$r_n(\theta) = \left(\frac{2D_r(\theta)D^*}{I_1\sqrt{D_{11}D_{22}}} \right)^{1/4} \sqrt{\pi n t} \quad (2.65)$$

where $D_r(\theta)$ is the radial plate bending stiffness in direction θ .

2.4.3 Half-space impact models

When the impactor mass is very small, and the target is fairly stiff, impact does not produce significant global structure response and can be approximated by impact on a half-space (i.e. the response is fully local). Then, this behavior can be approached by single mass-spring-damper model shown in Figure 2.7. The resulting governing equation is:

$$M_i \ddot{w}_i + F_c = 0 \quad (2.66)$$

where the contact law is defined by $F_c = k_\alpha \alpha^q = k_\alpha w_i^q$, and the initial conditions are $w_i(0) = 0$ and $\dot{w}_i(0) = V_0$.

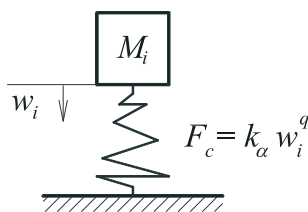


Figure 2.7: Spring-mass model for half-space impact behavior.

The dimensionless framework described in Yigit and Christoforou [45] defines the problem magnitudes as $[M] = M_i$, $[L] = \alpha_{cr}$, and $[T] = \left(k_\alpha^{-1} M_i \alpha_{cr}^{(1-q)}\right)^{1/2}$. The α_{cr} term is the yielding indentation for plastic indentation which is defined by Equation (2.28) (see Section 2.3.3). Using these definitions, the dimensionless form of the governing Equation (2.66) is:

$$\ddot{\bar{w}}_i + \bar{w}_i = 0 \quad (2.67)$$

On the other hand, the resulting normalized impact velocity β groups all the parameters for half-space behavior. Therefore, the β parameter fully characterizes the half-space behavior and is termed *characteristic impact parameter*. That is:

$$\beta = \frac{V_0}{\omega \alpha_{cr}} \quad (2.68)$$

where ω is the contact frequency given as:

$$\omega = [T]^{-1} = (k_\alpha^{-1} M_i \alpha_{cr}^{(1-q)})^{-1/2} \quad (2.69)$$

However, by using the dimensionless framework explained in Section 2.4.2, i.e. mass $[M] = M_i$, length $[L] = \alpha_{max}$, and time $[T] = (k_\alpha^{-1} M_i \alpha_{max}^{(1-q)})^{1/2}$, the β parameter remains constant. In particular, for linear contact law $q = 1$, β parameter is equal to 1, and for Hertzian contact law $q = 3/2$, β parameter is equal to $(5/4)^{-1/2}$. This result implies that the predicted normalized response given for this behavior is constant whatever the values of the governing parameters of this behavior. This interesting consideration is used in the impact characterization diagram of Chritoforou and Yigit [19, 26, 27] which is explained in Section 2.5.

On the other hand, the model defined for wave-controlled impact behavior can be used in order to describe the half-space behavior. As it has been noted, the half-space impact behavior will be obtained when the ζ parameter yields to zero.

2.4.4 Quasi-static impact models

For sufficiently large impact times, the response is more or less quasi-static, in the sense that load and deflection give the same relation as during a static loading. Based on extensive experimental and computational experience, researchers suggest that the response is almost quasi-static if the effective mass ratio μ is greater than a threshold value [66]. This effective mass ratio is given by:

$$\mu = \frac{M_i}{M_p^*} \quad (2.70)$$

where M_i is the impactor mass and M_p^* is the equivalent lumped mass of the structure which depends on the type of structure and support conditions. For rectangular and simply supported plates it is set equal to 1/4 of the total plate mass M_p , as can be deduced from Equation (2.36).

The most complete simplified model for quasi-static behavior description is shown in Figure 2.8.a [67], where the terms k_s , k_b and k_m are the shearing, bending and membrane stiffness of the plate under static load. The expression of k_s , k_b and k_m are function of the boundary conditions, the shape and the laminate configuration

of the structure. The stiffness values can be obtained experimentally, by using numerical methods, or analytically in cases with simple plate geometries [21]. A list of stiffness expressions for transverse isotropic plates is done in Sierakowski et al. [68].

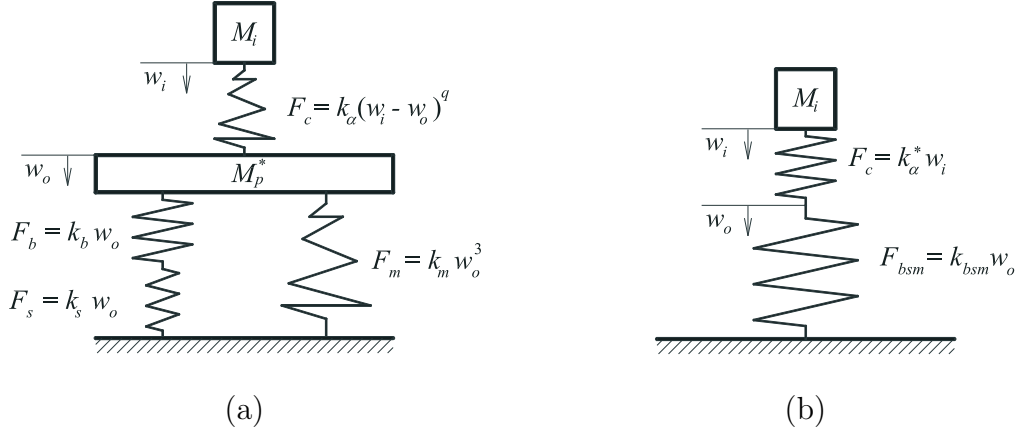


Figure 2.8: (a) Complete and (b) simplified spring-mass models for quasi-static impact behavior.

The governing equations for each mass by neglecting the gravitational forces are [67] (Figure 2.8.a):

$$M_i \ddot{w}_i + k_\alpha (w_i - w_o)^q = 0 \quad (2.71)$$

$$M_p^* \ddot{w}_o + k_s w_o + k_b w_o + k_m w_o^3 - k_\alpha (w_i - w_o)^q = 0 \quad (2.72)$$

where the initial conditions are $w_i = w_o = 0$, $\dot{w}_o = 0$ and $\dot{w}_i = V_0$. In Olsson [24] this model is used in conjunction with a delamination force threshold and a critical energy for delamination growth in order to predict the impact damage initiation and growth during quasi-static response caused by large mass impactors.

The equivalent plate mass M_p^* is negligible when the impactor mass is larger than twice the total plate mass. By neglecting the plate mass and linearizing the stiffness k_m and k_α (i.e. linear stiffness k_m^* and k_α^*), the model yields to the model shown in Figure 2.8.b [20]. In this case, all stiffness can be lumped to a single stiffness k_Σ which is defined by:

$$k_{\Sigma} = \frac{k_{\alpha}^* k_{bsm}}{k_{\alpha}^* + k_{bsm}}, \quad \text{where} \quad k_{bsm} = \left(\frac{1}{k_b} + \frac{1}{k_s} \right)^{-1} + k_m^* \quad (2.73)$$

The governing equation for this case is:

$$M_i \ddot{w}_i + k_{\Sigma} w_i = 0 \quad (2.74)$$

where the initial conditions are $w_i = 0$ and $\dot{w}_i = V_0$. More simplified versions are proposed in the literature, such as models with neglected membrane effects and/or shear effects [19]. Equation (2.74) can be written in a dimensionless form by using the magnitude definitions shown in Section 2.4.2 specified for a linear contact law (i.e. $q = 1$). That is:

$$\ddot{\bar{w}}_i + \left(\frac{k_{bsm}}{k_{bsm} + k_{\alpha}^*} \right) \bar{w}_i = 0 \quad (2.75)$$

2.5 Approaches for impact behavior description

There are approaches in the literature which predict the impact behavior type of rectangular, flat, and monolithic laminated composite plates. These approaches are based on simplified analytical models of extreme impact behaviors and develop key characterization parameters which inform of the behavior type. As it has been noted in Section 2.2, the behaviors considered are those that yield to Barely Visible Impact Damage (BVID) if the resulting peak load reaches a designed damage threshold. Ballistic impact behavior is beyond the scope of the present thesis.

The approaches detailed in this section are the characterization diagram proposed by Christoforou and Yigit [19, 26, 27], and the mass criterion proposed by Olsson [20]. It should be noted that not all impact cases are adequately characterized by the approaches explained at following. This is due to the fact that these approaches are based on simplified models based on certain hypothesis that may not be true for certain impact configurations.

2.5.1 Christoforou and Yigit characterization diagram

The characterization impact diagram proposed by Christoforou and Yigit [18, 19, 26, 27] predicts the behavior type, as well as the maximum elastic impact force for

a wide range of impact cases. The prediction of the maximum impact force is useful since it can be compared with a damage threshold for damage onset (see Section 2.6).

The construction of the diagram is based on simplified analytical models of the infinite plate and quasi-static impact behaviors, and uses the dimensionless framework described in Section 2.4.2 (i.e. the normalization with respect to the maximum indentation α_{max}). On the other hand, a linearized contact law of the elastic-plastic contact model proposed in Yigit and Christoforou [45] is used, that results in closed-form solutions for the impact models.

Infinite plate behavior

The closed-form solutions, Equation (2.76), are the expressions of the normalized impact force as a function of the relative mobility parameter ζ with $q = 1$ (see Equations (2.60) and (2.61)). It should be noted that ζ parameter is changed to $\zeta = 2\zeta_w$ which simplifies the resulting equations:

$$\bar{F}_w(\bar{t}) = \bar{\alpha}(\bar{t}) = \begin{cases} \frac{\exp^{-\zeta_w \bar{t}}}{\sqrt{1 - \zeta_w^2}} \sin\left(\sqrt{1 - \zeta_w^2} \bar{t}\right) & \text{if } \zeta_w < 1 \\ \bar{t} \exp^{-\bar{t}} & \text{if } \zeta_w = 1 \\ \frac{1}{2\sqrt{\zeta_w^2 - 1}} \left(\exp^{(-\zeta_w + \sqrt{\zeta_w^2 - 1}) \bar{t}} - \exp^{(-\zeta_w - \sqrt{\zeta_w^2 - 1}) \bar{t}} \right) & \text{if } \zeta_w > 1 \end{cases} \quad (2.76)$$

The dimensionless time at which the maximum impact force occurs can be found by setting the derivatives with respect to time equal to zero, in Equation (2.76), yielding:

$$\bar{t}_w = \begin{cases} \arccos\left(\frac{\zeta_w}{\sqrt{1 - \zeta_w^2}}\right) & \text{if } \zeta_w < 1 \\ 1 & \text{if } \zeta_w = 1 \\ \frac{1}{2\sqrt{\zeta_w^2 - 1}} \ln\left(\frac{\zeta_w + \sqrt{\zeta_w^2 - 1}}{\zeta_w - \sqrt{\zeta_w^2 - 1}}\right) & \text{if } \zeta_w > 1 \end{cases} \quad (2.77)$$

Then, the maximum normalized impact force can be calculated by replacing Equation (2.77) into Equation (2.76) as:

$$\bar{F}_{w,max}(\bar{t}_w) = \bar{\alpha}(\bar{t}_w) \quad (2.78)$$

From Equation (2.78), it is concluded that the infinite plate behavior is function of only the parameter ζ_w , because \bar{t}_w only depends on it.

Half-space behavior

As noted in Section 2.4.3, the half-space behavior can be described by the spring-mass model shown in Figure 2.7. Due to the dimensionless framework used, the dependence on the characterizing half-space parameter β is avoided and the normalized impact force can be obtained by normalizing Equation (2.66):

$$\bar{F}_{hs}(\bar{t}) = \bar{\alpha}(\bar{t}) = \bar{w}_i(\bar{t}) = \sin \bar{t} \quad (2.79)$$

Thus, if an impact response is locally dominated, the maximum normalized impact occurs at time $\bar{t}_{hs} = \pi/2$ and this force will be close to the unity $\bar{F}_{hs,max} = 1$. This development also can be deduced by means of the governing Equation (2.60) of the wave-controlled impact model and letting the ζ_w parameter equal to zero.

Quasi-static behavior

The quasi-static behavior is described by the model shown in Figure 2.8.b. Equating the linear contact stiffness k_α^* to k_y (Equation (2.27)), and defining $\lambda = k_{bsm}/k_y$ (i.e. *relative stiffness*), the solution of the dimensionless governing Equation (2.75) (see Section 2.4.4) is:

$$\bar{w}_i(\bar{t}) = \sqrt{\frac{1+\lambda}{\lambda}} \sin \left(\sqrt{\frac{\lambda}{1+\lambda}} \bar{t} \right) \quad (2.80)$$

and the normalized impact force for quasi-static behavior is:

$$\bar{F}_q(\bar{t}) = \sqrt{\frac{\lambda}{1+\lambda}} \sin \left(\sqrt{\frac{\lambda}{1+\lambda}} \bar{t} \right) \quad (2.81)$$

From Equation (2.81), the maximum normalized impact force occurs at time:

$$\bar{t}_q = \frac{\pi}{2} \sqrt{\frac{1+\lambda}{\lambda}} \quad (2.82)$$

and is defined as:

$$\bar{F}_{q,max} = \sqrt{\frac{\lambda}{1+\lambda}} \quad (2.83)$$

As Equation (2.83) shows, the maximum normalized impact force for quasi-static behavior only depends on λ parameter.

Impact characterization diagram

Using the analytical solutions of the extreme cases explained above, a characterization diagram can be constructed as shown in Figure 2.9. This diagram represents the variation of the maximum normalized impact force \bar{F}_{max} as a function of the relative mobility parameter ζ_w . For the construction of the diagram, the curve representing infinite plate behavior is obtained from Equation (2.78), and the horizontal lines with different values of relative stiffness λ are obtained by using Equation (2.83).

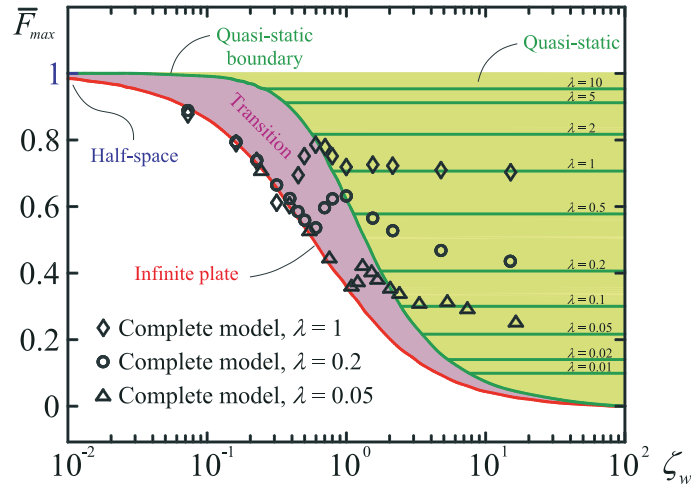


Figure 2.9: Impact characterization diagram (after Christoforou and Yigit [18, 19, 26, 27]), dimensionless maximum force \bar{F}_{max} versus relative mobility ζ_w .

Four different regions can be identified in the diagram. Impact configurations which define points in the right part of the diagram behave as quasi-static. For points which fall close to the red curve behave as infinite plate. Between the quasi-static

and the infinite plate behaviors there is a transition zone where the resulting response is a combination of both behaviors. The curve which represents the boundary of the quasi-static response is obtained by $\bar{F}_b = \sqrt{\frac{0.68}{0.68 + \zeta_w^2}}$, as suggested in [26, 66]. Finally, the points that fall close to the maximum dimensionless force $\bar{F} = 1$ results in the half-space behavior, and can be obtained by setting in the simplified models (infinite plate and quasi-static): $\zeta_w = 0$ or $\lambda \rightarrow \infty$.

In order to demonstrate the validity of the characterization diagram several impact situations covering all behavior type regions were simulated [26]. The simulations were carried out by numerical integration of the complete analytical model which considers classical laminated plate theory and simply supported boundary conditions (see Section 2.4.1). As can be seen, the simulations follow reasonably well the trends of the characterization diagram. In the transition zone, a complete analytical model is required in order to better describe the response.

Summarizing, the prediction of the behavior type as well as the maximum impact force for a given impact case can be done by calculating only two key parameters: λ (i.e. key parameter of quasi-static impact behavior) and ζ_w (i.e. key parameter of wave-controlled impact behavior). However, the contribution of structural dynamics should be included and it can be represented by the relative impactor mass μ given by Equation (2.70). When different impact situations (respect to their boundary conditions, materials, size, etc.) with similar key parameters are compared, the resulting dynamics, behavior type and normalized response are similar [54].

2.5.2 Olsson mass criterion

Olsson [20] developed a criterion for the prediction of the elastic impact behavior of orthotropic plates. The model is based on the models for infinite plate and quasi-static extreme behaviors described in Sections 2.4.2 and 2.4.4, respectively. This criterion demonstrates that the response type under elastic conditions (i.e. prior to damage onset) depends basically on the impactor/plate mass ratio. In order to develop the criterion, the dimensionless framework presented in Section 2.4.2 was also used.

Small-mass impactor

For small-mass impactor, it is demonstrated that the impact time t_i has the following approximate lower bound [20]:

$$t_i \geq \frac{1}{4} \frac{M_i}{\sqrt{I_1 D^*}} \quad (2.84)$$

The mass of the plate area affected by the first wave, $M_{p,wave}$, is approached by:

$$M_{p,wave} = \pi I_1 r_1(0^\circ) r_1(90^\circ) = \pi^2 t_i^2 \sqrt{2 I_1 D^*} \quad (2.85)$$

where $r_1(0^\circ)$ and $r_1(90^\circ)$ are respectively the distances at 0° and 90° directions from the impact point site to the leading edge of the first wave mode. They are calculated by means of Equation (2.65).

On the other hand, the largest plate mass which can remain unaffected by the boundaries, $M_{p,max}$, is found by considering the plate area affected when the first wave mode reaches a boundary. Therefore, it can be defined as:

$$M_{p,max} = \pi I_1 \min \left\{ \left(\frac{D_{22}}{D_{11}} \right)^{1/4} r_{x,min}^2, \left(\frac{D_{11}}{D_{22}} \right)^{1/4} r_{y,min}^2 \right\} \quad (2.86)$$

where $r_{x,min}$ and $r_{y,min}$ are the distances from the impact to the closest boundary in the x - (i.e. 0° direction) and y -direction (i.e. 90° direction). Therefore, an impact located at middle of the panel implies $r_{x,min} = a/2$ and $r_{y,min} = b/2$.

By replacing Equation (2.84) into Equation (2.85) and making the ratios respect the impactor mass, M_i , the condition for small-mass impact (i.e. infinite plate impact) is approached by:

$$\frac{M_i}{M_{p,max}} \leq \frac{M_i}{M_{p,wave}} \leq \frac{2\sqrt{2}}{\pi^2} \quad (2.87)$$

For rectangular plates with leading edges a and b (see Figure 2.5), the term I_1 is equal to $\frac{M_p}{ab}$. Therefore, the condition for small-mass impact can be expressed as:

$$\frac{M_i}{M_p} \leq \frac{1}{\sqrt{2}\pi} \min \left\{ \frac{a}{b} \left(\frac{D_{22}}{D_{11}} \right)^{1/4}, \frac{b}{a} \left(\frac{D_{11}}{D_{22}} \right)^{1/4} \right\} \quad (2.88)$$

Large-mass impactor

For large-mass impactor, the model considered is shown in Figure 2.8.b which neglects the lumped plate mass M_p^* and considers linear conditions. For this case, the natural frequency is:

$$\omega_i = \sqrt{\frac{k_\Sigma}{M_i}} \quad (2.89)$$

If the lumped plate mass is not neglected, the natural frequency of the plate is approached by:

$$\omega_p = \sqrt{\frac{k_{bsm}}{M_p^*}} \quad (2.90)$$

By means of Equation (2.89) the impact time is obtained:

$$t_i = \pi \sqrt{\frac{M_i}{k_\Sigma}} \quad (2.91)$$

On the other hand, using Equation (2.90) the first vibration mode of the plate results in:

$$t_{p,1} = \pi \sqrt{\frac{M_p^*}{k_{bsm}}} \quad (2.92)$$

Quasi-static response occurs for impact times much longer than the fundamental vibration period of the plate, which is described by:

$$t_i/t_{p,1} \gg 1 \quad (2.93)$$

Replacing Equations (2.91) and (2.92) in Equation (2.93), and considering $M_p^* = (1/4)M_p$, the criterion for quasi-static behavior yields to $\frac{M_i}{M_p} \gg \frac{1}{4}$. A sufficient condition is:

$$\frac{M_i}{M_p} \geq 2 \quad (2.94)$$

Intermediate-mass impactor

Finally, a complex response occurs for intermediate-mass impactors, which can be modeled by including the equivalent plate mass M_p^* as shown in Figure 2.8.a. Therefore, the condition for intermediate mass behavior for rectangular plates is:

$$\frac{1}{\sqrt{2\pi}} \min \left\{ \frac{a}{b} \left(\frac{D_{22}}{D_{11}} \right)^{1/4}, \frac{b}{a} \left(\frac{D_{11}}{D_{22}} \right)^{1/4} \right\} < \frac{M_i}{M_p} < 2 \quad (2.95)$$

2.6 Impact damage and analytical thresholds

The phenomenon of impact damage in laminated composite structures is very complex and difficult to model analytically due to the large variety of damage modes (matrix cracking, fiber-matrix interface debonding, delamination and fiber breakage) and to their complex interaction process. The identification of the initiation and propagation of the damage modes is quite relevant because it will yield information regarding the residual strength of the structure.

Similarly to the impact response, depending on the impact governing parameters, the resulting damage can be local, global or both [18, 21]. Local impact damage consists mainly of visible permanent indentation on the contact zone involving fiber and matrix damage modes, whereas global impact damage consists mainly of invisible extensive delaminations. The extreme local damage is the complete penetration of the plate. Associated with these types of damages, there are complicated patterns of matrix cracks and fiber fractures.

To bridge the analytical prediction of the impact behavior and the onset of damage, the impact force is typically used and compared with a damage threshold allowable. Damage occurs if the predicted elastic impact force is greater than a well-suited threshold for the corresponding dynamic response type [7, 18, 25, 69, 70]. Therefore, the impact force is a key parameter in determining the criticality of an impact, i.e. the risk for initiating damage.

2.6.1 Matrix cracking

The impact damage process starts with localized matrix cracks and fiber-matrix interfacial debondings which normally are not detectable neither by the impactor

load cells used during impact tests nor using the typical *Non-Destructive Inspection methods* (NDI), e.g. ultrasonic techniques. It has been shown by Sjöblom et al. [71] that the presence of matrix cracks does not dramatically affect the overall laminate stiffness during an impact event. However, matrix crack tips act as initiation points for delaminations at interfaces between plies with different fiber orientations. These delaminations change the local and/or global stiffness of the structure [31].

Two types of matrix cracks can be observed: vertical and oblique cracks (Figure 2.10). Vertical cracks are introduced by the flexural deformation of the plate due to tensile stresses and consequently they are located at the bottom plies. Therefore, vertical cracks are typical in impact events that behave as quasi-static. Oblique cracks are formed by the high transverse shear stresses resulting from the contact load and the flexural deformation of the plate. These cracks are typically located at top and middle plies.

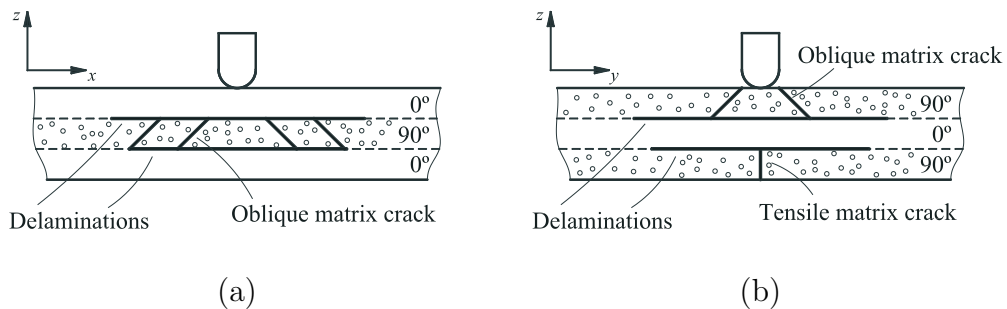


Figure 2.10: Type of matrix cracks in a [0/90/0] laminated composite plate (after Richardson and Wisheart [30]), (a) longitudinal view and (b) transverse view.

Typically, in thick laminates matrix cracking starts on the impacted face of the specimen as a result of the high and localized contact stresses. Damage propagates downward by a succession of intra-ply cracks and interface delaminations, resulting in a pine tree pattern (Figure 2.11.a). For thin laminates, bending stresses on the back of the laminate introduce tensile matrix cracks, and damage progresses from the non-impacted face up toward the impactor yielding a reverse pine tree appearance (Figure 2.11.b).

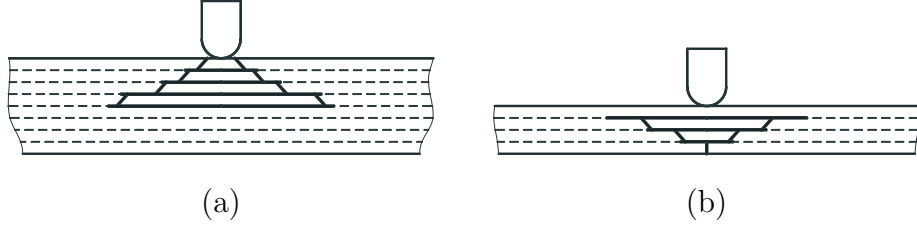


Figure 2.11: Projected damage patterns (after Abrate [7]), (a) pine tree and (b) reversed pine tree.

Threshold load for vertical matrix crack

A new damage threshold for the prediction of matrix cracking at the outer ply located at the back face of a rectangular laminated composite plate due to bending is proposed herein.

The maximum values of the in-plane tensile stresses due to the flexural deformation created by a uniformly distributed static load of radius R , $q_0 = F_{mc}^{ten} / (\pi R^2)$, centered at $(x, y, z) = (a/2, b/2, -h/2)$ in a simply supported, rectangular and orthotropic plate (see Figure 2.5), can be approximated by [61]:

$$(\sigma_x)_{max} = \frac{8b^2}{\pi^5 R^2 h^2} f_x(s, C_{ij}, D_{ij}/h^3) F_{mc}^{ten} \quad (2.96)$$

$$(\sigma_y)_{max} = \frac{8b^2}{\pi^5 R^2 h^2} f_y(s, C_{ij}, D_{ij}/h^3) F_{mc}^{ten} \quad (2.97)$$

where R is the impactor tip radius and h is the plate thickness. These maximum in-plane tensile stresses are located at $(x, y, z) = (a/2, b/2, h/2)$, i.e. at the impact point and at the opposite point at the back face of the plate, and are obtained by means of the classical laminated plate theory, using the Navier solution for simply supported plates, and neglecting membrane strains and local deflections. The terms $f_x(s, C_{ij}, D_{ij}/h^3)$ and $f_y(s, C_{ij}, D_{ij}/h^3)$ are defined respectively as:

$$f_x(s, C_{ij}, D_{ij}/h^3) = h^3 \sum_{m=1}^{\infty} \sum_{n=1}^{\infty} \frac{\xi}{\vartheta} (s^2 m^2 C_{11} + n^2 C_{12}) \quad (2.98)$$

$$f_y(s, C_{ij}, D_{ij}/h^3) = h^3 \sum_{m=1}^{\infty} \sum_{n=1}^{\infty} \frac{\xi}{\vartheta} (s^2 m^2 C_{12} + n^2 C_{22}) \quad (2.99)$$

where $s = b/a$, $\xi = \frac{1}{mn} \sin\left(\frac{m\pi R}{a}\right) \sin\left(\frac{n\pi R}{b}\right)$, $\vartheta = D_{11}m^4s^4 + 2(D_{12} + 2D_{66})m^2n^2s^2 + D_{22}n^4$, and C_{ij} and D_{ij} are respectively the constitutive and bending stiffness components of the laminated composite plate calculated by means of the homogenized engineering constants [72]. Equations (2.98) and (2.99) are valid only for odd values of m and n . By adding enough terms, the solution of Equations (2.96) and (2.97) can converge, whereas convergence is not possible for a point load case [61].

The maximum stresses given by Equations (2.96) and (2.97) must be transformed to the stress components on the back outer ply of the laminate (i.e. $(\sigma_1, \sigma_2, \sigma_6)_p$). This is done by calculating the strain components of the plate; afterwards, the strain components are rotated to the local coordinates of the ply (axis 1 is aligned with the fibers, and axis 2 corresponds to the transverse direction to the fibers); finally, by means of the constitutive matrix of the ply, the corresponding stresses are obtained. All these operations are collected in the following equation:

$$\begin{Bmatrix} \sigma_1 \\ \sigma_2 \\ \sigma_6 \end{Bmatrix}_p = [C]_p [T]_\gamma [S] \begin{Bmatrix} (\sigma_x)_{max} \\ (\sigma_y)_{max} \\ 0 \end{Bmatrix} \quad (2.100)$$

where $[C]_p$ is the constitutive matrix of the back outer ply in the ply coordinate system, $[T]_\gamma$ is the rotation matrix of the engineering strains from the plate coordinate system to the ply coordinate system (see Appendix A), and $[S]$ is the compliance matrix of the plate in the plate coordinate system (i.e. $[S] = [C]^{-1}$). Developing Equation (2.100), the resulting ply stresses are:

$$\begin{aligned} (\sigma_1)_p &= \left((C_{11})_p c^2 + (C_{12})_p s^2 \right) (S_{11} (\sigma_x)_{max} + S_{12} (\sigma_y)_{max}) \\ &\quad + \left((C_{11})_p s^2 + (C_{12})_p c^2 \right) (S_{12} (\sigma_x)_{max} + S_{22} (\sigma_y)_{max}) \end{aligned} \quad (2.101)$$

$$\begin{aligned} (\sigma_2)_p &= \left((C_{12})_p c^2 + (C_{22})_p s^2 \right) (S_{11} (\sigma_x)_{max} + S_{12} (\sigma_y)_{max}) \\ &\quad + \left((C_{12})_p s^2 + (C_{22})_p c^2 \right) (S_{12} (\sigma_x)_{max} + S_{22} (\sigma_y)_{max}) \end{aligned} \quad (2.102)$$

$$(\sigma_6)_p = 2cs (C_{66})_p \left[(S_{12} - S_{11}) (\sigma_x)_{max} + (S_{22} - S_{12}) (\sigma_y)_{max} \right] \quad (2.103)$$

where $c = \cos(\theta)$, $s = \sin(\theta)$, and θ is the fiber orientation of the ply respect to the plate coordinate system.

In addition, the in-situ transverse tensile strength Y_T^{is} and the in-situ in-plane shear strength S_L^{is} for an outer ply, which is considered thin enough in comparison with the whole laminate thickness, can be calculated as [73, 74] (see Chapter 6):

$$\text{Thin outer ply} \begin{cases} Y_T^{is} = 1.12^2 \sqrt{\frac{E_2}{1 - \nu_{12}\nu_{21}} \frac{\mathcal{G}_{Ic}}{\pi h_p}} \\ S_L^{is} = 2 \sqrt{\frac{G_{12} \mathcal{G}_{IIc}}{\pi h_p}} \end{cases} \quad (2.104)$$

where E_2 , G_{12} and ν_{21} are the elastic properties of the ply, h_p is the ply thickness, and \mathcal{G}_{Ic} and \mathcal{G}_{IIc} are respectively the fracture toughness in mode I and mode II. Equation (2.104) is obtained by applying Linear Elastic Fracture Mechanics (LEFM) for longitudinal crack growth and assuming a uniform stress state. On the other hand, the tensile strength and the in-plane shear strength for thick plies are approached to the values measured from tests on unidirectional laminates, $Y_T^{is} = Y_T$ and $S_L^{is} = S_L$.

Under the presence of both in-plane shear and transverse tension, the critical energy release rate \mathcal{G}_c depends on the combined effect of all microscopic energy absorbing mechanisms such as the creation of a new fracture surface. The LaRC failure criterion [73–77] is used to predict matrix cracking under multi-axial loading:

$$(1 - g) \frac{(\sigma_2)_p}{Y_T^{is}} + g \left(\frac{(\sigma_2)_p}{Y_T^{is}} \right)^2 + \left(\frac{(\sigma_6)_p}{S_L^{is}} \right)^2 \leq 1 \quad (2.105)$$

where $g = \mathcal{G}_{Ic}/\mathcal{G}_{IIc}$.

Replacing the transverse and shear stresses $((\sigma_2)_p$ and $(\sigma_6)_p$) in Equation (2.105), and the corresponding strengths for thin and thick outer plies, the threshold load for tensile matrix cracking F_{mc}^{ten} can be calculated by simply taking the maximum value of the two extreme cases, thin and thick: $F_{mc}^{ten} = \max \{ (F_{mc}^{ten})_{thin}, (F_{mc}^{ten})_{thick} \}$.

Threshold load for oblique matrix crack

The stress state at the impact point $(x, y, z) = (a/2, b/2, -h/2)$ is 3D due to the flexural deformation and the contact load. The in-plane compressive and shear stresses due to the flexural deformation can be approached in the same way as it

is indicated in the previous section for determining a threshold load for vertical matrix crack on the back outer ply of the laminate. Solutions for the stresses due to concentrated loads in anisotropic plates are scarce and closed-form solutions are limited to transversely isotropic plates loaded along their axis of symmetry, and assuming a Hertzian pressure distribution as well as that the plate is semi-infinite, i.e. half-space [36, 78]. To approximate in a simplified form the stress state at the impact point, the superposition of the flexural stresses and the contact stresses of a half-space plate can be applied as it was shown by Olsson [79].

On the other hand, the maximum through-the-thickness shear stresses due to the flexural deformation created by a transverse static point load F_{mc}^{sh} located at the center of a simply supported, rectangular and orthotropic plate (see Figure 2.5), can be computed using the 3D stress equilibrium equations [61]. These maximum stresses are located at the edges and middle plane of the plate (i.e. $(\sigma_r)_{max}$: $(x, y, z) = (0, b/2, 0)$, and $(\sigma_q)_{max}$: $(x, y, z) = (a/2, 0, 0)$).

For determining the threshold load for matrix cracking at the impact point or at the edges of plate, a 3D failure criterion is required. The appearance of matrix cracks located at these points is not as critical as the matrix cracks located at other points since the former do not act as crack tips for large delaminations. Therefore, these matrix cracks do not imply a significant reduction of the residual strength of the structure, and for this reason a threshold load for these matrix cracks is not developed here.

Olsson et al. [23] proposed a simple threshold load for matrix cracking due to the through-the-thickness shear stress created by a static concentrated contact load. The threshold load is calculated by considering the Hertz distribution of the contact pressure, and the corresponding maximum value of the shear stress in the through-the-thickness direction and inside the contact radius. In the same way of the simplified shear stress field indicated by Davies et al. [69], the distribution of the through-the-thickness shear stress is assumed parabolical with the maximum located in the middle plane. The threshold load is defined as:

$$F_{mc}^{sh} = \frac{8\sqrt{3}}{9} (\pi S_L h)^{3/2} \sqrt{\frac{R}{Q_\alpha}} \quad (2.106)$$

where h is the plate thickness, R is the impactor tip radius, and Q_α is the effective

contact modulus (see Equation (2.5)).

2.6.2 Delamination

Delaminations are induced by interlaminar shear stresses which are promoted by matrix cracks, by stiffness mismatch between the adjacent plies, by the thickness of the ply (ply clustering), and by the laminate deflection. Increasing any of these factors will result in an increased mismatch in the bending deformations of adjacent ply groups with different orientations, yielding to large delaminations.

The study of the stiffness mismatch yields important information regarding the location, orientation, and size of delaminations. Liu [80] proposed the following dimensionless mismatch parameter M_L for two-layer plates based on the difference of their bending stiffness respect the global coordinate system of the plate:

$$M_L = \frac{D_{ij}(\theta_b) - D_{ij}(\theta_t)}{D_{ij}(0_b) - D_{ij}(90_t)} \quad (2.107)$$

where D_{ij} are the components of the bending stiffness matrix. Each ply is considered separately, so $D_{ij}(\theta_b)$ is the stiffness of the bottom layer acting alone, and the subscript t refers to the top layer. While a mismatch coefficient can be defined for each bending coefficient D_{ij} , usually only D_{11} is considered.

The mismatch parameter proposed in Equation (2.107) is inadequate for unidirectional plates since M_L is not equal to 0 despite the fact that these laminates do not have interfaces with mismatched adjacent fiber angles. Moreover, for plates with more than one interface with mismatched fiber orientations of the adjacent plies, this parameter is not applicable. To solve these limitations, Morita et al. [81] proposed a new parameter M_M which is calculated as:

$$M_M = \frac{1}{2\pi} \int_0^{2\pi} \frac{[\Delta C_{11}(\theta) z_i]_{max}}{D_{11}(\theta)} d\theta \quad (2.108)$$

where $\Delta C_{11}(\theta)$ is the difference of the in-plane stiffness between the adjacent plies in direction θ , z_i is the through-the-thickness distance from the neutral surface to the considered interface, and $D_{11}(\theta)$ is the bending stiffness of the entire laminate in the direction θ . The parameter M_M is a measure of the maximum bending stress

discontinuity given as an integrated quantity with respect to θ . It is considered empirically that the larger the parameter M_M , the larger the impact damage area.

Delaminations only occur at interfaces between plies of different orientation. The shape of the delamination is generally that of an oblong peanut, where its major axis follows the orientation of the lower ply at the interface [7, 21]. These shapes are a result of the shear stress distribution around the surrounding area of the impactor, of the low interlaminar shear strength along or close to the direction of the fibers, and of the matrix cracks created by the flexural in-plane stresses [82]. Figure 2.12 shows a typical distribution of these delaminations.

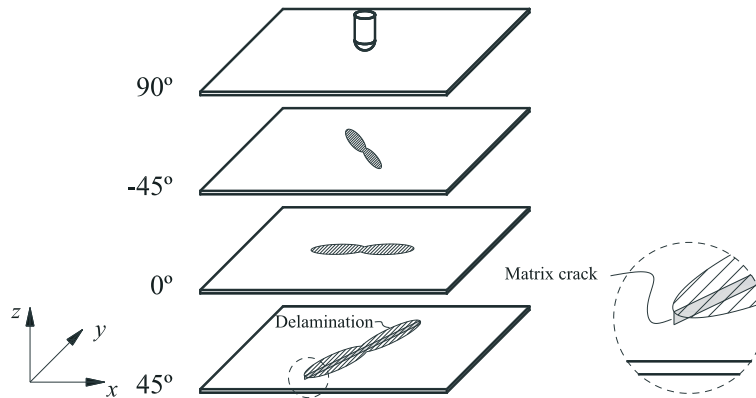


Figure 2.12: Example of peanut shaped delaminations.

There are two different phases during the impact driven delamination process (see Figure 2.13). Firstly, when the impact force reaches a threshold value F_d , there is unstable crack propagation leading to instantaneous large delaminated areas. This often causes the impact force to drop in the response, indicating sudden loss of stiffness [83]. The threshold load F_d does not physically represent the initiation of damage, as sub-critical matrix cracks and small delaminations may initiate at lower forces. Rather, it represents the initial value at which damage can be detected using the typical NDI methods, and a change in the stiffness properties of the laminate is expected [31, 59]. Normally, the threshold value is greater for thick laminates than for thin laminates, as shown in Figure 2.13. Secondly, after unstable crack growth, the size of the delaminations increase linearly with the force indicating stable delamination growths. Jackson and Poe [84] suggested the following semi-empirical formula which relates the maximum delamination size d_s and the impact force F :

$$d_s = \frac{1}{\pi S_L h} F \quad (2.109)$$

where S_L is the interlaminar shear strength and h is the plate thickness.

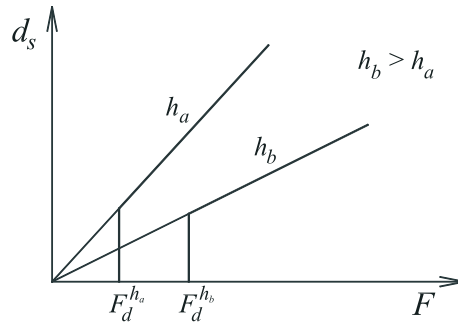


Figure 2.13: Maximum delamination size as a function of the impact force for plates with different thickness (after Christoforou [18]).

Figure 2.14 shows a typical profile of the impact force versus time history for a monolithic laminated composite plate, where the threshold load F_d and the peak force F_{max} are identified. Depending on the impact velocity, F_d can be equal to F_{max} . On the other hand, the identification of F_d is not always clear, due to the effects of the governing parameters (see Chapter 4), or due to the harmonic resonances of the impactor, of the load cell or of the plate during the impact event [59].

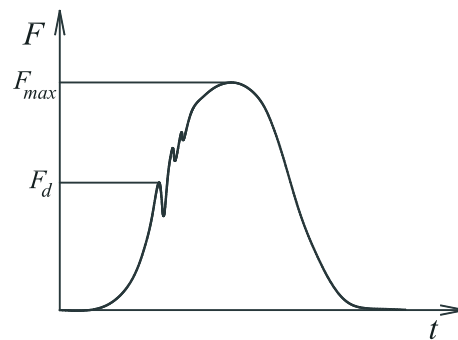


Figure 2.14: Representative impact force versus time history (after ASTM D7136 / D7136M [59]).

Threshold load for delamination

The criteria for matrix cracking given by Equations (2.105) and (2.106) can be used as delamination threshold loads assuming that the matrix crack tips act as initiation points for delaminations in impact events with quasi-static behavior.

A delamination growth criterion for static conditions was derived by Davies et al. [69, 85]. The model was based on Linear Elastic Fracture Mechanics (LEFM) and assumed that mode II fracture determines delamination growth in a simply supported circular plate. To simplify the development of the model, static loading conditions were considered, the laminate was treated as isotropic, only small deflections were considered (membrane effects are neglected), and the through-thickness distributed delaminations were collapsed into a single and perfectly circular mid-plane delamination. In detail, the relationship between the out-of-plane displacement w_o and an external point load F_{d1}^{stat} is given by the theory for thin plates as:

$$w_o = \frac{3r_p^2(1-\nu^2)}{4\pi Eh^3} F_{d1}^{stat} \quad (2.110)$$

where E , ν , h , and r_p are respectively the elastic modulus, the Poisson ratio, the thickness, and the radius of the plate. Assuming that the system is linear, it allows to apply the principle of superposition for the development of the elastic energy of a plate with a circular mid-plane delamination of radius a_c :

$$U = \frac{3r_p^2(1-\nu^2)}{8\pi Eh^3} (F_{d1}^{stat})^2 - \frac{3a_c^2(1-\nu^2)}{8\pi Eh^3} (F_{d1}^{stat})^2 + 2 \left(\frac{3a_c^2(1-\nu^2)}{8\pi E \left(\frac{h}{2}\right)^3} \left(\frac{F_{d1}^{stat}}{2}\right)^2 \right) \quad (2.111)$$

The first term of Equation (2.111) is the elastic energy of the plate without the delamination. The second term is the energy of a circular plate of radius a_c . The last term is related to the elastic energy of two circular plates of radius a_c and height $h/2$. Knowing that $\frac{\partial U}{\partial a_c} = 2\pi a_c \mathcal{G}_{IIc}$, the threshold load for a mid-plane circular delamination is:

$$F_{d1}^{stat} = \frac{\pi}{3} \sqrt{\frac{8E\mathcal{G}_{IIc}}{1-\nu^2}} h^{3/2} \quad (2.112)$$

By letting $E/(1 - \nu^2) = (12D)/h^3$, where D is the bending stiffness, Equation (2.112) can be rewritten as:

$$F_{d1}^{stat} = \pi \sqrt{\frac{32D\mathcal{G}_{IIc}}{3}} \quad (2.113)$$

Equations (2.112) and (2.113) show that delamination grows under a constant load independently of the delamination size. Therefore, an initial flaw is not required and thus the criterion can be used for the prediction of delamination onset. In addition, experimental data and finite element simulations indicate that the delamination threshold load is independent of the boundary conditions and of the in-plane size of the plate [23, 24, 31]. Although the delamination criterion was derived assuming static loading conditions it may, with a moderate correction factor, be used for impact responses with dynamic effects, such as in an infinite plate behavior [23]. Probably, this result is due to fact that F_{d1}^{stat} does not depend on the in-plane dimensions of the plate, in contrast with the threshold F_{mc}^{ten} developed in previously. In Davies et al. [86], this criterion was used in conjunction with a quasi-static, energy-balanced model based on finite element solutions to predict the threshold impact energy for delamination onset.

A more rigorous solution for an arbitrary number of delaminations located at same intervals through-the-thickness of the plate was derived by Suemasu and Majima [87]. The threshold impact load is defined as:

$$F_{dn_d}^{stat} = \pi \sqrt{\frac{32D\mathcal{G}_{IIc}}{n+1}} \quad (2.114)$$

where n is the number of same thickness plate regions separated by $n_d = n - 1$ same size delaminations. In the work developed by Olsson [24], Equation (2.114) is used for orthotropic plates by simply changing the isotropic plate stiffness D by the effective plate stiffness D^* for orthotropic plates (see Equation (2.55)).

The accumulation process of multiple delaminations was also described by Suemasu and Majima [87]. For equally sized multiple delaminations, the energy release rate is distributed nearly parabolic and symmetric about the middle surface, which corresponds to the location where the energy release rate reaches its maximum. For this case, the energy release rates are independent of the delamination size, and the more delaminations exist, the easier the delamination propagation is. Delaminations

of unequal size, they tend to an equal size by the growth of the smaller delaminations regardless of their location through-the-thickness of the laminate. These conclusions were obtained from closed-form energy release rate expressions summarized in Table 2.1, and by verifications with finite element analysis.

Table 2.1: Energy release rates for unequal size delaminations [87], where $S_0 = n^3 / (m^3 + (n - m)^3) - 1$, $S_1 = n^2 - S_0 - 1$, and m is the delamination number (numbering starts with the deepest back face delamination).

Delamination case	Energy release rates	
	m th delamination	$n - 2$ delaminations (average)
One delamination larger than the others	$\bar{\mathcal{G}}_{II} = \frac{F^2}{32\pi^2 D} S_0$	$\tilde{\mathcal{G}}_{II} = \frac{F^2}{32\pi^2 D} \frac{S_1}{n - 2}$
One delamination smaller than the others	$\bar{\mathcal{G}}_{II} = \frac{F^2}{32\pi^2 D} \frac{6n^2}{n + 6}$	$\tilde{\mathcal{G}}_{II} = \frac{F^2}{32\pi^2 D} \frac{n^2 + 2n + 3}{n + 6}$

Geometric nonlinear effects on the in-plane stresses becomes significant and must be considered when the deflection of the plate reaches the order of the plate thickness or that of the delaminated portions. A numerical Rayleigh-Ritz solution for large deflections was derived in a later paper of Suemasu and Majima [88]. Membrane effects increase the threshold load and cause an asymmetrical distribution of the energy release rate so that the delaminations near the back surface grow faster than those located elsewhere when the load is increased. Also, geometric non-linearity implies large impact energies for delaminations to propagate farther. Therefore, the result using the linear assumption that the more delaminations exist the easier is their propagation may not be true. Considering the finite bending strength and the critical perforation load, it can be said that a critical radius of the delaminations from which delamination propagation is difficult may exist. This critical radius is function of the interlaminar toughness and of an expected number of delaminations.

Olsson et al. [23] developed a fracture mechanics criterion for dynamic growth of an arbitrary number n_d of delaminations in a transverse isotropic plate. Again, the delaminations are located at the same intervals through-the-thickness of the laminate, small deflections are considered, and shear deformation is neglected. The

theory is validated for a wide range of test cases by comparison with 3D finite element simulations. The threshold impact load is:

$$F_{dn_d}^{dyn} = \frac{F_{dn_d}^{stat}}{\sqrt{1 - \frac{7\pi^2}{216}}} \approx 1.213F_{dn_d}^{stat} \quad (2.115)$$

where $F_{dn_d}^{stat}$ is the quasi-static threshold delamination load given by Equation (2.114). The resulting delamination threshold load is about 21% higher than the corresponding quasi-static threshold load.

2.6.3 Permanent indentation

An impact on a laminated composite plate, usually results with a visible permanent indentation at the impact point as a result of the matrix plasticity, disorder of the broken fibers, and friction between these fibers and the matrix. Just after the impact, the permanent indentation has its highest value and gradually its depth is reduced due to the material relaxation.

The prediction of the threshold load at which permanent indentation initiates can be approached by the following simple equation:

$$F_{ind} = k_y \alpha_{cr} \quad (2.116)$$

where k_y is a linearized stiffness of the elastic-plastic loading phase (Equation (2.27)), and α_{cr} is the critical indentation as from of it permanent indentation starts and is defined by Equation (2.28).

The corresponding threshold velocity for permanent indentation can be calculated by means of a simple energy balance of the simplified quasi-static model described in Section 2.4.4 and represented in Figure 2.8.b. Assuming that the impact energy is used for local and global deformation of the plate, the threshold velocity yields to:

$$V_{ind} = \frac{\alpha_{cr}}{M_i^{1/2}} \left[k_y + \frac{k_y^2}{k_{bsm}} \right]^{1/2} \quad (2.117)$$

where k_{bsm} is the plate global stiffness.

2.6.4 Fiber failure

Fiber failure generally occurs much later in the fracture process than matrix cracking and delamination, and it is considered as a precursor of plate perforation. Fiber failure occurs under the impactor due to locally compressive and shear stresses, and on the non-impacted face due to tensile bending stresses. More extensive fiber failure normally occurs in the central part of the delaminated region and appears to be fairly uniformly through-the-thickness of the laminate. Fiber failure in thin laminates generally affects more plies and is more extensive than in thick laminates, indicating the importance of membrane stresses in formation of fiber fracture [21].

2.6.5 Perforation

There are numerous modes of failure in which energy can be dissipated in impacts that result in complete penetration of the plates. Caprino and Lopresto [89] reported that the perforation energy depends on the total fiber volume of the plate and on the impactor tip shape, whereas the architecture of the fibers, the stacking sequence of the laminate and the type of matrix have no effect. Research into perforation impact is mainly concentrated on the ballistic range, although perforation can also occur for other types of impact behavior (see Section 2.2).

Perforation occurs when the fibers reach their critical strain, enabling the impactor to completely penetrate the material. Under this assumption, a conservative estimate of the quasi-static threshold load for perforation F_{per}^{ten} can be obtained by simply replacing the in-plane longitudinal stress on the back outer ply (Equation (2.101)) in the following fiber tensile failure criterion [76]:

$$\frac{(\sigma_1)_p}{X_T} \leq 1 \quad (2.118)$$

where X_T is the fiber tensile strength. Therefore, the threshold load for perforation F_{per}^{ten} yields:

$$F_{per}^{ten} = \frac{\pi^5 R^2 h^2 X_T}{8b^2 \mathcal{X}} \quad (2.119)$$

where \mathcal{X} is defined as:

$$\begin{aligned}
\mathcal{X} = & \left[\left((C_{11})_p c^2 + (C_{12})_p s^2 \right) S_{11} + \left((C_{11})_p s^2 + (C_{12})_p c^2 \right) S_{12} \right] \\
& \times f_x(s, C_{ij}, D_{ij}/h^3) \\
& + \left[\left((C_{11})_p c^2 + (C_{12})_p s^2 \right) S_{12} + \left((C_{11})_p s^2 + (C_{12})_p c^2 \right) S_{22} \right] \\
& \times f_y(s, C_{ij}, D_{ij}/h^3)
\end{aligned} \tag{2.120}$$

On the other hand, by considering the Hertz contact law and a uniform distribution of the through-the-thickness shear stress, a perforation threshold load due to laminate shear failure can be obtained [7, 90]. The resulting threshold load is:

$$F_{per}^{sh} = \sqrt{6} (\pi S_L h)^{3/2} \sqrt{\frac{R}{Q_\alpha}} \tag{2.121}$$

where S_L is the shear strength, h is the plate thickness, R is the impactor tip radius, and Q_α is the effective contact modulus (see Equation (2.5)). The corresponding velocity at which perforation occurs can be formulated by means of a simple energy balance similar to that used in the determination of the threshold velocity for permanent indentation. Assuming that impact energy is used for the perforation and for the global deformation of the plate, the threshold velocity yields:

$$V_{per}^{sh} = M_i^{-1/2} \left[\frac{4(2\pi)^{5/2}}{5} k_H^{-3/2} R^{5/4} (hS_L)^{5/2} + 8\pi^3 k_H^{-1} k_{bsm}^{-1} R^{3/2} (hS_L)^3 \right]^{1/2} \tag{2.122}$$

where k_{bsm} is the plate stiffness. If the global deformation of the plate is neglected (i.e. half-space behavior), the second term of Equation (2.122) is removed.

In Wen [91, 92], velocity thresholds for impact perforation on rectangular, flat, and monolithic laminated composite plates struck by impactors with different tip shapes are proposed. The approach is based on the assumption that the deformation is localized and the mean pressure offered by the plate to resist the impactor can be decomposed into two parts. One part is a cohesive quasi-static resistive pressure due to the elastic-plastic deformation of the plate. The other is a dynamic resistive pressure arising from velocity effects. The corresponding threshold for hemispherical-ended impactor is:

$$V_{per}^{com} = \frac{3\pi R^2 h \sqrt{\rho \sigma_{yc}}}{32M_i} \left[1 + \sqrt{1 + \frac{128M_i}{9\pi \rho R^2 h}} \right] \quad (2.123)$$

where R is the impactor tip radius, M_i is the impactor mass, h is the plate thickness, ρ is the density of the composite material, and σ_{yc} is the elastic limit of the plate in through-the-thickness compression which can be approached to the transverse compressive strength Y_C . It should be noted that Y_C is a strain rate dependent strength [93].

Chapter 3

Test configurations

3.1 Introduction

In the aeronautical industry, drop-weight impact tests are performed to assess the damage resistance of a structure. These tests create delaminations which are typically categorized as *Barely Visible Impact Damage* (BVID). Delaminations reduce significantly the compressive strength of the impacted structure. For this reason, *Compression After Impact tests* (CAI) are performed in order to assess the damage tolerance of the structure.

The sequential experimental tasks which are carried out in the present thesis in order to analyze laboratory coupons are: definition of the impact configurations (i.e. selection of the governing parameters), manufacturing of the specimens, non-destructive inspections for the detection of manufacturing flaws (e.g. ultrasonic techniques), drop-weight impact tests, non-destructive inspections to detect the BVID, and finally, CAI tests.

This chapter presents the definition of a set of low-velocity impact tests on laminated composite plates which allow the study of the effects of some governing parameters on the damage resistance. The goal is to obtain a range of different experimental results that will be used to assess whether the predictions given by the numerical simulations accurately account the complexity of the impact damage (see Chapter 7). It should be noted that all studies are focused on the effects of the governing parameters on the impact damage rather than on the results of the CAI tests. Furthermore, the description of the CAI test set-up is also explained in detail.

3.2 Impact tests

The procedure for the design of the experiments is of great importance since it must ensure that one given analysis is focused on the effects of only one governing parameter. Moreover, the procedure must provide a qualitative understanding whether damage will occur, as well as its type and extension.

The procedure used is mainly based on the impact characterization diagram proposed by Christoforou and Yigit [18, 19, 26, 27] (see Section 2.5). Given an impact configuration, the diagram predicts the behavior type and the maximum impact force by calculating only two key parameters, λ (i.e. relative stiffness) and ζ_w (i.e. relative mobility):

$$\lambda = \frac{k_{bsm}}{k_y} \quad (3.1)$$

$$\zeta_w = \frac{\sqrt{M_i k_y}}{16\sqrt{I_1 D^*}} \quad (3.2)$$

It should be noted that the key parameters are obtained by considering a linear contact law [19] (see Section 2.3.4), and a dimensionless framework based on the maximum indentation where the magnitudes are defined as: mass $[M] = M_i$, time $[T] = M_i^{1/2} k_y^{-1/2}$, and length $[L] = M_i^{1/2} k_y^{-1/2} V_0$ (see Section 2.4.2). In particular, the linear contact stiffness k_y is calculated by means of Equation (2.27) and the plate stiffness k_{bsm} can be approached experimentally, by using numerical methods, or analytically in cases with simple structure geometries. The expression used by Yigit and Christoforou [26] to predict the stiffness k_{bsm} , for a simply supported plate without considering shear and membrane effects, is:

$$k_{bsm} = k_b = \frac{D^*}{0.0116b^2} \quad (3.3)$$

where b is the smallest width of the plate [24].

The prediction of the maximum elastic impact force is useful because it can be compared with a damage threshold load (see Section 2.6). Using the dimensionless framework, the maximum dimensional elastic force can be obtained as:

$$F_{max} = \bar{F}_{max} V_0 \sqrt{M_i k_y} = \bar{F}_{max} \sqrt{k_y} \sqrt{2E_i} \quad (3.4)$$

where \bar{F}_{max} is the dimensionless maximum elastic force extracted from the impact characterization diagram by means of the key parameters λ and ζ_w . The variable E_i is the impact energy.

3.2.1 Benchmark: ASTM drop-weight impact test

The ASTM test method for measuring the damage resistance of a fiber-reinforced polymer matrix composite when subjected to a drop-weight impact event (i.e. ASTM D7136 / D7136M [59]) is taken as a reference in order to fix some of the governing parameters. Other guidelines for a drop-weight impact test provided by the aeronautical industry are available (e.g. Airbus AITM1-0010 [94]; Boeing 7260 [95]; NASA ST-1 [96]), however the set-ups are all essentially the same.

The standard is focused on rectangular, flat, and monolithic laminated composite plates with 150mm×100mm in-plane dimensions. If the laminates are manufactured using unidirectional plies, a balanced and symmetric stacking sequence $[(45/0/-45/90)_n]_S$ is defined. The whole number n is selected in such a way that the cured plate thickness is close to 5mm. The plate stacking sequence is defined by taking the 0° fiber orientation aligned with the longer in-plane dimension of the plate.

The specimens are placed over a flat support fixture base with a 125mm×75mm rectangular cut-out which allows the impactor to contact through the specimen without interferences (see Figure 3.1.a). Guiding pins are located such that the specimen can be centrally positioned over the cut-out. The support fixture base has four rubber-tipped clamps which restrain the specimen during impact and provide a minimum holding capacity of 1100N. These rubber-tipped points clamp the specimen at 12.5mm and 6mm from each edge of the open window of the fixture base (see Figure 3.1.b) [94]. The boundary conditions provided by the clamping system can be approximated to simply supported [60].

The impact tests are carried out with an impact tester, which includes a guide mechanism, a rigid clamping system, a drop-weight instrumented impactor, a velocity sensor, and a rebound catcher. The impacts are performed by releasing the impactor with a selected mass from a desired preset height, and dropped freely according to the gravitational force and following a guide mechanism. A normal incidence angle impact occurs at the center of the plate caused by a 16mm diameter

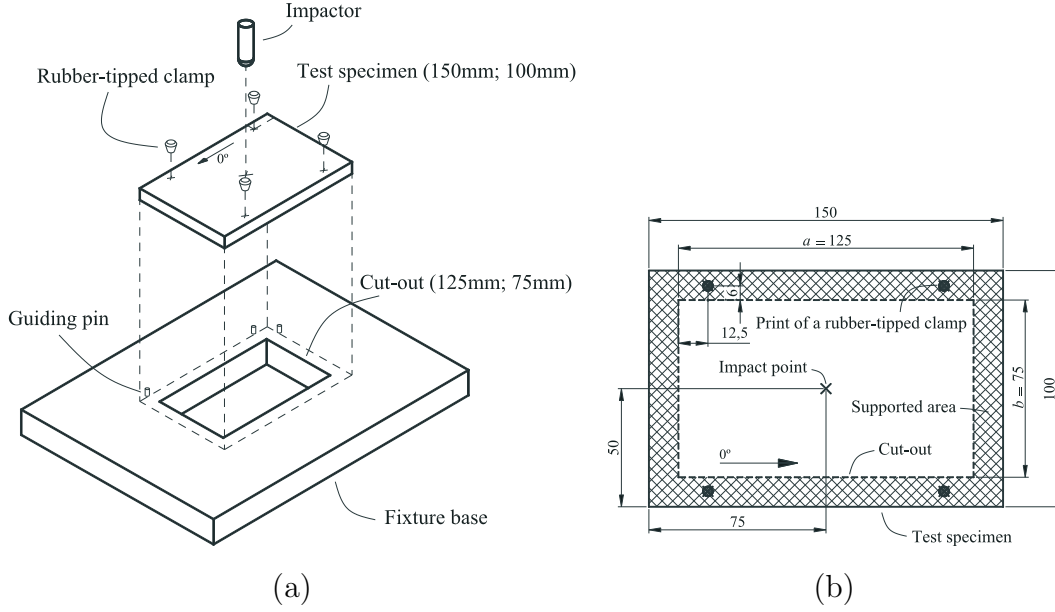


Figure 3.1: (a) Impact support fixture; (b) detail of the support area and clamping points of the specimen.

hemispherical-shaped impactor made of hardened steel. Just prior to impact on the specimen, a steel flag connected to the impactor is passed through an optical sensor which triggers the data acquisition system and calculates the initial impact velocity V_0 . The velocity is calculated from the distance between two edges of the flag and the time interval to pass through the sensor. Once impact begins, the contact force is detected by the force transducer attached to the impactor. The force history is stored in a computer. Finally, if perforation does not occur, a rebound catcher is also triggered by the optical sensor so that a re-strike does not occur.

The velocity and displacement history of the impactor, $V(t)$ and $w_i(t)$ respectively, can be calculated by integrating once and twice the force history:

$$V(t) = V_0 + gt - \int_0^t \frac{F(t)}{M_i} dt \quad (3.5)$$

$$w_i(t) = w_0 + V_0 t + \frac{gt^2}{2} - \int_0^t \left(\int_0^t \frac{F(t)}{M_i} dt \right) dt \quad (3.6)$$

where V_0 is the initial impact velocity, g is the acceleration due to the gravity, t is the time, and w_0 is the impactor position from reference location at time $t = 0$.

Additionally, the energy absorbed by the specimen, $E_a(t)$, can be calculated as:

$$E_a(t) = \frac{M_i (V_0^2 - V(t)^2)}{2} + M_i g w_i(t) \quad (3.7)$$

The standard suggests testing a sample of 5 specimens using a constant impactor mass of 5.5kg and a constant impact energy calculated in function of the specimen thickness:

$$E_i = C_E h \quad (3.8)$$

where h is the plate thickness and C_E is a ratio of the impact energy to the specimen thickness equal to 6.7J/mm. The reason for defining the impact energy by means of Equation (3.8) is related to the effects of the support conditions on the impact damage. When an impact is performed following the standard specifications, the specimen will develop damage sizes less than half of the unsupported specimen width (i.e. 38mm), thus avoiding significant interactions of the damage areas with the edge support conditions.

Tables 3.1 and 3.2 summarize the specifications of the standard regarding the specimen coupons and the impactor.

Table 3.1: ASTM D7136 / D7136M specifications for the specimen.

Specimen coupons	
Shape	Flat and rectangular
Thickness	$h \approx 5\text{mm}$
In-plane size	$a_t = 150\text{mm} \times b_t = 100\text{mm}$
Lamina type	Unidirectional or woven fabric
Stacking sequence	$[(45/0/ - 45/90)_n]_S$ (for unidirectional laminas)
Boundary conditions	Four rubber-tipped clamps

Following the specifications proposed by the standard, using the properties summarized in Table 7.1 for AS4/8552 carbon-epoxy composite material (see Chapter 7), and assuming a ply thickness of $h_p = 0.184\text{mm}$, the resulting laminate is

Table 3.2: ASTM D7136 / D7136M specifications for the impactor.

Impactor	
Shape	Hemispherical
Radius	$R = 8\text{mm}$
Material	Steel (60 to 62 HRC)
Mass	$M_i = 5.5\text{kg}$
Velocity	$V_0 = \sqrt{\frac{2(C_E h)}{M_i}}$
Incidence impact angle	Normal to the plate

$[(45/0/ - 45/90)_3]_S$ with a total nominal thickness $h = 4.42\text{mm}$. This plate thickness defines an impact energy of $E_i = 29.6\text{J}$ (see Equation (3.8)) and an impact velocity of $V_0 = 3.28\text{ms}^{-1}$.

The terms required to find the key parameters of the impact characterization diagram can be respectively calculated as: k_{bsm} by Equation (3.3), k_y by Equation (2.27), I_1 by Equation (A.47), and D^* by Equation (2.55). Using these definitions and assuming that the effective in-plane dimensions of the plate are $a = 125\text{mm}$ and $b = 75\text{mm}$ (see Figure 3.1.b), yield to: $\lambda = 0.71$ and $\zeta_w = 8.11$. These parameters predict a quasi-static behavior and a maximum dimensionless force of $\bar{F}_{max} = 0.65$. Finally, using Equation (3.4), the maximum impact force is $F_{max} = 14.28\text{kN}$.

The analytical damage thresholds can be calculated and compared with the maximum impact force in order to predict qualitatively the damage occurrence. As it is noted in the standard, matrix cracking and delamination damage are ensured if all the specifications of the standard are followed. This is demonstrated in Table 3.3, where the corresponding damage thresholds for matrix cracking and delamination are below the maximum predicted force.

Furthermore, the maximum load is close to the perforation threshold which indicates that perforation can occur. However, it is difficult to develop perforation because other damage mechanisms are generated previously so they absorb energy and avoid the subsequent perforation process.

Table 3.3: Damage thresholds for AS4/8552 carbon-epoxy composite material.

Damage mechanism	Equation	Value [kN]
Matrix cracking	(2.105)	$F_{mc}^{ten} = 5.92$
	(2.106)	$F_{mc}^{sh} = 1.82$
Delamination	(2.112), using D^*	$F_{dl}^{stat} = 5.66$
Permanent indentation	(2.116)	$F_{ind} = 0.33$
Perforation	(2.119)	$F_{per}^{ten} = 13.98$

3.2.2 Selected studies: fixed and variable parameters

Taking as a reference the standard for drop-weight impact test [59], different experimental studies will be performed. All these studies will be focused mainly on the damage onset which produces a significant reduction on the structure stiffness and/or residual strength, i.e. F_d (see Figure 2.14).

The variables selected in order to study their effects are: the ply thickness h_p (ply clustering), the laminate thickness h , stacking sequence, the impactor mass M_i and the impact velocity V_0 . The variation of these parameters yield to three main studies: effect of ply thickness (clustering), effect of the mismatch angles of the plies, and effect of the laminate thickness. As will be demonstrated in the following sections, all these studies are under quasi-static impact behavior. Therefore, the prediction of the maximum elastic impact force can also be obtained by means of Equation (2.83).

For all laminates, the composite material used is AS4/8552 carbon-epoxy unidirectional pre-preg. The properties of the material are summarized in Table 7.1 (see Chapter 7). It should be noted that for the calculation of the ply thickness, the corresponding cured value of the laminate thickness will be used (known after specimen manufacturing).

All the impact tests described below are performed using a commercially available CEAST Fractovis Plus instrumented impact drop-weight tower. The impact tester is equipped with a load cell of 22kN attached to the impactor, an automatic pneumatic rebound brake system, and a clamping system with a holding capacity of 3000N at each of the four clamping points (see Figure 3.2).

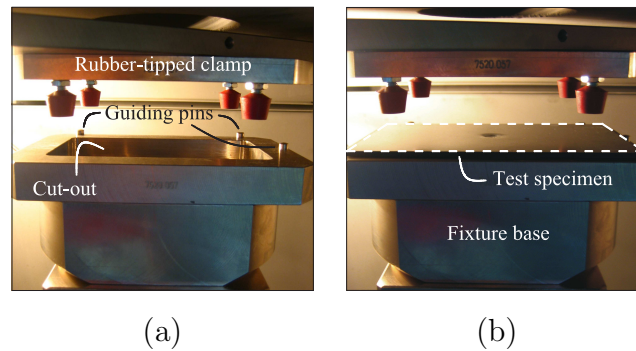


Figure 3.2: Detail of the clamping system, (a) without specimen and (b) with specimen.

Finally, the non-destructive inspections before and after impact will be performed by the C-scan ultrasonic technique, which gives the projected damaged areas over the structure thickness. Additionally, the measurements of the dent-depth are performed by means of a Mitutoyo 3D coordinate measuring machine. It should be noted that not all the impacted specimens are selected for the dent-depth measurements.

Effect of ply thickness (clustering)

Ply clustering was found to reduce the damage resistance of a laminate [60]. Stacking plies with the same fiber orientation increases the interlaminar shear stresses at the adjacent interfaces due to the increased difference in the bending stiffness of the ply groups. This increase in stress, in turn, leads to larger delaminations.

Ply clustering also reduces the number of interfaces available for delamination, because delamination typically occurs at interfaces with different fiber orientations. Reducing the number of locations available for delamination will increase the delamination size at the remaining interfaces [97, 98], since delamination acts as an energy dissipating mechanism during the impact event.

The transverse tensile and shear strengths of a ply are function of the ply thickness, of the ply position in the laminate, and of the fiber orientation of the adjacent plies. This is called the *in-situ effect*. Since matrix cracks act as initiation points for delaminations, the in-situ effect must be considered for a proper analysis of the ply clustering effect.

The effect of ply clustering on the damage tolerance, assessed by means of the

residual compressive load, is not yet fully clear. In fact, the compressive strength decreases if the plate bending stiffness is reduced. In addition, the laminate bending stiffness decreases if the size of the delaminations created by impact are large (i.e. when clustering is increased) but also when the number of delamination planes is increased (i.e. when clustering is reduced). Therefore, given these counteracting effects, it is difficult to assess whether ply clustering reduces the damage tolerance of a structure.

The stacking sequences proposed for this study are $[(45/0/-45/90)_4]_S$, $[(45_2/0_2/-45_2/90_2)_2]_S$, and $[45_4/0_4/-45_4/90_4]_S$ (in the following, these laminates are respectively identified as L02, L03, and L04). All laminates have the same plate thickness h because an equal number of plies is used (i.e. 32 plies; $h = 5.8\text{mm}$). However, the clusterings h_p are different (i.e. L02: $h_p = h_{pp}$, L03: $h_p = 2h_{pp}$, and L04: $h_p = 4h_{pp}$, where h_{pp} is the thickness of a single pre-preg ply), yielding to different number of interfaces for delamination (i.e. L02: $n_d = 30$, L03: $n_d = 14$, and L04: $n_d = 6$).

Three different impact energies are considered: 38.6J, 28.6J and 19.3J. Given that the impactor mass is kept constant at 5kg, the different energies also enable the study of the effects of velocity. In detail, Table 3.4 shows the impact configurations for all the laminates. Since the repeatability of the impact test is quite good (see Chapter 4), a sample of less than three specimens is used for some cases.

Table 3.4: Impact configurations for laminates: L02, L03 and L04.

Specimen name	Impact energy [J]	Impactor mass [kg]	Impact velocity [ms^{-1}]	Drop height [mm]
L0x-S01				
L0x-S02	38.6	5	3.93	787.5
L0x-S03				
L0x-S04	28.6	5	3.38	582.5
L0x-S05				
L0x-S06	19.3	5	2.78	394.0

Using the material properties summarized in Table 7.1, the resulting key parameters of the impact characterization diagram are: $\lambda = 1.62$ and $\zeta_w = 4.48$ for laminate L02, $\lambda = 1.60$ and $\zeta_w = 4.50$ for laminate L03, and $\lambda = 1.55$ and $\zeta_w = 4.58$

for laminate L04. Since the key parameters are independent of the impact velocity, the resulting values are constant for each laminate at any impact energy (see Equations (3.1) and (3.2)). Additionally, the key parameters are almost equal for all laminates due to the fact that the stiffness of the laminates is similar. Therefore, the dimensional elastic response of the laminates for each impact energy is also expected to be similar.

Introducing the key parameters in the impact characterization diagram, a quasi-static behavior and a maximum dimensionless force of $\bar{F}_{max} = 0.78$ are predicted for all the laminates. The dimensionless force yields to the following maximum elastic impact forces for each impact energy: $F_{max} = 19.8\text{kN}$ for $E_i = 38.6\text{J}$, $F_{max} = 17.1\text{kN}$ for $E_i = 28.6\text{J}$, and $F_{max} = 14.0\text{kN}$ for $E_i = 19.3\text{J}$.

Finally, the damage thresholds explained in Section 2.6 are summarized in Table 3.5. Again, these thresholds are constant for each impact energy since no dependence with velocity is considered in the formulations. Comparing the threshold loads with the maximum elastic impact forces, the occurrence for damage can be analyzed easily.

Table 3.5: Damage thresholds for laminates: L02, L03 and L04.

Damage mechanism	Equation		Values [kN]		
			L02	L03	L04
Matrix cracking	(2.105)	F_{mc}^{ten} :	10.34 (thin)	7.20 (thin)	4.92 (thin)
	(2.106)	F_{mc}^{sh} :	2.74	2.74	2.74
Delamination	(2.112), using D^*	F_{dl}^{stat} :	8.53	8.49	8.34
	(2.114), using D^*	$F_{dn_d}^{stat}$:	2.61	3.68	5.11
	(2.115), using D^*	F_{dl}^{dyn} :	10.35	10.30	10.11
	(2.115), using D^*	$F_{dn_d}^{dyn}$:	3.17	4.46	6.19
Permanent indentation	(2.116)	F_{ind} :	0.33	0.33	0.33
Perforation	(2.119)	F_{per}^{ten} :	24.23	23.88	23.16

The most significant damage threshold loads are the ones which indicate important reductions on the plate stiffness and/or strength. Basically, these thresholds are given by Equations (2.105) and (2.112) (i.e. F_{mc}^{ten} and F_{dl}^{stat} , respectively). The first gives a value for matrix cracking on the back outer ply which can create an

elongated delamination at the first interface from the back face of the plate. The second gives a threshold for a circular mid-plane delamination.

As shown in Table 3.5, for laminate type L02 the first delamination appears in the mid-plane of the plate ($F_d = F_{d1}^{stat}$), and for laminate types L03 and L04 the delamination is located on the back face ($F_d = F_{mc}^{ten}$). Figure 3.3 shows these threshold loads as a function of the ply thickness on a logarithmic scale. Only F_{mc}^{ten} for thin plies depends on the ply thickness (see Equation (2.104)). The solid gray line shows the trend of the analytical threshold load in function of the ply thickness for the laminates considered.

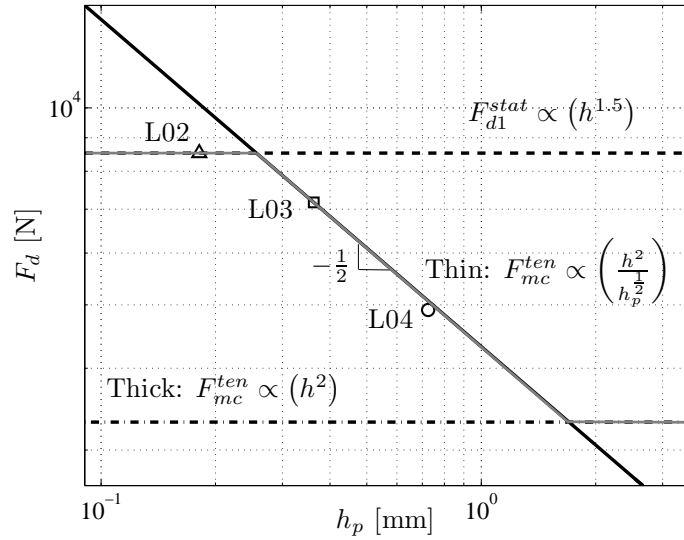


Figure 3.3: Analytical threshold load trend in function of h_p , for laminates L02, L03 and L04. The damage threshold F_{mc}^{ten} for laminates with thin plies is computed from the stresses of laminate type L03.

Furthermore, it is predicted that perforation will not occur for any impact energy because all the maximum elastic forces are below the perforation threshold.

Finally, the values of the mismatch parameter proposed by Morita et al. [81] (see Equation (2.108)) for each laminate are: $M_M = 0.270\text{mm}^{-2}$ for L02, $M_M = 0.235\text{mm}^{-2}$ for L03, and $M_M = 0.198\text{mm}^{-2}$ for L04. The mismatch parameter provides information about the effects of the mismatch interface angles of the plies on the resulting projected delamination area. It is considered that the larger the parameter M_M is, the larger the projected delamination area is. The results obtained

indicate that the laminate with thin plies will have larger projected delamination area than that of the laminate with thick plies. However, this deduction is not valid because it is expected that laminate L04 will have larger delaminations due to the reduced number of available interfaces for delamination. Therefore, the Morita parameter is not suitable to compare different stacking sequences to predict the largest resulting delamination area.

Effect of ply mismatch angle at interfaces

The mismatch angle of an interface is the difference in the fiber orientation of the adjacent plies. Increasing the mismatch angle increases the stress concentration at the interface due to an increased difference in the bending stiffness. Therefore, the damage resistance can be reduced if the mismatch angle is increased because larger delaminations are expected. For this reason, the damage tolerance is also expected to be reduced.

For this study, the laminate type L02 presented in previous study is compared with a new laminate $[(0/90)_9]_s$ (in the following, it is identified as L06). As it can be seen, laminate L06 has a stacking sequence with increased mismatch angles in comparison with laminate L02. Laminates L02 and L06 have practically equal cured ply thickness h_p , but different laminate thickness h since more plies are used for L06 (i.e. L02: $h = 5.8\text{mm}$ and L06: $h = 6.8\text{mm}$).

The impact configurations considered are the same as the described ones for ply clustering study. Accordingly, three different impact energies are defined 38.6J, 28.6J and 19.3J, with a constant impactor mass of 5kg (see Table 3.4). Therefore, the predictions for laminate type L02 given in previous study can be reused herein.

Using the material properties summarized in Table 7.1, the resulting key parameters of the impact characterization diagram for laminate type L06 are: $\lambda = 2.52$ and $\zeta_w = 3.31$. Introducing the key parameters in the impact characterization diagram, a quasi-static behavior and a maximum dimensionless force of $\bar{F}_{max} = 0.85$ are expected for all the impact energies. The dimensionless force yields to the following maximum elastic impact forces: $F_{max} = 21.4\text{kN}$ for $E_i = 38.6\text{J}$, $F_{max} = 18.4\text{kN}$ for $E_i = 28.6\text{J}$, and $F_{max} = 15.1\text{kN}$ for $E_i = 19.3\text{J}$.

Table 3.6 summarizes the main damage threshold loads. The significant first damage for laminate L06 is $F_d = F_{d1}^{stat}$ which predicts a circular mid-plane delam-

ination. In addition, it should be noted that the threshold load F_{mc}^{ten} is close to F_{d1}^{stat} . Therefore, the first drop in the impact load history may be triggered by a combination of both delamination types.

Finally, it is predicted that perforation will not occur for any impact energy because all the maximum elastic forces are below the perforation threshold.

Table 3.6: Damage thresholds for laminate L06.

Damage mechanism	Equation	Values [kN]
Matrix cracking	(2.105)	F_{mc}^{ten} : 11.26 (thin)
	(2.106)	F_{mc}^{sh} : 3.47
Delamination	(2.112), using D^*	F_{d1}^{stat} : 10.65
	(2.114), using D^*	$F_{dn_d}^{stat}$: 3.07
	(2.115), using D^*	F_{d1}^{dyn} : 12.92
	(2.115), using D^*	$F_{dn_d}^{dyn}$: 3.73
Permanent indentation	(2.116)	F_{ind} : 0.33
Perforation	(2.119)	F_{per}^{ten} : 37.16

Effect of the laminate thickness

Another proposed study is to analyze the effects of the laminate thickness on the damage resistance. Modifying the plate thickness and the impactor mass, the behavior of an impact can be local or global dominated. Because of that, the resulting damage mechanisms as well as their extensions can vary. For instance, in thick laminates, the delaminations initiate close to the loaded surface since contact stresses are high. However, in thin laminates, the delaminations initiate close to the mid-plane since contact stresses are negligible. In addition, thin laminates stand large global bending deflections which often generate, at a certain point, geometric nonlinear effects, i.e. membrane effects. These effects stiff the impact response of the structure because the stiffness evolves from bending to axial.

On the other hand, it is obvious that the damage tolerance is also improved if the laminate thickness is increased. However, the resulting structures are heavier and more expensive.

For this study, the laminate type L02 presented in the previous studies is compared with two new laminates: $[(45/0/ - 45/90)_2]_S$ and $[(45/0/ - 45/90)_6]_S$ (in the following, they are identified as L01 and L05, respectively). As it can be verified, the stacking sequences are equal but the number of repeated ply groups are different, yielding to three different laminate thicknesses (i.e. L01: $h = 3.0\text{mm}$, L02: $h = 5.8\text{mm}$, and L05: $h = 8.8\text{mm}$).

The impact configurations considered for laminates L01 and L05 are respectively summarized in Tables 3.7 and 3.8 (see Table 3.4 for the configurations of the laminate type L02). The comparable cases of impact energy which allow to analyze the effects of laminate thickness are: 19.3J for laminates L01 and L02, and 38.6J for laminates L01, L02 and L05. For both cases of energy, the impactor mass is kept constant and equal to 5kg.

Table 3.7: Impact configurations for laminate type L01.

Specimen name	Impact energy [J]	Impactor mass [kg]	Impact velocity [ms^{-1}]	Drop height [mm]
L01-S01	38.6	5	3.93	787.5
L01-S02	19.3	5	2.78	394.0
L01-S03	19.3	6	2.54	328.9
L01-S04	19.3	6	2.54	328.9
L01-S05	19.3	6	2.54	328.9
L01-S06	12.0	2	3.46	610.4

Table 3.8: Impact configurations for laminate type L05.

Specimen name	Impact energy [J]	Impactor mass [kg]	Impact velocity [ms^{-1}]	Drop height [mm]
L05-S01	38.6	5	3.93	787.5
L05-S02	38.6	5	3.93	787.5
L05-S03	57.8	6	4.39	982.6
L05-S04	57.8	6	4.39	982.6
L05-S05	57.9	15	2.78	394.0
L05-S06	57.9	15	2.78	394.0

Besides the configurations considered for the study of the laminate thickness, Tables 3.7 and 3.8 describe other impact configurations for laminates L01 and L05,

respectively. These configurations allow to analyze the effects of changing the impactor mass and the impact velocity but keeping constant the impact energy. In detail, this study is performed by means of: specimens S02 and S03 ($M_i = 5\text{kg}$) compared with S04 and S05 ($M_i = 6\text{kg}$) for laminate L01, and specimens S03 and S04 ($M_i = 6\text{ kg}$) compared with S05 and S06 ($M_i = 15\text{kg}$) for laminate L05. In addition, the impact configuration of specimen L01-S06 is used in order to analyze if the resulting damage behavior is more localized than other configurations with larger impactor mass.

Using the material properties summarized in Table 7.1, the resulting key parameters of the impact characterization diagram and the resulting maximum elastic impact forces are summarized in Table 3.9 for laminate L01, and in Table 3.10 for laminate L05.

Table 3.9: Maximum elastic impact force predictions for laminate type L01.

Specimen	M_i [kg]	λ	ζ_w	\bar{F}_{max}	V_0 [ms^{-1}]	F_{max} [kN]
L01-S01	5	0.22	16.82	0.43	3.93	10.8
L01-S02	5	0.22	16.82	0.43	2.78	7.6
L01-S03						
L01-S04	6	0.22	18.42	0.43	2.54	7.6
L01-S05						
L01-S06	2	0.22	10.64	0.43	3.46	6.0

Table 3.10: Maximum elastic impact force predictions for laminate type L05.

Specimen	M_i [kg]	λ	ζ_w	\bar{F}_{max}	V_0 [ms^{-1}]	F_{max} [kN]
L05-S01	5	5.67	1.94	0.92	3.93	23.32
L05-S02						
L05-S03	6	5.67	2.13	0.92	4.39	28.5
L05-S04						
L05-S05	15	5.67	3.36	0.92	2.78	28.5
L05-S06						

Table 3.11 summarizes the main damage threshold loads for laminates L01 and L05. Perforation damage clearly will occur for specimen L01-S01 because the maximum elastic impact force is higher than the perforation threshold load. Additionally, specimens from L01-S02 to L01-S05 (i.e. with an impact energy of 19.3J), the maximum load is close to the perforation threshold which indicates that perforation can also occur. In reality, it is difficult to develop perforation in these specimens because other damage mechanisms are generated previously so they absorb energy and avoid the subsequent perforation process. Therefore, except for specimen L01-S01, it is expected that all impact configurations of laminate L01 will develop a first drop in the impact load history produced by a narrow and elongated delamination at the first interface from the back face of the plate ($F_d = F_{mc}^{ten}$). On the other hand, perforation will not occur for any impact configuration of laminate type L05. Moreover, the significant first damage for laminate L05 is $F_d = F_{d1}^{stat}$. Thus, it is expected that the first drop in the impact load histories is produced by a circular mid-plane delamination as it was also predicted for laminate type L02.

Table 3.11: Damage thresholds for laminates: L01 and L05.

Damage mechanism	Equation		Values [kN]	
			L01	L05
Matrix cracking	(2.105)	F_{mc}^{ten} :	2.68 (thin)	23.80 (thin)
	(2.106)	F_{mc}^{sh} :	1.02	5.11
Delamination	(2.112), using D^*	F_{d1}^{stat} :	3.16	15.97
	(2.114), using D^*	$F_{dn_d}^{stat}$:	1.37	3.99
	(2.115), using D^*	F_{d1}^{dyn} :	3.83	19.37
	(2.115), using D^*	$F_{dn_d}^{dyn}$:	1.66	4.84
Permanent indentation	(2.116)	F_{ind} :	0.33	0.33
Perforation	(2.119)	F_{per}^{ten} :	6.39	56.04

As a summary of the analytical threshold loads for all the laminates described in the previously proposed studies, Figure 3.4 shows the trends of these loads in function of the ply thickness on a logarithmic scale. The predicted critical values have been divided by h^2 in order to keep constant the profiles for matrix cracking on the back outer ply for each stacking sequence type (i.e. type TI: $[(45_x/0_x/ - 45_x/90_x)_n]_s$;

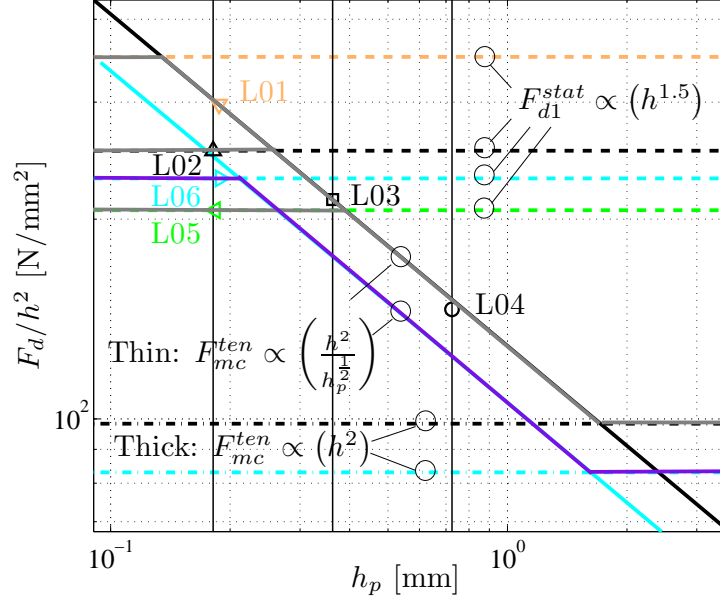


Figure 3.4: Analytical threshold trends for all laminates.

type CP: $[(0_x/90_x)_n]_S$). The ticked gray lines indicate the threshold trend for the stacking sequence type TI, and the blue lines indicate the expected trend for the stacking sequence type CP.

Summary of selected laminates

As a summary, the laminate types selected for the impact and compression impact tests are collected in Table 3.12. As was noted previously, the sample for each laminate are 6 specimens, most of them with different impact configurations.

The laminated composite plates proposed were manufactured using Hexply AS4-8552 carbon-epoxy unidirectional pre-preg. The pre-preg was cut automatically and the lamination was done manually. The laminated plates were cured in an autoclave following the curing cycle specified by the supplier. The cured ply thickness varies in function of the plate thickness.

Table 3.12: Selected laminates.

Name	Stacking sequence	Number of plies	Number of interfaces for delamination (n_d)	Cured ply thickness (h_{pp}) [mm]	Cured plate thickness (h) [mm]
L01	$[(45/0/-45/90)_2]_S$	16	14	0.1875	3.0
L02	$[(45/0/-45/90)_4]_S$	32	30	0.18125	5.8
L03	$[(45_2/0_2/-45_2/90_2)_2]_S$	32	14	0.18125	5.8
L04	$[45_4/0_4/-45_4/90_4]_S$	32	6	0.18125	5.8
L05	$[(45/0/-45/90)_6]_S$	48	46	0.1833	8.8
L06	$[(0/90)_9]_S$	36	34	0.1889	6.8

3.3 Compression after impact tests (CAI)

The *Compression After Impact test* (CAI) is performed to obtain the compressive residual strength of drop-weight impacted laminates. This is often called the study of damage tolerance since it refers to the experimental determination or the numerical prediction of the residual mechanical properties of the damaged structure [7].

Compressive loading causes buckling of sub-laminates in the *Barely Visible Impact Damage* (BVID) region which forces opening delaminations and then allowing the damage to propagate from the initial state until the subsequent failure of the structure. Figure 3.5 shows different buckling modes which can be done during the CAI test.

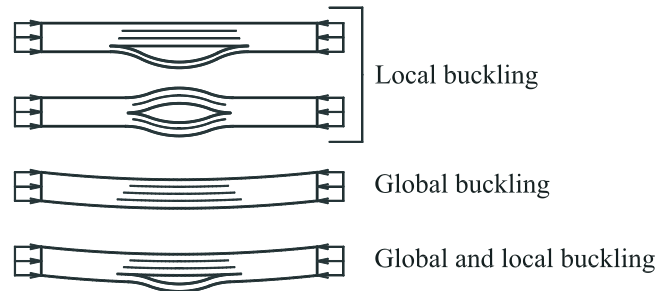


Figure 3.5: Buckling modes of delaminated plates in compression (after Davies and Olsson [21]).

3.3.1 Benchmark: ASTM compression after impact test

The ASTM test method for measuring the compressive residual strength of a damaged fiber-reinforced polymer matrix composite plate (i.e. ASTM D7137 / D7137M [99]) is taken as a reference in order to perform the CAI tests. This guideline is linked to the standard ASTM D7136 / D7136M [59] for drop-weight impact test (see Section 3.2.1).

The CAI test consists on install the damaged laminate in a multi-piece support fixture (see Figure 3.6.a), that has been aligned to minimize loading eccentricities and induced specimen bending. The specimen fixture assembly is placed between flat plates and end-loaded under compressive force until specimen failure.

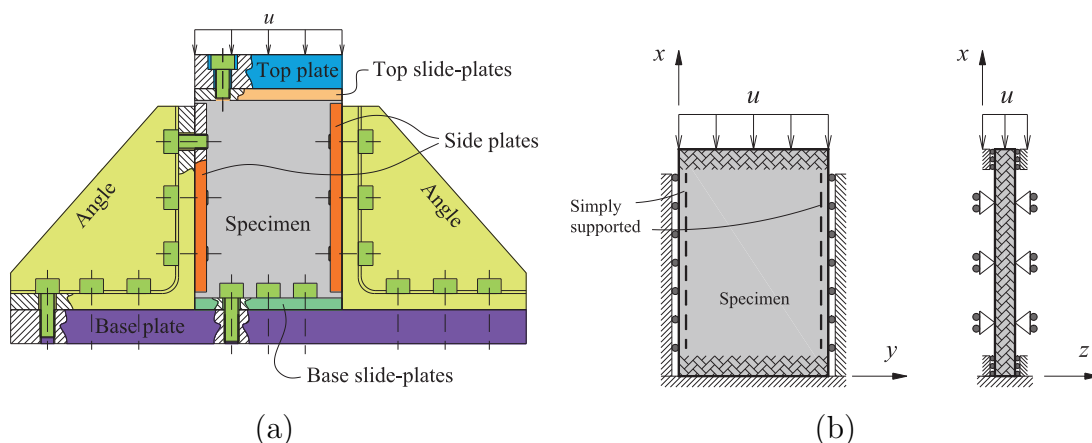


Figure 3.6: (a) CAI support fixture and (b) the corresponding constraints.

The standard compressive test fixture uses adjustable retention plates to support the specimen edges. In detail, the top and bottom supports extend the compressive displacement to the specimen. These supports are ground flat and parallel, and provide no clamp-up but some restraint to out-of-plane rotation due to the fixture geometry. The unloaded edges of the specimen are constrained by side supports which are knife-edge type supports and provide no rotational restraint. All these constraints are represented in Figure 3.6.b.

The configuration of the support fixture system can have a significant effect on the test results [99]. Results are affected by the geometry of the various slide plates. Results are also affected by the presence of gaps between the slide plates and the specimen, which can reduce the effective edge support and can result in concentrated

load introduction conditions at the top and bottom specimen surfaces. Additionally, results may be affected by variations in torque applied to the slide plate fasteners. Loose fasteners may also reduce the effective edge support.

Errors can result if the test fixture is not centered with respect to the loading axis of the test machine. For this reason, the standard proposes to glue four strain gages at selected locations (see Figure 3.8) in order to detect evidence of specimen bending before and during the test.

The test procedure starts with a compressive displacement which pre-loads the specimen fixture assembly with 450N. This pre-load is applied in order to ensure that all loading surfaces are in contact and to align the plates if necessary. After, the load is reduced to 150N and the test machine is reset to zero. Next, a compressive displacement is applied at the specified rate (i.e. maximum rate: $\dot{u} = 1.25\text{mm/min}$) while recording data, until approximately 10% of the anticipated ultimate force (normally, the ultimate force is unknown). Subsequently, the compressive force is again reduced to 150N with an equivalent unloading rate. Finally, the recorded strain gage data is reviewed to evidence any specimen bending. A difference in the stress-strain or force-strain slope from opposite faces of the specimen indicates bending in the specimen. Equation (3.9) determines a percent of bending P_B at the maximum applied force for each of the back-to-back gage locations:

$$P_B = \frac{\varepsilon_{SG1} - \varepsilon_{SG3}}{\varepsilon_{SG1} + \varepsilon_{SG3}} \times 100 \quad (3.9)$$

where ε_{SG1} and ε_{SG3} are the strains from the gages on one face and on the opposite face, respectively (see Figure 3.8). The sign of the calculated percent of bending indicates the direction in which the bending is occurring. It should be noted that bending is often introduced by the own asymmetry of the specimen created by the impact damage.

After verifications of the strain gage lectures and re-alignments of the specimen fixture assembly, the CAI test is performed by loading the specimen at the specified rate while recording data. The specimen is loaded until the maximum force is reached and the force has dropped off about 30% from the maximum.

3.3.2 Resources used and specimen instrumentation

In the present thesis, all CAI tests are performed using an Instron-4208 electro-mechanic universal testing machine with a load cell of 300kN. The fixture support used follows the ASTM specifications (see Figure 3.7).

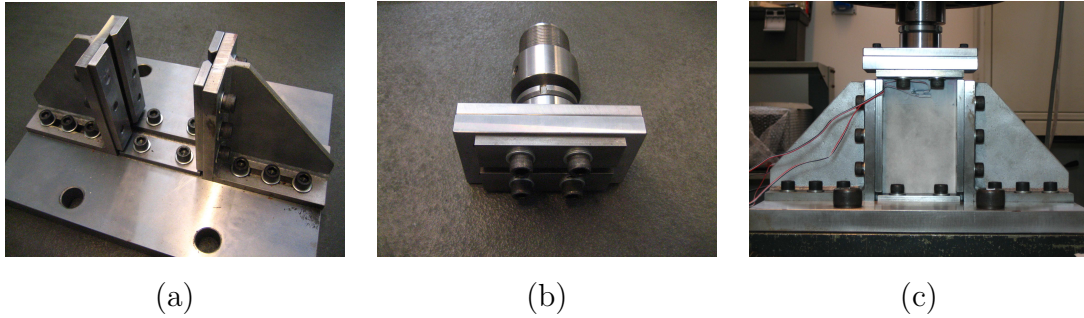


Figure 3.7: CAI test fixture: (a) base support, (b) top support adapted for the crosshead test machine, and (c) whole fixture.

It should be noted that not all the specimens described in the impact studies were tested for CAI. A suitable sample of the impacted specimens was selected.

The instrumentation of the specimens is composed by: two displacement transducers (LVDT) which are used to measure the out-of-plane displacement on two points of the non-impacted face of the specimen, and four back-to-back strain gages (SG). The LVDT's allow to evidence the buckling mode at one face and are located at the specimen points indicated in Figure 3.8. The strain gages are used to detect evidence of specimen bending during the test and are located at 25mm from each specimen edge (see Figure 3.8). Therefore, the results obtained are the applied force, the crosshead displacement, the strain data from the gages and the out-of-plane displacement given by the LVDT's.

In addition, for some CAI tests the *Digital Image Correlation* (DIC) method is used to analyze the impacted face of the specimen (GOM ARAMIS software and measurement system (version 6.02)). This method provides the measurement of the 3D displacement field of the surface of interest of an object, generated when this is submitted to an external loading. The surface to be analyzed must have a textured pattern in which the light intensity, reflected on the surface, will vary continuously with a suitable contrast. Therefore, a speckle pattern is created by

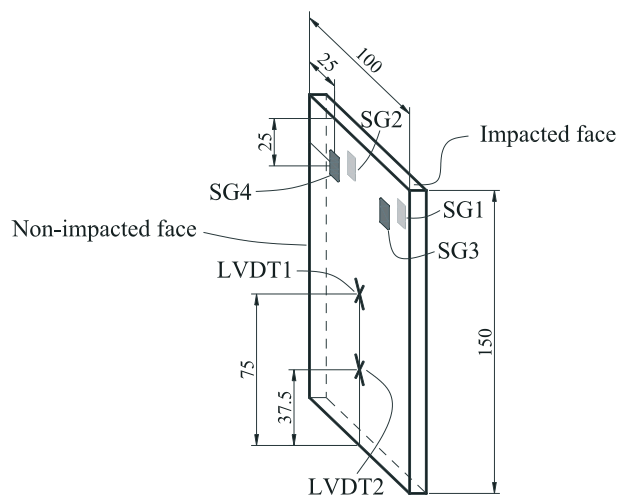


Figure 3.8: Instrumentation of CAI tests (SG x : strain gage; LVDT x : displacement transducer).

applying a thin coating of white spray paint followed by a spread distribution of spots of black spray paint. The optical system uses two cameras and a computer to record the deformation pattern of the panel surface at regular intervals. The computer calculates the motion of each location based on the two photographs from different angles to the surface of the specimen. In-plane displacements and strains, and out-of-plane displacements can accurately be determined based on these figures.

Chapter 4

Experimental results

4.1 Introduction

In this chapter, the experimental results of the configurations explained in Chapter 3 are shown and discussed in detail. Moreover, comparisons between the experimental results and the analytical predictions are also analyzed.

The experimental results comprise the data from the impact tests, non-destructive inspections (NDI) and compression after impact (CAI) tests. It should be noted that for test configurations with a sample greater than one specimen, the mean values are used. The C-scan inspections performed before impact are not shown here because all specimens were not shown manufacturing flaws. Finally, not all the specimens described in the impact studies were tested for CAI, a sample of the impacted specimens was selected.

The content of this chapter is structured according to the three main proposed studies, which are: effect of the ply thickness (clustering), effect of the mismatch angles of the plies, and effect of the laminate thickness.

4.2 Effect of ply thickness (clustering)

4.2.1 Impact tests

Impact force versus time

In order to illustrate the excellent repeatability of the impact tests, Figures 4.1 and 4.2 show the evolutions of the impactor reaction force for repeated impact configurations of laminates L02 and L04, respectively. Therefore, for configurations with more than one specimen, the mean value is used.

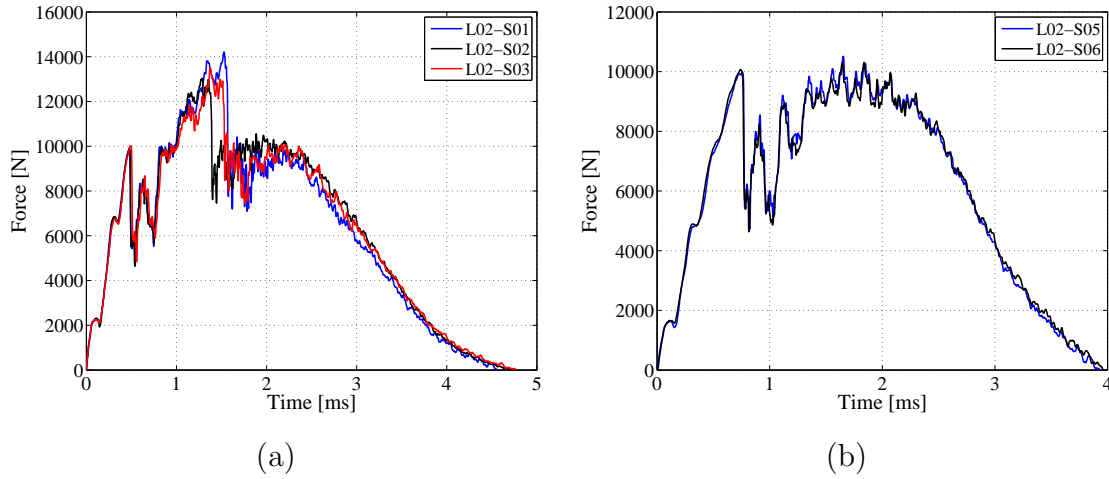


Figure 4.1: Impact force histories of laminate L02 with (a) $E_i = 38.6\text{J}$ and $M_i = 5\text{kg}$, and (b) $E_i = 19.3\text{J}$ and $M_i = 5\text{kg}$.

Figures 4.3, 4.4 and 4.5 show the histories of the impactor reaction force for each impact energy of laminates L02, L03 and L04, respectively. An interesting piece of evidence on these Figures is that the threshold load, F_d , at which significant loss of stiffness occurs, remains constant for each laminate independently of the impact energy. Therefore, F_d is independent of the impact velocity since the impactor mass is the same for all the energies defined. Moreover, as expected, the peak loads F_{max} and the slopes of the elastic regime increase by increasing the velocity, for all laminate types.

It is also observed that, increasing the velocity, the response is extended in time because the plate develops more damage. In other words, the impact time increases because the bending stiffness of the structure is reduced. This argument

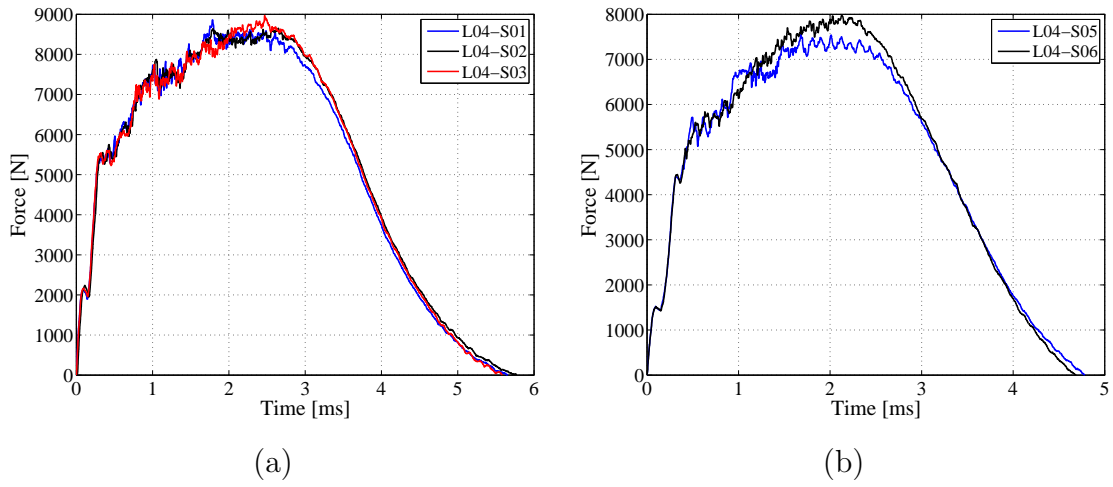


Figure 4.2: Impact force histories of laminate L04 with (a) $E_i = 38.6\text{J}$ and $M_i = 5\text{kg}$, and (b) $E_i = 19.3\text{J}$ and $M_i = 5\text{kg}$.

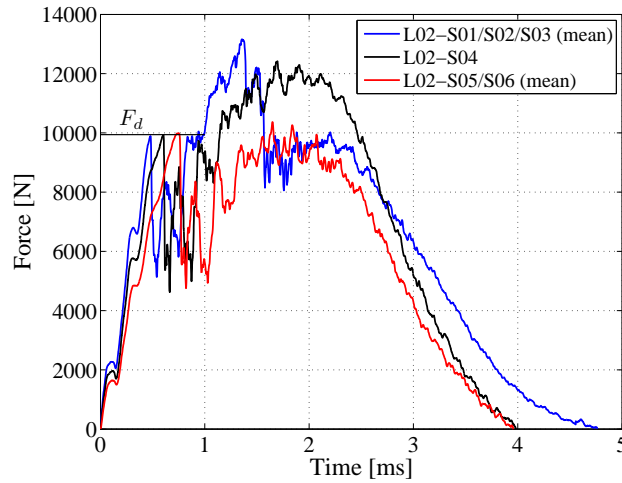


Figure 4.3: Impact force histories of laminate L02 for each impact energy (blue: 38.6J; black: 28.6J; red: 19.3J).

can be explained using the complete analytical models for the elastic prediction of the impact response. For instance, Figure 4.6 shows the analytical predictions of laminate type L02 for the impact configurations with 38.6J and 19.3J energies. These predictions are obtained by using the complete analytical impact model fed with the classical laminated plate theory and the bi-linear elastic-plastic contact law proposed by Yigit and Christoforou [45]. The number of modes considered for

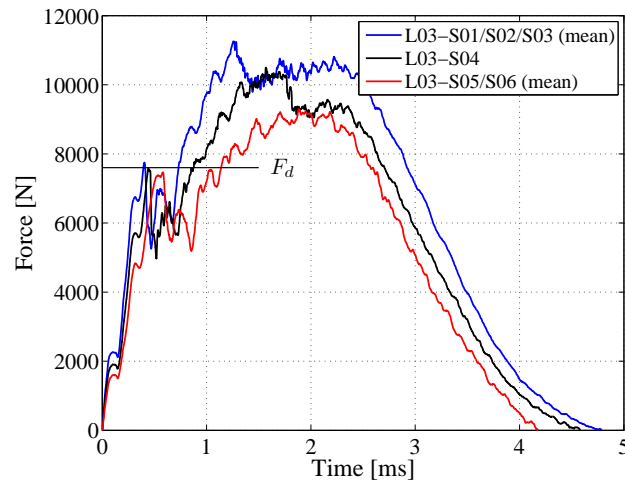


Figure 4.4: Impact force histories of laminate L03 for each impact energy (blue: 38.6J; black: 28.6J; red: 19.3J).

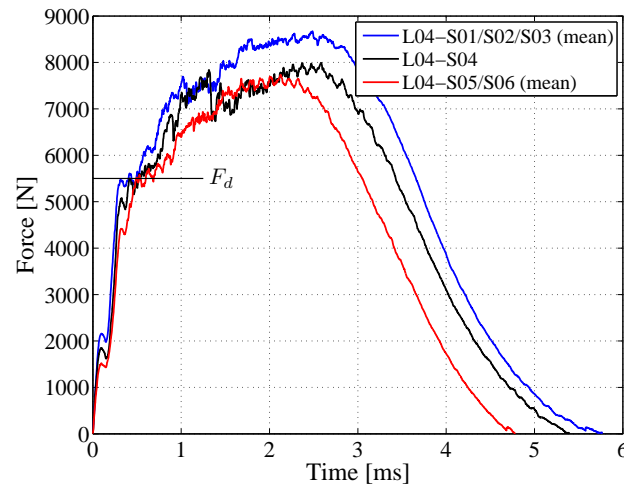


Figure 4.5: Impact force histories of laminate L04 for each impact energy (blue: 38.6J; black: 28.6J; red: 19.3J).

the Navier solution is 5 for each in-plane x and y directions, although the first mode alone is enough since the behaviors are quasi-static. As can be observed, the resulting elastic responses yield different slopes and peak loads, but the contact times are the same. Therefore, the experimental force histories show that when the velocity increases, larger damaged areas develop and so the impact contact duration

increases.

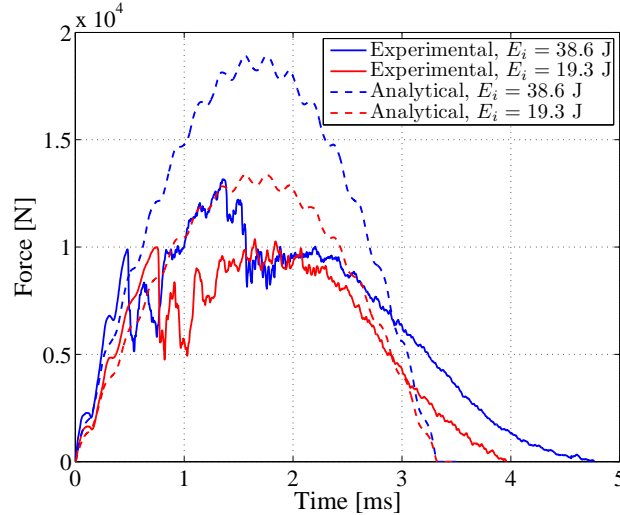


Figure 4.6: Experimental and analytical impact force histories of laminate L02 for 38.6J and 19.3J impact energies.

Focusing again on Figures 4.3, 4.4 and 4.5, the determination of the threshold loads for laminates L02 and L03 can be easily identified whereas for the laminate with the thickest plies, L04, this identification is more difficult. Moreover, the whole profile of the force history of laminate L04 does not have the large oscillations which occur for laminates L02 and L03. This fact indicates that changes in the stiffness during the impact are expected to be more progressive and smooth for laminates with thick plies than for laminates with thin plies. This behavior can be caused by the large matrix cracks which can occur when the plies are thick.

Despite the fact that all the laminate types considered have practically the same stiffness, the resulting impact force histories are clearly different from the point where significant damage starts. This is due to the differences in the ply thicknesses of the laminates, and further highlighted in Figures 4.7, 4.8 and 4.9, which compare the results for the different laminates for each impact energy 38.6J, 28.6J and 19.3J. The first part of the results is the elastic regime of the impact process which is common for all laminates at each impact energy. However, the points where significant damage starts are clearly different, and from these points, the force histories separate and follow different paths. Table 4.1 shows the differences in the threshold

loads as well as in the peak loads for each impact energy.

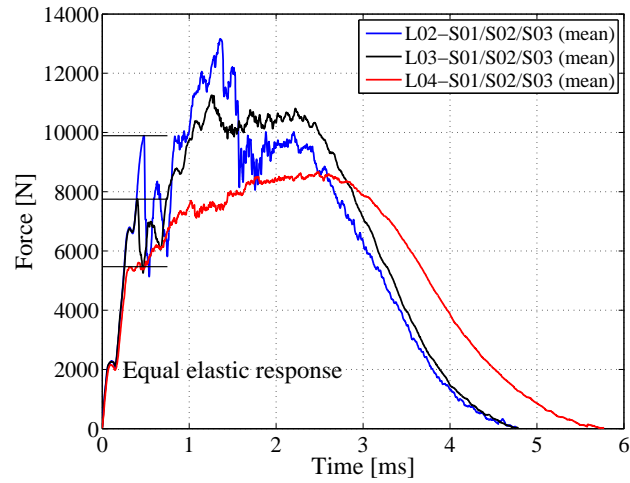


Figure 4.7: Impact force histories for 38.6J of laminates L02 (blue), L03 (black), and L04 (red).

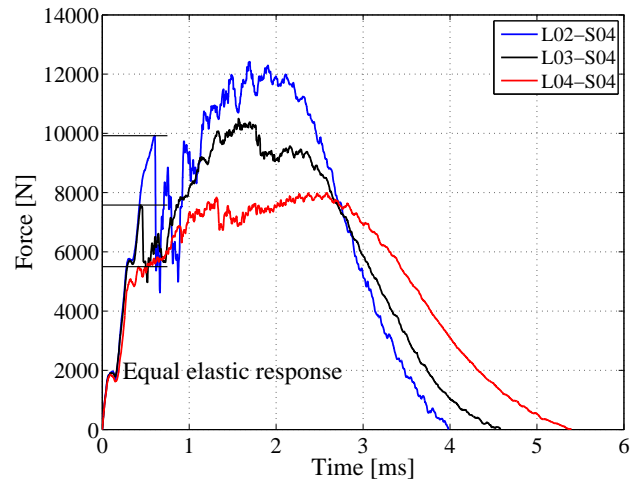


Figure 4.8: Impact force histories for 28.6J of laminates L02 (blue), L03 (black), and L04 (red).

Furthermore, Figures 4.7, 4.8 and 4.9 show that the impact response is elongated by increasing the ply clustering of the laminate. Since delaminations cause a reduction of the stiffness, it is clear that larger delaminations should develop for laminate

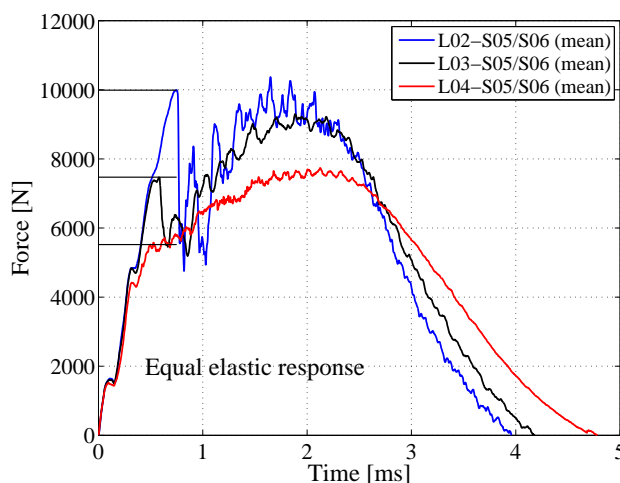


Figure 4.9: Impact force histories for 19.3J of laminates L02 (blue), L03 (black), and L04 (red).

Table 4.1: Experimental threshold loads F_d and peak loads F_{max} .

Laminate	Threshold loads F_d [kN]				Peak loads F_{max} [kN]				
	Energy [J]:	38.6 (mean)	28.6	19.3 (mean)	Mean	Energy [J]:	38.6 (mean)	28.6	19.3 (mean)
L02	9.89	9.92	9.99	9.94	13.57	12.42	10.41		
L03	7.75	7.58	7.47	7.60	11.37	10.50	9.34		
L04	5.47	5.50	5.52	5.50	8.83	8.00	7.78		

L04 because less interfaces are available for delamination in comparison with the other laminates.

Focusing on the values of the experimental damage thresholds F_d (see Table 4.1), these can be represented as a function of the ply thickness on a natural logarithmic scale, as shown in Figure 4.10. The black points and lines describe the analytical predictions, whereas the points colored in gray correspond to the experimental values for each laminate type. As can be observed, the analytical threshold load for matrix cracking in thin outer plies located on the back face of the laminate is in agreement with all the experimental points. Additionally, if the line which fits the experimental results is calculated, the corresponding slope is equal to -0.427. This value is close to the slope of the analytical threshold F_{mc}^{ten} (i.e. slope: -0.5, since $F_{mc}^{ten} \propto h^2 h_p^{-0.5}$). The small difference in the slopes can be due to scattering of the material properties or

to the assumptions considered in the formulation of the damage threshold functions, such as strain rate effects.

Therefore, according to the analytical predictions, the first significant damage for all laminate types can be an elongated delamination at the first interface from the back face of the plate. This result disagrees with the initial prediction for laminate L02, where the first damage was linked to a mid-plane delamination $F_d = F_{d1}^{stat}$. However, it can be considered that this delamination may occur subsequently because the predicted load is slightly smaller than the experimental value.

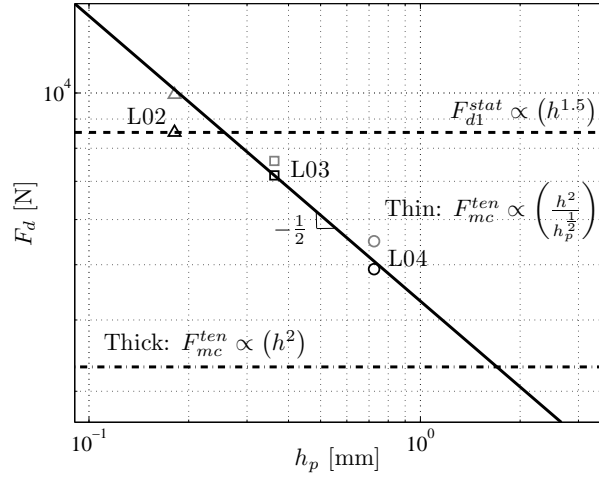


Figure 4.10: Experimental points (in gray) and analytical predictions (in black) of the impact force as a function of the ply thickness for the creation of the first significant damage.

Impactor displacement, impactor velocity, and absorbed energy

Using Equations (3.6) and (3.5), the displacement and velocity histories of the impactor can be calculated, respectively. As an example, Figure 4.11 shows the displacement and the velocity histories of all the laminates for an impact energy of 28.6J. As detected in the impact force histories, the displacement of L04 is the largest because a higher bending occurs. Accordingly, the velocity history of L04 is the slowest due to the same reason.

Using Equation (3.7), the histories of the absorbed energy by the specimens,

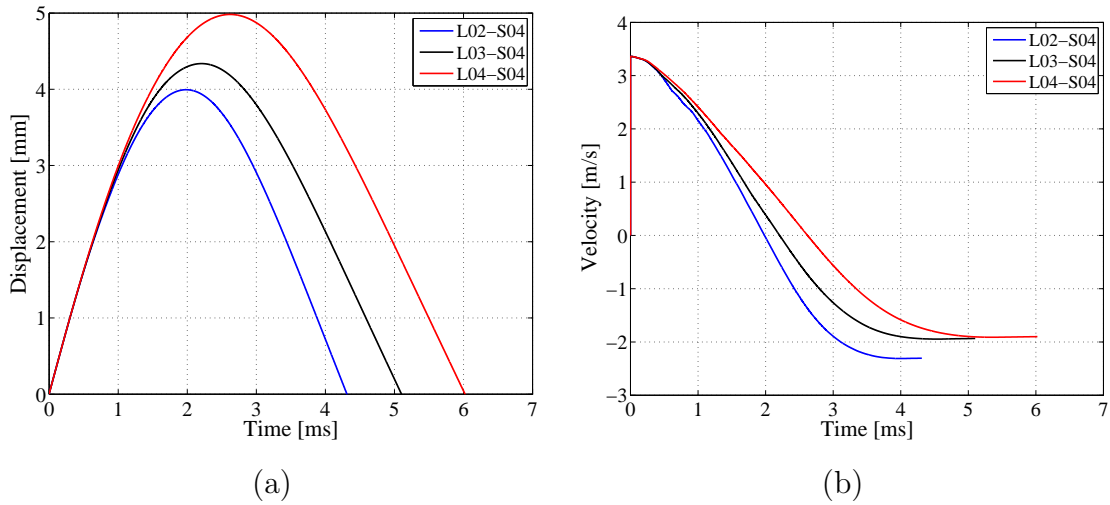


Figure 4.11: Impactor (a) displacements and (b) velocities of all the laminates for 28.6J energy.

$E_a(t)$, can be obtained. Figures 4.12.a, 4.13.a and 4.14.a show these histories of each laminate type for each impact energy 38.6J, 28.6J and 19.3J, respectively. From these evolutions, it is possible to know the dissipated energy by the specimen as it is indicated for laminate type L04 in Figure 4.12.a. In addition, the impact force can be plotted as a function of the impactor displacement. These plots are shown in Figures 4.12.b, 4.13.b and 4.14.b. It results that the area enclosed in these charts corresponds to the dissipated energy identified in the evolutions of the absorbed energy. For instance, Figure 4.12.b indicates, in gray color, the corresponding energy dissipated by the laminate L04.

As can be observed in Table 4.2, the dissipated energies for laminate L04 are slightly greater than the values of the other laminate types. However, it is reasonable to conclude that the energy dissipated is fairly independent of the laminate type. Moreover, as expected, the dissipated energies increase by increasing the velocity, for all laminate types.

4.2.2 NDI: C-scan after impact

The ultrasonic C-scan inspections of the impacted laminates identify the projection of the delamination areas over the structure thickness. Therefore, the delaminations

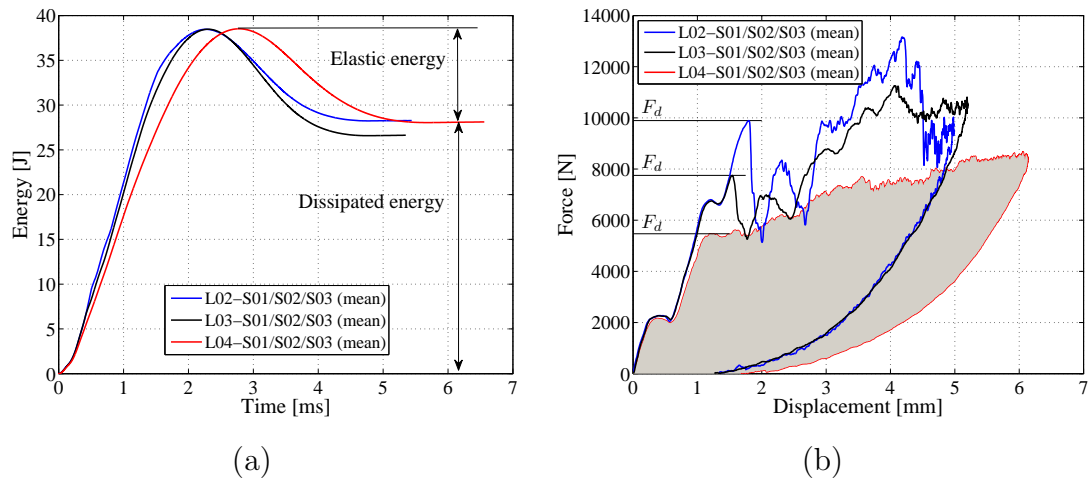


Figure 4.12: Evolution of the (a) absorbed energy and the (b) impact force versus impactor displacement of each laminate for 38.6J.

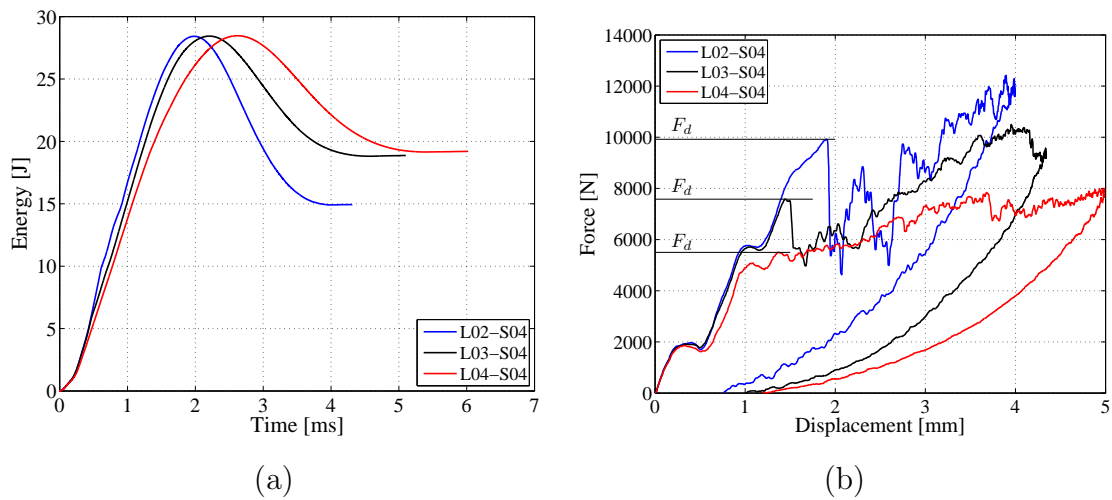


Figure 4.13: Evolution of the (a) absorbed energy and the (b) impact force versus impactor displacement of each laminate for 28.6J.

which are close to the impact face hide the existence of deeper delaminations. However, the delaminations are often larger as the interface is deeper in the laminate, and they can usually be seen.

Normally, each delamination has the so-called peanut shape and the superposition of all these delaminations yields to a circular projected area. The proper

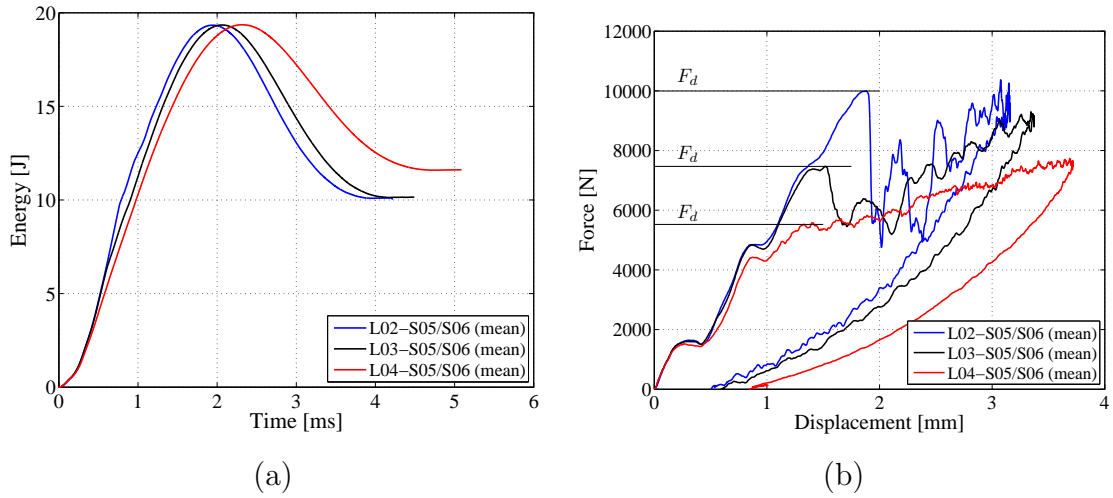


Figure 4.14: Evolution of the (a) absorbed energy and the (b) impact force versus impactor displacement of each laminate for 19.3J.

Table 4.2: Absorbed energies of all laminates for each impact energy (in [J]).

Laminate	$E_i = 38.6\text{J}$	$E_i = 28.6\text{J}$	$E_i = 19.3\text{J}$
L02	28.3	14.9	10.1
L03	27.2	18.9	10.2
L04	28.8	19.2	12.0

interpretation of the through-the-thickness location of the delamination depends on the quality of the inspections performed. Figure 4.15 shows a sample of the C-scan inspections of each laminate type for each impact energy.

It is observed that by increasing the impact velocity the projected area increases for all the laminates. This result correlates with the plots of the impact force histories shown previously (see Figures 4.3, 4.4 and 4.5), where the responses are extended in time when the velocity is increased due to the reduction of the bending stiffness as a consequence of the damage developed.

In addition, by reducing the number of interfaces available for delamination, the resulting projected delamination area is increased. This result is also related to the impact force histories (see Figures 4.7, 4.8 and 4.9), where the impact times for laminate type L04 are larger since the bending stiffness values are reduced due to

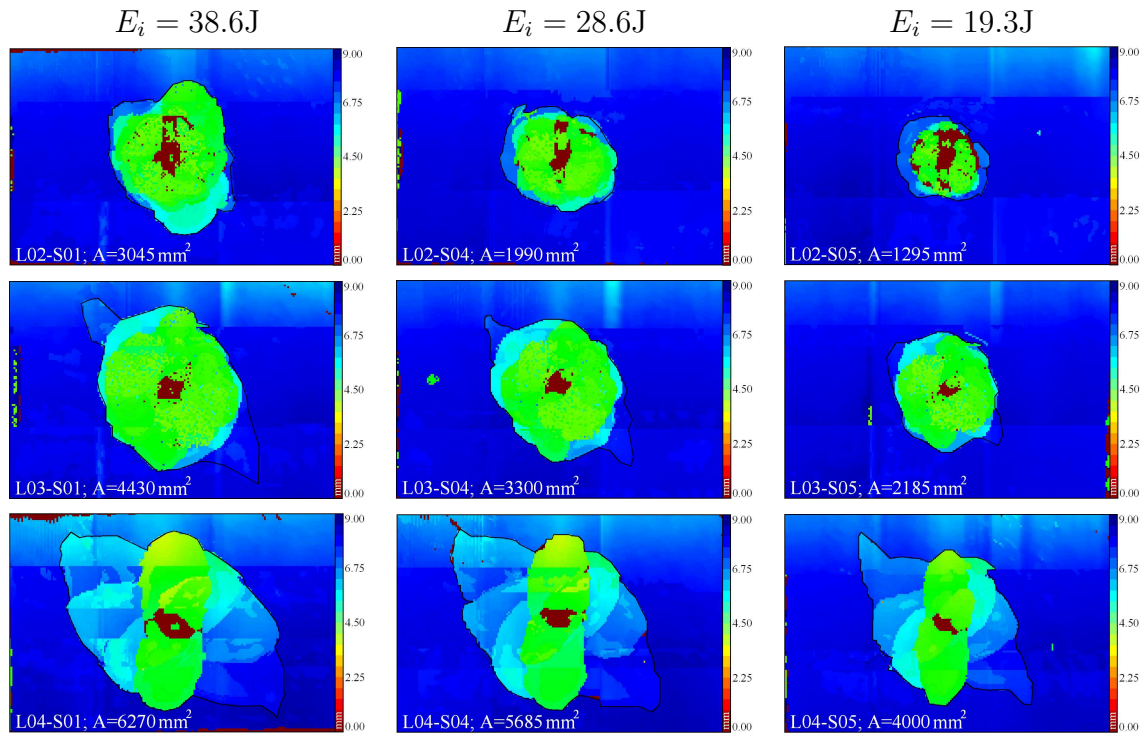


Figure 4.15: Sample of C-scan inspections of laminates L02, L03 and L04.

the large delaminations created.

The shapes of the projected delamination areas are clearly different for each laminate type. The shape of laminates L02 follow a quite similar circular pattern at each impact energy. Likewise, the shapes of laminate type L03 are also fairly circular, although in contrast with laminate L02, a narrow and elongated delamination appears at the deepest interface which is more evident for the highest impact energy. Finally, the delamination shapes of laminate type L04 significantly differ from the other laminates. The areas are very large, and their shapes and locations through-the-thickness of the laminate can be easily recognized.

Although the C-scan inspections provide the resulting damaged areas after the impact tests, they can be used to check approximately if the analytical predictions for the first significant damage threshold load F_d are in agreement with the experimental results. Initially, it was predicted that the first significant damage for laminate type L02 would be a circular mid-plane delamination. However, the experimental point plotted in Figure 4.10 has evidenced that the first damage is rather a delamination

at the first interface from the back face of the plate. The shape of the C-scan inspections for laminate L02 are almost circular for all the impact energies, and then it is difficult to determine what is the associated delamination for the first drop in the impact load. For laminate type L03, the prediction was a delamination at the first interface from the back face of the plate. Observing the inspections, it is reasonable to consider that a delamination has appeared at that interface, although its existence is difficult to prove due to the fact that it is hidden by the delaminations close to the impact front face. The prediction for laminate type L04 was also a delamination at the first interface from the back face of the plate. The prediction can be considered correct since the delamination areas at the deepest interface are peanut shaped, which are typical when a large matrix crack appears on the back outer ply of the plate. However, further testing is required to verify these arguments, especially with critical impact energies which generate maximum impact forces similar to the damage threshold loads.

It is important to point out that the growth of delaminations can be affected by the finite in-plane dimensions of the plates, the stacking sequences, the impactor mass and velocity, and the edge supports. All the impact configurations and stacking sequences tested are in agreement with the recommendations suggested by ASTM D7136 / D7136M [59]. The standard remarks that if all the recommendations are followed, the maximum delamination diameter will be less than half of the unsupported specimen width (38mm). However, most of the delamination areas obtained are greater than this value.

Laminate type L04 has fewer interfaces for delamination than laminates L02 and L03. As such, the energy is dissipated by means of large damage areas which could be stopped by the membrane effects and/or the edge supports. The larger delaminations generated by ply clustering result in larger deflections and associated stronger membrane effects, which are known to suppress delamination growth [24]. This is suggested by the relation between the projected delamination areas and the impact energy, as shown in Fig. 4.16, where the fitting line of laminate type L04 has the lowest slope. Furthermore, since the delaminations cannot grow, the energy must be dissipated by other means, such as large indentation and fiber breakage.

Table 4.3: Projected delamination areas given by C-scan inspections.

Impact energy: $E_i = 38.6\text{J}$		Impact energy: $E_i = 28.6\text{J}$		Impact energy: $E_i = 19.3\text{J}$	
Specimen	Area [mm^2]	Specimen	Area [mm^2]	Specimen	Area [mm^2]
L02-S01	3045	L02-S04	1990	L02-S05	1295
L02-S02	2710			L02-S06	1340
L02-S03	3310				Mean: 1318
	Mean: 3022				
L03-S01	4430	L03-S04	3300	L03-S05	2185
L03-S02	4115			L03-S06	1800
L03-S03	3320				Mean: 1993
	Mean: 3955				
L04-S01	6270	L04-S04	5686	L04-S05	4000
L04-S02	5930			L04-S06	6750
L04-S03	6275				Mean: 5375
	Mean: 6158				

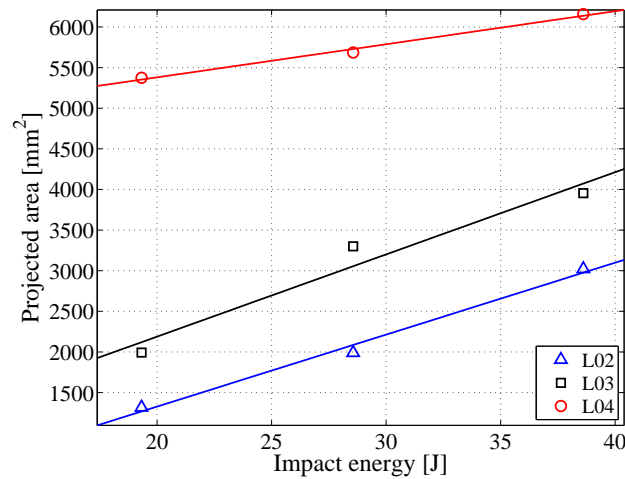


Figure 4.16: Projected delamination areas in function of the impact energy.

4.2.3 Dent-depth measurements

In Figure 4.17 are summarized the contour plots of the dent-depth measurements of the whole selected specimen sample. All these measurements were performed by

means of a 3D coordinate measuring machine.

Related to the arguments commented in previous sections, it is reasonable that by reducing the number of interfaces for delamination the indentation is increased. The impact energy can be dissipated in different ways, mainly by matrix cracking, delaminations and fiber failure. When delaminations can not growth because they have reached their maximum size (due to the fact that the clamping system stops the delamination growth and/or because high loads are needed in order to increase their size due to the membrane effect [20]), the indentation could be increased, such as it is evidenced for laminates L04 in comparison with laminates L03 and L02, or laminates L03 in comparison with laminates L02.

Furthermore, it is obvious that increasing the impact velocity, the resulting indentation is increased.

4.2.4 CAI tests

It should be noted that not all the specimens impacted are tested for CAI. Moreover, no a single CAI test performed experienced unacceptable damage modes, such as those related to load introduction by the support fixture.

Residual compressive load

Table 4.4 summarizes the residual compressive loads F_{fc} obtained. It is observed that increasing the impact energy (or the impact velocity), the residual compressive loads are reduced for all the laminates tested.

In addition, the damage tolerance estimated by means of the residual compressive load does not seem to be reduced by increasing the ply thickness, because all laminate types show similar values of the residual compressive loads at each impact energy (except for specimen L04-S05). As it was noted in Section 3.2.2, this result is due to the fact that the compressive load depends on a combination of variables such the number of delamination planes, the size of the delaminations, and their locations through-the-thickness of the laminate. However, more tests are needed in order to further support these conclusions since the repeatability of the CAI tests is not as good as in the impact tests.

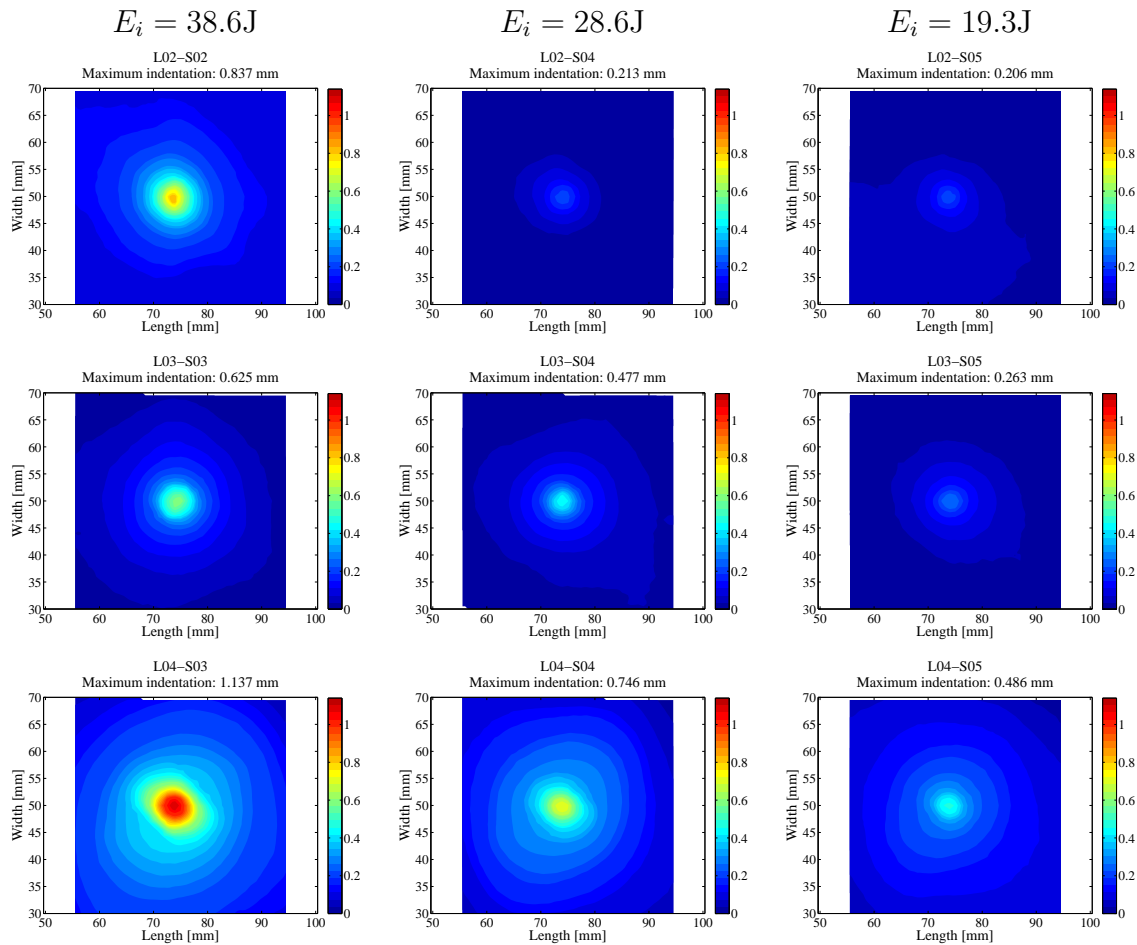


Figure 4.17: Dent-depth inspections of laminates L02, L03 and L04.

Lectures of the displacement transducers (LVDT)

Table 4.5 summarizes the maximum values of the readings of the two displacement transducers used during the CAI tests (see Figure 3.8 in Chapter 3). As it can be observed, the displacements of laminate type L04 are often higher than in the other laminate types. However, this evidence does not imply that the damage tolerance is worse than in the other laminates because the failure loads read have been quite similar.

By means of the profile of the two out-of-plane displacement histories, it is possible to describe the buckling mode which is experienced at the instrumented back face of the corresponding impacted specimens. For instance, Figure 4.18 shows the

Table 4.4: Failure compressive loads F_{fc} of laminates L02, L03 and L04.

Impact energy: $E_i = 38.6\text{J}$		Impact energy: $E_i = 28.6\text{J}$		Impact energy: $E_i = 19.3\text{J}$	
Specimen	F_{fc} [kN]	Specimen	F_{fc} [kN]	Specimen	F_{fc} [kN]
L02-S01	93	L02-S04	103	L02-S05	133
L02-S02	99				
Mean: 96					
L03-S01	89	L03-S04	100	L03-S05	134
L03-S02	91				
Mean: 90					
L04-S01	98	L04-S04	103	L04-S05	105
L04-S02	97				
Mean: 98					

Table 4.5: Maximum lectures of the displacement transducers of laminates L02, L03 and L04.

Impact energy: $E_i = 38.6\text{J}$			Impact energy: $E_i = 28.6\text{J}$			Impact energy: $E_i = 19.3\text{J}$		
Specimen	LVDT1 [mm]	LVDT2 [mm]	Specimen	LVDT1 [mm]	LVDT2 [mm]	Specimen	LVDT1 [mm]	LVDT2 [mm]
L02-S01	1.67	0.09	L02-S04	1.73	0.16	L02-S05	1.11	0.41
L02-S02	2.06	0.33						
L03-S01	2.18	0.14	L03-S04	1.93	0.08	L03-S05	Not read	Not read
L03-S02	1.94	0.15						
L04-S01	2.85	0.18	L04-S04	2.88	0.30	L04-S05	2.91	0.19
L04-S02	Not read	Not read						

lectures for each laminate type of the specimens impacted with 29.6J. It can be concluded that the buckling mode of each laminate type is practically the same and is presented as a local bubble concentrated in the middle of the specimens, which propagates suddenly to a bubble that takes up the whole in-plane dimensions of the specimens when the failure load is reached.

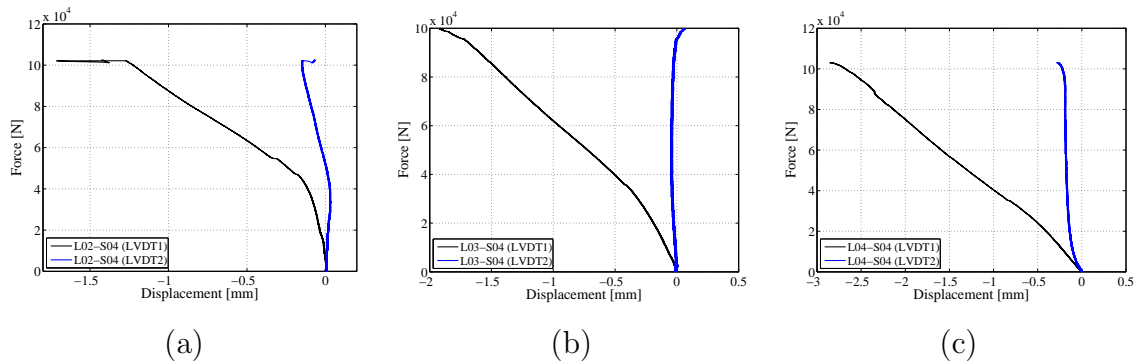


Figure 4.18: Displacement transducer lectures of the specimens impacted with 29.6J: (a) L02, (b) L03, and (c) L04.

Lectures of the strain gages (SG) and Digital Image Correlation (DIC)

During the preparatory of the CAI test set-up, four strain gages are used in order to avoid loading eccentricities and induced specimen bending (see Figure 3.8 in Chapter 3). In addition, the lectures of these gages can be stored in a computer during the test in order to check if some bending has appeared. For instance, Figure 4.19 contains the four strain lectures of each laminate type for the impact energy of 29.6J. As it can be verified, there are differences between the lectures of the gages located at the same face (SG1 with SG2; SG3 with SG4), and also between the lectures of the back-to-back gages (SG1 with SG3; SG2 with SG4). The first offset indicates that the load applied is not completely uniform, due to the support fixture, by the frame of the test machine, or by the asymmetry induced to the laminate in the impact test. The second offset indicates that the back-to-back sub-laminates are standing different deformations due to the fact that the laminate is also subjected to a little bending. Despite the attempts previous to the CAI test to avoid possible eccentricities, bending finally appears due to the asymmetry induced by the damage created in the impact test.

These effects also can be evidenced by means of the Digital Image Correlation (DIC) lectures. For instance, Figure 4.20 shows the displacement field lectures for the specimen L04-S04 at different points of the compression test. The first column of images corresponds to the horizontal displacement field, the second corresponds to the vertical displacement field, and finally the third corresponds to the out-of-plane

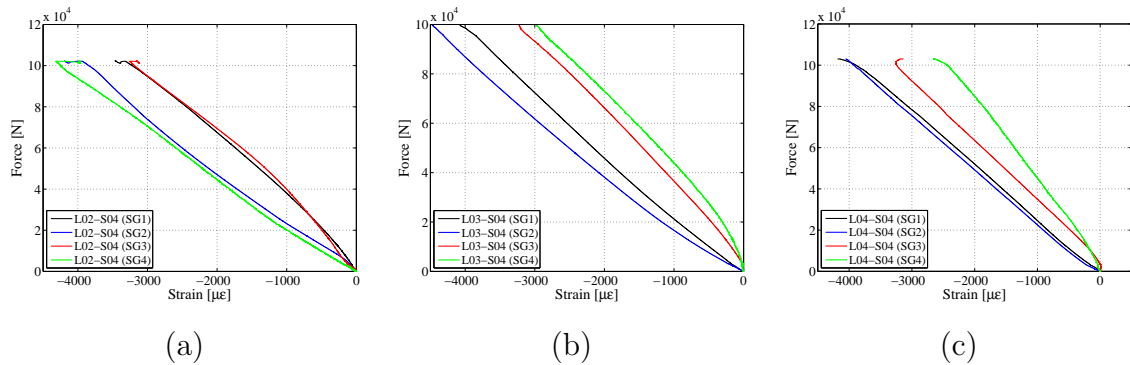
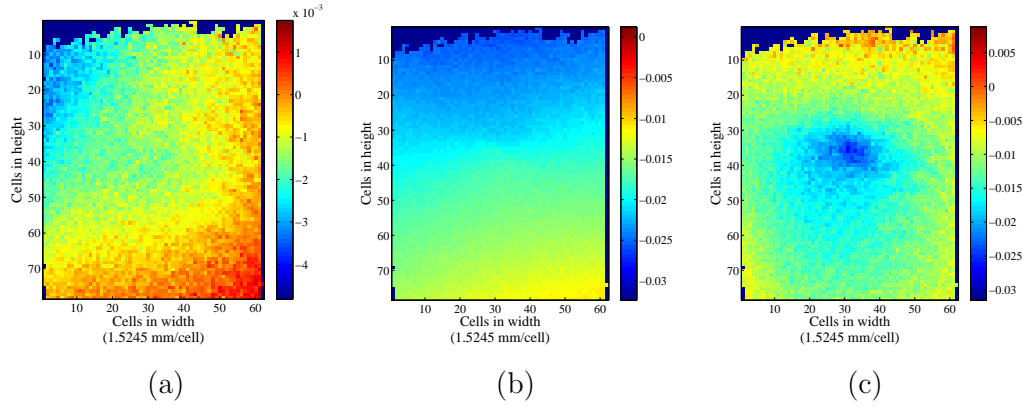


Figure 4.19: Strain gage lectures of the specimens impacted with 29.6J: (a) L02, (b) L03, and (c) L04.

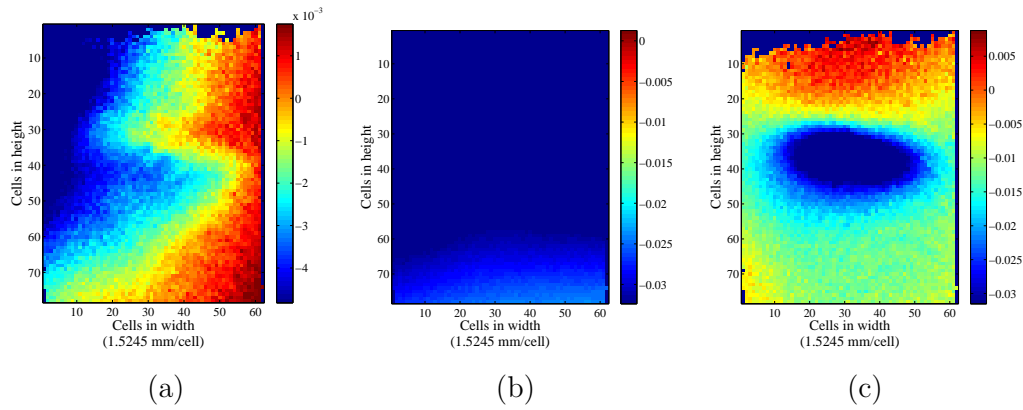
displacement field. Also, the horizontal, vertical and in-plane shear strain fields can be obtained. As it was detected by the strain gages (SG1 and SG2), the vertical displacement field is not uniform during the first loads of the CAI test. Also, the horizontal displacement field is not completely symmetric.

The direct comparison between the lectures of the DIC device and the strain gages located at the same laminate face (SG1 and SG2) is not possible since the locations of the gages are far from the range of the lecture field of the DIC device.

Crosshead lectures: displacement=-0.29mm; load=40kN



Crosshead lectures: displacement=-1.10mm; load=80kN



Crosshead lectures: displacement=-1.42mm; load=103kN (failure)

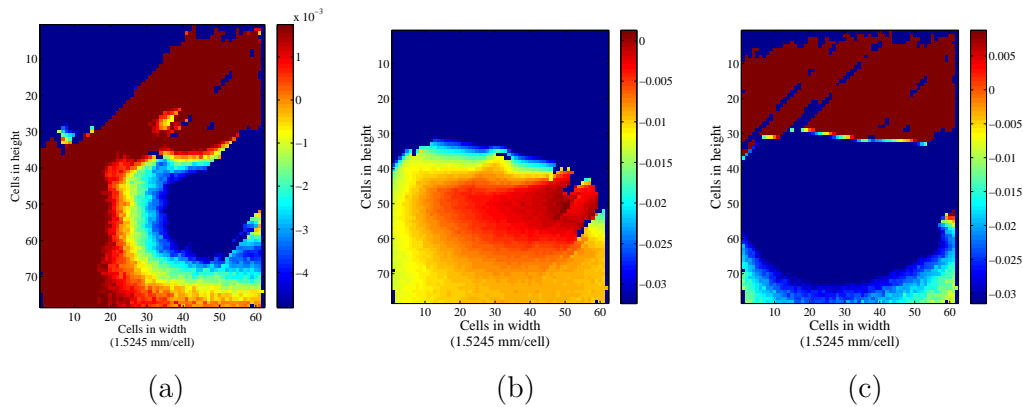


Figure 4.20: DIC lectures of the specimen L04-S04 impacted at 29.6J: (a) horizontal displacement field, (b) vertical displacement field, and (c) out-of-plane displacement field (positive values indicate displacements in the out-of-plane direction).

4.3 Effect of ply mismatch angle at interfaces

4.3.1 Impact tests

Impact force versus time

Figure 4.21 shows the histories of the impactor reaction force for each impact energy of the cross-ply laminate L06. As verified in previous study, the threshold load F_d remains constant at any impact energy, and the peak loads F_{max} and the slopes of the elastic regime increase by increasing the velocity. It can be verified that for the minimum impact energy 19.3J, the damage threshold load F_d coincides with the peak load.

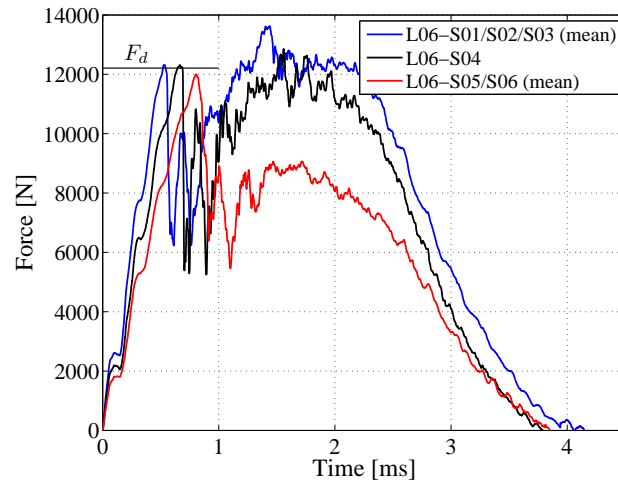


Figure 4.21: Impact force histories of laminate L06 for each impact energy (blue: 38.6J; black: 28.6J; red: 19.3J).

In addition, increasing the velocity, the response is extended in time because the plate develops more damage. Figure 4.22 shows the analytical predictions of laminate L06 for the impact configurations with 38.6J and 19.3J energies, along with the corresponding experimental profiles. The resulting elastic responses for each energy yield different slopes and peak loads, but the contact times are equal. Therefore, again it is evidenced that increasing the velocity, larger damaged areas are developed and so the impact contact duration is enlarged.

Figures 4.23, 4.24 and 4.25 compare the profiles of laminates L02 and L06 for

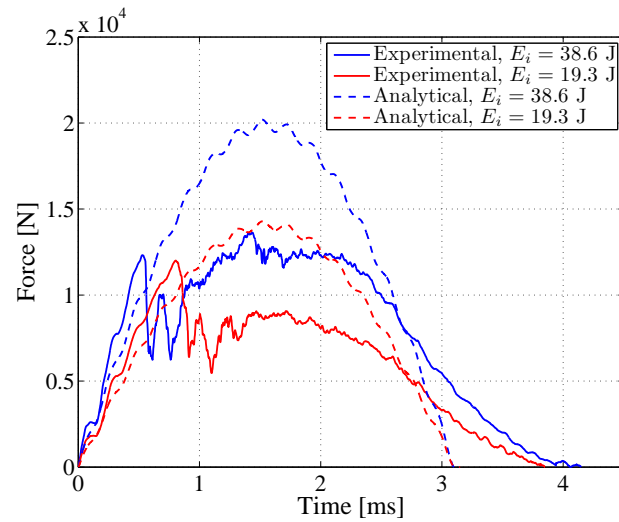


Figure 4.22: Experimental and analytical impact force histories of laminate L06 for 38.6J and 19.3J impact energies.

each impact energy 38.6J, 28.6J and 19.3J, respectively. The elastic responses of laminate type L06 are stiffer than for L02 due to the fact that the laminate L06 is thicker. Accordingly, the contact durations for laminate L02 are larger, because L02 yields to a more quasi-static behavior in comparison with L06. Table 4.6 summarizes the threshold loads and peak loads of each laminate for each impact energy.

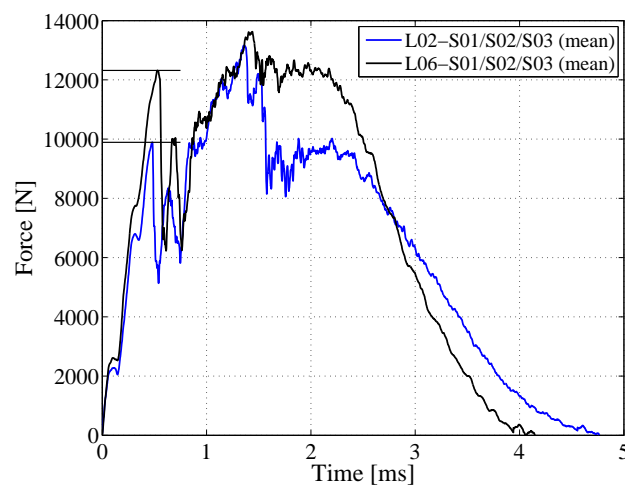


Figure 4.23: Impact force histories for 38.6J of laminates L02 (blue) and L06 (black).

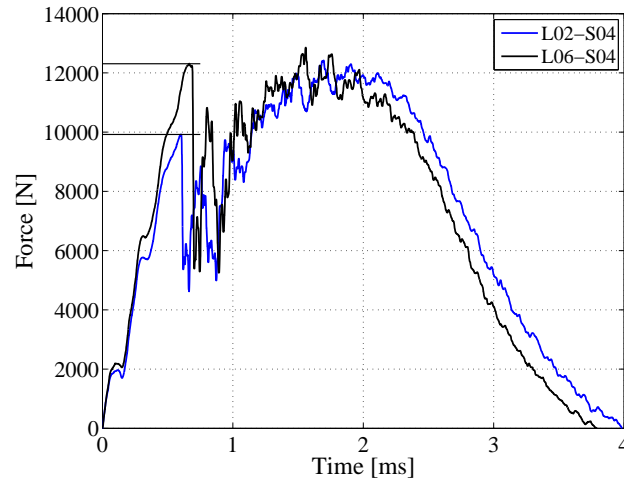


Figure 4.24: Impact force histories for 28.6J of laminates L02 (blue) and L06 (black).

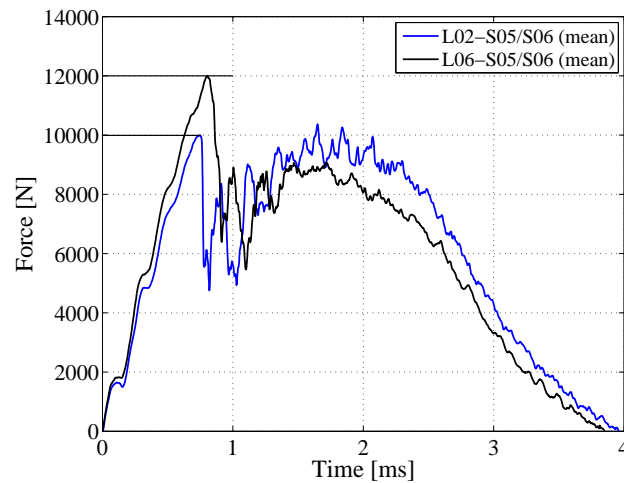


Figure 4.25: Impact force histories for 19.3J of laminates L02 (blue) and L06 (black).

Figure 4.26 shows the corresponding analytical trends (in black) and the experimental value (in cyan) for the first significant damage F_d of laminate L06. The analytical prediction of F_d for L06 was a mid-plane delamination, i.e. F_{d1}^{stat} . However, the experimental point is more close to the trend for a back face delamination, as happened for laminate L02. It can be considered that a combination of both delamination types can occur simultaneously since that both thresholds are fairly close.

Table 4.6: Experimental threshold loads F_d and peak loads F_{max} of laminates L02 and L06.

Laminate	Threshold loads F_d [kN]				Peak loads F_{max} [kN]				
	Energy [J]:	38.6 (mean)	28.6	19.3 (mean)	Mean	Energy [J]:	38.6 (mean)	28.6	19.3 (mean)
L02		9.89	9.92	9.99	9.94		13.57	12.42	10.41
L06		12.32	12.31	12.00	12.21		13.92	12.86	12.00

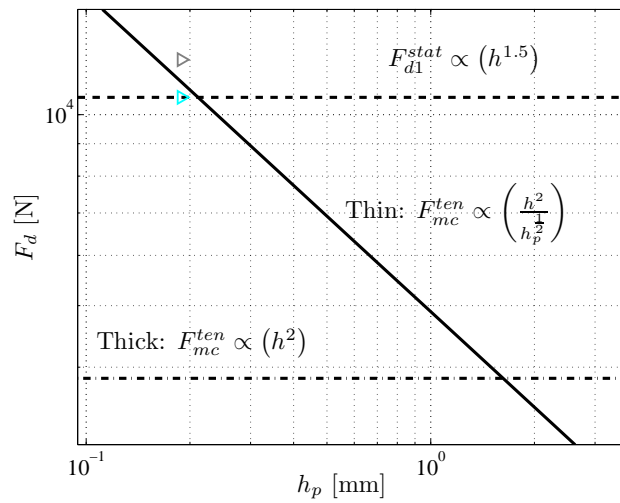


Figure 4.26: Experimental and analytical trends of the impact force as a function of the ply thickness for the creation of the first significant damage.

Impactor displacement, impactor velocity, and absorbed energy

As an example, Figure 4.27 shows the displacement and the velocity histories of laminates L02 and L06 for the impact energy 28.6J. The sudden changes observed in the impact force histories at F_d are also reflected in the velocity profiles.

Furthermore, the fact that laminate type L02 is thinner than laminate L06 is reflected in the displacement and velocity responses. Since the impactor mass is the same for both impact tests on L02 and L06, the impactor displacement is larger for L02 because more deflection of the plate was experimented. In other words, the quasi-static behavior is emphasized for L02 as was noted in Chapter 3, since the ζ_w parameter of L02 was greater than the one of L06. Accordingly, the velocity histories of L02 are slower than for L06.

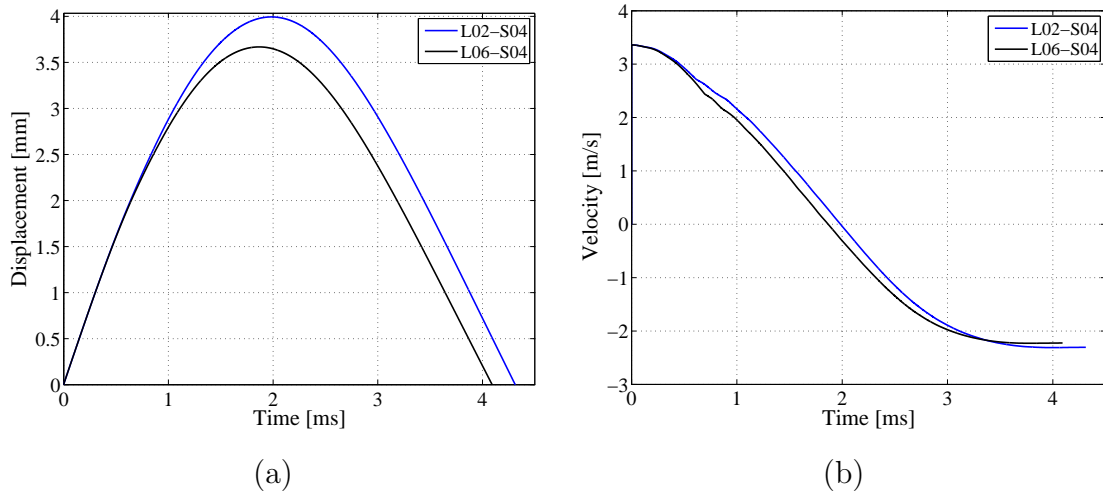


Figure 4.27: Impactor (a) displacements and (b) velocities of laminates L02 and L06 for 28.6J energy.

Figures 4.28.a, 4.29.a and 4.30.a show the histories of the absorbed energy $E_a(t)$ of laminates L02 and L06 for each impact energy 38.6J, 28.6J and 19.3J, respectively. In addition, Figures 4.28.b, 4.29.b and 4.30.b show the impact force as a function of the impactor displacement. As noted in the study of the ply thickness, the area enclosed in these charts corresponds to the dissipated energy identified in the evolutions of the absorbed energy. Table 4.7 summarizes these levels of energy and evidences that practically both laminates dissipate the same energy for each impact configuration.

Table 4.7: Absorbed energies of laminates L02 and L06 for each impact energy (in [J]).

Laminate	$E_i = 38.6\text{J}$	$E_i = 28.6\text{J}$	$E_i = 19.3\text{J}$
L02	28.3	14.9	10.1
L06	26.3	15.8	11.8

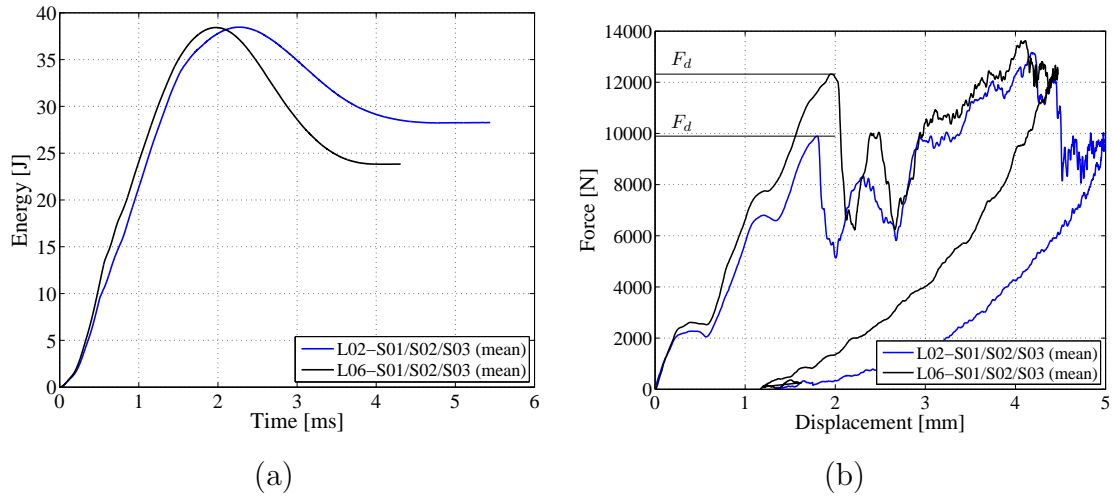


Figure 4.28: Evolution of the (a) absorbed energy and the (b) impact force versus impactor displacement of laminates L02 and L06 for 38.6J.

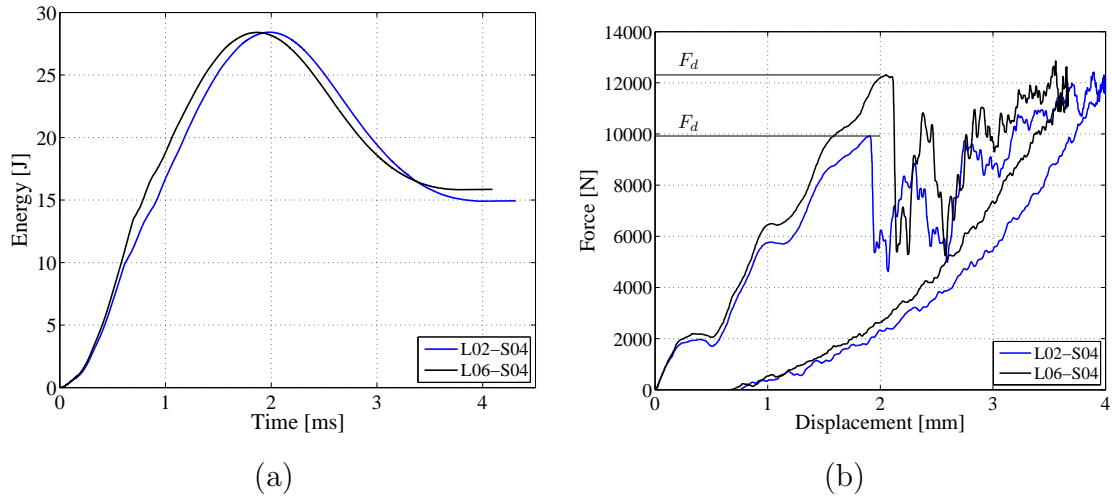


Figure 4.29: Evolution of the (a) absorbed energy and the (b) impact force versus impactor displacement of laminates L02 and L06 for 28.6J.

4.3.2 NDI: C-scan after impact

Figure 4.31 shows a sample of C-scan inspections of laminates L02 and L06 for each impact energy. The projected delamination areas of L06 are among square and circular shaped. Although the C-scan inspections give the resulting damaged areas after impact tests, these results can be associated with the analytical predictions

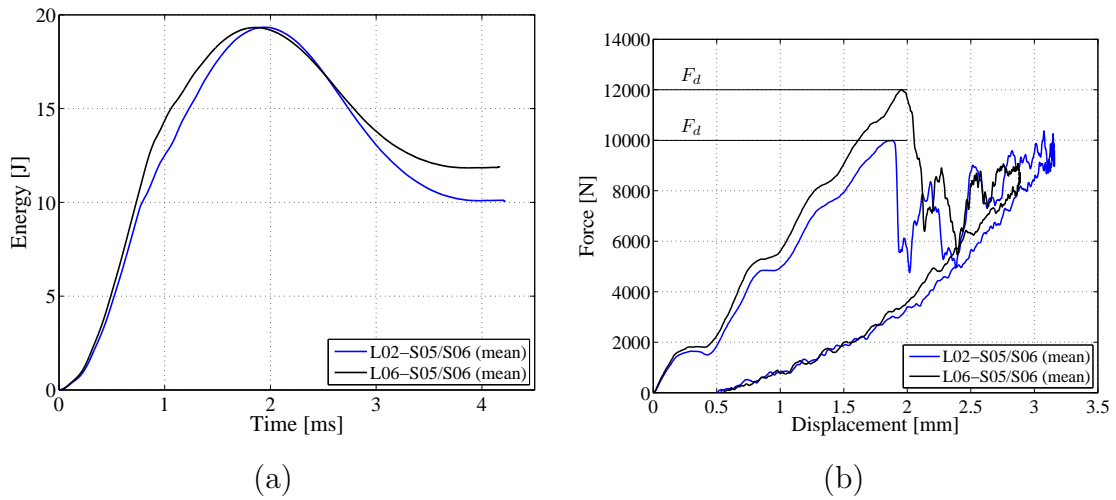


Figure 4.30: Evolution of the (a) absorbed energy and the (b) impact force versus impactor displacement of laminates L02 and L06 for 19.3J.

for the first significant damage F_d . As was noted in the discussion of the impact force histories, F_d can be triggered by a circular mid-plane delamination. In an approximate point of view, this argument suits with the resulted inspections.

According to the results of the ply thickness study, increasing the impact velocity increases the projected delamination area for all laminates.

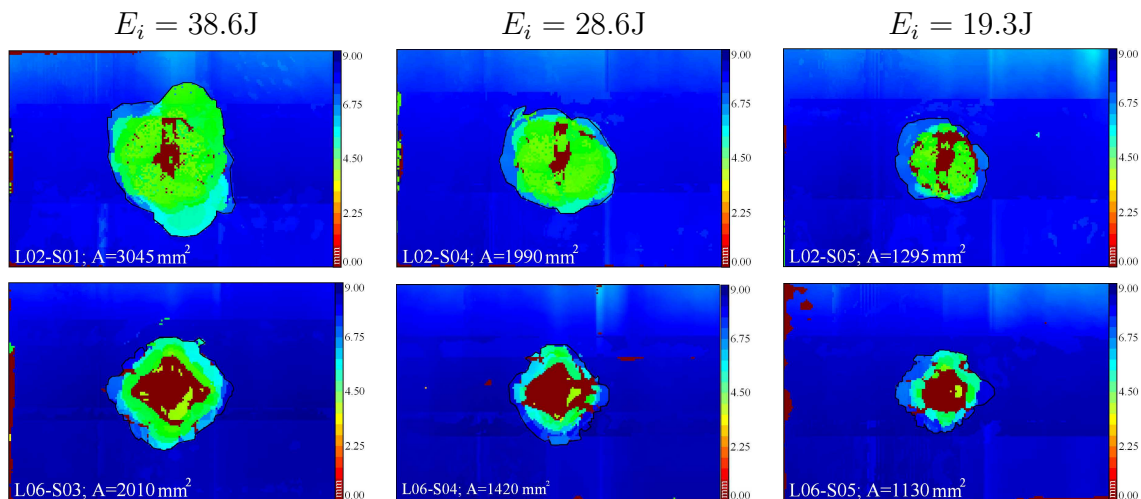


Figure 4.31: Sample of C-scan inspections of laminates L02 and L06.

Looking the results presented, the mismatch angle of the interfaces has not a

clear effect on the damage resistance of the plate, despite the fact that laminate L06 was selected because its stacking sequence has increased mismatch angles in comparison with laminate L02. This lack of contrast may be generated by the differences in the plate thicknesses of L02 and L06 which make difficult to extract a possible concluding result, or simply because really the mismatch angle does not affect the damage resistance significantly.

4.3.3 Dent-depth measurements

In Figure 4.32 are collected the contour plots of the dent-depth measurements of the whole selected specimen sample of laminates L02 and L06. The shape of the contour plots for L06 are circular in the center and changes into a square shape as more far from the impact point the lecture is. As can be observed, increasing the impact velocity, the resulting indentation obviously is increased. On the other hand, an effect of the mismatch angle is not detected.

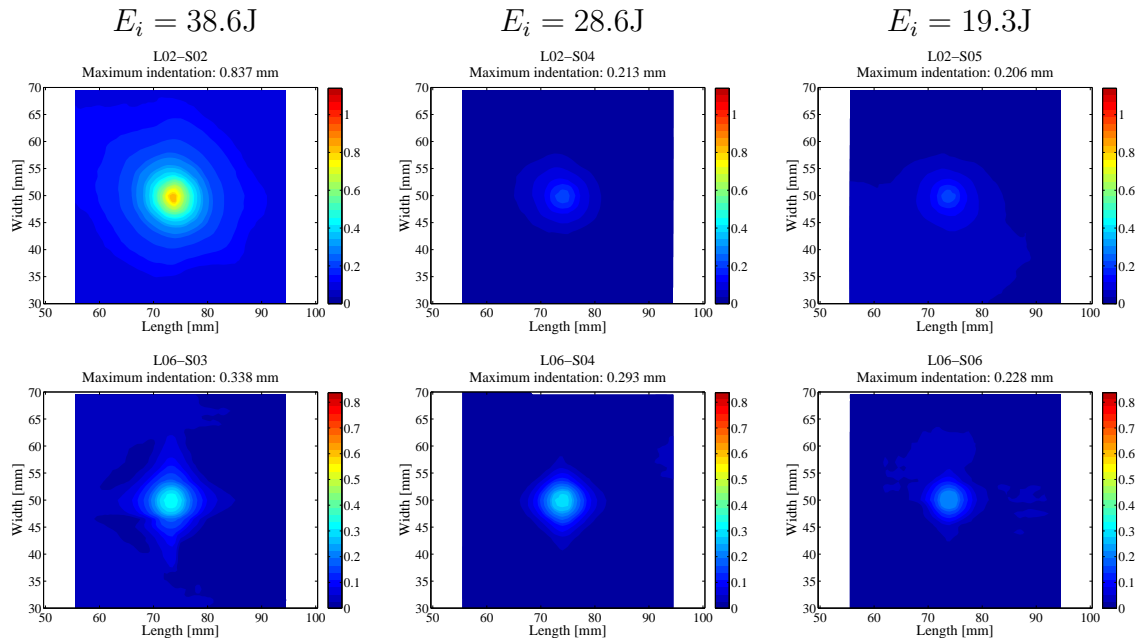


Figure 4.32: Dent-depth inspections of laminates L02 and L06.

4.3.4 CAI tests

Residual compressive load

Table 4.8 summarizes the residual compressive loads F_{fc} obtained. As it can be evidenced, increasing the impact energy (or the impact velocity), the residual compressive loads are reduced for any laminate.

Table 4.8: Failure compressive loads F_{fc} of laminates L02 and L06.

$E_i = 38.6\text{J}$		$E_i = 28.6\text{J}$		$E_i = 19.3\text{J}$	
Specimen	F_{fc} [kN]	Specimen	F_{fc} [kN]	Specimen	F_{fc} [kN]
L02-S01	93	L02-S04	103	L02-S05	133
L02-S02	99				
Mean: 96					
L06-S01	113	L06-S04	130	L06-S06	145
L06-S02	114				
Mean: 114					

In addition, the compressive loads of L06 are larger than for L02. This result can not be attributed to the effect of the ply mismatch angle, and even more when it is expected that the mismatch angle should give a reduced damage tolerance as noted in Chapter 3. Really, the residual loads of L06 are larger because laminate L06 has more plies than L02. Therefore, if these loads are normalized by the corresponding section subjected in compression (i.e. $b \times h$), the compressive residual strengths obtained for both laminates are practically equal at each impact energy (see Table 4.9).

Table 4.9: Residual compressive strengths σ_{fc} of laminates L02 and L06.

Laminate	$E_i = 38.6\text{J}$		$E_i = 28.6\text{J}$		$E_i = 19.3\text{J}$	
	F_{fc} [kN]	σ_{fc} [MPa]	F_{fc} [kN]	σ_{fc} [MPa]	F_{fc} [kN]	σ_{fc} [MPa]
L02	96	16.6	103	17.8	133	22.9
L06	114	16.8	130	19.1	145	21.3

Lectures of the displacement transducers (LVDT) and the strain gages (SG)

Table 4.10 summarizes the maximum values of the lectures of the two displacement transducers used during the CAI tests. As it can be observed, the values obtained are quite similar for both laminate types. In addition, Figure 4.33 shows the lectures for laminates L02 and L06 of the specimens impacted with 29.6J. As in the ply clustering study, the buckling mode of each laminate type is practically the same.

Table 4.10: Maximum lectures of the displacement transducers of laminates L02 and L06.

Impact energy: $E_i = 38.6\text{J}$			Impact energy: $E_i = 28.6\text{J}$			Impact energy: $E_i = 19.3\text{J}$		
Specimen	LVDT1 [mm]	LVDT2 [mm]	Specimen	LVDT1 [mm]	LVDT2 [mm]	Specimen	LVDT1 [mm]	LVDT2 [mm]
L02-S01	1.67	0.09	L02-S04	1.73	0.16	L02-S05	1.11	0.41
L02-S02	2.06	0.33						
L06-S01	2.08	0.30	L06-S04	1.55	0.37	L06-S06	1.50	0.22
L06-S02	2.22	0.26						

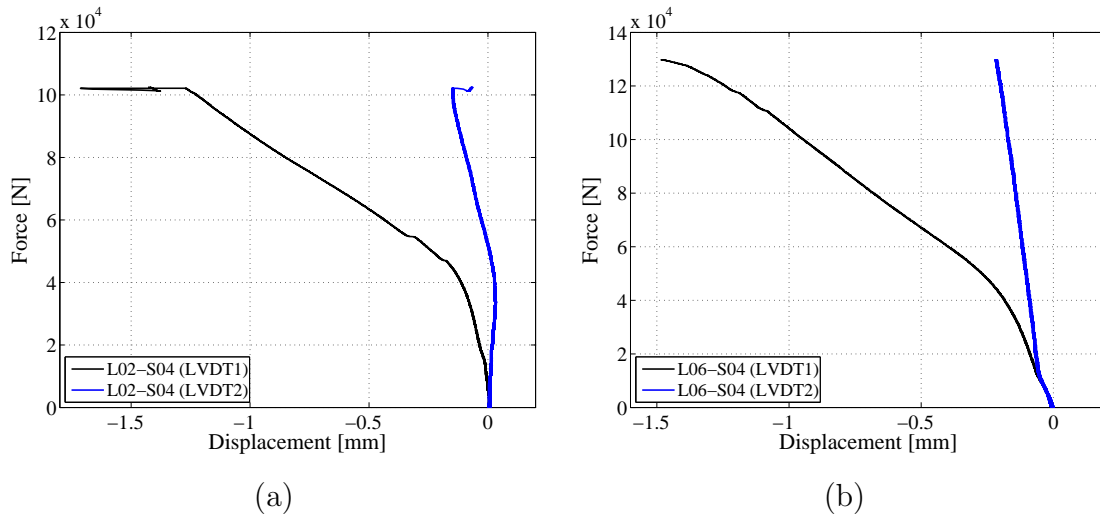


Figure 4.33: Displacement transducer lectures of the specimens impacted with 29.6J: (a) L02 and (b) L06.

Finally, Figure 4.34 shows the lectures of the four strain gages of each laminate type for the impact energy of 29.6J. Again, differences between the lectures of the

gages located at the same face (SG1 with SG2; SG3 with SG4), and between the lectures of the back-to-back gages (SG1 with SG3; SG2 with SG4) are evidenced. As mentioned in Section 4.2, these differences are caused by a non-uniform application of the load and also by the asymmetry of the impacted plate which produces a little bending during the test.

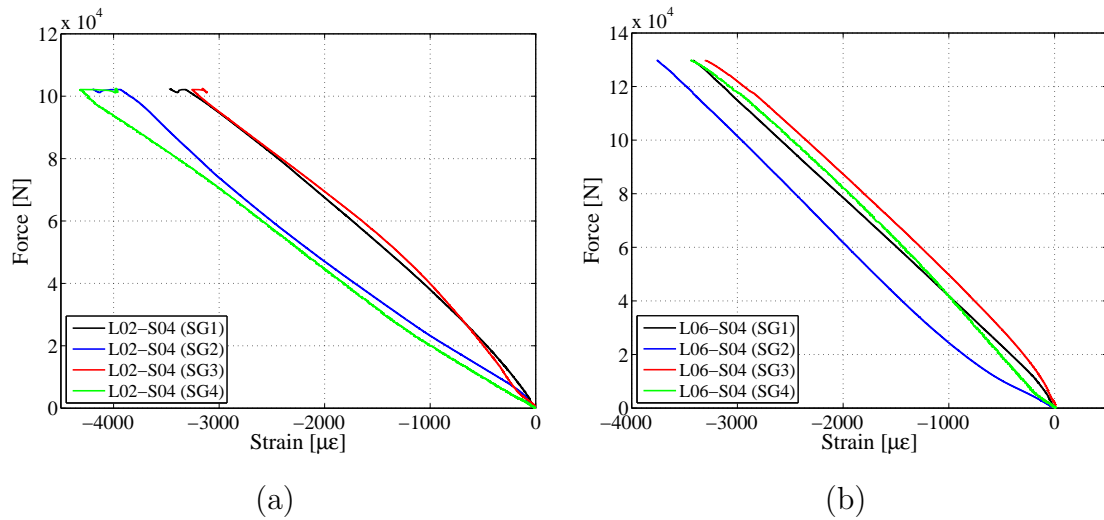


Figure 4.34: Strain gage lectures of the specimens impacted with 29.6J: (a) L02 and (b) L06.

4.4 Effect of the laminate thickness

4.4.1 Impact tests

Impact force versus time

Figures 4.35 and 4.36 show the histories of the impactor reaction force for each impact configuration of laminates L01 and L05, respectively (see Chapter 3). A clear first drop in the force histories of laminate L05 is evidenced and it is constant for all impact configurations. However, the profiles of L01 are smooth and do not have a clear first drop of the impact force. This result could mean that there is not a sudden loss of stiffness after damage onset and can be related to the fact that laminate L01 stands large global deflections which generate membrane effects. These effects mean

that the stiffness of the plate increases as the plate deflection is increased. As the contact time advances, more fibers are subjected to tensile stresses and they stand the majority of the impact load. The matrix and delamination damage that can occur do not change the impact response. However, the impact response is affected by progressive fiber breakage. This behavior seems to be common for any of the impact configurations of laminate L01, even with the configuration with the smaller impact energy, i.e. specimen L01-S06.

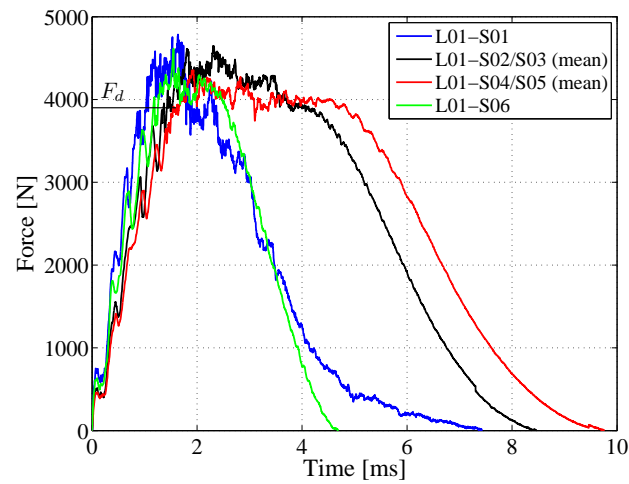


Figure 4.35: Impact force histories of laminate L01 for each impact configuration (blue: $E_i = 38.6\text{J}$, $M_i = 5\text{kg}$; black: $E_i = 19.3\text{J}$, $M_i = 5\text{kg}$; red: $E_i = 19.3\text{J}$, $M_i = 6\text{kg}$; green: $E_i = 12.0\text{J}$, $M_i = 2\text{kg}$).

Tables 4.11 and 4.12 summarize the threshold loads F_d and the peak loads F_{max} for each impact configuration of laminates L01 and L05, respectively.

Table 4.11: Experimental threshold loads F_d and peak loads F_{max} for laminate L01.

Load [kN]	Energy [J]:	38.6	19.3	19.3	12.0	Mean
	Mass [kg]:	5.0	5.0	6.0	2.0	
Threshold loads F_d		4.00	3.90	3.72	4.03	3.9
Peak loads F_{max}		4.79	4.65	4.35	4.62	-

In detail, Figure 4.37.a shows the force responses of the impact configurations of laminate L01 with a constant impact energy, but different impactor masses and

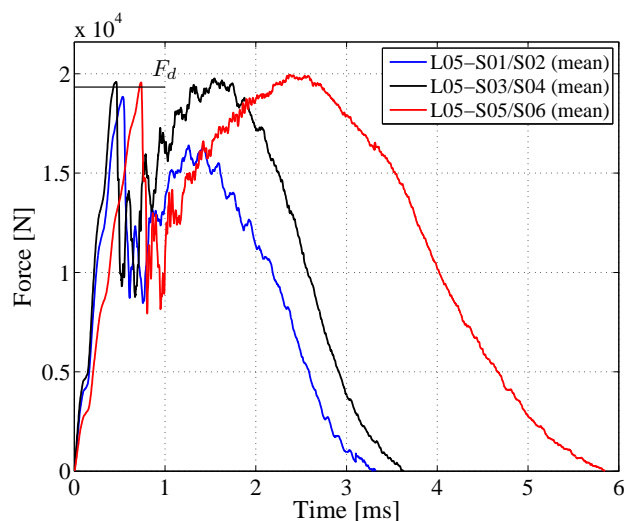


Figure 4.36: Impact force histories of laminate L05 for each impact configuration (blue: $E_i = 38.6\text{J}$, $M_i = 5\text{kg}$; black: $E_i = 57.8\text{J}$, $M_i = 6\text{kg}$; red: 57.9J , $M_i = 15\text{kg}$).

Table 4.12: Experimental threshold loads F_d and peak loads F_{max} for laminate L05.

Load [kN]	Energy [J]:	38.6	57.8	57.9	Mean
	Mass [kg]:	5.0	6.0	15.0	
Threshold loads F_d		18.84	19.59	19.56	19.33
Peak loads F_{max}		18.84	19.77	19.95	-

velocities. As can be observed, increasing the impactor mass the response is more quasi-static, which means that the response is slowed down. In addition, Figure 4.37.b also shows the same analysis for laminate L05, but in this case the difference in the impactor mass is increased, yielding to more differentiable responses.

The effect of the impactor mass M_i was shown in the impact characterization diagram by means of the relative mobility parameter ζ_w (see Chapter 2). Increasing M_i , ζ_w is increased and then the behavior is changed to a more quasi-static behavior. This effect can also be observed by means of the complete analytical models of the impact event. Accordingly, Figure 4.38 show the experimental and the analytical responses of laminate L01 for the impact energy 19.3J. In detail, the analytical predictions plotted in Figure 4.38.a are given by a complete model fed with the bi-

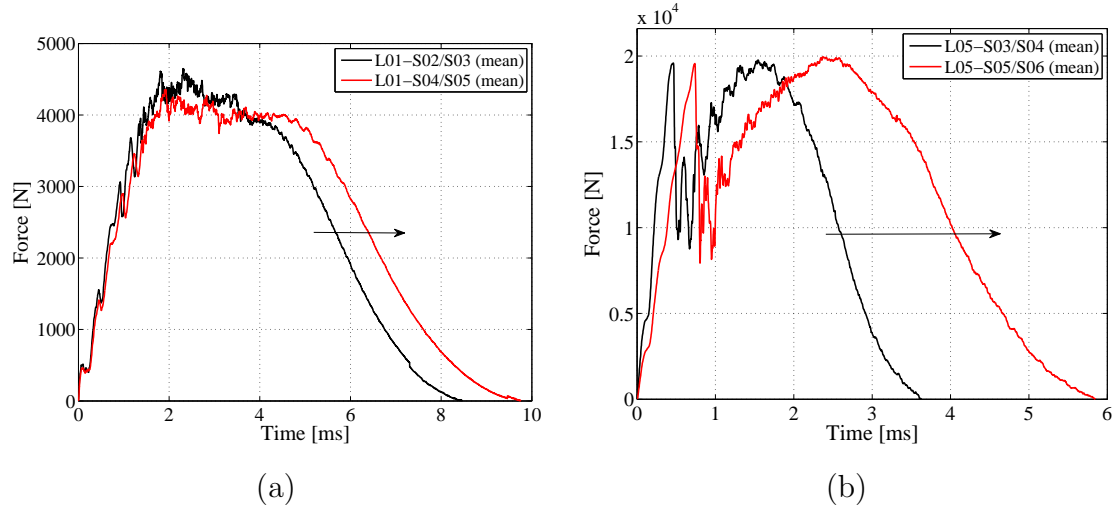


Figure 4.37: (a) Impact force histories of laminate L01 for 19.3J (black: $M_i = 5\text{kg}$; red: $M_i = 6\text{kg}$), and (b) impact force histories of laminate L05 for 58J (black: $M_i = 6\text{kg}$; red: $M_i = 15\text{kg}$).

linear elastic-plastic contact law proposed by Yigit and Christoforou [45]. However, for the model used for the predictions plotted in Figure 4.38.b, the Hertz contact law is considered. For all the simulations, the number of modes applied for the Navier solution is 5 for each in-plane x and y directions. The analytical models show clearly the effect of changing the mass and the velocity under equal impact energy. As expected, the contact time of the elastic responses is enlarged when the impactor mass is increased. Finally, related to the contact laws used for the analytical models, both cases suit the experimental profile and then no significant dependence with the contact law is detected. This result is explained with the fact that laminate L01 has small peak loads and an emphasized global behavior. Therefore, the role that plays the contact law in these impact configurations is small.

Additionally, Figure 4.39 illustrates also the effect of changing the impactor mass for laminate L05. In contrast with the predictions given for laminate L01, the role that plays the contact law is significant because a more localized behavior is experimented. As can be observed, the model which uses the Hertz contact law (in Figure 4.39.b), suits better the experimental results than the model fed with the bilinear elastic-plastic contact law (in Figure 4.39.a). Therefore, given the predictions of the complete models, it could be interesting to carry out quasi-static indentation

tests or finite element simulations in order to know what is the proper contact law.

Finally, the effects of changing the impactor mass and the velocity but keeping constant the impact energy on the damage creation, can be simply analyzed, in a qualitative point of view, by observing the peak loads of the analytical profiles or by calculating the maximum elastic impact force as: $F_{max} = \bar{F}_{max} \sqrt{k_y} \sqrt{2E_i}$ (see Section 3.2). Since the impact energy E_i is kept constant, it yields to a constant maximum elastic impact force. Therefore, the resulting extension and type of damage is expected to be the same.

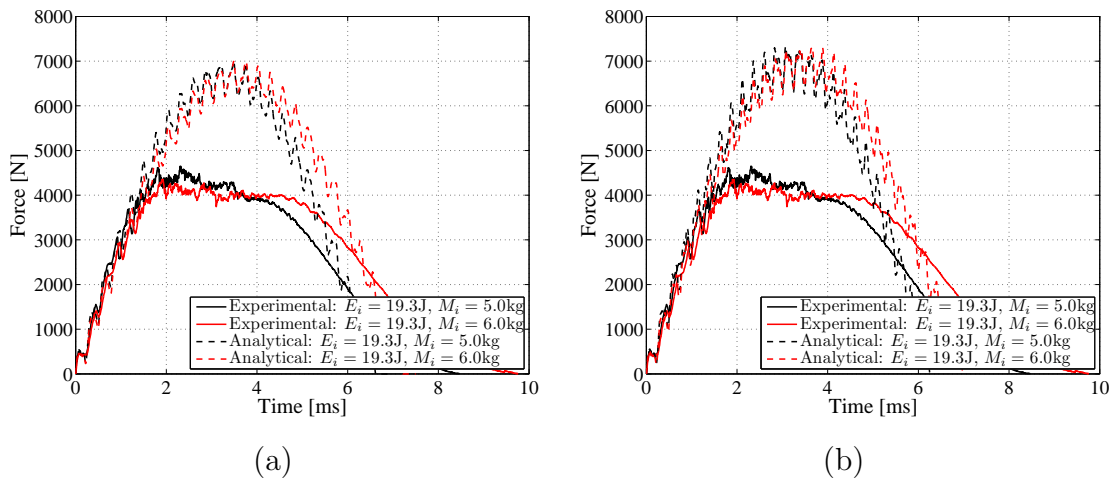


Figure 4.38: Experimental and analytical impact force histories of laminate L01 for a constant impact energy 19.3J: $M_i = 5\text{kg}$ (black), and $M_i = 6\text{kg}$ (red). Two different contact laws are used: (a) bi-linear elastic-plastic contact law [45], and (b) the Hertz contact law.

In Figure 4.40.a, the impact force histories corresponding to laminates L01 and L02 for an impact energy of 19.3J and an impactor mass of 5kg are compared. The effect of the plate thickness is clearly evidenced. Increasing the thickness, the response is faster, the peak load increases, and a clear first drop of the force appears. In addition, in Figure 4.40.b the impact force histories corresponding to laminates L01, L02 and L05 for an impact energy of 38.6J and an impactor mass of 5kg are compared. Again, the effects of the plate thickness under equal impact conditions can be observed. As shown, laminate L01 was perforated under an impact with a quasi-static behavior, as predicted in Chapter 3.

Recovering the experimental damage thresholds F_d of all laminates with equal

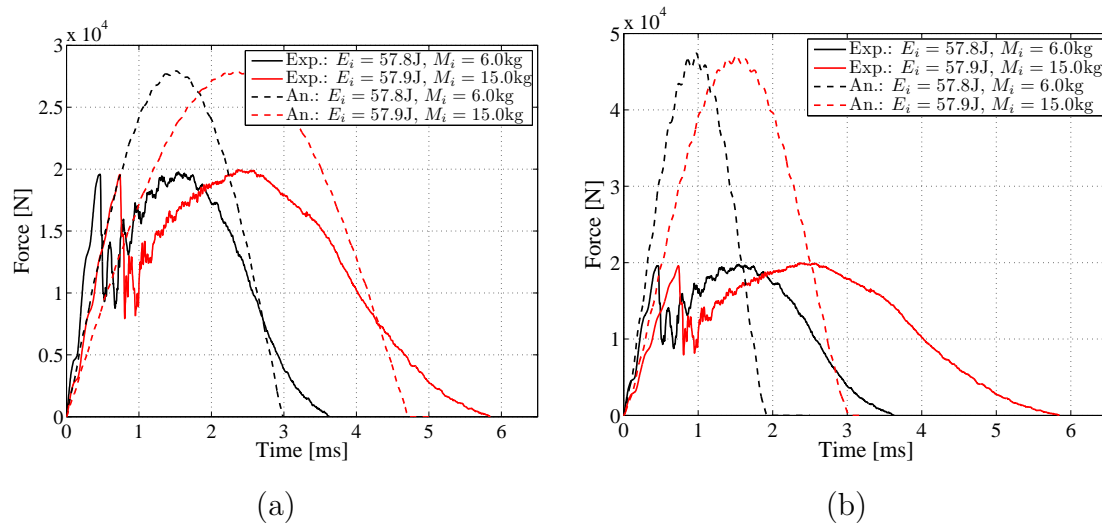


Figure 4.39: Experimental and analytical impact force histories of laminate L05 for a constant impact energy 57.8J : $M_i = 6\text{kg}$ (black), and $M_i = 15\text{kg}$ (red). Two different contact laws are used: (a) bi-linear elastic-plastic contact law [45], and (b) the Hertz contact law.

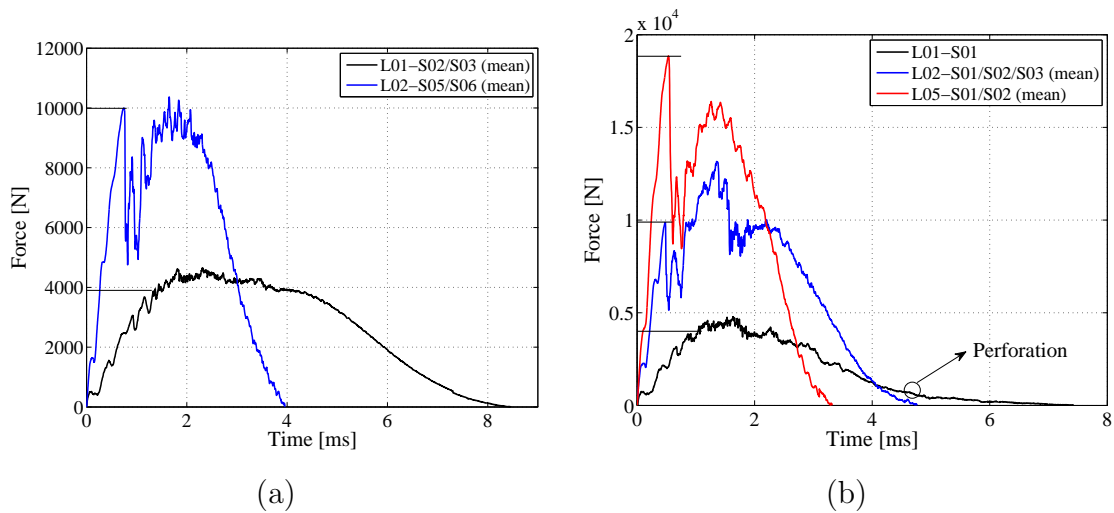


Figure 4.40: (a) Impact force histories of laminates L01 (black) and L02 (blue) for 19.3J ; (b) impact force histories of laminates L01 (black), L02 (blue) and L05 (red), for 38.6J .

ply thickness (L01, L02, L05 and L06), these can be plotted as a function of the plate thickness h in a natural logarithmic scale, as shown in Figure 4.41. If a fit

of the experimental points is performed (in gray), a slope of 1.47 is obtained. This value is quite close to the slope of the analytical threshold for a circular mid-plane delamination (in black), i.e. 1.5, since $F_{d1}^{stat} \propto h^{1.5}$. Despite the constant offset that exists between the experimental and the analytical values, the significant conclusion is that the analytical trend seems to be in agreement with the experimental results. This result suggests that these laminates have a threshold load that corresponds approximately to a circular mid-plane delamination. The offset can be due to scattering of the material properties or to the assumptions considered in the formulation of the damage threshold, e.g. strain rate effects are neglected. Additionally, this result agrees with the analytical prediction for the first significant damage explained in Section 3.2.2, in exception of laminate L01. The damage threshold for L01 was related to a back face delamination ($F_d = F_{mc}^{ten}$). This inaccurate prediction can be attributed to the fact that the identification of F_d in the impact force history is not clear, or simply a sudden delamination does not occur.

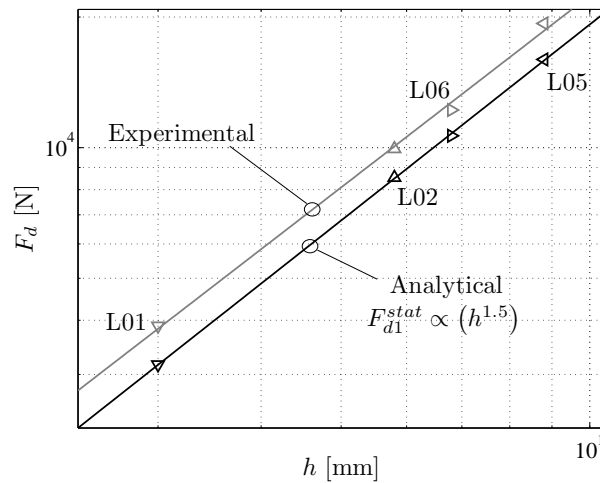


Figure 4.41: Experimental and analytical threshold loads as a function of the plate thickness.

Impactor displacement, impactor velocity, and absorbed energy

Accordingly to the impact force histories, the effect of changing the impactor mass and the velocity, but keeping constant the impact energy, can also be observed in

the histories of the impactor displacement and velocity plotted in Figure 4.42 for laminate L01, and in Figure 4.43 for laminate L05. Increasing the impactor mass, the displacements are enlarged and so the velocity responses are slower.

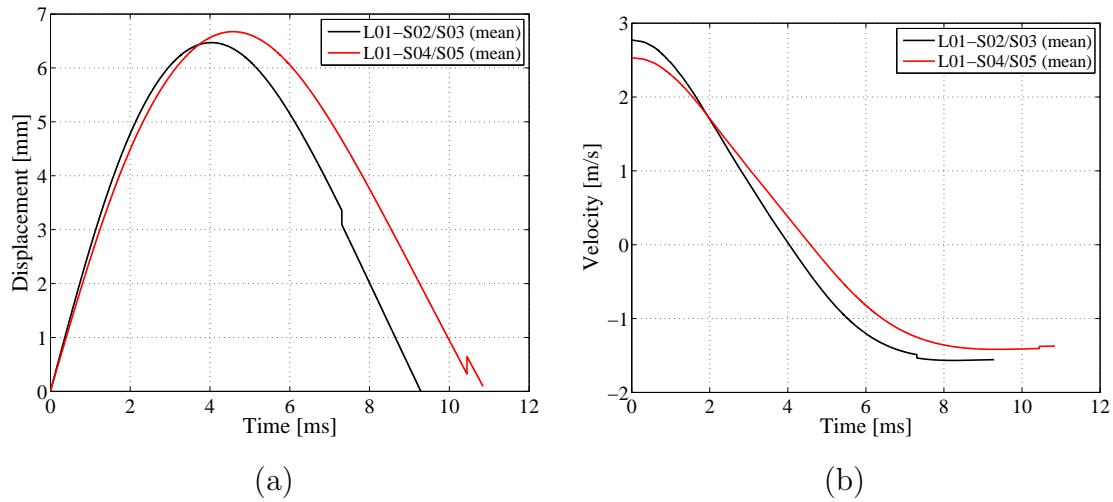


Figure 4.42: Impactor (a) displacement and (b) velocity of laminate L01 for 19.3J (black: $M_i = 5\text{kg}$; red: $M_i = 6\text{kg}$).

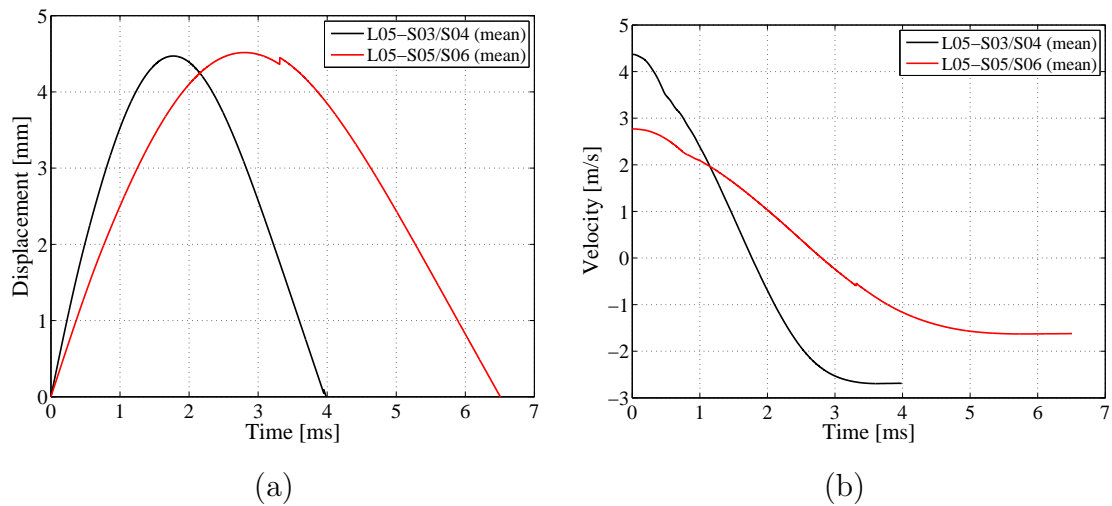


Figure 4.43: Impactor (a) displacement and (b) velocity of laminate L05 for 58J (black: $M_i = 6\text{kg}$; red: $M_i = 15\text{kg}$).

Moreover, Figure 4.44.a shows the histories of the absorbed energy of laminates L01, and Figure 4.44.b shows the evolutions of the impact force as a function of the

impactor displacement. It can be seen that the absorbed energies are practically equal for both impact configurations, but the whole dissipation occurs at different instants. In addition, Figure 4.45 also shows these charts for laminates L05, where the effect of the impactor mass is more clear because the differences between configurations are greater than for L01.

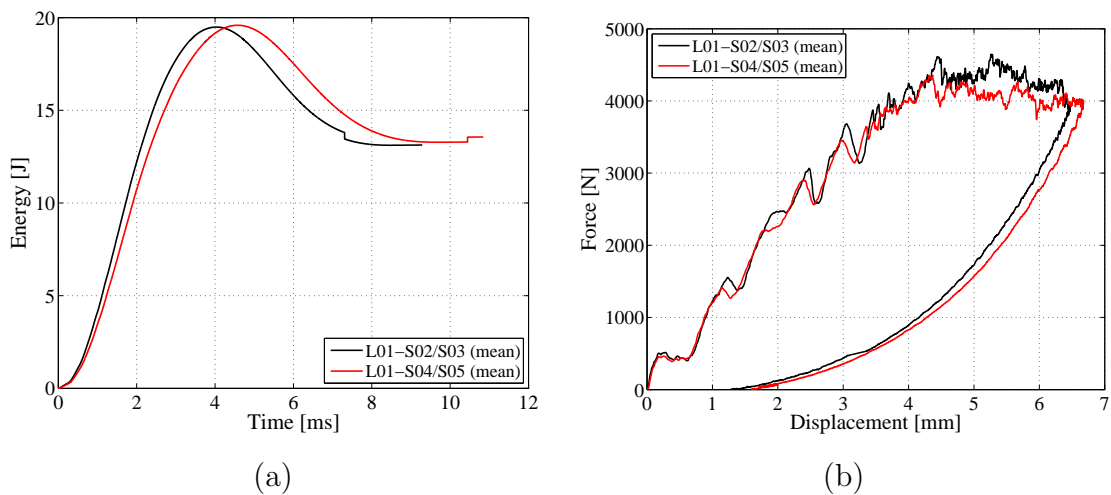


Figure 4.44: Evolution of the (a) absorbed energy and the (b) impact force versus impactor displacement of laminate L01 for 19.3J (black: $M_i = 5\text{kg}$; red: $M_i = 6\text{kg}$).

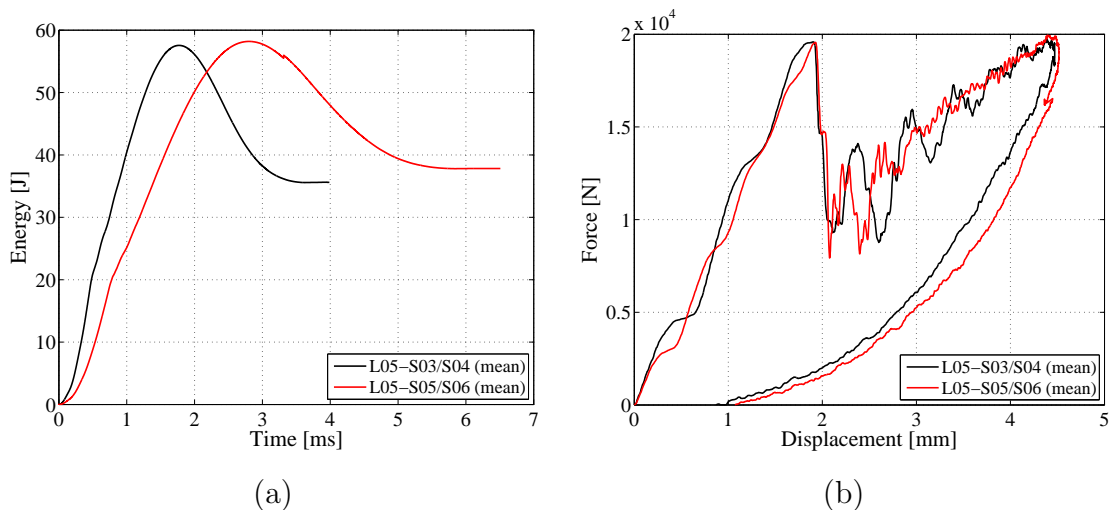


Figure 4.45: Evolution of the (a) absorbed energy and the (b) impact force versus impactor displacement of laminate L05 for 58J (black: $M_i = 6\text{kg}$; red: $M_i = 15\text{kg}$).

The result detected in Figures 4.44 and 4.45 agrees with the procedure of the guidelines for a drop-weight impact test provided by the aeronautical industry, which often do not specify the impactor mass or the velocity, rather they establish the impact energy (e.g. Airbus AITM1-0010 [94]). The reason for defining the set-up in this way is related to the fact that independently of the impactor mass and velocity selected, at the end of the test the energy dissipated will be the same. In other words, the damage developed in the specimens is the same if the impact energy is kept constant.

On the other hand, Figure 4.46 shows the displacement and the velocity histories of laminates L01 and L02 for the impact energy 19.3J. In addition, Figure 4.47 shows the corresponding histories of laminates L01, L02 and L05 for the impact energy 38.6J. Again, the effect of the laminate thickness is evidenced. Increasing the thickness, the response is more localized. This result means that the impactor displacement is smaller because less global deflection of the plate is experienced, and accordingly the response is much faster.

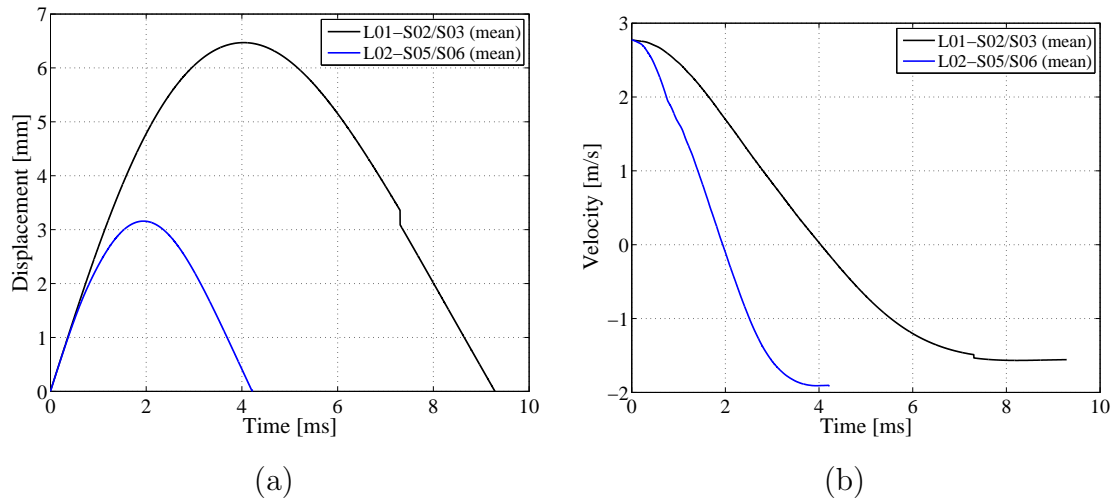


Figure 4.46: Impactor (a) displacement and (b) velocity of laminates L01 and L02 for 19.3J.

The absorbed energy is not the same for each laminate thickness under equal impact conditions. The trend is if the laminate thickness is increased, the absorbed energy is reduced. This effect can be observed in Figure 4.48, which shows the histories of the absorbed energy and the evolutions of the impact force as a function

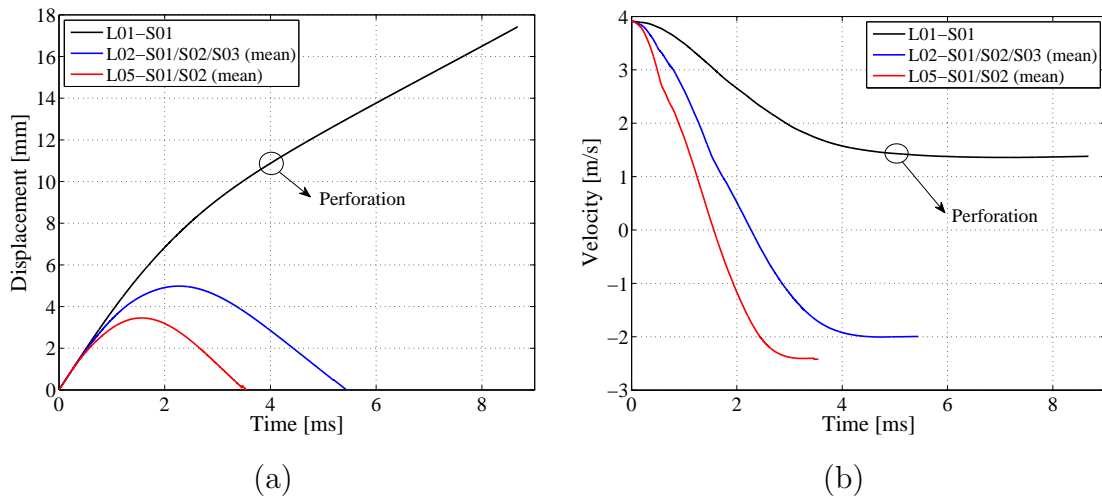


Figure 4.47: Impactor (a) displacement and (b) velocity of laminates L01, L02 and L05 for 38.6J.

of the impactor displacement of laminates L01 and L02 for the impact energy 19.3J. The dissipated energies at the end of the tests are 13.1J for L01 and 10.1J for L02. Additionally, Figure 4.49 shows these evolutions corresponding to laminates L01, L02 and L05 for the impact energy 38.6J. In this case, the dissipated energies at the end of the tests are 34.3J for L01, 28.3J for L02, and 23.6J for L05. Finally, a recovering of the elastic energy in the evolution of E_a of the perforated specimen L01-S06 is not observed.

4.4.2 NDI: C-scan after impact

The observations commented before about the effects of changing the impactor mass and the velocity, but keeping constant the impact energy, also can be associated with the ultrasonic C-scan inspections. Figures 4.50 and 4.51 show a sample of the projected delamination areas corresponding to laminate L01 and laminate L05, respectively. It is observed that the projected area is practically the same when the impact energy is kept constant. This result suits with the fact that the dissipated energy is also the same for two impact cases which have the same impact energy.

On the other hand, between specimens with the same impact configuration but different laminate thicknesses, the resulting values of the projected area are quite similar, such as it is shown in Figures 4.52 and 4.53. However, it could be interesting

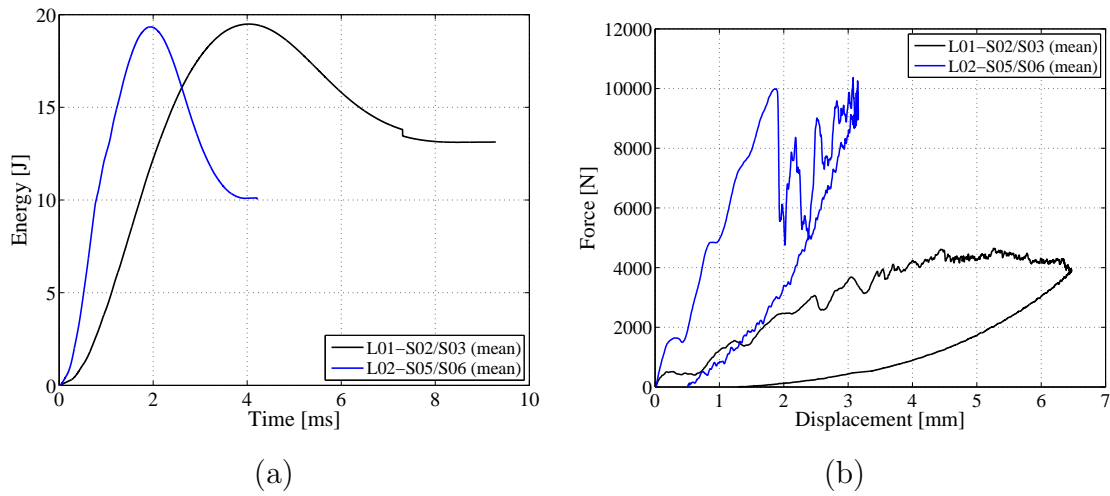


Figure 4.48: Evolution of the (a) absorbed energy and the (b) impact force versus impactor displacement of laminates L01 and L02 for 19.3J.

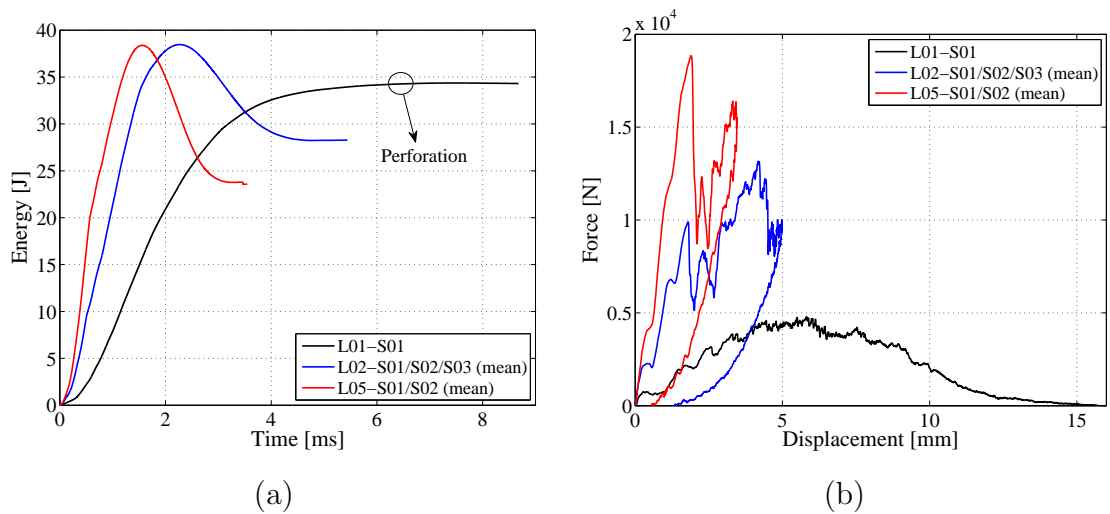


Figure 4.49: Evolution of the (a) absorbed energy and the (b) impact force versus impactor displacement of laminates L01, L02 and L05 for 38.6J.

to have at one's disposal the total values of the sum of each delaminated area of the interfaces, and then to compare these values between laminates with different thicknesses. Therefore, it could be expected that the largest area would be from laminate L01 as it was detected in the profiles of the dissipated energy. If this does not occur, then other damage mechanisms should have absorbed the energy in

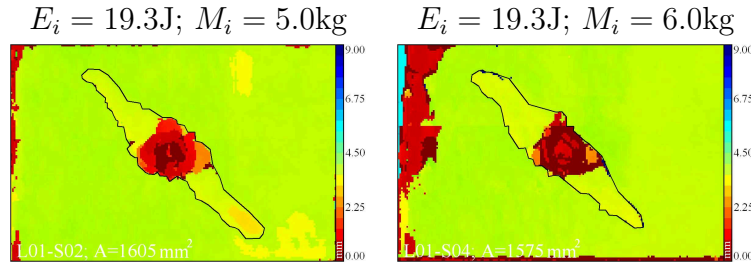


Figure 4.50: Sample of C-scan inspections of laminate L01 with equal impact energies, but different impactor masses.

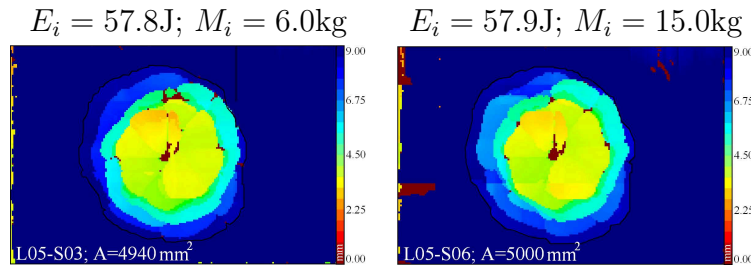


Figure 4.51: Sample of C-scan inspections of laminate L05 with equal impact energies, but different impactor masses.

laminate L01, such as fiber breakage.

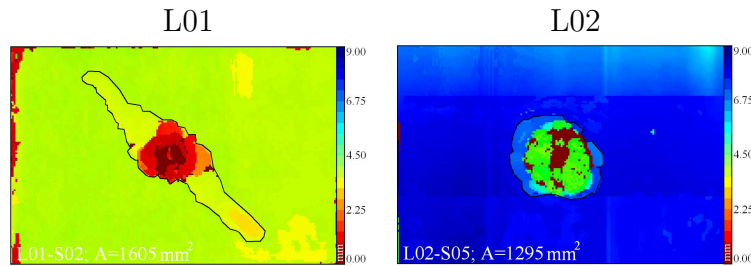


Figure 4.52: Sample of C-scan inspections of laminates L01 and L02 for 19.3J (laminate thickness).

The shapes of the projected delamination areas can be related to the analytical predictions of F_d . For laminate type L01 was predicted a delamination at the first interface from the back face of the plate (i.e. F_{mc}^{ten} for thin ply thickness). However, the experimental value obtained fits with the global linear trend for a circular

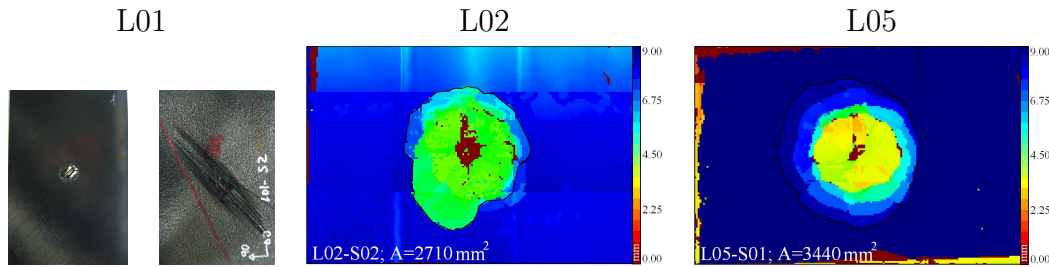


Figure 4.53: Sample of C-scan inspections of laminates L02 and L05 for 38.6J (laminate thickness).

mid-plane delamination F_{d1}^{stat} , as it was seen in Figure 4.41. Figure 4.54 shows the ultrasonic inspection for the laminate L01 with the lowest impact energy. As can be observed, the shape is equal in comparison with the shapes resulted from higher impact energies, just that with a smaller size. Therefore, for laminate L01 it is difficult to know what is the damage type associated to F_d . As was noted previously, these difficulties can be due to different factors. On the other hand, the prediction of F_d for both laminate types L02 and L05 was a mid-plane circular delamination. The shapes obtained are quite circular, but it should be noted that these circular shapes are rather a result of the superposition of peanut shaped delaminations. Furthermore, the deeper the delamination is, the larger the delamination is. These distribution of delaminations yield to the so-called pine pattern delamination distribution. In conclusion, for laminates L02 and L05 the prediction of F_d can be considered well suited although the considerations commented.

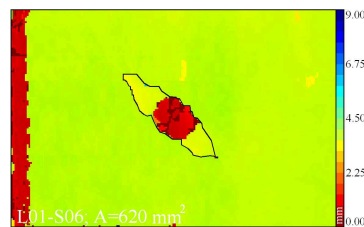


Figure 4.54: C-scan inspection of specimen L01-S06 ($E_i = 12.0\text{J}$, $M_i = 2.0\text{kg}$).

4.4.3 Dent-depth measurements

Figures 4.55 and 4.56 show the contour plots of the dent depth measurements of the impacted specimens L01 and L05, respectively. Consistent with previous observations, the resulting lectures of the dent depths are quite similar for impact cases with different impactor mass and velocity, but with equal impact energy.

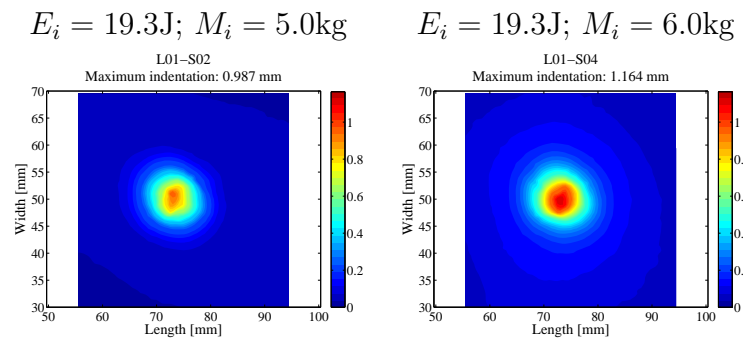


Figure 4.55: Dent-depth inspections of laminate L01 with equal impact energies, but different impactor masses.

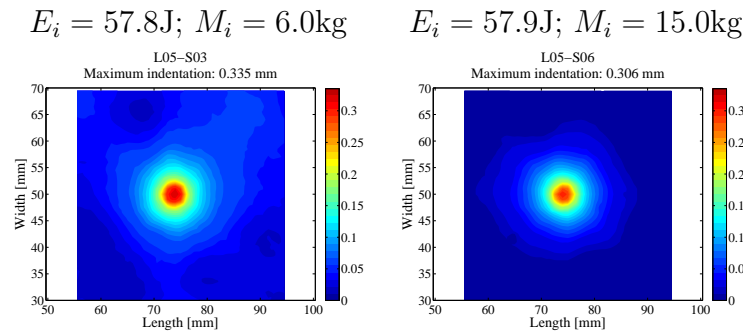


Figure 4.56: Dent-depth inspections of laminate L05 with equal impact energies, but different impactor masses.

Figures 4.57 and 4.58 show a sample of dent-depth measurements of laminates with different thicknesses. As it was observed in the histories of the impact force, increasing the laminate thickness, the response results more localized because less laminate deflection is experimented. Conversely, the dent-depth measurements demonstrate that also the indentation values are higher for thin plates. Nevertheless, it

should be noted that for thin plates the indentation measurements are affected by the residual global deflection of the plate which increases the measurements obtained.

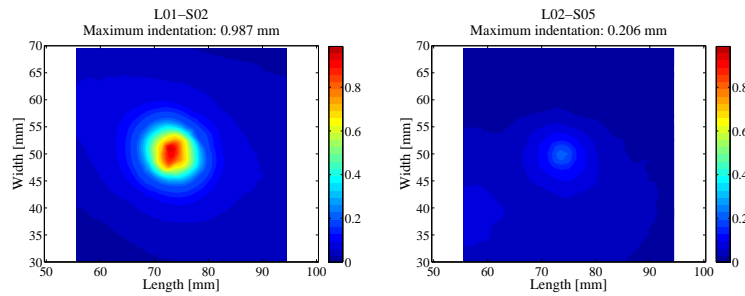


Figure 4.57: Dent-depth inspections of laminates L01 and L02 for 19.3J.

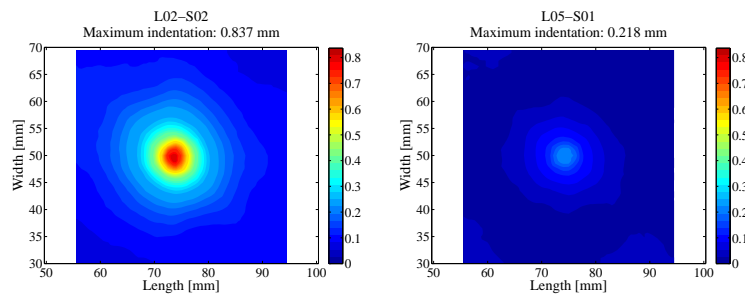


Figure 4.58: Dent-depth inspections of laminates L02 and L05 for 38.6J.

4.4.4 CAI tests

Residual compressive load

The results available from the CAI test to check the effects of changing the impactor mass but keeping constant the impact energy are those from laminate L05. The residual compressive loads F_{fc} are: 164.5kN for $E_i = 57.8\text{J}$ and $M_i = 6.0\text{kg}$, and 156.9kN for $E_i = 57.9\text{J}$ and $M_i = 15.0\text{kg}$. It can be concluded that the values obtained are quite similar as can be expected after the discussion of the results presented before.

Increasing the laminate thickness under equal impact conditions, the residual compressive load increases. However, in order to compare properly these data, the normalized loads σ_{fc} must be computed. The resulting values are summarized in

Table 4.13. It can be expected that the values should be similar for each impact energy, however it is not completely true because the size and the number of interface delaminations created in the impact tests are different in function of the laminate thickness. Therefore, given the available data, a valid argument can not be deduced.

Table 4.13: Residual compressive strengths σ_{fc} of laminates L01, L02 and L06.

	$E_i = 19.3\text{J}$		$E_i = 38.6\text{J}$	
	L01	L02	L02	L05
σ_{fc} [MPa]	19.7	22.9	16.5	20.6

Lectures of the displacement transducers (LVDT) and the strain gages (SG)

As an example of the displacement transducer and strain gage lectures, Figure 4.59 shows the results obtained for laminate L05. Despite the differences in the impactor mass and velocity, the responses are quite similar.

Finally, in order to illustrate the differences obtained in the responses of the transducer displacement and strain gages due to the differences in the laminate thickness, Figures 4.60 and 4.61 show the results obtained. It is observed that laminate types L01 and L02 suffer a clear global buckling on the instrumented plate face. This behavior is not observed in Figure 4.61, where both laminates L02 and L05 suffer a more localized buckling in the middle point of the specimen lengths.

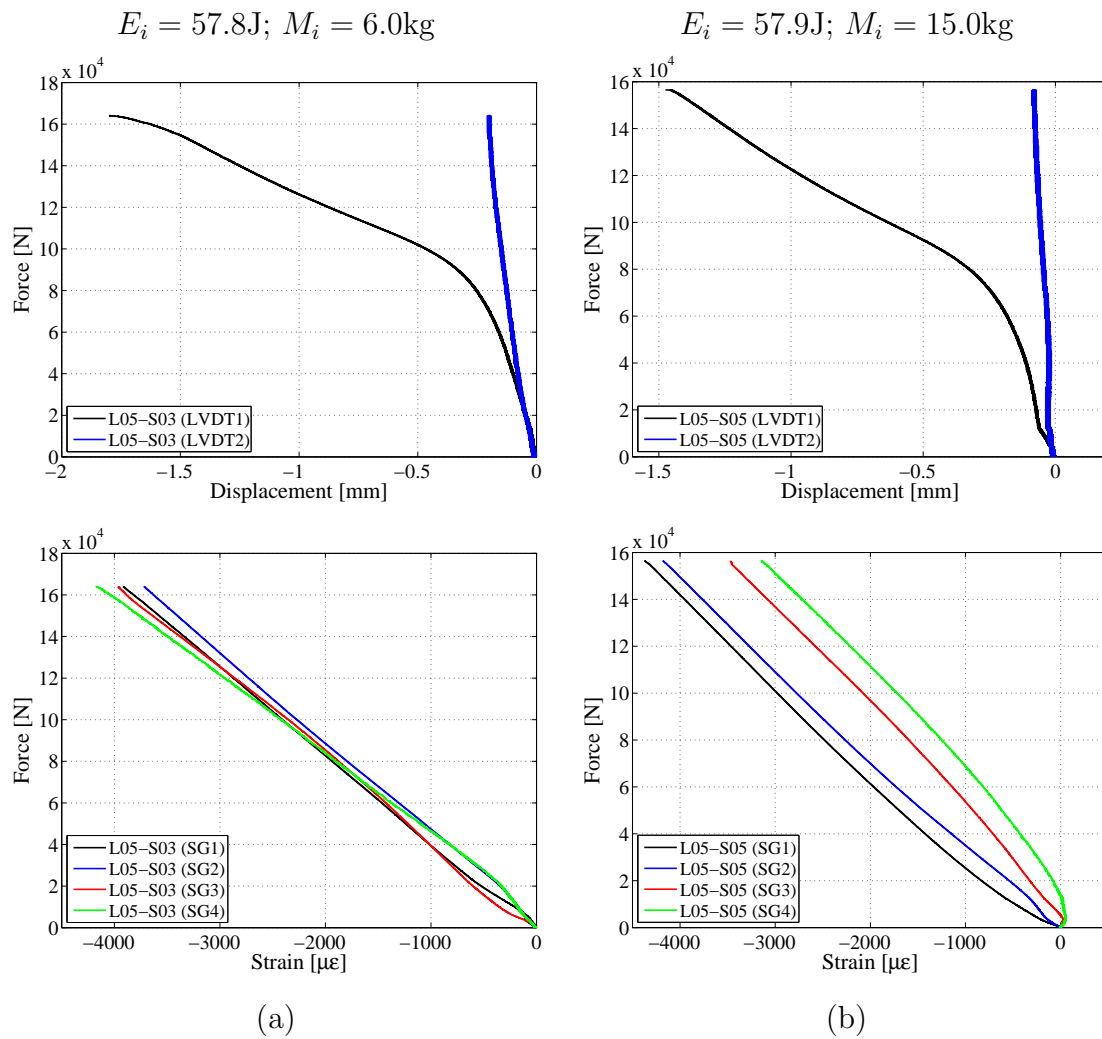


Figure 4.59: (a) Displacement transducer and (b) strain gage lectures of laminate L05.

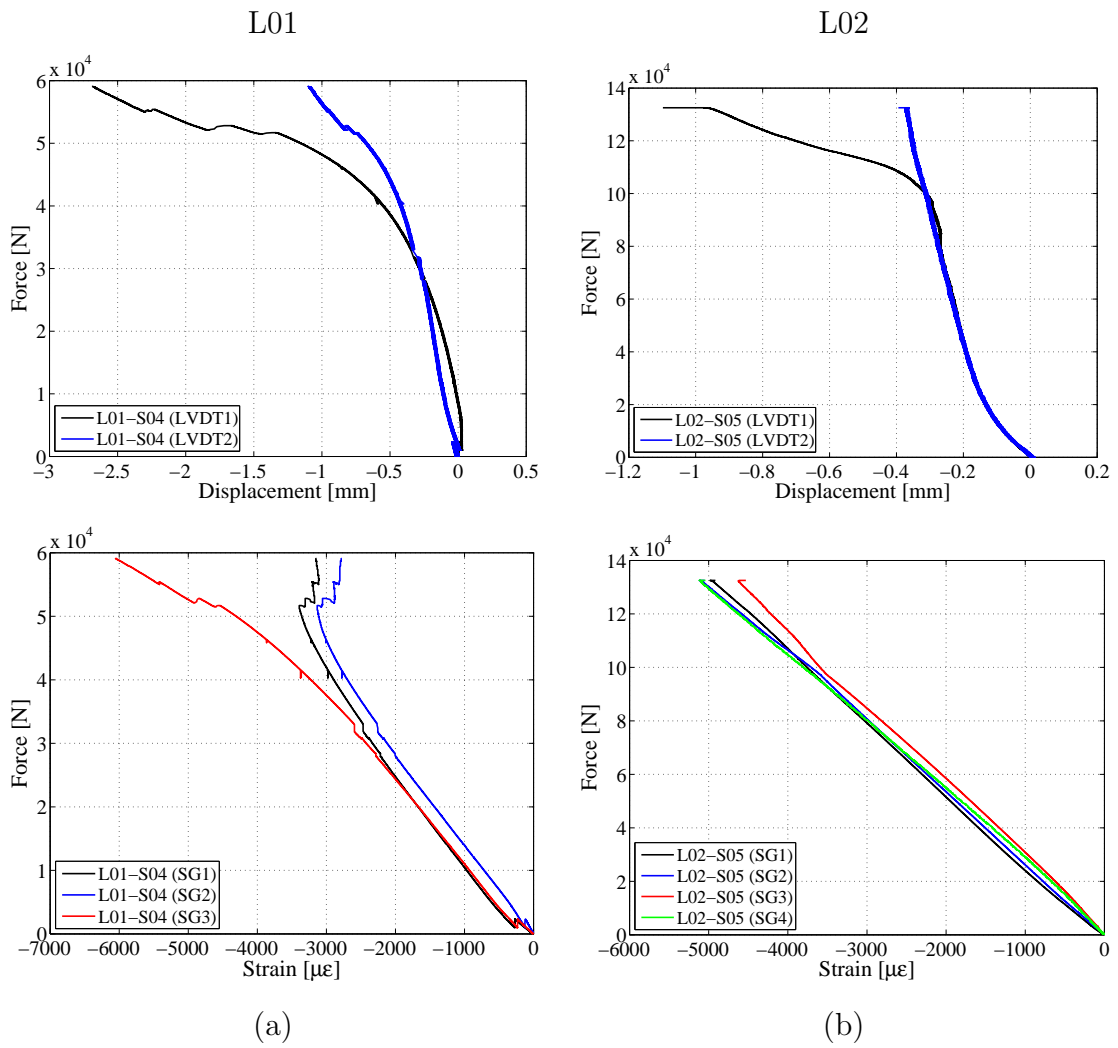


Figure 4.60: (a) Displacement transducer and (b) strain gage lectures of laminates L01 and L02 for 19.3J.

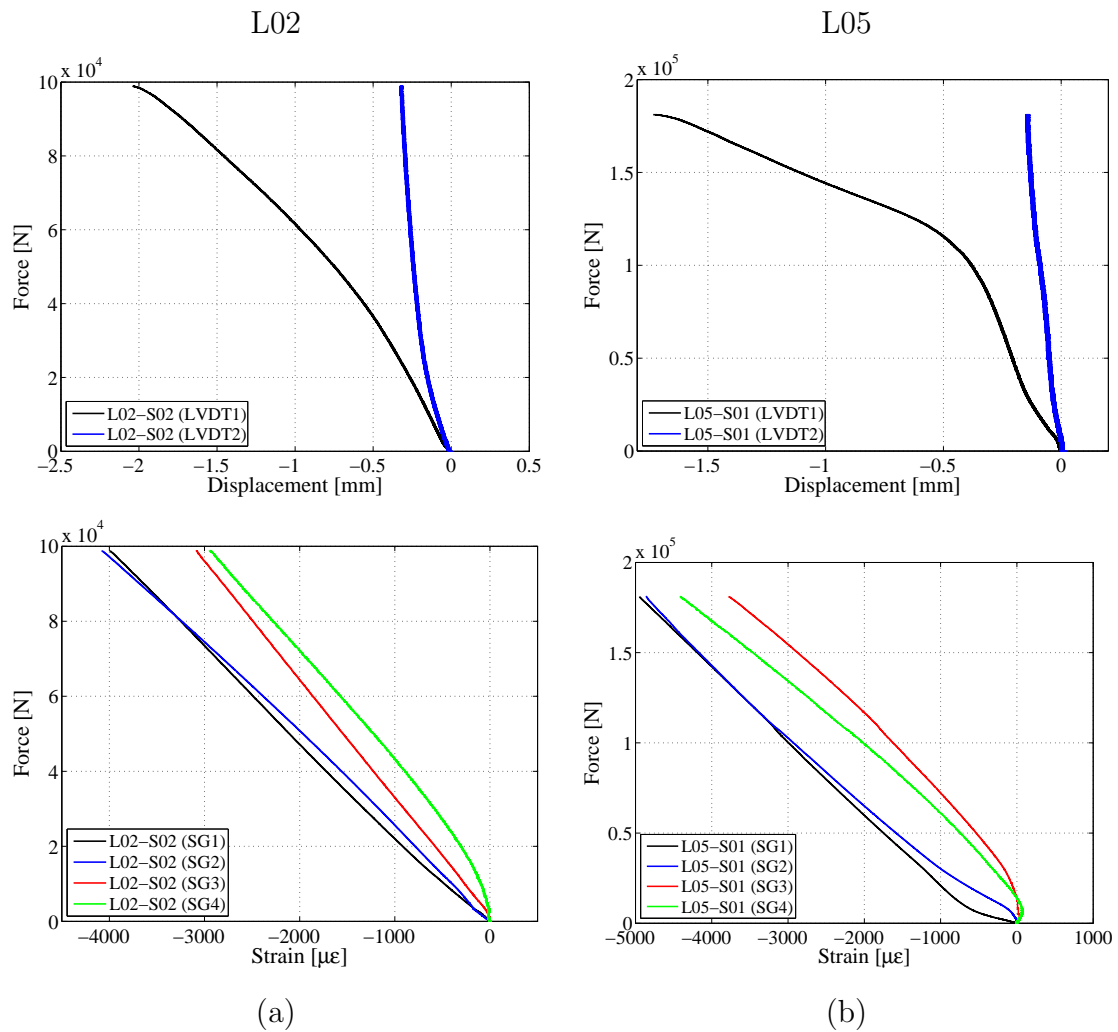


Figure 4.61: (a) Displacement transducer and (b) strain gage lectures of laminates L02 and L05 for 38.6J.

4.5 Summary of conclusions

The main conclusions from the previous discussions of the experimental results and the analytical predictions are presented herein. These conclusions are valid for drop-weight impact events (i.e. low-velocity impacts), and most of them reaffirm some of the arguments explained in the design of the experiments of Chapter 3.

Effect of the impact velocity

- The threshold load, F_d , remains constant in front of changes of the impact velocity.
- Increasing the impact velocity, the slope of the elastic regime is increased, as predicted by means of the analytical impact models. Accordingly, the predicted maximum elastic impact force increases, indicating that more damage is created.
- Increasing the impact velocity, the response is extended in time because the plate develops more damage. Accordingly, the post-impact residual compressive strength is reduced.

Effect of changing the impactor mass and the velocity

- The threshold load, F_d , remains constant in front of changes of the impactor mass and velocity, but keeping constant the impact energy.
- Increasing the impactor mass, the response is more quasi-static, which means that the response is slowed down. This behavior was also predicted by means of the impact characterization diagram and the complete analytical impact models.
- Given a stacking sequence, the dissipated energy or the damage developed is the same between impacts with equal impact energy. In addition, the residual compressive strength remains constant under the same impact energy level. This result agrees with some of the guidelines provided by the aeronautical industry for a drop-weight impact test, where the energy is specified, and the impactor mass and the velocity can be selected freely by the engineer.

Effect of ply thickness (clustering)

- If the ply clustering is increased, under equal impact conditions the values of F_d and F_{max} are reduced.
- Increasing the ply clustering, the changes in the stiffness during the impact are more progressive and smooth when compared with laminates with thin plies. This result implies difficulties in the detection of F_d for laminates with thick plies.
- The response is elongated by increasing the ply clustering of the laminate. This result indicates that more damage develops for laminates with thick plies. Accordingly, by reducing the number of interfaces available for delamination, the resulting projected delamination area is increased. Therefore, ply clustering results in a lower damage resistance of a composite structure.
- Increasing the ply clustering, the indentation is increased.
- The free growth of the delaminations can be affected by the finite in-plane dimensions of the plates. In other words, the growth of the delaminations could be braked by the clamping system. This effect occurs basically in laminates with thick plies.
- The trend of the proposed analytical thresholds for delamination are in agreement with the experimental points for all laminate types. However, the analytical values under-predict the real values. This offset can be due to scattering of the material properties or to the assumptions considered in the formulation of the damage threshold, e.g. strain rate effects are neglected. Further testing is required to verify these arguments, especially with critical impact energies which generate maximum impact forces similar to the damage threshold loads.
- The damage tolerance, quantified using the residual compressive load, is not affected by increasing the ply thickness, because all presented laminate types have shown similar values of compressive loads at each impact energy.

Effect of ply mismatch angle at interfaces

- The analytical prediction of F_d for the selected cross-ply laminate has been in agreement with the experimental result, although an offset also has appeared.
- The mismatch angle of the interfaces for delamination has not presented a clear effect on the damage resistance and on the damage tolerance. This result can be due to the fact that the plate thicknesses of the selected laminates for this study are slightly different.

Effect of the laminate thickness

- Increasing the laminate thickness, the response is faster and the drop in the impact force from point F_d increases. For the thinner laminate tested, the profiles of the impact force are smooth and do not present a clear first drop on the impact force. This result could mean that a sudden loss of stiffness from the point F_d does not occur, or the matrix and delamination damage that appear do not change the response of the impact, rather it is affected by progressive fiber breakage. This last argument can be related to the membrane effects.
- The predictions of the threshold load F_d for the different laminates considered have been in agreement except for the thinner laminate, i.e. L01. This result can be attributed to different causes: the membrane effects, the possibility that really the delaminations can not be detected in the force histories, or the fact that simply a sudden large delamination does not occur and rather the delaminations grow progressively.
- Increasing the laminate thickness, the damage resistance is improved since the energy dissipated is lower than for thin laminates. Likewise, the damage tolerance is improved. However, the resulting structures are heavier and more expensive.







Usefulness of the analytical impact models and analytical thresholds

- With the studies presented, it has been demonstrated that the analytical impact models for the prediction of the elastic response are a powerful tool: to

define a suitable test matrix of specimens, to obtain a qualitative understanding of the effects of the governing parameters on the impact response, and to interpret the experimental results obtained.

- The analytical impact models are completed with the analytical thresholds for the prediction of the damage mechanisms that can occur in a laminated composite plate under low-velocity impact loading. For low-velocity impacts, the most critical damage is the delamination. In general, it has been shown that the damage thresholds for delamination follow the trends of the experimental results. Table 4.14 summarizes the analytical and experimental thresholds obtained.

Table 4.14: Summary of analytical and experimental thresholds.

Laminate	Analytical F_d [kN]		Experimental F_d [kN]	C-scan shape
	F_{d1}^{stat}	F_{mc}^{ten}		
L01	3.16	2.68	3.90	
L02	8.53	10.34	9.94	
L03	8.49	7.20	7.60	
L04	8.34	4.92	5.50	
L05	15.97	23.80	19.33	
L06	10.65	11.26	12.21	

Chapter 5

Interlaminar damage model

5.1 Introduction

Delamination is one of the most common failure mechanisms in laminated composite materials and can appear at any life time of the structure (manufacturing, transportation, assembly, and service). Delamination reduces seriously the integrity of a structural element and can produce its collapse. Therefore, accurate analysis tools for the simulation of delamination are required.

Delamination has been largely studied and modeled in the literature. When material nonlinearities can be neglected and an initial crack is present, methods based on Linear Elastic Fracture Mechanics (LEFM) have been proven to be effective in predicting delamination growth, such as the Virtual Crack Closure Technique (Irwin [100]; Rybicki and Kanninen [101]; Raju [102]; Zou et al. [103]; Krueger [104]), the J-integral method (Rice [105]), the virtual crack extension (Hellen [106]), and the stiffness derivative (Parks [107]). These techniques are used to calculate the components of the energy release rate. Delamination growth is predicted when a combination of the components of the energy release rate is equal to, or greater than, a critical value (Griffith [108]).

When no initial macroscopic defects are present, a local approach has been frequently used to detect delamination onset, in which the key parameters are critical values of tractions (e.g. Pagano and Pipes [109], and Hashin [110]).

Another approach for delamination modeling can be developed within the framework of Damage Mechanics. Models formulated using Damage Mechanics considers

an interface as a third independent material defined by its own constitutive law. This interface links the two structural components and is based on the concept of the cohesive crack model introduced by Barenblatt [111], Dugdale [112], Hillerborg et al. [113] and others: a cohesive damage zone or softening plasticity is developed near the crack front. Cohesive damage zone models relate tractions to displacement jumps at an interface where a crack may occur. Damage initiation is related to the interfacial strength (i.e. the maximum traction on the traction-displacement jump relation). When the area under the traction-displacement jump relation is equal to the fracture toughness, the traction is reduced to zero and new crack surfaces are formed. The use of cohesive models is extremely powerful for the simulation of general fracture processes due to its simplicity and the unification of crack initiation and growth within one model.

The implementation of cohesive constitutive models normally is carried out by means of user-written subroutines in finite element codes. Generally, the examples presented in the literature implement cohesive elements (e.g. Schellekens and De Borst [114], Allix et al. [115], Mi et al. [116], Alfano and Crisfield [117], Camanho et al. [118], and De Borst [119]) or a user material definition (e.g. Pinho et al. [120], Iannucci [121], and Aymerich et al. [122]), although surface-based cohesive behaviors which eliminate the need to define cohesive elements have been also implemented (e.g. Zhang et al. [123], and Abaqus 6.8 [124]).

In cases where crack path is known in advance, either from experimental evidence, or because of the material configuration, discrete interface elements equipped with a cohesive constitutive relation are inserted a priori in the finite element mesh (e.g. Corigliano and Allix [125]). To allow for a more arbitrary direction of crack propagation, interface elements can be inserted between all continuum elements (Xu and Needleman [126]). However, this approach is limited to a number of predefined orientation crack angles since the interface elements are aligned with the element boundaries. Some authors (e.g. Martha et al. [127], and De Borst [119]) use meshing tools to redefine the position of cohesive elements in function of the stress state evolution. When the position for the appearance and progression of a crack is detected, the structure is again meshed and an interface element is located in a proper position. Alternatively, another research line in fracture modeling is to improve the kinematic description of finite elements by enriching the shape functions by means

of adding degrees of freedom. Initially, these models consider a law which relates the stresses and the strains until damage localization is detected in one plane. At this point, the law is rewritten and relates stresses and crack opening. Some of these approaches are: elements with embedded discontinuities (e.g. Oliver [128]) based on the enhanced assumed strain (Simo and Rifai [129]), and extended finite elements (e.g. Belytschko et al. [130]) based on partition of unity method (Babuska and Melenk [131]).

In the formulation of cohesive models, the energy dissipated during the crack opening has to be controlled, i.e. it is necessary to assure that the model satisfies the Clausius-Duhem inequality. Some models are well suited to simulate delamination under constant mixed-mode conditions, such as Mi et al. [116], Alfano and Crisfield [117]. However, these models do not satisfy the Clausius-Duhem inequality when the crack grows in variable mixed-mode conditions, because generally they define the damage threshold parameter as the maximum displacement and the damage variable as a function of material parameters that depend on the mixed-mode ratio. Examples of cohesive models which develop in a thermodynamically consistent way are Ortiz and Pandolfi [132], and Jansson and Larsson [133].

Turon et al. [9] proposed a thermodynamically consistent damage model for the simulation of progressive delamination in composite materials under variable mixed-mode ratio. The constitutive law follows a bilinear relationship between relative displacements and tractions at the interface, and it is defined by using a delamination onset and propagation criteria. The delamination onset criterion is based on energy terms and is proposed so the model formulation accounts for loading mode changes in a consistent thermodynamically way. The formulation also accounts for crack closure effects to avoid interfacial penetration of two adjacent layers. This model was implemented by using a user element subroutine called UEL. The zero-thickness cohesive element was focused for implicit analysis in Abaqus finite element software [124].

Some structural problems cannot be solved by using an implicit finite element code due to convergence difficulties related to material softening. To avoid these difficulties an explicit code should be used. An implicit analysis requires the assembly of the global stiffness matrix and its subsequent inversion to solve the equilibrium equations system for each iteration, whereas with an explicit analysis these opera-

tions are not necessary. Explicit integration schemes do not require the solution of a global set of equilibrium equations as the accelerations, velocities and displacements are calculated explicitly at each node recurring to a simple central differences rule applied over a time increment. Consequently, the explicit formulation is often proper in cases where severe changes in stiffness matrix occur, such as analysis with failure or degradation of the material. Other applications where explicit code is recommended and implicit analysis may lead to severe convergence difficulties are problems with complex contacts, post-buckling, and high-speed dynamic events such as impact. Explicit codes can also be used to solve problems that are essentially static by controlling some simulation variables, such as the kinetic energy that must be less than 5% of the internal energy of the system [124].

In this chapter, a modified formulation and implementation in an explicit finite element code of the cohesive model originally developed by Turon et al. [9] are presented. The model is implemented by using a user-written material subroutine, called VUMAT [124]. The user material developed is defined on sets of elements that represent the possible location for delamination. The elements can be selected to have zero-thickness (surface elements) or non-zero-thickness (continuum elements). The possibility of using continuum-based cohesive elements enables the simulation of an interface with non negligible thickness. Therefore, the macroscopic properties of the interface material, such as stiffness and strength, can be measured experimentally and used directly in the cohesive model.

In the literature, there are also available cohesive models implemented in a user-written material subroutine for explicit finite element analysis. Generally, these models are checked by simulating quasi-static standard delamination toughness tests, and a simulation of delamination in a monolithic laminated composite plate subjected to low-velocity impact is presented as the most challenging application. Under impact loading, delamination growth develops under variable mixed-mode conditions, and this phenomenon must be accounted properly in the cohesive model. However, the formulations available in the literature often do not control the crack growth in a consistent thermodynamically way.

The goal of the work detailed in this chapter is to apply the proposed model for the explicit simulation of low-velocity impact events on laminated composite plates. Loading rate effects as well as frictional effects that occur when complete separation

of the interface takes place, are not considered in the formulation.

The content of this chapter is structured as follows: first, the updated formulation of the cohesive model given by Turon et al. [9] is presented. Next, the adaptations of the formulation to be implemented in a continuum interface are described. After, the implementation of the model in a user-written material is also explained in detail. Finally, the numerical predictions of interlaminar fracture tests of polymer-based composite materials are compared with experimental data in order to validate the model.

5.2 Damage model formulation

The main aspects of the delamination model proposed by Turon et al. [9] are presented in this section with some modifications of the original formulation.

The constitutive law used is shown in Figure 5.1. This law is a bilinear relationship between relative displacements and tractions. The first line represents an elastic relationship, prior to damage onset. Damage onset is related to the interface strength τ^o . When the area under the traction-displacement relation is equal to the fracture toughness, \mathcal{G}_c , the interface tractions revert to zero and a new crack surface is created.

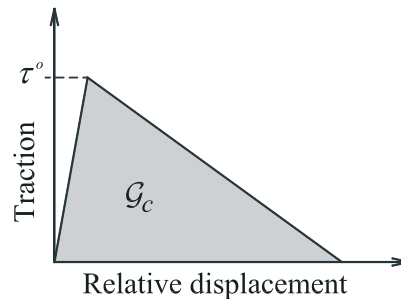


Figure 5.1: Bilinear constitutive law.

The different relative displacements between the nodes of a surface element are shown in Figure 5.2, where each displacement is directly associated with the corresponding propagation mode by assuming that the crack front is located at the indicated line. At finite element scale level, it is not possible to distinguish the

shear modes II and III because the crack front is in fact unknown. For this reason, shear modes are generally grouped together in the formulation of the cohesive models (see Section 5.2.1).

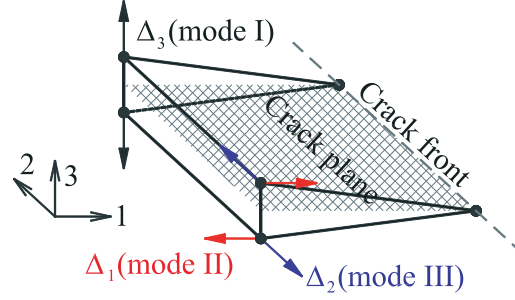


Figure 5.2: Propagation modes.

The damage model follows the general formulation of continuum damage models proposed by Mazars [134], and Simo and Ju [135]. The Helmholtz free energy by surface unit of the interface under isothermal conditions is defined as:

$$\Psi(\Delta_i, d) = (1 - d) \Psi^o(\Delta_i); \quad i = 1, 2, 3 \quad (5.1)$$

where d is the scalar isotropic damage variable and $\Psi^o(\Delta_i)$ is a function of the relative displacement space defined as:

$$\Psi^o(\Delta_i) = \frac{1}{2} \Delta_i D_{ij}^o \Delta_j; \quad i, j = 1, 2, 3 \quad (5.2)$$

Equation (5.1) indicates that the relative displacement components, Δ_i , are the free variables of the system (i.e. displacement driven formulation), and d is the internal variable that ensures the irreversibility of the model.

Negative values of Δ_3 (mode I) have no physical sense because the cracks are closed and no damage is produced. Therefore, the damage model has a unilateral behavior for this propagation mode, which means that the damage variable can be activated or deactivated as a function of the loading state. Therefore, Equation (5.1) is modified as:

$$\Psi(\Delta_i, d) = (1 - d) \Psi^o(\Delta_i) - d \Psi^o(\delta_{3i} \langle -\Delta_3 \rangle); \quad i = 1, 2, 3 \quad (5.3)$$

where $\langle x \rangle$ is the Macaulay brackets defined as $\langle x \rangle := \frac{1}{2}(x + |x|)$, and δ_{ij} is the Kronecker delta.

Applying Coleman method [135], the constitutive equation reads:

$$\tau_i = \frac{\partial \Psi}{\partial \Delta_i} = (1 - d) D_{ij}^o \Delta_j - d D_{ij}^o \delta_{3j} \langle -\Delta_3 \rangle; \quad i, j = 1, 2, 3 \quad (5.4)$$

D_{ij}^o is the undamaged stiffness tensor, defined as:

$$D_{ij}^o = \delta_{ij} K; \quad i, j = 1, 2, 3 \quad (5.5)$$

where K is a scalar parameter corresponding to the slope of the first line in the constitutive law, typically called penalty stiffness. As Equation (5.5) shows, the penalty stiffness is the same for any propagation mode.

To ensure the thermodynamic consistency of the model, the dissipated energy by surface unit during the damage propagation process, Ξ , has to be equal or greater than zero:

$$\Xi = Y \dot{d} \geq 0 \quad (5.6)$$

where the thermodynamic force Y associated with the internal variable d is defined as:

$$Y = -\frac{\partial \Psi}{\partial d} \quad (5.7)$$

The value of the damage variable has to be evaluated at each time increment during the loading process. Therefore, it is necessary to define a suitable norm of the relative displacement vector, the surface for damage activation, a law for damage evolution, and criteria for damage onset and damage propagation.

5.2.1 Norm of the relative displacement vector

The selected norm of the relative displacement components is defined as:

$$\lambda = \sqrt{\langle \Delta_3 \rangle^2 + \Delta_{shear}^2} \quad (5.8)$$

where Δ_3 is the relative displacement in mode I, and Δ_{shear} is the Euclidian norm of the relative displacements in mode II and mode III:

$$\Delta_{shear} = \sqrt{\Delta_1^2 + \Delta_2^2} \quad (5.9)$$

Normally, the shear modes II and III are represented together because their individual evaluation depends on the relative displacement between homologous nodes with respect to the crack front orientation. Since at finite element scale level the crack orientation is generally unknown, it is not possible to distinguish between modes II and III.

5.2.2 Surface of damage activation and law for damage evolution

The surface of damage activation from Turon et al. [9] is modified by the expression:

$$F(\mathbf{\Delta}_t, d_t) = G(\mathbf{\Delta}_t) - d_t \leq 0 \quad \forall t \geq 0 \quad (5.10)$$

where $G(\mathbf{\Delta}_t)$ is a monotonic loading function which depends on the relative displacement vector $\mathbf{\Delta} = \{\Delta_1, \Delta_2, \Delta_3\}^T$ at time t , and d_t is the damage variable at time t which is used as the threshold function.

The evolution of the damage variable is defined by means of the Kuhn-Tucker constraints which provide the formulation of the loading-unloading-reloading conditions as [136]:

$$\dot{d} \geq 0; \quad F(\mathbf{\Delta}_t, d_t) \leq 0; \quad \dot{d}F(\mathbf{\Delta}_t, d_t) = 0 \quad \forall t \geq 0 \quad (5.11)$$

On the other hand, to ensure that the surface of damage activation will grow as much as the internal variable grows, the persistence (or consistency) condition is required. This is:

$$F(\mathbf{\Delta}_t, d_t) = 0 \Rightarrow \dot{F}(\mathbf{\Delta}_t, d_t) = 0 \quad \forall t \geq 0 \quad (5.12)$$

Therefore, the damage variable d_t is explicitly defined by:

$$d_t = \max \left\{ 0, \max_s (G(\Delta_t)) \right\} \quad 0 \leq s \leq t \quad \forall t \geq 0 \quad (5.13)$$

which fully describes the evolution of the internal variable for any loading-unloading-reloading situation. On the other hand, by using the constitutive equation (see Figure 5.3) for any mixed-mode ratio β (see Equation (5.21)), the function $G(\Delta_t)$ is defined as:

$$G(\Delta_t) = \min \left\{ \frac{\Delta_t^f (\lambda_t - \Delta_t^o)}{\lambda_t (\Delta_t^f - \Delta_t^o)}, 1 \right\} \quad \forall t \geq 0 \quad (5.14)$$

Equation (5.14) defines the loading function by means of the bilinear constitutive equation, where Δ_t^o and Δ_t^f are the onset and propagation damage parameters at time t , respectively. The values of Δ^o and Δ^f are obtained by means of the onset and propagation damage criteria, respectively. These values will be constant unless the mixed-mode ratio changes. The variables used in Equation (5.14) are identified in Figure 5.3.

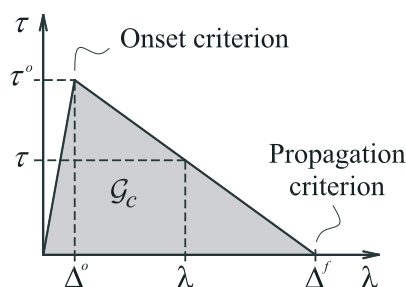


Figure 5.3: Parameters of the bilinear constitutive equation.

5.2.3 Criterion for damage propagation

The propagation criterion for delamination growth under mixed-mode loading conditions is established in terms of energy release rates and fracture toughnesses. The criterion is based on the work of Benzeggagh and Kenane [137], and was originally defined for mixed-mode I and II:

$$\mathcal{G}_c = \mathcal{G}_{Ic} + (\mathcal{G}_{IIc} - \mathcal{G}_{Ic}) \left(\frac{\mathcal{G}_{II}}{\mathcal{G}_I + \mathcal{G}_{II}} \right)^\eta \quad (5.15)$$

where \mathcal{G}_{Ic} and \mathcal{G}_{IIc} are the fracture toughnesses in mode I and II, respectively; \mathcal{G}_I and \mathcal{G}_{II} are the energy release rates in mode I and II, respectively. The η parameter is found by least-square fit of experimental data points of the fracture toughnesses under different mixed-mode ratios.

The propagation criterion can be rewritten as follows:

$$\mathcal{G}_c = \mathcal{G}_{Ic} + (\mathcal{G}_{shear_c} - \mathcal{G}_{Ic}) \left(\frac{\mathcal{G}_{shear}}{\mathcal{G}_I + \mathcal{G}_{shear}} \right)^\eta \quad (5.16)$$

where \mathcal{G}_{shear} and \mathcal{G}_{shear_c} are the shear energy release rate and the pure mode II fracture toughness, respectively. The expressions of \mathcal{G}_{shear} and \mathcal{G}_{shear_c} are defined by Equations (5.17) and (5.18), respectively [118].

$$\mathcal{G}_{shear} = \mathcal{G}_{II} + \mathcal{G}_{III} \quad (5.17)$$

$$\mathcal{G}_{shear_c} = \mathcal{G}_{IIc} (= \mathcal{G}_{IIIc}) \quad (5.18)$$

Equation (5.17) is valid whenever the constitutive equations of modes II and III are equal. This hypothesis is very common because the fracture toughness of mode III is difficult to obtain and typically it is considered equal to \mathcal{G}_{IIc} .

On the other hand, Equation (5.18) ensures that the propagation criterion is consistent for pure mode loading cases II or III. As in the case of Equation (5.17), Equation (5.18) means that the constitutive equations for mode II and III are equal.

The ratio of the second term of Equation (5.16) defines the parameter B :

$$B = \frac{\mathcal{G}_{shear}}{\mathcal{G}_I + \mathcal{G}_{shear}} \quad (5.19)$$

The mixed-mode ratio β defined by Turon et al. [9] is given by:

$$\beta = \frac{\Delta_{shear}}{\langle \Delta_3 \rangle + \Delta_{shear}} \quad (5.20)$$

However, the definition of β is changed by Equation (5.21), which allows the B parameter to be equal to β by developing Equation (5.19) and considering the same penalty stiffness for all propagation modes.

$$\beta = \frac{\Delta_{shear}^2}{\langle \Delta_3 \rangle^2 + \Delta_{shear}^2} = \frac{\Delta_{shear}^2}{\lambda^2} \quad (5.21)$$

Finally, the propagation criterion defined in relative displacement terms can be obtained by means of Equation (5.16) and by knowing that the crack propagates when the fracture energy release rate is equal to the critical value. In other words, by using Equation (5.22) (deduced by means of Equation (5.16) and Equation (5.23)), the propagation criterion yields to Equation (5.24).

$$\mathcal{G}_c(\beta) = \frac{1}{2}K\Delta_3^o\Delta_3^f + \left(\frac{1}{2}K\Delta_{shear}^o\Delta_{shear}^f - \frac{1}{2}K\Delta_3^o\Delta_3^f \right) \beta^\eta \quad (5.22)$$

$$\mathcal{G}_c(\beta) = \frac{1}{2}K\Delta^o\Delta^f \quad (5.23)$$

$$\Delta^f = \frac{\Delta_3^o\Delta_3^f + \left(\Delta_{shear}^o\Delta_{shear}^f - \Delta_3^o\Delta_3^f \right) \beta^\eta}{\Delta^o} \quad (5.24)$$

Δ_3^o and Δ_{shear}^o are the relative displacements for damage onset in pure mode I and shear mode respectively, and Δ_3^f and Δ_{shear}^f are the relative displacements for damage propagation in pure mode I and shear mode respectively. The parameter Δ^o is the displacement for damage onset, and it is determined by means of the damage initiation criterion. Normally, the damage propagation criterion is formulated independently of the initiation criterion. However, Equation (5.24) shows that both criteria are linked in this model.

5.2.4 Criterion for damage onset

In this model, the criterion for damage onset is assumed the same as the applied criterion for damage propagation. This means that the onset damage criterion is also based on energy terms, which is a different characteristic of the usual cohesive damage formulations where a stress-based criterion is used. The models that account for the interaction of the stress components are usually based on Ye criterion [138].

However, experimental data of material strengths for the initiation of delamination under mixed-mode loading are not really available, and consequently, these failure criteria do not have been fully validated.

Therefore, by replacing in Equation (5.16) only the elastic energy terms of the constitutive equation, Equation (5.25) is obtained which is finally equalled to Equation (5.26) in order to find the criterion for damage onset defined in terms of relative displacements (Equation (5.27)).

$$\mathcal{G}^o(\beta) = \frac{1}{2}K(\Delta_3^o)^2 + \left(\frac{1}{2}K(\Delta_{shear}^o)^2 - \frac{1}{2}K(\Delta_3^o)^2 \right) \beta^\eta \quad (5.25)$$

$$\Psi^o(\beta) = \frac{1}{2}K(\Delta^o)^2 \quad (5.26)$$

$$\Delta^o = \left((\Delta_3^o)^2 + ((\Delta_{shear}^o)^2 - (\Delta_3^o)^2) \beta^\eta \right)^{\frac{1}{2}} \quad (5.27)$$

5.3 Formulation adaptations

Having formulated a cohesive model for zero-thickness elements, the required modifications to enable also the use of non-zero-thickness elements (i.e. continuum elements) are described in this section.

5.3.1 Relation between relative displacements and strains

If a continuum element is used, the input data are not the relative displacements, but the strain tensor. Therefore, to model a cohesive continuum model with softening, the relative displacement Δ_i and the corresponding strain component ε_{ij} can be related by means of the expression:

$$\Delta_i = h_e \varepsilon_{ij} n_j (2 - \delta_{3i}); \quad i, j = 1, 2, 3 \quad (5.28)$$

where h_e is the element thickness, and n_j is the corresponding component of the unitary normal vector to the crack plane, $\mathbf{n} = \{0, 0, 1\}^T$ (see Figure 5.2).

As explained in the model formulation, the area under the constitutive equation g_e defined by stresses and relative displacements is directly the fracture toughness

of the material \mathcal{G}_c . However, if the constitutive model is defined in terms of stresses and strains, the law has to be adjusted in function of the element thickness h_e . Then, the resultant area g_e is the dissipated energy by unit of volume at the corresponding integration point of the finite element. This energy is equal to the fracture toughness of the material divided by the finite element thickness (see Equation (5.29)). This approach follows the called Crack Band Model suggested by Bažant and Oh [139], which is the procedure normally used to ensure the correct energy dissipation and mesh independency in continuum damage models.

$$\mathcal{G}_c A_{crack} = g_e (A_{crack} h_e) \quad \Rightarrow \quad g_e = \frac{\mathcal{G}_c}{h_e} \quad (5.29)$$

The dissipated energies for each case are illustrated in Figure 5.4.

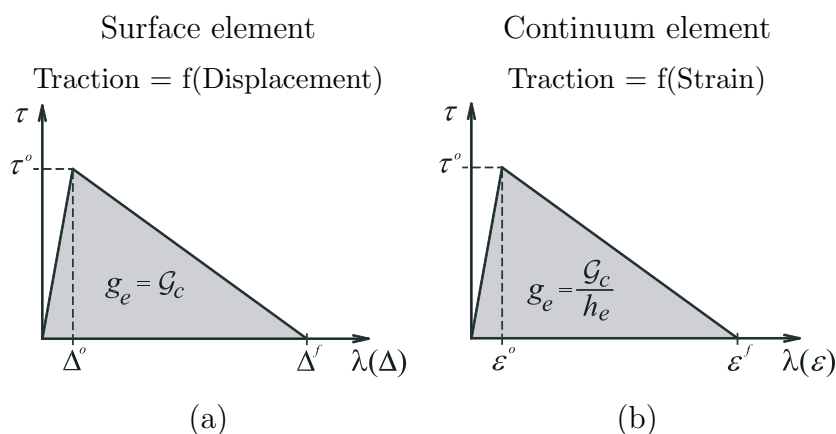


Figure 5.4: Constitutive charts defined by: (a) stresses and relative displacements, or by (b) stresses and strains.

5.3.2 Penalty stiffness

If cohesive volumetric elements are used, the penalty stiffness is here varied in function of the mixed-mode ratio. Its definition can be done in function of the element thickness and the elastic properties of the modeled interface material [115]. In particular, Equation (5.30) defines the penalty stiffness for pure mode I, and Equation (5.31) defines the penalty stiffness for pure modes II or III (shear):

$$K_1 = \frac{E_m}{h_e} \quad (5.30)$$

$$K_2 = \frac{G_m}{h_e} \quad (5.31)$$

where E_m is the Young modulus and G_m is the shear elastic modulus of the interface material. Normally, the elastic properties of the interface material are considered as the neat material, although it is generally not true [125].

For surface cohesive elements, the penalty stiffness is selected with a fixed value for all mixed-mode ratios. Ideally, the value of the penalty stiffness is infinite because these elements do not have thickness, and then they do not affect the compliance of the whole structure [140]. However, too high value of the interface stiffness can generate numerical problems such as the generation of spurious oscillations in the tractions of the element [114]. Therefore, a suitable value of the penalty stiffness should be selected in order to provide a reasonable stiffness without generating numerical problems. Based in mechanical considerations, Turon et al. [12] proposed Equation (5.32) in order to estimate the interface stiffness K for mode I crack propagation.

$$K = \frac{\alpha E_3}{h_a} \quad (5.32)$$

where E_3 is the elastic modulus through-the-thickness of the composite material, α is an increasing parameter (normally it is taken about $\alpha \approx 50$), and h_a is the laminate thickness adjoining to the cohesive element. Equation (5.32) also can be developed for shear modes, by replacing E_3 by the shear elastic modulus. However, since the model formulation for surface elements assumes the same penalty stiffness for each mixed-mode ratio, Equation (5.32) is used for all cases because it gives the biggest value.

5.3.3 Redefined onset and propagation damage criteria

Since the penalty stiffness for the volumetric elements is a function of the mixed-mode ratio, the onset and propagation damage criteria written in terms of relative displacements must be redefined. However, the procedure used in Sections 5.2.3

and 5.2.4 to find these expressions can not be exactly applied here because the function which describes the variation of the penalty stiffness under a determined mixed-mode ratio is unknown.

In order to find the onset criterion, Equation (5.33) is used. This equation is the damage criterion with the corresponding elastic energy terms replaced (i.e. Equation (5.25) with different penalty stiffness for pure mode I and pure shear mode). On the other hand, Equation (5.34) represents the elastic energy of the constitutive equation defined in terms of relative displacements of pure mode I, $\Delta_3^o(\beta)$, and pure shear mode, $\Delta_{shear}^o(\beta)$, for damage onset in a determined mixed-mode ratio.

$$\mathcal{G}^o(\beta) = \frac{1}{2}K_1(\Delta_3^o)^2 + \left(\frac{1}{2}K_2(\Delta_{shear}^o)^2 - \frac{1}{2}K_1(\Delta_3^o)^2 \right) B^n \quad (5.33)$$

$$\Psi^o(\beta) = \frac{1}{2}K_1 \langle \Delta_3^o(\beta) \rangle^2 + \frac{1}{2}K_2 (\Delta_{shear}^o(\beta))^2 \quad (5.34)$$

Using Equation (5.33) and (5.34), and the selected definition of the mixed-mode ratio (Equation (5.21)), the terms $\Delta_3^o(\beta)$ and $\Delta_{shear}^o(\beta)$ can be found:

$$\langle \Delta_3^o(\beta) \rangle = \left(\frac{2\mathcal{G}^o(\beta)}{K_1 + \left(\frac{\beta}{1-\beta} \right) K_2} \right)^{\frac{1}{2}} \quad (5.35)$$

$$\Delta_{shear}^o(\beta) = \left(\frac{\beta}{1-\beta} \right)^{\frac{1}{2}} \langle \Delta_3^o(\beta) \rangle \quad (5.36)$$

Finally, the onset damage criterion is obtained by taking the Euclidian norm of the relative displacements described by Equations (5.35) and (5.36) (see Section 5.2.1):

$$\Delta^o = \left(\langle \Delta_3^o(\beta) \rangle^2 + (\Delta_{shear}^o(\beta))^2 \right)^{\frac{1}{2}} \quad (5.37)$$

In the same sense, the propagation damage criterion can be deduced. In this case, Equation (5.38) represents the damage criterion with the corresponding pure fracture toughness terms replaced (i.e. Equation (5.22) with different penalty stiffness for pure mode I and pure shear mode). On the other hand, Equation (5.39) is the fracture toughness for a given mixed-mode ratio defined in terms of relative

displacements for damage onset in pure modes I and shear, $\Delta_3^o(\beta)$ and $\Delta_{shear}^o(\beta)$, and for damage propagation, $\Delta_3^f(\beta)$ and $\Delta_{shear}^f(\beta)$.

$$\mathcal{G}_c(\beta) = \frac{1}{2}K_1\Delta_3^o\Delta_3^f + \left(\frac{1}{2}K_2\Delta_{shear}^o\Delta_{shear}^f - \frac{1}{2}K_1\Delta_3^o\Delta_3^f\right)B^\eta \quad (5.38)$$

$$\mathcal{G}_c(\beta) = \frac{1}{2}K_1\langle\Delta_3^o(\beta)\rangle\langle\Delta_3^f(\beta)\rangle + \frac{1}{2}K_2(\Delta_{shear}^o(\beta))(\Delta_{shear}^f(\beta)) \quad (5.39)$$

where $\Delta_3^o(\beta)$ and $\Delta_{shear}^o(\beta)$ are previously found by means of Equations (5.35) and (5.36).

Equalling Equations (5.38) and (5.39), and using again the definition of the mixed-mode ratio (Equation (5.21)), the terms $\Delta_3^f(\beta)$ and $\Delta_{shear}^f(\beta)$ can be found:

$$\langle\Delta_3^f(\beta)\rangle = \frac{K_1(1-B^\eta)\Delta_3^o\Delta_3^f + K_2B^\eta\Delta_{shear}^o\Delta_{shear}^f}{\langle\Delta_3^o(\beta)\rangle\left(K_1 + \left(\frac{\beta}{1-\beta}\right)K_2\right)} \quad (5.40)$$

$$\Delta_{shear}^f(\beta) = \left(\frac{\beta}{1-\beta}\right)^{\frac{1}{2}}\langle\Delta_3^f(\beta)\rangle \quad (5.41)$$

Finally, the propagation damage criterion is obtained by making the Euclidian norm of the relative displacements described by Equations (5.40) and (5.41) (see Section 5.2.1):

$$\Delta^f = \left(\langle\Delta_3^f(\beta)\rangle^2 + \left(\Delta_{shear}^f(\beta)\right)^2\right)^{\frac{1}{2}} \quad (5.42)$$

It should be noted that the B parameter must be redefined by Equation (5.43), since the penalty stiffnesses in pure mode I and shear modes are different and then they can not be simplified.

$$B = \frac{K_2\beta}{K_2\beta + K_1(1-\beta)} \quad (5.43)$$

If Equations (5.30) and (5.31) are replaced in Equation (5.43), the B parameter can be also defined in function of the elastic properties considered for the interface material. That is:

$$B = \frac{G_m\beta}{G_m\beta + E_m(1-\beta)} \quad (5.44)$$

5.4 Model implementation

5.4.1 Strategy of implementation

The delamination model presented by Turon et al. [9] was implemented in a user-written element subroutine called UEL [124]. This implementation was used to simulate problems in an implicit finite element code. However, the model formulated in Sections 5.2 and 5.3 is here implemented in a user-written material subroutine, called VUMAT, assigned for explicit finite element analysis.

The user material implemented has to be defined on sets of elements which represent the delamination layers. These elements can be zero-thickness (i.e. surface elements) or non-zero-thickness (i.e. continuum elements) types. In particular, when a zero-thickness interface is used, in-plane cohesive elements with four integration points of the Abaqus element library must be used [122]. This element is called COH3D8. However, when non-zero-thickness interface is desired, any tri-dimensional solid element can be applied.

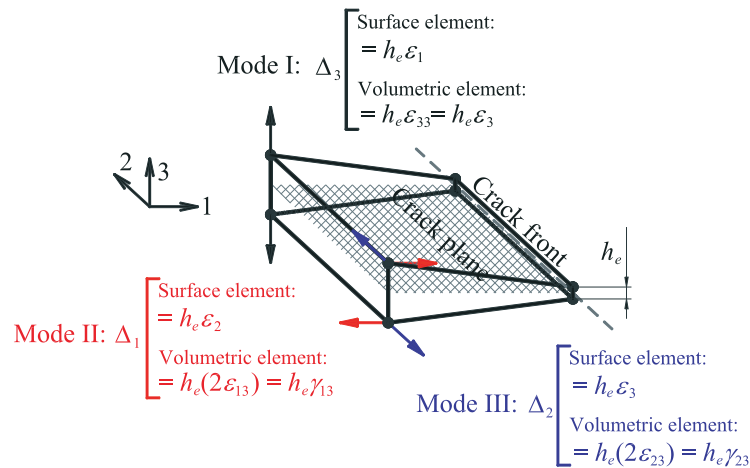


Figure 5.5: Transformations from strains to relative displacements for each propagation mode.

When surface elements are used, the input data given by the finite element software to the user material subroutine is directly the increment of the relative displacement vector, whereas the input data for continuum elements is the increment of the strain tensor. In order to use the same subroutine for both element

types, Equation (5.28) is applied to transform easily the corresponding strain tensor components to relative displacements (see Figure 5.5). On the other hand, if surface elements are used, a constitutive thickness equal to the unity has to be introduced in the user material subroutine which ensures that the strains are equal to the relative displacements.

5.4.2 Input variables to define the model

The parameters required to define completely the model in a user material subroutine are described below:

- Elastic properties (isotropic) and density of the interface material: E_m , ν_m and ρ_m .

By means of E_m and ν_m the value of G_m can be calculated by using Equation (5.45). If surface elements are used, normally the value of E_m is taken between 10^5 and $5 \times 10^6 \text{Nmm}^{-3}$ for a sub-laminate thickness between 0.125mm and 5mm [12], and the Poisson coefficient ν_m must be equal to -0.5 in order to obtain the same penalty stiffness for all mixed-mode ratios.

$$G_m = \frac{E_m}{2(1 + \nu_m)} \quad (5.45)$$

- Thickness of the interface cohesive element: h_e .

If surface elements are used, the value of the constitutive thickness introduced in the subroutine must be equal to the unity (although the geometrical thickness defined in the model is equal to zero).

- Interface strengths for pure mode I and pure shear modes (II and III): τ_3^o and τ_1^o .

By means of the interface strengths, the relative displacements which give the damage onset for pure mode loading cases are obtained. The corresponding equations are:

$$\Delta_3^o = \frac{\tau_3^o}{K_1} \quad (5.46)$$

$$\Delta_{shear}^o = \frac{\tau_1^o}{K_2} \quad (5.47)$$

- Interface fracture toughness for pure mode I and shear modes (II and III): \mathcal{G}_{Ic} and \mathcal{G}_{IIc} .

The relative displacements which give the damage propagation for pure mode loading cases are obtained by means of pure mode fracture toughnesses. The corresponding equations are:

$$\Delta_3^f = \frac{2\mathcal{G}_{Ic}}{K_1\Delta_3^o} = \frac{2\mathcal{G}_{Ic}}{\tau_3^o} \quad (5.48)$$

$$\Delta_{shear}^f = \frac{2\mathcal{G}_{IIc}}{K_2\Delta_{shear}^o} = \frac{2\mathcal{G}_{IIc}}{\tau_1^o} \quad (5.49)$$

- Parameter of the least-square fit: η .

The experimental data used to calculate η can be obtained from MMB tests (Mixed-Mode Bending) at different mode ratios.

In a recent paper of Turon et al. [13], it was detected that changes in the local mode ratio during the evolution of damage under mixed-mode loading can cause errors in the determination of the energy dissipation and result in inaccurate predictions of the global load-displacement response. This fact occurs even under conditions where, according to Linear Elastic Fracture Mechanics, the global mode ratio is constant (e.g. Mixed-Mode Bending Test (MMB)). This is a common difficulty in current formulations of the cohesive models. To solve this problem, an engineering solution which relates the interlaminar strengths was proposed. It was demonstrated that this relation yields to accurate predictions which ensures correct energy dissipations when delamination propagates. This relation is defined as:

$$\tau_1^o = \tau_3^o \sqrt{\frac{\mathcal{G}_{IIc}}{\mathcal{G}_{Ic}}} \quad (5.50)$$

Therefore, seven input parameters are necessary in order to feed on the present cohesive model: E_m , ν_m , ρ_m , h_e , τ_3^o , \mathcal{G}_{Ic} and \mathcal{G}_{IIc} .

5.4.3 Algorithm

After to read the input parameters and to calculate the model constants (see previous Sections 5.3.2 and 5.4.2), the steps of the algorithm which are repeated for each stable time increment δt are numbered below:

1. Calculate the strain components at time $t + \delta t$.

$$\varepsilon_{i_{t+\delta t}} = \varepsilon_{i_t} + \delta\varepsilon_{i_{t+\delta t}} \begin{cases} i = 1, \dots, 3 & \text{surface element} \\ i = 1, \dots, 6 & \text{volumetric element} \end{cases} \quad (5.51)$$

2. Calculate the relative displacements at time $t + \delta t$ for each propagation mode (see Figure 5.5).

$$\text{Mode I: } \Delta_{3_{t+\delta t}} = \begin{cases} h_e \varepsilon_{1_{t+\delta t}} & \text{surface element} \\ h_e \varepsilon_{3_{t+\delta t}} & \text{volumetric element} \end{cases} \quad (5.52)$$

$$\text{Mode II: } \Delta_{1_{t+\delta t}} = \begin{cases} h_e \varepsilon_{2_{t+\delta t}} & \text{surface element} \\ h_e \gamma_{13_{t+\delta t}} & \text{volumetric element} \end{cases} \quad (5.53)$$

$$\text{Mode III: } \Delta_{2_{t+\delta t}} = \begin{cases} h_e \varepsilon_{3_{t+\delta t}} & \text{surface element} \\ h_e \gamma_{23_{t+\delta t}} & \text{volumetric element} \end{cases} \quad (5.54)$$

3. Application of the damage model, where the following terms are calculated:

$$\Delta_{shear_{t+\delta t}} = \sqrt{\left(\Delta_{1_{t+\delta t}}\right)^2 + \left(\Delta_{2_{t+\delta t}}\right)^2} \quad (5.55)$$

$$\lambda_{t+\delta t} = \sqrt{\left\langle \Delta_{3_{t+\delta t}} \right\rangle^2 + \left(\Delta_{shear_{t+\delta t}}\right)^2} \quad (5.56)$$

$$\beta_{t+\delta t} = \frac{\Delta_{shear_{t+\delta t}}^2}{\left\langle \Delta_{3_{t+\delta t}} \right\rangle^2 + \Delta_{shear_{t+\delta t}}^2} \quad (5.57)$$

$$B_{t+\delta t} = \frac{K_2 \beta_{t+\delta t}}{K_2 \beta_{t+\delta t} + K_1 (1 - \beta_{t+\delta t})} \quad (5.58)$$

$$\langle \Delta_3^o(\beta) \rangle_{t+\delta t} = \left(\frac{K_1 (1 - B_{t+\delta t}^\eta) (\Delta_3^o)^2 + K_2 B_{t+\delta t}^\eta (\Delta_{shear}^o)^2}{K_1 + \left(\frac{\beta_{t+\delta t}}{1 - \beta_{t+\delta t}} \right) K_2} \right)^{\frac{1}{2}} \quad (5.59)$$

$$\langle \Delta_3^f(\beta) \rangle_{t+\delta t} = \frac{K_1 (1 - B_{t+\delta t}^\eta) \Delta_3^o \Delta_3^f + K_2 B_{t+\delta t}^\eta \Delta_{shear}^o \Delta_{shear}^f}{\langle \Delta_3^o(\beta) \rangle_{t+\delta t} \left(K_1 + \left(\frac{\beta_{t+\delta t}}{1 - \beta_{t+\delta t}} \right) K_2 \right)} \quad (5.60)$$

$$(\Delta_{shear}^o(\beta))_{t+\delta t} = \left(\frac{\beta_{t+\delta t}}{1 - \beta_{t+\delta t}} \right)^{\frac{1}{2}} \langle \Delta_3^o(\beta) \rangle_{t+\delta t} \quad (5.61)$$

$$(\Delta_{shear}^f(\beta))_{t+\delta t} = \left(\frac{\beta_{t+\delta t}}{1 - \beta_{t+\delta t}} \right)^{\frac{1}{2}} \langle \Delta_3^f(\beta) \rangle_{t+\delta t} \quad (5.62)$$

$$\Delta_{t+\delta t}^o = \left(\langle \Delta_3^o(\beta) \rangle_{t+\delta t}^2 + (\Delta_{shear}^o(\beta))_{t+\delta t}^2 \right)^{\frac{1}{2}} \quad (5.63)$$

$$\Delta_{t+\delta t}^f = \left(\langle \Delta_3^f(\beta) \rangle_{t+\delta t}^2 + (\Delta_{shear}^f(\beta))_{t+\delta t}^2 \right)^{\frac{1}{2}} \quad (5.64)$$

$$G(\Delta_{t+\delta t}) = \min \left\{ \frac{\Delta_{t+\delta t}^f (\lambda_{t+\delta t} - \Delta_{t+\delta t}^o)}{\lambda_{t+\delta t} (\Delta_{t+\delta t}^f - \Delta_{t+\delta t}^o)}, 1 \right\} \quad (5.65)$$

- If $G(\Delta_{t+\delta t}) \leq d_t \Rightarrow d_{t+\delta t} = d_t$: elastic reloading, unloading or neutral loading.
- If $G(\Delta_{t+\delta t}) > d_t \Rightarrow d_{t+\delta t} = G(\Delta_{t+\delta t})$: loading.

4. Calculate the stress vector at time $t + \delta t$:

$$\tau_{t+\delta t} = C_{t+\delta t} \varepsilon_{t+\delta t} \quad (5.66)$$

where:

- For surface elements:

$$C_{t+\delta t} = \begin{bmatrix} (1 - d_{t+\delta t}^*) E_m & 0 & 0 \\ 0 & (1 - d_{t+\delta t}) G_m & 0 \\ 0 & 0 & (1 - d_{t+\delta t}) G_m \end{bmatrix} \quad (5.67)$$

where:

$$d_{t+\delta t}^* = d_{t+\delta t} \frac{\langle \varepsilon_{1_{t+\delta t}} \rangle}{|\varepsilon_{1_{t+\delta t}}|} \quad (5.68)$$

- For volumetric elements:

$$C_{t+\delta t} = \begin{bmatrix} \frac{E_m(1-(1-d_{t+\delta t}^*)\nu_m^2)}{\Upsilon} & -\frac{\nu_m E_m(-1-(1-d_{t+\delta t}^*)\nu_m)}{\Upsilon} \\ -\frac{\nu_m E_m(-1-(1-d_{t+\delta t}^*)\nu_m)}{\Upsilon} & \frac{E_m(1-(1-d_{t+\delta t}^*)\nu_m^2)}{\Upsilon} \\ \frac{\nu_m E_m(1-d_{t+\delta t}^*)}{\Phi} & \frac{\nu_m E_m(1-d_{t+\delta t}^*)}{\Phi} \\ 0 & 0 \\ 0 & 0 \\ 0 & 0 \\ \frac{\nu_m E_m(1-d_{t+\delta t}^*)}{\Phi} & 0 & 0 & 0 \\ \frac{\nu_m E_m(1-d_{t+\delta t}^*)}{\Phi} & 0 & 0 & 0 \\ -\frac{E_m(1-d_{t+\delta t}^*)(1-\nu_m)}{\Phi} & 0 & 0 & 0 \\ 0 & G_m & 0 & 0 \\ 0 & 0 & (1 - d_{t+\delta t}) G_m & 0 \\ 0 & 0 & 0 & (1 - d_{t+\delta t}) G_m \end{bmatrix} \quad (5.69)$$

where:

$$\Phi = 1 - 2\nu_m^2 (1 - d_{t+\delta t}^*) - \nu_m \quad (5.70)$$

$$\Upsilon = 1 - 2\nu_m^3 (1 - d_{t+\delta t}^*) - \nu_m^2 (3 - 2d_{t+\delta t}^*) \quad (5.71)$$

$$d_{t+\delta t}^* = d_{t+\delta t} \frac{\langle \varepsilon_{3_{t+\delta t}} \rangle}{|\varepsilon_{3_{t+\delta t}}|} \quad (5.72)$$

5. Calculate the energy dissipated at time $t + \delta t$:

$$\Xi_{t+\delta t} = \Xi_t + \Xi_{\delta t} \quad (5.73)$$

where Ξ_t and $\Xi_{\delta t}$ are the accumulated and the increment of the dissipated energy, respectively. The determination of $\Xi_{\delta t}$ is given by Equation (5.74):

$$\begin{aligned} \Xi_{\delta t} = \frac{1}{2} \left(\frac{d_{t+\delta t} - d_t}{\delta t} \right) & \left(K_1 \left(\Delta_{3_{t+\delta t}}^2 + \Delta_{3_{t+\delta t}} \langle -\Delta_{3_{t+\delta t}} \rangle \right) \right. \\ & \left. + K_2 \left(\Delta_{1_{t+\delta t}}^2 + \Delta_{2_{t+\delta t}}^2 \right) \right) \end{aligned} \quad (5.74)$$

6. Calculate the free energy at time $t + \delta t$:

$$\begin{aligned} \Psi_{t+\delta t} = \frac{1}{2} \left((1 - d_{t+\delta t}) \left(K_2 \left(\Delta_{1_{t+\delta t}}^2 + \Delta_{2_{t+\delta t}}^2 \right) + K_1 \left(\Delta_{3_{t+\delta t}}^2 \right) \right) \right. \\ \left. - \frac{1}{2} d_{t+\delta t} K_1 \left(\Delta_{3_{t+\delta t}} \langle -\Delta_{3_{t+\delta t}} \rangle \right) \right) \end{aligned} \quad (5.75)$$

7. Calculate the internal energy at time $t + \delta t$:

$$E_{I_{t+\delta t}} = \Psi_{t+\delta t} + \Xi_{t+\delta t} \quad (5.76)$$

5.5 Size of cohesive elements

5.5.1 Maximum thickness of volumetric cohesive elements

For each mixed-mode ratio there is a maximum thickness of the cohesive elements in the direction perpendicular to the crack propagation plane. This is due to the fact that the propagation criterion defined in terms of relative displacements remains constant and the onset criterion changes whether the element thickness changes. The

reason of the onset criterion changes is due to the introduction of penalty stiffness dependency with element thickness (see Equations (5.30) and (5.31)). Since the onset criterion should be reached before the propagation criterion, equalizing both criteria for a given mixed-mode ratio β , the maximum cohesive thickness $(h_e)_{max}$ is obtained. The resulting equation which defines the maximum thickness of the cohesive element is:

$$(h_e)_{max} = \frac{2(\mathcal{G}_{Ic} + (\mathcal{G}_{IIc} - \mathcal{G}_{Ic})B^\eta)}{\frac{(\tau_3^o)^2}{E_m} + \left(\frac{(\tau_1^o)^2}{G_m} - \frac{(\tau_3^o)^2}{E_m}\right)B^\eta} \quad (5.77)$$

By means of Equation (5.77) it is possible to plot the variation of the maximum cohesive element thickness as a function of the mixed-mode ratio, which is included in parameter B by Equation (5.44). Taken into account the material properties shown in Tables 5.2 and 5.3, the evolution of the maximum thickness is plotted in Figure 5.6.

Equation (5.77) can also be obtained by using the onset and propagation criteria defined in terms of strains. In this case, the onset criterion remains constant versus the variations of the thickness, whereas the propagation criterion changes in order to assess the correct energy dissipation independently of the mesh size.

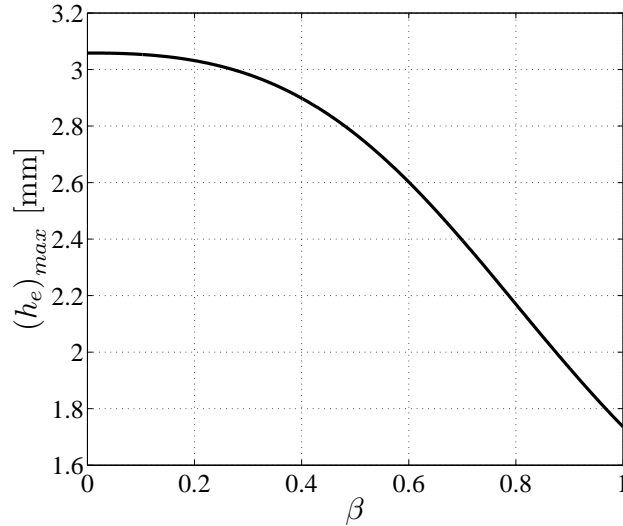


Figure 5.6: Evolution of the maximum element thickness in function of the mixed-mode ratio.

Normally, the cohesive element thickness is defined with a small value (e.g. between 0.001 and 0.1mm) and certainly the value used will be smaller than the maximum value given by Equation (5.77).

Using again the material properties shown in Tables 5.2 and 5.3, the variation of the onset criterion of the constitutive equation defined in terms of relative displacements and the variation of the propagation criterion of the constitutive equation chart defined in terms of strains are shown in Figure 5.7. These charts correspond to the simulations in one element with constant in-plane dimensions under pure mode I loading.

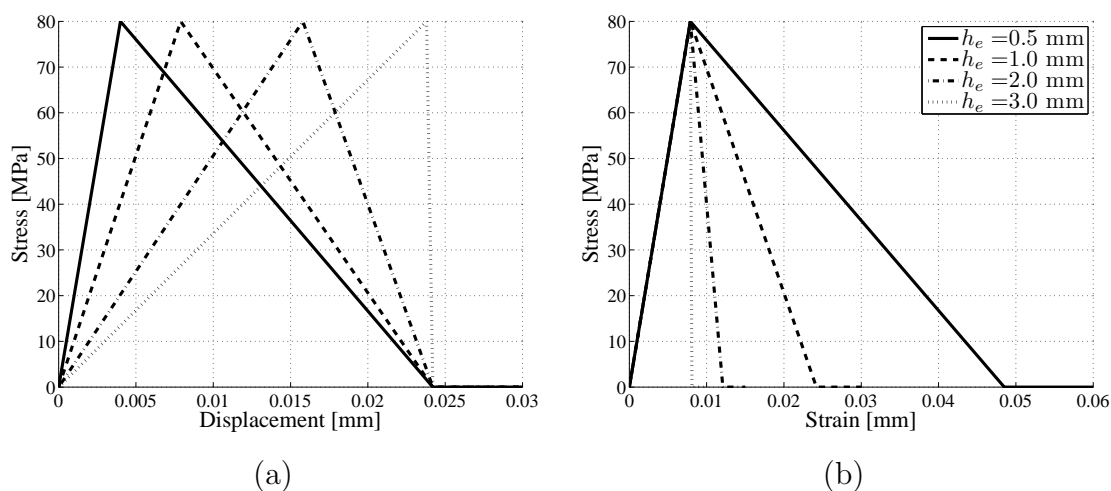


Figure 5.7: Constitutive equation charts defined by (a) relative displacements and by (b) strains in function of the element thickness.

5.5.2 In-plane dimensions of the cohesive elements

The in-plane dimensions of the cohesive elements are selected following the considerations and equations proposed by Turon et al. [12]. In particular, the in-plane dimensions are defined by means of the cohesive zone length l_{cz} , which is a material and structural property [141]. It is defined as the distance from the crack front until the point with the maximum interface strength τ^o . To obtain suitable results by using cohesive zone models, the tractions in the cohesive zone have to be represented correctly by a proper number of elements.

The model that will be used in this work in order to predict the length of the cohesive zone was proposed by Rice [142], and reads:

$$l_{cz} = \frac{9\pi}{32} E_m \frac{\mathcal{G}_c(\beta)}{(\tau^o(\beta))^2} \quad (5.78)$$

where E_m is the Young modulus, and $\mathcal{G}_c(\beta)$ and $\tau^o(\beta)$ are the fracture toughness and the maximum strength of the interface for a given mixed-mode ratio, respectively.

The length of the cohesive elements l_e is easily calculated by means of:

$$l_e = \frac{l_{cz}}{N_e} \quad (5.79)$$

where N_e is the number of elements in the cohesive zone. Normally, the smallest value of the cohesive zone length resulted from the different values of mixed-mode ratio is used, and it is recommended to apply at least three or four elements in order to describe the cohesive zone accurately.

5.6 Simulations

This section presents the application of cohesive elements in the simulation of interlaminar fracture tests of composite specimens under quasi-static loading conditions. These tests allow the validation of the damage model presented without consider the interaction with other damage mechanisms which can appear inside the plies, because the damage is normally concentrated in interfaces where only delamination occurs.

Mixed-Mode Bending (MMB) and End-Notched Flexure (ENF) tests of unidirectional zero degree lay-up specimens with an initial pre-crack are considered (see Section 5.6.2). The MMB allows to test any mixed-mode case except pure mode II, which is obtained by the ENF test. The cases simulated are $B = 0.0$ (pure mode I), $B = 0.2$, $B = 0.5$, $B = 0.8$ and $B = 1.0$ (pure mode II). It should be noted that only non-zero-thickness elements have been used in all the simulations considered, which represent a resin-rich interface layer.

Different mixed-mode analysis at one finite element were simulated previously in order to check that the predicted dissipated energy at each integration point is

equal to the corresponding fracture toughness adjusted by the least square fit of experimental data points of the selected material (see Table 5.3).

Simulations of quasi-static Transverse Crack Tension tests (TCT) of unidirectional zero degree lay-up specimens are also shown (see Section 5.6.3). The TCT test is an alternative to the ENF test, which determines pure mode II interlaminar fracture toughness [143].

Finally, the numerical considerations in order to carry out quasi-static simulations by using an explicit finite element code are explained in detail.

5.6.1 Considerations for quasi-static explicit simulations

The proposed simulations are solved by means of an explicit finite element code. As it has been explained in the introduction, the explicit integration schemes determine a solution to the dynamic equilibrium of the global set equations by explicitly advancing the kinematic state from the previous time increment, without solving simultaneously equations and without iterating for each time increment. For this reason, the formulation of the tangent stiffness tensor is not derived here since no iterations are carried out.

Static problems have a large time solution, which often it is unworkable to analyze the simulation in its real scale of time using an explicit code because requires an excessive number of stable small increments of time. To obtain a faster solution, the event should be accelerated in some way, but ensuring that the inertial forces remain insignificant. There are some actions to alter one or more of the factors influencing the time increment. The action here considered for increasing the efficiency of the proposed simulations is to scale the mass density of these critical elements (i.e. mass scaling). In order to control the proposed simulations, the kinetic energy and the internal energy are monitored in order to keep the kinetic energy less than 5% of the internal energy of the system.

On the other hand, the loading velocity should be such that the solution obtained is close to the real static solution and the dynamic effects remain insignificant. In an approximate way, the maximum loading velocity v_L can be estimated by means of:

$$v_L < 0.01 \sqrt{\frac{E_m}{\rho_m}} \quad (5.80)$$

The loading velocity defined in all the simulations is 0.5mm/s, which is much lower than the maximum value given by Equation (5.80) (see interface properties in Tables 5.3 and 5.6).

Quasi-static analysis in explicit algorithms require the application of loading as smooth as possible. Sudden movements cause stress waves, which can introduce noisy or inaccurate results. Applying the load in the smoothest possible manner requires that the acceleration changes only a small amount from one time increment to the next. Then, if the acceleration is smooth, it follows that the changes in velocity and displacement are also smooth. This option can be defined easily in Abaqus software by selecting a smooth amplitude table of loading in all the proposed simulations. By defining it, Abaqus software connects automatically each of the user data pairs of loading with curves, whose first and second derivatives are smooth, and whose values are zero at each of user loading data points.

It has to be noted that the selected mass scaling factor for critical elements is considerably high (i.e. approximately 10.0^3). However, since the boundary displacements are applied in a smooth manner and in a large time scale, the kinetic energy and the inertial forces of the model remain small.

Finally, the cohesive elements which reach the maximum damage value at their integration points are deleted from the mesh. These deleted elements have no ability to carry stresses and, therefore, have no contribution to the stiffness of the model. This action avoids large distortions of the damaged elements, and possible spurious stress transfer to the bodies around them. However, if damaged elements are deleted, penetration between the joined laminates can occur, mainly in tests with high percentage of mode II. To avoid it, a contact pair surfaces without friction have been defined between the two laminate surfaces that were initially linked by the cohesive elements.

5.6.2 MMB and ENF fracture toughness tests

The simulations of quasi-static MMB and ENF tests of unidirectional zero degree lay-up specimens are analyzed in this section.

Test configurations

The loading conditions in the MMB simulations are defined by means of the linear Equation (5.81) which relates the displacements in three different points of the specimen [118]:

$$\delta_{LP} = \left(\frac{c}{L}\right) \delta_I + \left(\frac{c+L}{L}\right) \delta_M \quad (5.81)$$

where L is the half specimen length and c is the length from the loading point LP to the middle point M of the specimen. The different mixed-mode cases are generated by modifying the length c , which reads:

$$c = \frac{L \left(\frac{1}{2} \sqrt{3 \left(\frac{1-B}{B} \right)} + 1 \right)}{3 - \frac{1}{2} \sqrt{3 \left(\frac{1-B}{B} \right)}} \quad (5.82)$$

In Figure 5.8.a are marked the points LP , M , and I where the displacements are prescribed.

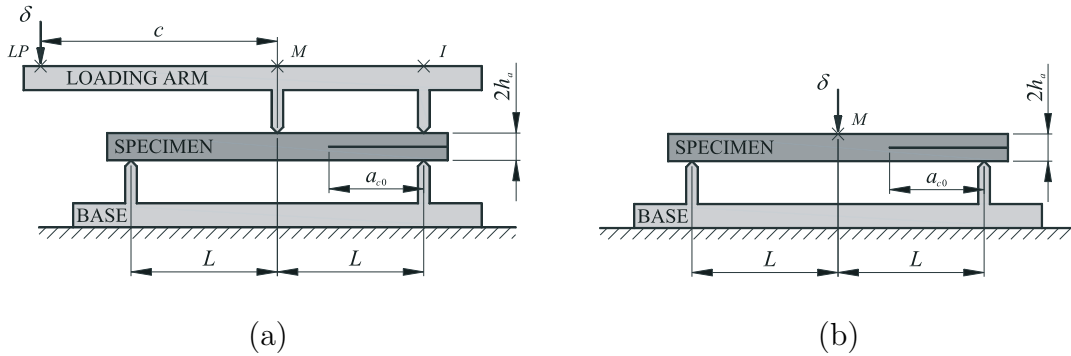


Figure 5.8: Sketches of the (a) MMB test and the (b) ENF test configurations.

The loading conditions of the ENF test are also defined by displacements. Just as indicates Figure 5.8.b, it is applied a displacement in the middle point M of the specimen.

The numerical results are compared with experimental data performed by Reeder and Crews [144–146] to validate the model. These results are presented in a force-displacement chart. For the MMB test, the results are read at point LP , and in point M for the ENF test.

Sizes and types of the elements

An 8-node solid element with reduced integration (one integration point) is used to model the laminates and volumetric cohesive elements. This element is called C3D8R. For all simulations, each laminate thickness is modeled by four elements, which is enough to capture accurately the laminate rotations during the simulations. The thickness defined for the interface elements is 0.01mm, which is much smaller than the value obtained by means of Equation (5.77) (see Figure 5.6).

On the other hand, the in-plane length of the cohesive element is determined by Equations (5.78) and (5.79). If three elements are desired to be along the cohesive length, the maximum in-plane length at the crack propagation direction is of 0.45mm. The length finally used is 0.3mm for all the simulations. It is not necessary to define a small length element at width specimen direction because the crack propagates on the opposite direction. Therefore, the specimen width is modeled by using only two elements.

Materials and specimen dimensions

The material used is a thermoplastic matrix-based reinforced by unidirectional carbon fibers (AS4/PEEK). The properties are set in Table 5.1:

Table 5.1: AS4/PEEK properties.

E_1 [MPa]	$E_2 = E_3$ [MPa]	$G_{12} = G_{13}$ [MPa]	G_{23} [MPa]	$\nu_{12} = \nu_{13}$	ν_{23}	ρ [tmm ⁻³]
122700	10100	5500	3700	0.25	0.45	1600e-12

The material properties defined to the interface elements are summarized in Table 5.2, and are selected by considering that these elements represent a resin-rich layer. The pure mode fracture toughnesses of the interface are written in Table 5.3. The shear strength τ_1^o is defined by means Equation (5.50), which yields to 106MPa.

The parameter η is taken 2.284, which is obtained by means of a least-square fit of the experimental data shown in Table 5.3.

The specimen dimensions are: 102mm long, 25.4mm wide, and each laminate arm is 1.56mm thick.

Table 5.2: Interface properties.

E_m [MPa]	ν_m	ρ_m [tmm ⁻³]	τ_3^o [MPa]
10100	0.3	1600e-12	80

Table 5.3: Fracture toughnesses of the interface for different mixed-mode ratios [145, 146].

$\frac{\mathcal{G}_{II}}{\mathcal{G}_T}$	0%	20%	50%	80%	100% (ENF)
\mathcal{G}_c [N/mm]	0.969	1.103	1.131	1.376	1.719
a_{c0} [mm]	32.9	33.7	34.1	31.4	39.2

Results

The force-displacement relations obtained in the experiments and in the finite element simulations of the MMB test for each proposed mixed-mode case: $B = 0.0$ (pure mode I), $B = 0.2$, $B = 0.5$, and $B = 0.8$ are respectively shown in Figures 5.9, 5.10, 5.11, and 5.12. The results of the ENF test ($B = 1.0$, pure mode II) are shown in Figure 5.13.

The corresponding analytical expressions for MMB test with $B = 0.0$ (pure mode I) and ENF test which give the relationship of the critical load and the displacement during propagation are also plotted in the corresponding figures. These equations are set in Table 5.4, and are deduced by using Linear Elastic Fracture Mechanics and Simple Beam Theory [147, 148]. In these equations, E_1 is the longitudinal elastic modulus of the specimen, a_c is the crack length, and b , h_a and L are the width, the arm height and the half length of the specimen, respectively.

Table 5.4: Analytical equations of MMB test with $B = 0.0$, and ENF test ($B = 1.0$).

Test	Critical load	Compliance
MMB ($B = 0.0$)	$P_c = \sqrt{\frac{E_1 b^2 h_a^3 \mathcal{G}_{Ic}}{12 a_c^2}}$	$C = \frac{8 a_c^3}{E_1 b h_a^3}$
ENF ($B = 1.0$)	$P_c = \sqrt{\frac{16 E_1 b^2 h_a^3 \mathcal{G}_{IIc}}{9 a_c^2}}$	$C = \frac{3 a_c^3 + 2 L^3}{8 E_1 b h_a^3}$

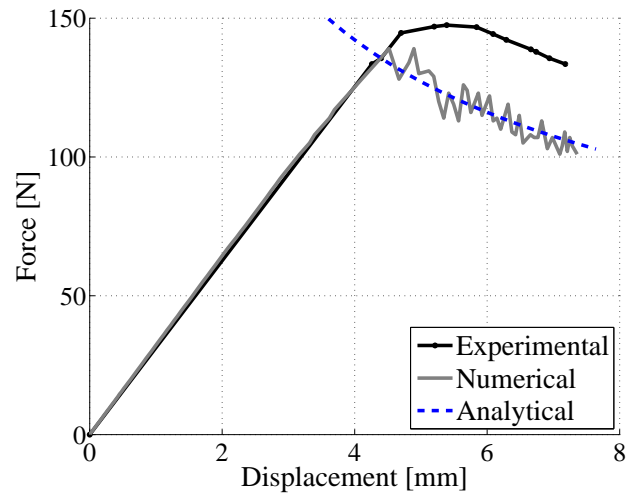


Figure 5.9: Experimental and numerical force-displacement relation of the MMB test $B = 0.0$ (pure mode I).

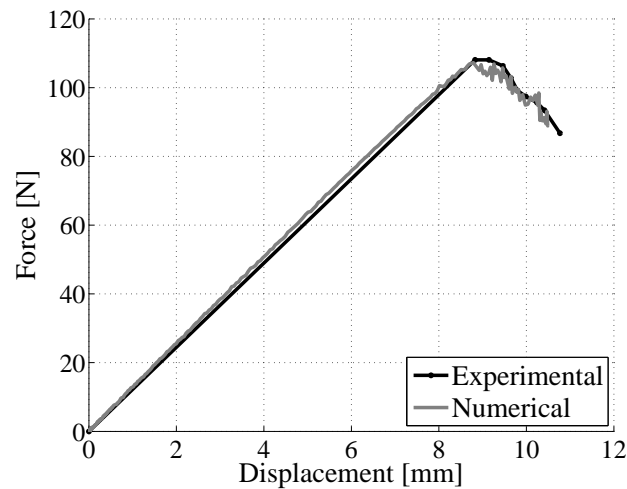


Figure 5.10: Experimental and numerical force-displacement relation of the MMB test $B = 0.2$.

Discussion

The charts obtained by numerical simulations of the proposed tests are in a good agreement with the experimental data. The predicted case of $B = 0.0$ (pure mode I) is the most far of the corresponding experimental chart. This difference is not due to limitations of the numerical simulations, but rather to the fact that the experimental

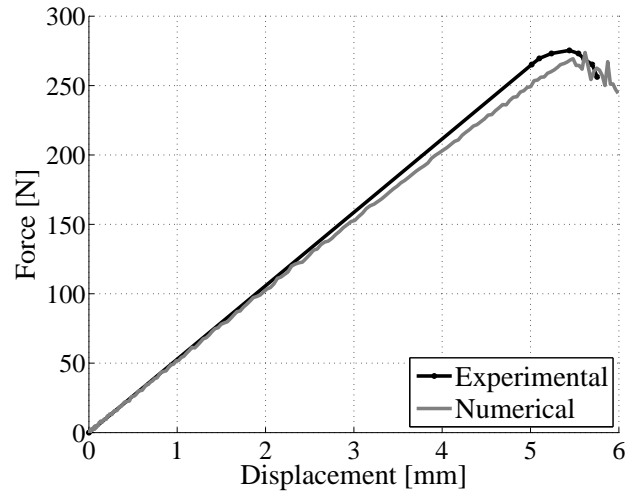


Figure 5.11: Experimental and numerical force-displacement relation of the MMB test $B = 0.5$.

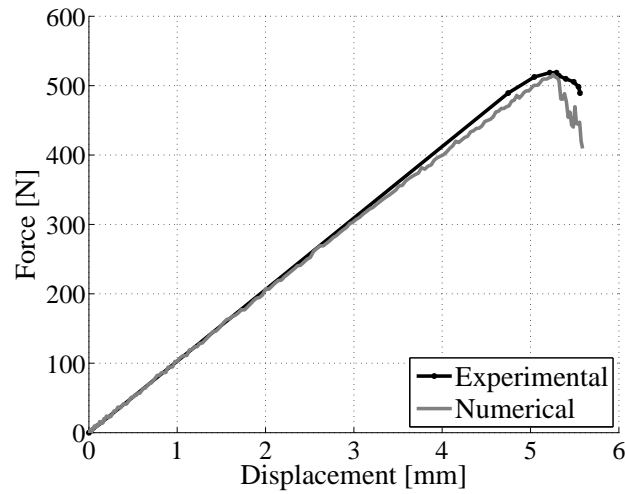


Figure 5.12: Experimental and numerical force-displacement relation of the MMB test $B = 0.8$.

fracture toughness used corresponds to the onset delamination and not to the propagation, which is normally larger than the onset fracture toughness. The analytical model which gives the relationship of the critical load and the displacement during propagation is plotted. The fracture toughness specified is $\mathcal{G}_c = 0.969\text{N/mm}$ (see Table 5.3), and the numerical curve shows an excellent correlation with the descend-

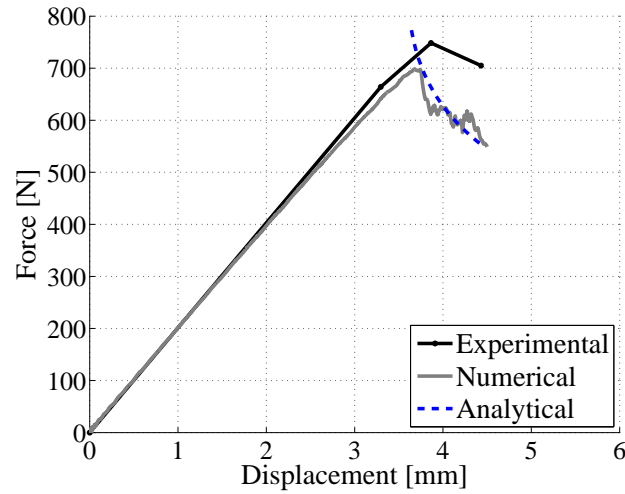


Figure 5.13: Experimental and numerical force-displacement relation of the ENF test (pure mode II).

ing part of the analytical load-displacement curve. On the other hand, the analytical model corresponding to the ENF test with a fracture toughness of $\mathcal{G}_c = 1.719\text{N/mm}$ (see Table 5.3) is plotted in Figure 5.13, which also shows a good agreement between the analytical load-displacement curve and the numerical prediction.

Once the delamination is initiated, oscillations are observed in all predictions. However, the amplitude of these oscillations has been reduced by increasing the mesh refinement and by reducing the loading velocity. Other possibility allowed for propagation tests which was not shown here is to reduce the interface strength. In part, the oscillations which appear in a quasi-static explicit simulation may be a consequence of the constitutive equation shape. For implicit simulations, the shape of the constitutive equation does not affect to the results, whenever the fracture toughness is correctly accounted and the initial stiffness and maximum traction are reasonably consistent with the stiffness and strength of the material being modeled. However, in quasi-static explicit simulations, the shape has an important role for the stability simulation. The equation used has two discontinuities, one at initiation damage onset and other in the damage propagation. In some cases, stress waves appear at these points whose generate high frequency vibrations that break the cohesive element at the neighborhood. Therefore, an attractive solution is to use constitutive equation shapes without discontinuities [120].

5.6.3 TCT tests

The simulations of quasi-static Transverse Crack Tension tests (TCT) of unidirectional zero degree lay-up specimens are analyzed in this section.

Configuration of the TCT tests

The TCT specimens are manufactured by continuous fiber laminates with unidirectional stacking order whose central plies are cut prior to curing, as shown in Figure 5.14. When these specimens are loaded by tension, delaminations develop under pure mode II. Such laminates are referred by $[0_m, \emptyset_n]_S$, where the slash indicates the cut plies.

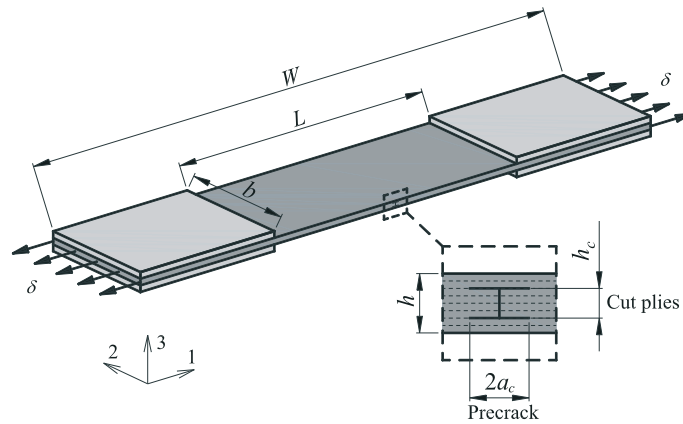


Figure 5.14: TCT specimen.

The TCT specimens can be tested with or without pre-cracks previously induced. The specimens with pre-cracks are those undergoing a determined number of fatigue cycles at near-threshold loading for delamination growth. For no pre-cracked specimens, the gap between cut plies is a resin rich region which delaminates under pure mode I. Next, at certain load level, delamination starts at the corner point between cut and continuous plies along the fiber direction and quickly develops under pure mode II to certain length or full-scale. For pre-cracked specimens, this pre-delamination phase is not experimented since small initial interface cracks are previously created [149]. Consequently, the resulting critical load and fracture toughness are more representative in these specimens than for no pre-cracked specimens.

The TCT test is then an alternative to the ENF test [150]. It is assumed that in the TCT test there is less sliding friction between the delaminated plies than in the ENF test. A second advantage concerns compliance calibration for data reduction. The compliance of the TCT specimen is less sensitive to the error in crack length measurement, because the compliance is related linearly to the crack length a_c (see Equation (5.83)), whereas for the ENF specimen the compliance is related to a_c^3 (see Table 5.4).

$$C = \frac{L(h - h_c) + 2a_ch_c}{bh(h - h_c)E_1} \quad (5.83)$$

E_1 is the longitudinal elastic modulus of the specimen, and h_c is the whole thickness of cut central plies. The geometrical variables L , b and h are the length, width, and total thickness of the specimen, respectively.

From the evaluation of the compliance C and the delamination length a_c , the fracture toughness \mathcal{G}_{IIc} can be derived for a constant specimen width b as:

$$\mathcal{G}_{IIc} = \frac{1}{4} \frac{h_c P_c^2}{b^2 E_1 h (h - h_c)} \quad (5.84)$$

The factor $1/4$ is introduced because there are four crack tips. Equation (5.84) shows that \mathcal{G}_{IIc} can be obtained by determining solely the critical load P_c .

Only non pre-cracked specimens are simulated. The laminates considered are: $[0_2, \emptyset_4]_S$, $[0_4, \emptyset_4]_S$ and $[0_4, \emptyset_8]_S$. The numerical results obtained are basically the critical load P_c for delamination propagation, and are compared with experimental values performed by Ye et al. [149].

Sizes and types of the elements

Two delamination planes are modeled in the TCT specimens, as shown in Figure 5.15. One corresponds to the interface of the cut central plies which delaminates under pure mode I, and is modeled by using zero-thickness type elements with four integration points of the Abaqus element library (i.e. COH3D8). The other delamination plane corresponds to the interface between cut and continuous plies along the fiber direction which delaminates under pure mode II. In this case, the interface is modeled by using non-zero-thickness type elements with reduced integration (i.e.

C3D8R). The thickness defined for this interface is 0.01mm, which is much smaller than the value obtained by means of Equation (5.77). The in-plane length of these elements at the crack propagation direction is determined by means of Equations (5.78) and (5.79). If three elements are desired to be along the cohesive length, the maximum in-plane length is of 0.37mm. The length finally used is 0.33mm.

The specimen width is meshed with five elements, and each ply thickness with two elements. The composite material is modeled by using also C3D8R elements. Only half thickness of the specimen is modeled by defining symmetric boundary conditions.

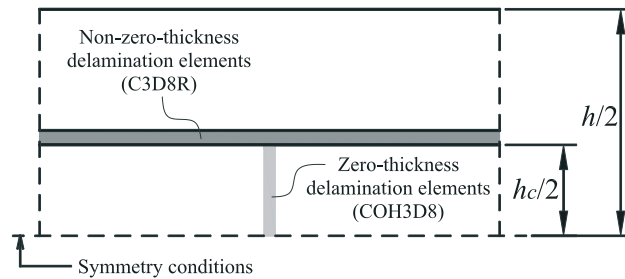


Figure 5.15: Detail of the location of the cohesive elements.

Materials and specimen dimensions

The composite material used is an epoxy matrix-based reinforced by unidirectional carbon fibers (T300/914C). The properties are extracted from Ye et al. [149] and set in Table 5.5.

The material properties defined to the interface elements located between cut and continue plies are shown in Table 5.6, and are selected by considering that these elements represent a resin-rich layer. The fracture toughness \mathcal{G}_{IIc} is obtained by testing pre-cracked TCT specimens. For zero-thickness cohesive elements the properties are equal than those set in Table 5.6 except the elastic modulus (i.e. penalty stiffness) which is set 10^6 , and in order to obtain the same penalty stiffness for all propagation modes the Poisson modulus is set equal to -0.5. The shear strength τ_1^o is defined by means Equation (5.50), which yields to 83MPa.

The parameter η is approached to 1.47, which is obtained by means of least-square fit of mixed-mode fracture toughnesses obtained in MMB tests [150]. The

Table 5.5: T300/914C properties.

E_1 [MPa]	$E_2 = E_3$ [MPa]	$G_{12} = G_{13}$ [MPa]	G_{23} [MPa]	$\nu_{12} = \nu_{13}$	ν_{23}	ρ [tmm ⁻³]
129000	9256	5000	3306	0.28	0.4	1600e-12

Table 5.6: Interface properties.

E_m [MPa]	ν_m	ρ_m [tmm ⁻³]	τ_3^o [MPa]	\mathcal{G}_{Ic} [N/mm]	\mathcal{G}_{IIc} [N/mm]
9256	0.3	1600e-12	50	0.17	0.467

dimensions of the specimens are: 140mm long (L), 20mm wide (b), and the ply thickness is approximately 0.125mm. The total length of the specimens is 380mm (W).

Results and discussion

The load-displacement relations obtained in the finite element simulations of each TCT specimen are plotted in Figure 5.16. These plots show a peak load which corresponds to the point where the interface of the cut central plies is completely damaged. Next, stationary load values appear after the drop of the peak loads (i.e. after the pre-delamination phase).

These stationary loads are the critical loads for pure mode II delamination of the interface between cut and continue plies. By means of Equation (5.84) and the numerical critical loads obtained, the fracture toughness \mathcal{G}_{IIc} can be predicted. The results are set in Table 5.7 and show a good agreement with the value defined in the model: $\mathcal{G}_{IIc} = 0.467\text{N/mm}$. In addition, a comparison of the results shown in Table 5.7 indicates good correlation between the predicted peak loads and the corresponding experimental values.

5.7 Conclusions

The formulation and implementation of a thermodynamically consistent damage model for the simulation of progressive delamination in composite materials under

Table 5.7: Experimental and numerical results.

Laminate	Experimental		Numerical	
	F_{peak} [N]	F_{peak} [N]	P_c [N]	\mathcal{G}_{IIc} [N/mm]
$[0_2, \emptyset_4]_S$	8500	8963	8600	0.478
$[0_4, \emptyset_4]_S$	15219	14380	14200	0.488
$[0_4, \emptyset_8]_S$	14321	13080	12100	0.473

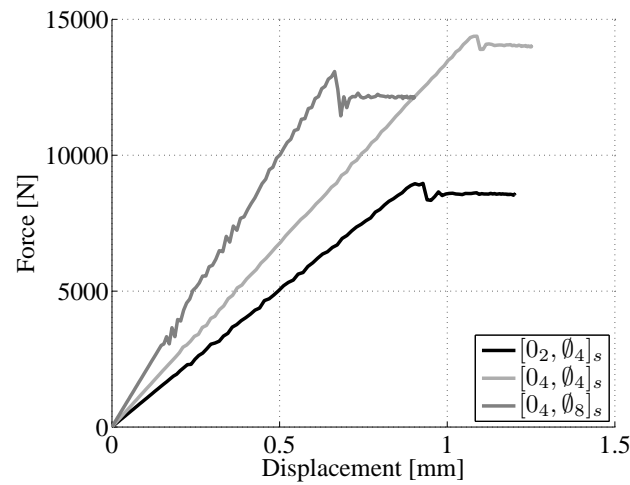


Figure 5.16: Numerical load-displacement relations for the TCT specimens.

variable mixed-mode ratio by using an explicit finite element code was presented. The model was formulated in the context of Damage Mechanics, and implemented by means of a user-written material subroutine. The user material can be defined on sets of elements that represent the possible location for delamination. The elements can be selected to have zero-thickness (surface elements) or non-zero-thickness (continuum elements).

The model was used to simulate the initiation and propagation of delamination in fracture toughness tests (MMB, ENF and TCT) under quasi-static loading conditions. The examples analyzed are in good agreement with the test results, and they indicate that the proposed formulation can predict the delamination process of composite structures that exhibit progressive delamination. It should be noted that some numerical predictions have shown some stability problems or oscillations

which have been reduced significantly by increasing the mesh refinement and by reducing the loading velocity during the crack propagation process. However, these oscillations may be reduced even more by modifying the shape of the constitutive equation to one without discontinuity points.

To make use of the damage model implemented and of the explicit finite element code, the next step is to simulate low-velocity impacts of foreign objects on monolithic laminated composite plates, where the delamination generally propagates under variable mixed-mode conditions (see Chapter 7). In these analysis, the study of the shape and extension of the delamination at interfaces between mismatch orientation plies is of great interest since the delamination reduces dramatically the damage tolerance of the structure. In order to carry out an accurately prediction, an intralaminar damage model must be added in these analysis (see Chapter 6), since impact loading conditions creates intralaminar damage mechanisms which interact with the delamination failure mode.

Chapter 6

Intralaminar damage model

6.1 Introduction

Strength-based failure criteria can be used to predict the onset of the damage mechanisms which contribute to final failure of a composite structure. However, these criteria are inaccurate in predicting the ultimate structural failure of composite structures that can accumulate damage before final collapse. Continuum Damage Mechanics is a more accurate methodology to predict the quasi-brittle failure of composites, from the onset up to final collapse. The prediction of the damage accumulation is a key information since it defines the damage tolerance and the eventual collapse of a structure.

The intralaminar damage model developed by Maimí et al. [14–17] is summarized in the present chapter. This model accounts the matrix cracking and the fiber breakage damage mechanisms for 3D plies, and will be used, together with the delamination damage model presented in Chapter 5, for the simulation of the impact and the CAI tests in Abaqus/Explicit finite element code [124].

The model is developed in the context of the mechanics of continuum mediums, using a rigorous thermodynamic framework where the irreversibility of the damage processes are ensured. The main features of the model are listed below:

- The majority of the material properties required for the definition of the damage model can be measured using standard ply-based test methods.
- The damage activation functions, which predict the different failure mech-

anisms occurring at the ply level, are based mainly on the LaRC04 failure criteria [76, 77]. This criteria accounts for the in-situ effect of the thickness of a ply on its transverse tensile and shear strengths.

- The model accounts for crack-closure effects under load reversal conditions. The consideration of these effects are significant in structures that are subjected to multi-axial loading, such as in the impact and the CAI tests.
- The objectivity of the finite element model is ensured using the crack band model proposed by Bažant and Oh [139], by regularizing the computed dissipated energy of each failure mechanism using a characteristic dimension of the finite element and the corresponding fracture toughness.

Finally, simple FE simulations which illustrate the well-known limitations of using a continuum damage model for capturing matrix macro-crack paths in absence of fiber breakage are shown.

6.2 Continuum damage model

6.2.1 Constitutive model

The constitutive equation is obtained by the definition of a thermodynamic potential. In this case, the complementary free energy density is used, and it is defined as:

$$\begin{aligned}
 G &= \frac{\sigma_{11}^2}{2(1-d_1)E_1} + \frac{\sigma_{22}^2}{2(1-d_2)E_2} + \frac{\sigma_{33}^2}{2(1-d_3)E_2} - \frac{\nu_{12}}{E_1}\sigma_{11}(\sigma_{22} + \sigma_{33}) - \\
 &- \frac{\nu_{23}}{E_2}\sigma_{22}\sigma_{33} + \frac{\sigma_{23}^2}{2(1-d_4)G_{23}} + \frac{\sigma_{13}^2}{2(1-d_5)G_{12}} + \\
 &+ (\alpha_{11}\sigma_{11} + \alpha_{22}(\sigma_{22} + \sigma_{33}))\Delta T + (\beta_{11}\sigma_{11} + \beta_{22}(\sigma_{22} + \sigma_{33}))\Delta M
 \end{aligned} \tag{6.1}$$

where E_1 , E_2 , ν_{12} and G_{12} are the in-plane elastic properties of a unidirectional lamina. The damage variable d_1 is associated with longitudinal (fiber) failure, whereas d_2 and d_3 are the damage variables associated with transverse (matrix cracking) failure controlled by in-plane and out-of-plane loads, respectively. The damage variables d_4 , d_5 , and d_6 are influenced by longitudinal and transverse cracks. α_{11} and α_{22}

are the coefficients of thermal expansion in the longitudinal and transverse directions, respectively. β_{11} and β_{22} are the coefficients of hygroscopic expansion in the longitudinal and transverse directions, respectively. ΔT and ΔM are the differences of temperature and moisture content with respect to the corresponding reference values.

By ensuring the thermodynamical irreversibility of the damage process, the constitutive relationship of strains, $\varepsilon = \{\varepsilon_{11}, \varepsilon_{22}, \varepsilon_{33}, \varepsilon_{12}, \varepsilon_{13}, \varepsilon_{23}\}^T$, and stresses, $\sigma = \{\sigma_{11}, \sigma_{22}, \sigma_{33}, \sigma_{12}, \sigma_{13}, \sigma_{23}\}^T$, can be found:

$$\varepsilon = \frac{\partial G}{\partial \sigma} = \mathbf{H} : \sigma + \alpha \Delta T + \beta \Delta M \quad (6.2)$$

where the lamina compliance tensor $\mathbf{H} = \frac{\partial^2 G}{\partial \sigma \otimes \partial \sigma}$ is defined as:

$$\mathbf{H} = \begin{bmatrix} \frac{1}{(1-d_1)E_1} & -\frac{\nu_{12}}{E_1} & -\frac{\nu_{12}}{E_1} & 0 & 0 & 0 \\ -\frac{\nu_{12}}{E_1} & \frac{1}{(1-d_2)E_2} & -\frac{\nu_{23}}{E_2} & 0 & 0 & 0 \\ -\frac{\nu_{12}}{E_1} & -\frac{\nu_{23}}{E_2} & \frac{1}{(1-d_3)E_2} & 0 & 0 & 0 \\ 0 & 0 & 0 & \frac{1}{(1-d_6)G_{12}} & 0 & 0 \\ 0 & 0 & 0 & 0 & \frac{1}{(1-d_5)G_{12}} & 0 \\ 0 & 0 & 0 & 0 & 0 & \frac{1}{(1-d_4)G_{23}} \end{bmatrix} \quad (6.3)$$

The closure of transverse cracks under load reversal, is taken into account making:

$$\begin{aligned} d_1 &= d_{1+} \frac{\langle \sigma_{11} \rangle}{|\sigma_{11}|} + d_{1-} \frac{\langle -\sigma_{11} \rangle}{|\sigma_{11}|} \\ d_2 &= d_{2+} \frac{\langle \sigma_{22} \rangle}{|\sigma_{22}|} + d_{2-} \frac{\langle -\sigma_{22} \rangle}{|\sigma_{22}|} \end{aligned} \quad (6.4)$$

where $\langle x \rangle$ is the Macaulay operator defined as $\langle x \rangle := \frac{1}{2}(x + |x|)$. The model tracks damage caused by tension loads (d_+) separately from damage caused by compression loads (d_-). The model assumes that the shear damage variables are not affected by the closure effect.

6.2.2 Damage activation functions

The elastic domain is enclosed by four surfaces, each of them accounts one failure mechanism: longitudinal and transverse fracture under tension and compression. Those surfaces are formulated by the damage activation functions based on the LaRC04 failure criteria, neglecting the out-of-plane stresses. These damage activation functions F_N , associated with damage in the longitudinal ($N = 1+, 1-$) and transverse ($N = 2+, 2-$) directions represented in Figure 6.1, are defined as:

$$F_{1+} = \phi_{1+} - r_{1+} \leq 0 \quad ; \quad F_{1-} = \phi_{1-} - r_{1-} \leq 0 \quad (6.5)$$

$$F_{2+} = \phi_{2+} - r_{2+} \leq 0 \quad ; \quad F_{2-} = \phi_{2-} - r_{2-} \leq 0$$

where the loading functions ϕ_N ($N = 1+, 1-, 2+, 2-$) depend on the strain tensor and material constants (elastic and strength properties). The elastic domain thresholds r_N ($N = 1+, 1-, 2+, 2-$) take an initial value of 1 when the material is undamaged, and they increase with damage. The elastic domain thresholds are internal variables of the constitutive model, and are related to the damage variables d_M ($M = 1+, 1-, 2+, 2-, 6$) by the damage evolution laws.

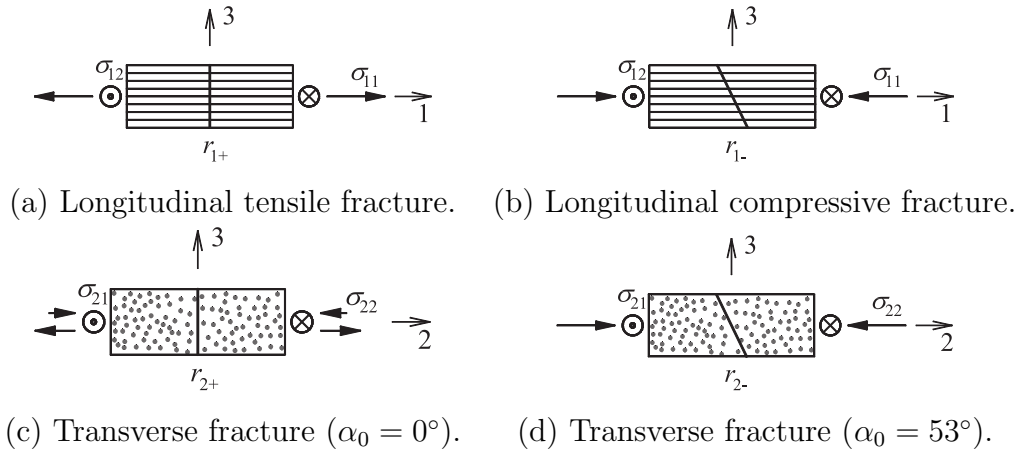


Figure 6.1: Fracture surfaces and corresponding internal variables for four different modes.

The elastic domain thresholds r_N define the level of elastic strains that can be attained before the accumulation of additional damage. The elastic domain thresholds

are obtained applying the Kuhn-Tucker and consistency conditions. Considering the effect of the cracks when load reversal occurs, the elastic domain thresholds are:

$$\begin{aligned} r_{N+} &= \max \left\{ 1, \max_{s=0,t} \{ \phi_{N+}^s \}, \max_{s=0,t} \{ \phi_{N-}^s \} \right\}; \quad N = 1, 2 \\ r_{N-} &= \max \left\{ 1, \max_{s=0,t} \{ \phi_{N-}^s \} \right\}; \quad N = 1, 2 \end{aligned} \quad (6.6)$$

Longitudinal tensile fracture

The LaRC04 criterion for fiber tension failure is a maximum allowable strain criterion defined as:

$$\phi_{1+} = \frac{E_1}{X_T} \varepsilon_{11} = \frac{\tilde{\sigma}_{11} - \nu_{12} \tilde{\sigma}_{22}}{X_T} \quad (6.7)$$

where X_T is the tensile strength of the fiber. The effective stress tensor $\tilde{\sigma}$ is computed as $\tilde{\sigma} = \mathbf{H}_0^{-1} : \varepsilon$. \mathbf{H}_0 is the undamaged compliance tensor obtained from Equation (6.3) using $d_N = 0$ ($N = 1, 2, \dots, 6$).

Longitudinal compressive fracture

The damage activation function used to predict damage under longitudinal compression ($\tilde{\sigma}_{11} < 0$) and in-plane shear (fiber kinking) is established as a function of the components of the stress tensor $\tilde{\sigma}^{(m)}$ in a coordinate system (m) representing the fiber misalignment:

$$\phi_{1-} = \frac{\langle |\tilde{\sigma}_{12}^m| + \eta^L \tilde{\sigma}_{22}^m \rangle}{S_L} \quad (6.8)$$

where the longitudinal friction coefficient η^L can be approximated as [76]:

$$\eta^L \approx -\frac{S_L \cos(2\alpha_0)}{Y_C \cos^2 \alpha_0} \quad (6.9)$$

with $\alpha_0 = 53^\circ$. The components of the effective stress tensor in the coordinate system associated with the rotation of the fibers are calculated as [76]:

$$\begin{aligned} \tilde{\sigma}_{22}^m &= \tilde{\sigma}_{11} \sin^2 \varphi^C + \tilde{\sigma}_{22} \cos^2 \varphi^C - 2 |\tilde{\sigma}_{12}| \sin \varphi^C \cos \varphi^C \\ \tilde{\sigma}_{12}^m &= (\tilde{\sigma}_{22} - \tilde{\sigma}_{11}) \sin \varphi^C \cos \varphi^C + |\tilde{\sigma}_{12}| (\cos^2 \varphi^C - \sin^2 \varphi^C) \end{aligned} \quad (6.10)$$

The misalignment angle φ^C is determined using standard shear and longitudinal compression strengths, S_L and X_C , respectively [76]:

$$\varphi^C = \arctan \left(\frac{1 - \sqrt{1 - 4 \left(\frac{S_L}{X_C} + \eta^L \right) \frac{S_L}{X_C}}}{2 \left(\frac{S_L}{X_C} + \eta^L \right)} \right) \quad (6.11)$$

Transverse fracture perpendicular to the mid-plane of the ply

Transverse matrix cracks perpendicular to the mid-plane of the ply, i.e. with $\alpha_0 = 0^\circ$, are created by a combination of in-plane shear stresses and transverse tensile stresses, or in-plane shear stresses and small transverse compressive stresses. These conditions are represented by the following failure criteria:

$$\phi_{2+} = \begin{cases} \sqrt{(1-g) \frac{\tilde{\sigma}_{22}}{Y_T} + g \left(\frac{\tilde{\sigma}_{22}}{Y_T} \right)^2 + \left(\frac{\tilde{\sigma}_{12}}{S_L} \right)^2} & \text{if } \tilde{\sigma}_{22} \geq 0 \\ \frac{1}{S_L} \langle |\tilde{\sigma}_{12}| + \eta^L \tilde{\sigma}_{22} \rangle & \text{if } \tilde{\sigma}_{22} < 0 \end{cases} \quad (6.12)$$

where Y_T is the transverse tensile strength, and g is the fracture toughness ratio defined as $g = \mathcal{G}_{2+}/\mathcal{G}_6$. \mathcal{G}_{2+} is the transverse tensile fracture toughness, and \mathcal{G}_6 is the shear fracture toughness.

Transverse compressive fracture

The matrix failure criterion for transverse compressive stresses consists of a quadratic interaction between the effective shear stresses acting on the fracture plane:

$$\phi_{2-} = \sqrt{\left(\frac{\tilde{\tau}_{\text{eff}}^T}{S_T} \right)^2 + \left(\frac{\tilde{\tau}_{\text{eff}}^L}{S_L} \right)^2} \quad \text{if } \tilde{\sigma}_{22} < 0 \quad (6.13)$$

where the effective stresses $\tilde{\tau}_{\text{eff}}^T$ and $\tilde{\tau}_{\text{eff}}^L$ are computed as [76]:

$$\begin{aligned} \tilde{\tau}_{\text{eff}}^T &= \langle -\tilde{\sigma}_{22} \cos(\alpha_0) (\sin(\alpha_0) - \eta^T \cos(\alpha_0) \cos(\theta_s)) \rangle \\ \tilde{\tau}_{\text{eff}}^L &= \langle \cos(\alpha_0) (|\tilde{\sigma}_{12}| + \eta^L \tilde{\sigma}_{22} \cos(\alpha_0) \sin(\theta_s)) \rangle \end{aligned} \quad (6.14)$$

with $\theta_s = \arctan\left(\frac{-|\tilde{\sigma}_{12}|}{\tilde{\sigma}_{22} \sin(\alpha_0)}\right)$ (sliding angle), $\eta^T = \frac{-1}{\tan(2\alpha_0)}$ (coefficient of transverse influence), and $S_T = Y_C \cos(\alpha_0) \left[\sin(\alpha_0) + \frac{\cos(\alpha_0)}{\tan(2\alpha_0)}\right]$ (transverse shear strength).

6.2.3 Damage evolution laws

The internal variables r_N define the threshold of the elastic domains, and are related to the damage variables by means of the damage evolution laws. These laws are expressed in the following general form:

$$d_M = 1 - \frac{1}{f_N(r_N)} \exp\{A_M [1 - f_N(r_N)]\}; \quad M = 1+, 1-, 2+, 2-, 6 \quad (6.15)$$

where the function $f_N(r_N)$ ($N = 1+, 1-, 2+, 2-$) is selected to force the softening of the constitutive relation.

The parameters A_M ($M = 1+, 1-, 2+, 2-, 6$) are calculated to ensure that the computed density of the dissipated energy g_M is independent of the finite element size, hence it is selected to accomplish the following condition for all failure modes:

$$g_M = \int_1^\infty \frac{\partial G}{\partial d_M} \frac{\partial d_M}{\partial r_M} dr_N = \frac{\mathcal{G}_M}{\ell^*}; \quad M = 1+, 1-, 2+, 2-, 6 \quad (6.16)$$

where ℓ^* is the characteristic finite element length.

In detail, the damage evolution laws and the corresponding related parameters are listed below:

- **Longitudinal tension.** The longitudinal tension damage evolution law follows a linear-exponential law to consider the process of fiber-matrix failure followed by fiber bridging and fiber pull-out. The softening is linear until the stress reaches the pull-out stress X_{PO} , and the corresponding energy dissipation per unit area is \mathcal{G}_{1+}^L . As the strains continue to increase, the softening response follows an exponential law and the energy dissipated per unit area is \mathcal{G}_{1+}^E . The corresponding damage evolution law is defined as:

$$d_{1+} = 1 - (1 - d_{1+}^L) (1 - d_{1+}^E) \quad (6.17)$$

where:

$$\begin{aligned}
d_{1+}^L &= 1 + \frac{K_1}{E_1} - \left(\frac{K_1}{E_1} + 1 \right) \frac{1}{r_{1+}^L} & ; & \quad d_{1+}^E = 1 - \frac{1}{r_{1+}^E} \exp [A_{1+} (1 - r_{1+}^E)] \\
r_{1+}^L &= \max [1, \min (r_{1+}, r_{1+}^F)] & ; & \quad r_{1+}^E = \max \left[1, (1 - d_{1+}^F) \frac{X_T}{X_{PO}} r_{1+} \right] \\
K_1 &= \frac{\ell^* X_T E_1 (X_T - X_{PO})}{2 \mathcal{G}_{1+}^L E_1 - \ell^* X_T (X_T - X_{PO})} & ; & \quad r_{1+}^F = 1 + \frac{E_1}{K_1} \left(1 - \frac{X_{PO}}{X_T} \right) \\
d_{1+}^F &= 1 + \frac{K_1}{E_1} - \left(\frac{K_1}{E_1} + 1 \right) \frac{1}{r_{1+}^F} & ; & \quad A_{1+} = \frac{2 \ell^* X_{PO}^2}{2 (1 - d_{1+}^F) E_1 \mathcal{G}_{1+}^E - \ell^* X_{PO}^2}
\end{aligned} \tag{6.18}$$

- **Longitudinal compression.** The longitudinal compression damage evolution law can be expressed as a combination of the failure mechanisms caused by tension loads, $d_{1+} (r_{1+})$, and the failure mechanisms generated under compression, $d_{1-} (r_{1-})$:

$$d_{1-} = 1 - [1 - d_{1-}^* (r_{1-})] [1 - A_1^\pm d_{1+} (r_{1+})] \tag{6.19}$$

where $d_{1-}^* = 1 - \frac{1}{r_{1-}} \exp [A_{1-} (1 - r_{1-})]$. The parameter A_1^\pm takes into account the effect of the stiffness recovery of the broken fibers by means of the parameter b that varies between 0 and 1: $A_1^\pm \approx b \frac{E_1 - E_2}{E_1}$.

- **Transverse tensile.** It is defined as:

$$d_{2+} = 1 - \frac{1}{f_{2+} (r_{2+})} \exp [A_{2+} (1 - f_{2+} (r_{2+}))] \tag{6.20}$$

where $f_{2+} (r_{2+}) = \frac{1}{2g} \left[g - 1 + \sqrt{(1 - g)^2 + 4gr_{2+}^2} \right]$.

- **Transverse compression.** It is defined as:

$$d_{2-} = 1 - \frac{1}{r_{2-}} \exp [A_{2-} (1 - r_{2-})] \tag{6.21}$$

- **In-plane shear.** The shear stress stiffness is reduced as a result of longitudinal and transverse cracks:

$$d_6 = 1 - [1 - d_6^*(r_{2+})](1 - d_{1+}) \quad (6.22)$$

where:

$$d_6^*(r_{2+}) = 1 - \frac{1}{r_{2+}} \exp [A_6 (1 - r_{2+})] \quad (6.23)$$

$$A_6 = \frac{2\ell^* S_L^2}{2G_{12}\mathcal{G}_6 - \ell^* S_L^2}$$

The parameters A_{1-} , A_{2+} and A_{2-} are calculated numerically using the algorithms proposed in [15]. Finally, the out-of-plane damage variables are defined as:

$$\begin{aligned} d_3(r_{1-}, r_{2-}) &= 1 - [1 - d_{1-}(r_{1-})][1 - d_{2-}(r_{2-})] \\ d_4(r_{2+}) &= d_6(r_{2+}) \\ d_5(r_{1+}) &= d_1(r_{1+}) \end{aligned} \quad (6.24)$$

6.2.4 Maximum in-plane finite element size

The slope of the softening law for each damage mode is determined to dissipate the correct energy according to the element size, i.e. the area under the stress-strain chart is the corresponding fracture toughness divided by the finite element characteristic length \mathcal{G}_M/ℓ^* ($M = 1+, 1-, 2+, 2-, 6$), see Equation (6.16). In order to avoid snap-back of the softening branch for each failure mode, a maximum characteristic element length ℓ_{max}^* can be found by equating the elastic energy of the element, $\frac{1}{2}X_M\varepsilon_M(\ell^*)^2h_{el} = \frac{1}{2}\frac{X_M}{E_M}(\ell^*)^2h_{el}$, with the energy dissipated in the fracture process, $\mathcal{G}_M\ell^*h_{el}$:

$$\ell_{max}^* = \frac{2E_M\mathcal{G}_M}{X_M^2}; \quad M = 1+, 1-, 2+, 2-, 6 \quad (6.25)$$

where h_{el} is the element thickness. E_M , \mathcal{G}_M , and X_M , are, respectively, the Young modulus, fracture toughness and ply strengths corresponding to each failure mode (it is assumed that $E_6 = G_{12}$ and $X_6 = S_L$).

For elements larger than the maximum element size ℓ_{max}^* , it is not possible to guarantee the correct energy dissipation without avoiding snap-back in the constitutive response. For these elements, a reduction of the corresponding damage mode strength can be computed as:

$$X_M = \sqrt{\frac{2E_M \mathcal{G}_M}{\ell_{max}^*}}; \quad M = 1+, 1-, 2+, 2-, 6 \quad (6.26)$$

6.2.5 Material properties

Standard test methods are available to measure the majority of the independent ply material properties needed for the definition of the damage model described. The model requires the following inputs:

- Ply elastic properties (E_1 ; E_2 ; G_{12} ; G_{23} ; ν_{12} ; ν_{23}) and ply strengths (X_T ; X_C ; Y_T ; Y_C ; S_L). These properties can be measured using test standards defined by the American Society for Testing Materials (ASTM) [151–153], or others defined by the product manufacturer.
- Four components of the fracture toughness, associated with longitudinal failure in tension and compression (\mathcal{G}_{1+} and \mathcal{G}_{1-} , respectively) and with transverse failure in tension and shear (\mathcal{G}_{2+} and \mathcal{G}_6 , respectively). \mathcal{G}_{2+} can be measured using a standard test procedure devised by the ASTM [154]. \mathcal{G}_6 can be measured using the four-point bending end-notched flexure test proposed by Martin et al. [155]. \mathcal{G}_{1+} and \mathcal{G}_{1-} are measured using compact tension and compact compression tests developed by Pinho et al. [156] (there is no standard test method to measure the fracture toughness associated with fracture in the longitudinal direction).

The fracture toughness \mathcal{G}_{2-} is dependent on \mathcal{G}_6 and on the fracture angle α_0 in the form $\mathcal{G}_{2-} = \mathcal{G}_6 / \cos(\alpha_0)$ [14, 15]. Additionally, the model requires the input of the in situ strengths Y_T^{is} and S_L^{is} , which are functions of the independent material properties.

6.2.6 In-situ strengths

The damage activation functions are based on the LaRC04 failure criteria, which take into account the in-situ effect. The in-situ effect is the capacity of the plies to increase their strengths when they are in a laminate, compared with the strength of the same ply in a unidirectional laminate. The transverse and the shear strengths are affected by the in-situ effect, and they are function of the ply thickness h_p , of the ply position in the laminate, and of the fiber orientation of the adjacent plies. The equations which define the corresponding in-situ strengths in function of the position and thickness of the ply are listed below [74]:

In-situ transverse tensile strength

- For a thick embedded ply: $Y_T^{is} = 1.12\sqrt{2}Y_T$
- For a thin embedded ply: $Y_T^{is} = 2\sqrt{\frac{E_2}{1 - \nu_{12}\nu_{21}} \frac{\mathcal{G}_{2+}}{\pi h_p}}$
- For an outer ply: $Y_T^{is} = 1.12^2\sqrt{\frac{E_2}{1 - \nu_{12}\nu_{21}} \frac{\mathcal{G}_{2+}}{\pi h_p}}$

In-situ shear strength

$$S_L^{is} = \sqrt{\frac{(1 + \varsigma\chi G_{12}^2)^{1/2} - 1}{3\varsigma G_{12}}} \quad (6.27)$$

where ς defines the non-linearity of the shear stress-shear strain relation, which is zero for a linear behavior. The parameter χ is defined according to the configuration of a given ply:

- For a thick embedded ply: $\chi = \frac{12S_L^2}{G_{12}} + \frac{72}{4}\varsigma S_L^4$
- For a thin embedded ply: $\chi = \frac{48\mathcal{G}_6}{\pi h_p}$
- For an outer ply: $\chi = \frac{24\mathcal{G}_6}{\pi h_p}$

6.3 Limitations of continuum damage models

It is important to capture properly the location and the shape of the damage, specially in laminated composite materials subjected to impact events, where matrix cracking can trigger delaminations with peculiar patterns at certain locations. This information is interesting for any loading condition and structure, because it indicates the weakest regions where the structure could fail.

The simulation of progressive failure of laminated composite structures using continuum damage models formulated at the meso-scale level, and implemented in a finite element code, has some limitations. The predicted results may exhibit dependence on the shape and the orientation of the finite elements, due to the fact that a crack simply tends to grow following the shortest way, and also due to the so-called stress locking effect. As documented Jirásek [157], stress locking means spurious stress transfer across a widely open crack and arises after strain localization due to softening. Basically, it is caused by the poor kinematic representation of the discontinuous displacement field around a macroscopic crack. Triangular and quadrilateral element shapes are analyzed by Jirásek [157] in order to demonstrate the apparition of spurious shear strains which yields to the transfer of stresses across the crack.

The stress locking produces mainly two limitations. On the one part, a spurious stress transfer occurs across a widely opened crack allowing the structure to stand more loading. Therefore, the appearance of spurious damage in other regions of the structure can be done. On the other part, the simulated crack bands exhibit strong directional bias and propagate aligned with the element sides of the mesh. The dependence of the crack path on the mesh pattern is specially true for problems with strain localization, such as failure on laminated composite structures due to fiber pull-out and matrix cracking, without fiber breakage.

There are fast solutions to decrease the effect of these limitations. Concerning to the spurious stress transfer, a solution is to delete the damaged elements from the mesh. Deleted elements have no ability to carry stresses and, therefore, have no contribution to the stiffness of the model [124]. However, this solution has a drawback. Certainly, for directional damage models is not suitable to consider an element completely damaged when one of the damage variables reaches the maximum value, and

even more when the loading conditions can change during the simulation. Typically, in laminated composite plates, it is considered that an element is completely damaged when the fiber breaks. However, this criterion is unsuitable for cases where the structure fails without fiber breakage. In addition, when an explicit finite element code is used, spurious new crack bands can be triggered after the creation of the first band and the corresponding deletion of elements. This fact is caused when the simulation is too much accelerated artificially.

Concerning to the capture of crack paths, the solution is to generate meshes that are oriented in the corresponding fiber direction, as used by Laš and Zemčík [158]. This solution can be applied easily for the composite structures considered herein, because each ply has straight fibers.

In order to check if the intralaminar damage model shown in previous section captures properly the matrix cracking path, different simulations are carried out on an off-axis single ply subjected to tensile loading. For off-axis angles of 45° and more, the stiffness in fiber direction remains almost completely unaffected, and during the analysis the specimen should fail with a matrix crack running in the fiber direction.

The 3D specimen virtually tested is depicted in Figure 6.2. In detail, the dimensions are: 5mm in width, 28mm in length, and 0.125mm in thickness. Elastic elements are defined at the left and right parts, and comprise the 40% of the total length. The nodes located at the left edge are constrained in the y direction, in exception of one of these nodes that has all displacements constrained. The tensile displacement is applied on the column of nodes located at the right edge. The material properties for unidirectional plies used to feed on the intralaminar damage model are summarized in Table 7.1. In order to trigger localization, the strengths of the central element are reduced a 20%. Five orientations are tested: $\theta = 0^\circ, 10^\circ, 45^\circ, 60^\circ$, and 90° . The in-plane element size is defined as 0.25mm at each direction, and the elements are not oriented according to the fiber orientations (in exception of $\theta = 0^\circ$ and $\theta = 90^\circ$). Finally, the elements that are damaged in the local transverse direction, i.e. matrix damage, are deleted from the mesh in order to avoid spurious stress transfer when the first macro-crack is created.

Figure 6.3 shows the predicted matrix crack bands for each off-axis angle, using a mesh which is not oriented according to the fiber orientation (in exception of $\theta = 0^\circ$ and $\theta = 90^\circ$). The field output plotted corresponds to the damage variable at the

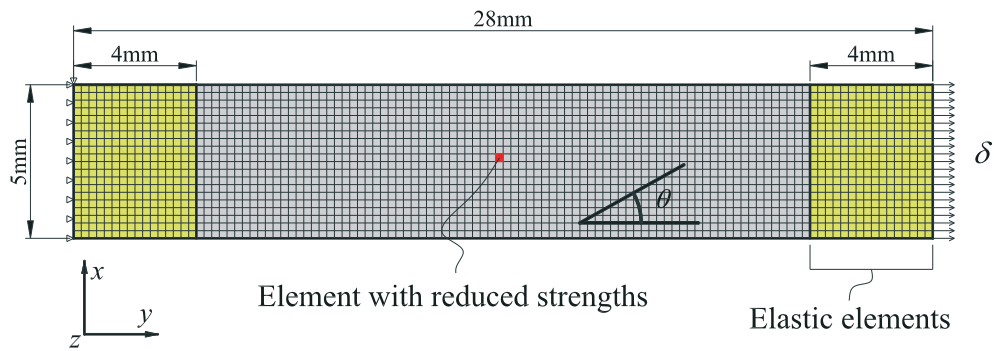


Figure 6.2: Details of the off-axis ply subjected to tensile loading.

local transverse direction. As can be observed, for angles $\theta = 45^\circ$ and $\theta = 60^\circ$ the crack path is not well predicted, clarifying the dependence of the crack path on the mesh pattern.

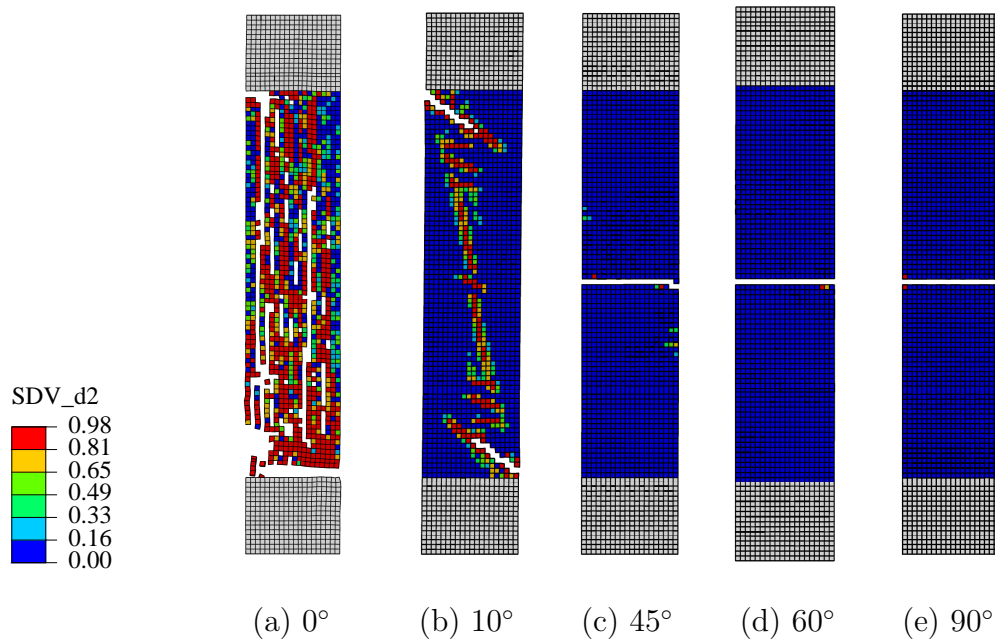


Figure 6.3: Predictions of the matrix cracks in an off-axis ply subjected to tensile loading (using non-structured mesh).

Accordingly, Figure 6.4 shows the same simulations but using a structured mesh which follows the corresponding fiber orientation. As expected, the damage patterns are captured properly. For the fiber angle $\theta = 10^\circ$, additional cracks have appeared

with different orientations. However, this result can be attributed to the loading conditions that do not yield to an homogeneous stress state which promotes edge effects [159].

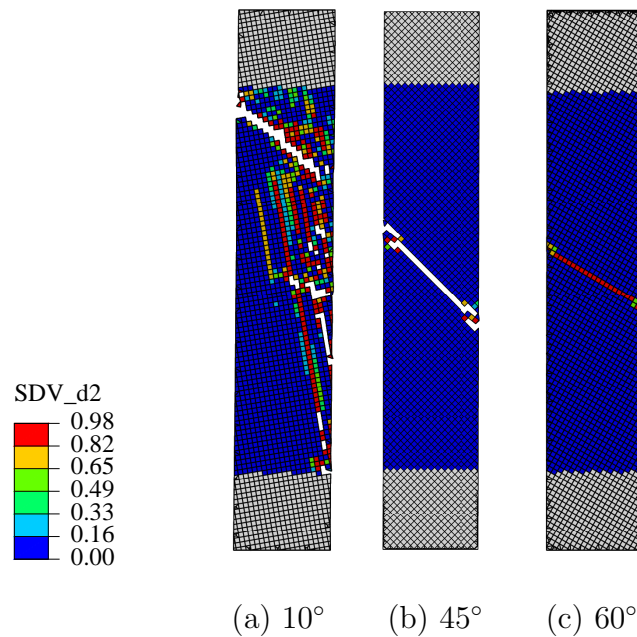


Figure 6.4: Predictions of the matrix cracks in an off-axis ply subjected to tensile loading (using a structured mesh).

Although the crack pattern is not well predicted when the mesh is not oriented according to the fiber angle, the resulting ultimate strengths for both types of meshes are equal, as can be seen in Figure 6.5.

Using the definitions considered in previous test, at following is presented another interesting simulation of a $[45/-45]_S$ laminate subjected to tensile loading. The mesh is oriented according to the corresponding fiber orientation. Non-zero thickness cohesive elements are modeled at each of the two interfaces with different orientation of the adjacent plies ($h_e = 0.01\text{mm}$). The central plies are modeled together, with an element thickness of 0.25mm . The outer plies are modeled with an element thickness of 0.125mm . The properties used to fed on the cohesive elements are summarized in Table 7.2. The strategy to generate the model is as suggested in Figure 7.2.a of next Chapter 7. It is expected that the specimen should fail in tension by pull-out without any fiber failure, as it is depicted in Figure 6.6.

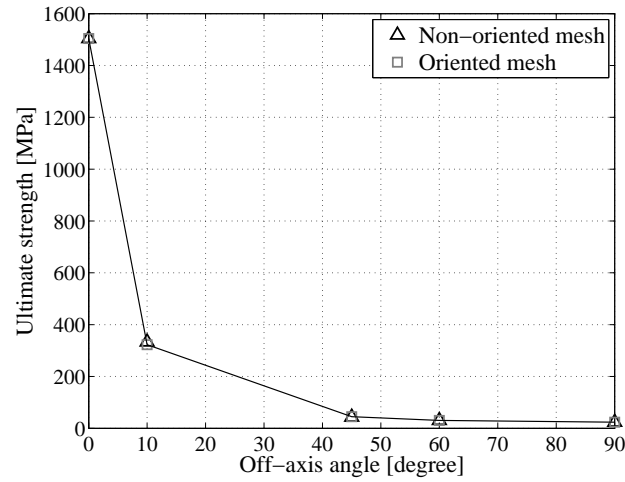


Figure 6.5: Ultimate tensile strengths versus off-axis angle.

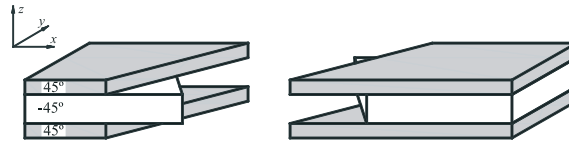


Figure 6.6: Schematic of pull-out failure of $[45/-45]_S$ laminate with no fiber fracture (after Wisnom [160]).

As can be seen in Figure 6.7, the expected crack bands are not well predicted. All plies have broken following the orientation of the middle ply fibers. Therefore, it is concluded that although structured meshes improve the description of the damage crack bands, more research is required in order to predict better these phenomena.

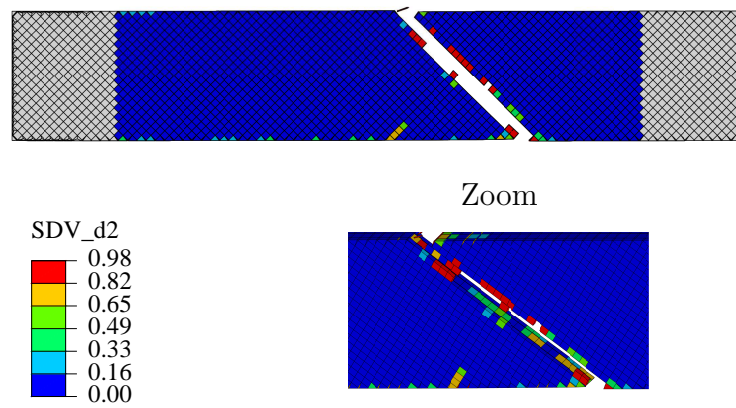


Figure 6.7: Prediction of the matrix crack bands of laminate $[45/ - 45]_S$ subjected to tensile loading.

Chapter 7

Virtual testing

7.1 Introduction

The simulation of the drop-weight impact and CAI tests, which were defined in Chapter 3, is presented herein. Accordingly, a description of the key FE pre-processing definitions for the proper working of the virtual tests is done. All these definitions are capabilities offered by the commercial FE code Abaqus/Explicit [124], in exception of the constitutive models for the description of the material behavior (the delamination and the intralaminar damage mechanisms). These constitutive models, presented in Chapters 5 and 6, are included in the FE simulations by the implementation of user-written subroutines of Abaqus/Explicit. It should be noted that due to the formulations considered, the simulations presented are limited to quasi-static loading and low strain rates situations where drop-weight impact can be considered well fitted.

The results of the virtual tests and the corresponding comparison with the experimental data are also shown and discussed in detail.

7.2 Description of the FE models

7.2.1 Explicit FE code

There are several factors that contribute to decide to use an explicit FE code for the simulation of the impact event. The drop-weight impact on laminated composite

plates is a fast dynamic problem with severe material nonlinearities and discontinuities, such as contact. In addition, large number of elements should be used in order to describe suitably the damage type and extension in the material. All these factors make difficult or impossible the convergence of the model when an implicit FE code is applied.

The explicit dynamic integration method is also known as the forward Euler or the central difference algorithm. At each time increment, the explicit dynamics procedure solves a wave propagation problem: out-of-balance forces are propagated as stress waves between neighboring elements. It uses the central difference time integration scheme for integrating the resultant set of nonlinear dynamic equations. The method assumes a linear interpolation for velocities between two subsequent time steps and no stiffness matrix inversions are required during the analysis. The drawback of the explicit method is that it is conditionally stable for nonlinear dynamic problems.

The increment of time used for each calculation, δt , is based on a critical stable value, δt_{stable} . A bounded solution is obtained only when the time increment is less than the stable increment. For linear and nonlinear problems alike, explicit methods require a small time increment which is independent of the type and duration of loading, and depends solely on the highest natural frequency ω_{max} and on the critical damping ξ in the mode with the highest frequency. That is:

$$\delta t_{stable} \leq \frac{2}{\omega_{max}} \left(\xi \sqrt{1 + \xi^2} \right) \quad (7.1)$$

Alternately, instead of looking at the global model, a simple estimate which is efficient and conservative can be used. It is based on the highest frequency of each individual finite element of the model, which is always associated with the dilatational mode. It can be shown that the highest element frequency is always higher than the highest frequency in the assembled finite element model. Then, this method is more conservative, because it will give a smaller stable time increment than the true stability limit based on the maximum frequency of the entire model. Based on these observations, the stability limit is defined as the smallest time for a dilatational wave to cross any element in the mesh. It can be approached by means of the called Courant condition which considers the minimum dimension of the element ℓ_{min} and the wave speed of the material c_m as:

$$\delta t_{stable} \leq \frac{\ell_{min}}{c_m} \quad (7.2)$$

where the wave speed is a material property defined as $c_m = \sqrt{\frac{E}{\rho}}$. E and ρ represent the bulk stiffness and the density, respectively, of the considered finite element [124, 161].

7.2.2 Plate modeling

Alternatives for plate modeling

The constitutive models for the description of the delamination and the intralaminar damage mechanisms have been formulated with the aim of simulating the composite structure at the meso-scale level. Although the initiation and the propagation of failure inside of each ply occur on the micro-scale, the meso-scale approach is adopted because the modeling of the entire microstructure is computationally unaffordable. At this scale level, the interaction of both constitutive models is ensured since they are used in the same FE model.

In this way, the level of FE discretization considered for a laminated composite plate is illustrated in Figure 7.1. In the through-the-thickness direction, each ply is represented by a single layer of 3D solid elements, at which the intralaminar damage model is assigned. In the case of delamination, the crack planes are known a-priori. Under impact loading, delamination only occurs between plies with different fiber orientation. Therefore, cohesive connections described by means of the delamination model are introduced only in these locations. This simplification goes in favor of reducing the computational time of the analysis, since in ply clusterings with equal fiber orientation no cohesive connections are defined.

According to the capabilities offered by the Abaqus/Explicit software, different alternatives for plate modeling can be considered, as shown in Figure 7.2. Basically, these alternatives are differentiated as how the cohesive connections are modeled.

For all cases shown in Figure 7.2, the intralaminar damage model is assigned to the corresponding finite elements by means of the implementation of a user-written material subroutine, called VUMAT [124].

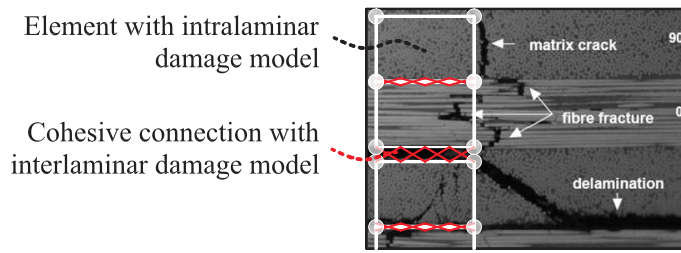


Figure 7.1: Superposition of the finite element discretization with an image of a laminated composite material (image of the composite material from Olsson [162]).

The case depicted in Figure 7.2.a is the most common way to model the composite plate. It consists of modeling the cohesive connections using solid (non-zero thickness, $h_e \neq 0$) or surface finite elements (zero thickness, $h_e = 0$), and the in-plane size of the mesh of all layers is defined equal, including composite plies and cohesive type layers. Therefore, the nodes of each layer are shared with the neighboring layers. In this case, the delamination model can be implemented using a user-written material subroutine VUMAT (as shown in Chapter 5), or a user-written finite element subroutine, called VUEL. A drawback of using cohesive elements is that it makes worse the runtime analysis, because their thickness is small, yielding to small stable time increments.

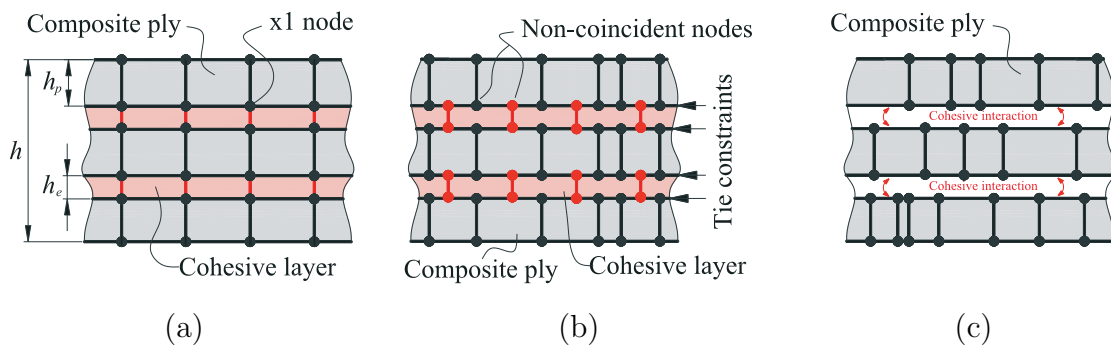


Figure 7.2: Strategies for modeling a laminated composite plate: (a) using cohesive elements and a regular mesh, (b) using cohesive elements and tie constraints, or (c) using surface-based cohesive interactions. The variables shown are: h , the plate thickness; h_e , the thickness of the cohesive connection; and h_p , the thickness of the ply clustering.

If non-coincident meshes are used because the mesh of each ply is structured according to the corresponding fiber orientation (as suggested in Section 6.3 in order to describe properly matrix cracks and thus to reduce the mesh dependency), or simply because it is desired to use different in-plane mesh sizes for each layer, the use of *Tie Constraints* is needed (see Figure 7.2.b). A tie constraint is a capability of Abaqus/Explicit that provides a simple way to bond surfaces together permanently, making the translational and rotational motion equal for the pair of surfaces. However, the use of tie constraints requires additional computational resources and runtime for the pre-processing and analysis phases of the FE model, often making the acquisition of the virtual solution unaffordable.

Alternately to the case depicted in Figure 7.2.b, it is possible to use a surface-based cohesive interaction by the implementation of a user-written subroutine type VUINTER [124] (see Figure 7.2.c). This approach is a quick and easy way to model cohesive connections, avoiding the need of defining cohesive elements and tie constraints, which oppose in improving the runtime of the analysis. However, surface-based cohesive interactions also can yield to large runtime analysis because contact algorithms are computationally heavy, especially when the connected meshes are highly refined. In addition, this type of interaction requires to define one of the connected surfaces (the slave surface), smaller than the other surface which acts as a reference (master surface), in order to know at any increment of time the surface locations for the corresponding nodal calculations. Therefore, it supposes that a small part of the surfaces can not be linked, and if the cohesive connection is subjected to large relative in-plane sliding, the cohesive connection can yield to inaccurate results. Finally, another limitation of using a surface-based cohesive interaction is that the visualization of user state variables of the implemented subroutine for the post-processing FE phase is not available. Therefore, to plot the virtual extensions and shapes of the delaminated areas is not possible.

Despite the fact that using in-plane structured meshes oriented with the fiber direction has clear advantages, the solution finally adopted for the plate discretization is the case depicted in Figure 7.2.a, by using two user-written material subroutines VUMAT coded with FORTRAN programming language. After several tests using the different alternatives, the case adopted yields to a well-balanced compromise of required and available computer resources, capabilities for pre- and post-processing

FE phases, as well as the acquisition of suitable results in an acceptable runtime analysis, which is the fact with more weight.

Type of finite element and dimensions

All layers of the laminated composite plate, including composite plies and cohesive layers, are modeled by means of 3D hexahedral continuum solid elements with eight nodes and reduced integration (one integration point), called C3D8R [124].

As noted previously, in the through-the-thickness direction each ply clustering or cohesive layer is represented by a single layer of solid elements. The thickness of all cohesive layers is subtracted from the corresponding real plate thickness. In detail, the thickness of each cohesive layer, h_e , is defined with 0.01mm. Using the properties summarized in Table 7.2, the cohesive thickness selected is much smaller than the maximum value obtained by means of Equation (5.77) in order to guarantee the correct interlaminar energy dissipation without causing snap-back in the constitutive response.

With the aim of reducing the CPU analysis time, the in-plane mesh size is variable. A central zone of 60mm×60mm with a refined regular mesh of 0.3mm×0.3mm is defined ($\ell_x \times \ell_y$), and as from of it and until the plate free edges a biased mesh is modeled (see Figure 7.3). The elements of the plies located in the central zone are driven by the intralaminar damage model, whereas the behavior of the remaining elements is described by a transversally isotropic elastic material from the Abaqus/Explicit material library. However, different in-plane regions with different materials are not considered for the cohesive layers, which are described exclusively by the delamination damage model.

The reason of using elements with small in-plane sizes in comparison with the plate dimensions is due to requirements of the damage models for the accurate prediction of the structure response.

On the one hand, for intralaminar damage elements with a characteristic length (defined as $\ell^* = \sqrt{\ell_x \ell_y}$) higher than the maximum size ℓ_{max}^* given by Equation (6.25), the strength of the corresponding damage mode is reduced in order to avoid snap-back in the constitutive response. These reductions are not adequate in cases where the results depend strongly on the strengths for damage onset, such as the prediction of the critical impact load F_d for the sudden loss of the structure stiffness.

The in-plane dimensions of the intralaminar damage elements are defined small enough to avoid these strength reductions as can be deduced using the properties summarized in Table 7.1.

On the other hand, the in-plane size of the cohesive elements should be selected so the cohesive zone length is suitably split with enough elements (at least with three or four elements). Accordingly, the in-plane element size selected in the central zone of the plate is suitable for a proper discretization of the cohesive zone length, as can be deduced using the properties of Table 7.2 and by means of Equations (5.78) and (5.79). However, the cohesive description in regions close to the edges of the plate is deteriorated, but it is not of significance since the delaminations occur mainly into or near to the central region.

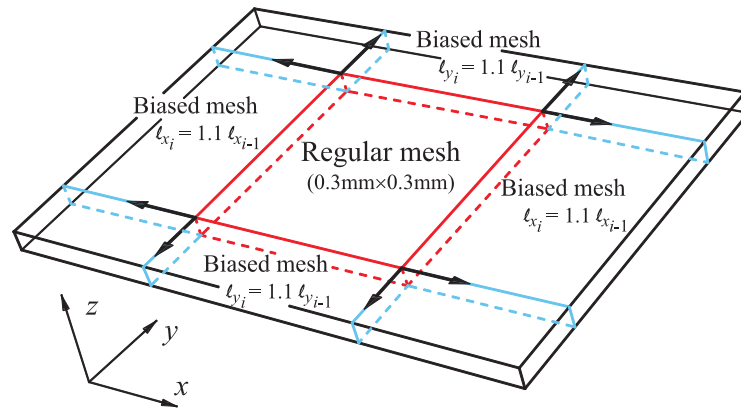


Figure 7.3: In-plane mesh size of the plate.

Definitions to control finite element instabilities

The use of first-order and reduced-integration finite elements can result in a mesh instability problem, commonly referred to as *hourglassing*. The hourglassing problem means that the elements can distort in such a way that the strains calculated at the integration point are all zero, which, in turn, leads to uncontrolled distortion of the mesh with no stresses resisting the deformation. Abaqus/Explicit includes control methods for suppressing hourglassing, where the *Enhanced Hourglass Control* approach is the method selected for all simulations.

Moreover, a *Distortion Control* is used in order to prevent elements from inverting (negative element volumes) or other excessive distorting which are not caused by

hourglassing instabilities, rather by the loading conditions and by the level of material degradation. This control applies penalty loads when the element is inverted a predefined proportion of the corresponding original element size.

Additionally, a damping associated with the volumetric straining of the elements, called *Bulk Viscosity*, is introduced with the purpose of improving mainly the dynamic simulation of the impact tests. A bulk viscosity pressure that varies linearly with the volumetric strain is defined in order to damp ringing in the highest element frequency. Moreover, a pressure that varies quadratically with the volumetric strain is also introduced with the aim of preventing elements from collapsing under extremely high velocity gradients. The damping coefficients used are the ones suggested by the FE software, 0.06 and 1.2 for linear and quadratic damping, respectively.

Once the stiffness of a finite element is fully degraded, this element has no contribution to the stiffness of the model, but can reduce the stable time increment during the simulation. Abaqus/Explicit offers the choice to remove these elements from the mesh. It is selected that a cohesive element is removed when its scalar damage variable d reaches the value of 0.99. However, the criterion for deleting ply elements is more complex since a directional damage model describes their constitutive behavior. In the simulations proposed here, these elements are removed when the longitudinal damage variable d_1 reaches 0.999, i.e. fiber breakage. As can be seen, the elements are removed before the damage variables reach the unity in order to avoid possible sudden element distortions because of the absence of residual stiffness. Accordingly, the transverse and shear damage variables d_2 , d_3 , d_4 , d_5 and d_6 are also limited to a maximum value of 0.99.

Mainly, the cohesive elements will determine the stable time increment of the whole model due to their small thickness, as it can be deduced from Equation (7.2). The computational efficiency of the simulations is improved by scaling the mass of these elements by means of the *Variable Mass Scaling* capability of Abaqus/Explicit. In detail, it is selected to scale the masses of only the cohesive elements whose stable time increment is less than a predefined value. Such definitions are selected taking care of never increase significantly the overall mass of the plate.

In order to verify if excessive use of the solutions mentioned for decreasing numerical difficulties (hourglass control, the distortion control, the viscosity damping,

and mass scaling) occurs during the simulations, an engineering judgment based on the lecture of the corresponding energy variables should be performed. Typically, the energy generated by each one of these solutions must be less than 1% of the internal energy of the system.

Material properties

The material properties of the AS4/8552 carbon-epoxy unidirectional pre-preg are summarized in Table 7.1. These properties are inputs to fed on the intralaminar damage model. Some of the properties were obtained by testing specimens manufactured with the same pre-preg roll of the specimens used for the experimental impact and CAI tests. The properties which were not obtained experimentally, are extracted from the literature.

Table 7.1: Hexply AS4/8552 properties. The properties pointed out with (*) are extracted from [97].

Density [kg/mm ³]	1590×10^{-9}
Elastic properties	$E_1 = 128.00\text{GPa}; E_2 = 7.63\text{GPa};$ $E_6 = G_{12} = 4.36\text{GPa};$ $\nu_{12} = 0.35; \nu_{23} = 0.45$
Strength [MPa]	$X_{1+} = X_T = 2300.0; X_{1-} = X_C = 1531.0^*;$ $X_{2+} = Y_T = 26.0; X_{2-} = Y_C = 199.8^*;$ $X_6 = S_L = 78.4$
Fracture toughness [N/mm]	$\mathcal{G}_{1+} = 81.5^*; \mathcal{G}_{1-} = 106.3^*; \mathcal{G}_{2+} = 0.28^*; \mathcal{G}_6 = 0.79^*$

Other definitions required by the intralaminar damage model are: $X_{PO} = 0.1X_T$ (pull-out strength), $\mathcal{G}_{1+}^L = 0.2\mathcal{G}_{1+}$ (energy dissipated at linear softening), $\mathcal{G}_{1+}^E = \mathcal{G}_{1+} - \mathcal{G}_{1+}^L$ (energy dissipated at exponential softening), $\mathcal{G}_{2-} = \mathcal{G}_6 / \cos(\alpha_0)$, and $\alpha_0 = 53^\circ$. Since the differences of temperature and moisture are not considered in the simulations, the definition of the thermal coefficients and of the hygroscopic expansion are not required. In addition, the transverse tensile strength Y_T and the in-plane shear strength S_L are adjusted in order to consider the in-situ effect

according to the equations shown in Chapter 6. For the calculation of the in-situ in-plane shear strength, it is taken $\varsigma = 2.98 \times 10^{-8}$.

On the other hand, the properties used for the interlaminar damage model are summarized in Table 7.2.

Table 7.2: Interface properties.

Density [kg/mm ³]	1590×10^{-9}
Elastic properties	$E = 7.63\text{GPa}; \nu = 0.45$
Mode I strength [MPa]	$\tau_3^o = Y_T = 26.0$
Fracture toughness [N/mm]	$\mathcal{G}_{Ic} = \mathcal{G}_{2+} = 0.28; \mathcal{G}_{IIc} = \mathcal{G}_6 = 0.79$

Other definitions required to fed on the interlaminar damage model are: mode II interlaminar shear strength, $\tau_1^o = \tau_3^o \sqrt{\frac{\mathcal{G}_{IIc}}{\mathcal{G}_{Ic}}}$ [13]; and the parameter of the least-square fit of the mixed-mode fracture toughness values, $\eta = 1.45$ [97].

7.2.3 Virtual test set-up

Drop-weight impact tests

According to the impact test set-up used for the real tests shown in Figure 3.1, the virtual models should reproduce the same conditions but in the most simplified way in order to avoid unnecessary computer time consuming.

In Figure 7.4 is shown the assembly of the different components considered for the simulation of the impact test. The fixture base support and the hemispherical impactor are defined as a rigid bodies since they are stiff steel parts whose stresses and strains are not of interest. In detail, the impactor is modeled by a lumped mass element and the fixture base by 3D rigid elements with four nodes, called R3D4. If domain parallelization is used for the analysis calculation, the fixture base should be meshed with enough elements in order to split it in enough element sets, just as much as the number of domains. The maximum element length selected for the fixture base mesh is of 5mm.

The motion of a rigid body is governed by the motion of a single reference point at which the boundary conditions, initial conditions and physical parameters are defined. Certainly, the fixture base is defined with all the degree of freedom

constrained. The impactor is also defined with all the degree of freedom fixed, in exception of the out-of-plane displacement. In order to capture the effect of the impactor drop, the impactor is modeled just before of the impact position by specifying an initial impact velocity consistent with the height of free fall. In addition, a concentrated load is defined on the impactor to describe the weight load, although its effect is practically insignificant since the impact forces reaches much higher values.

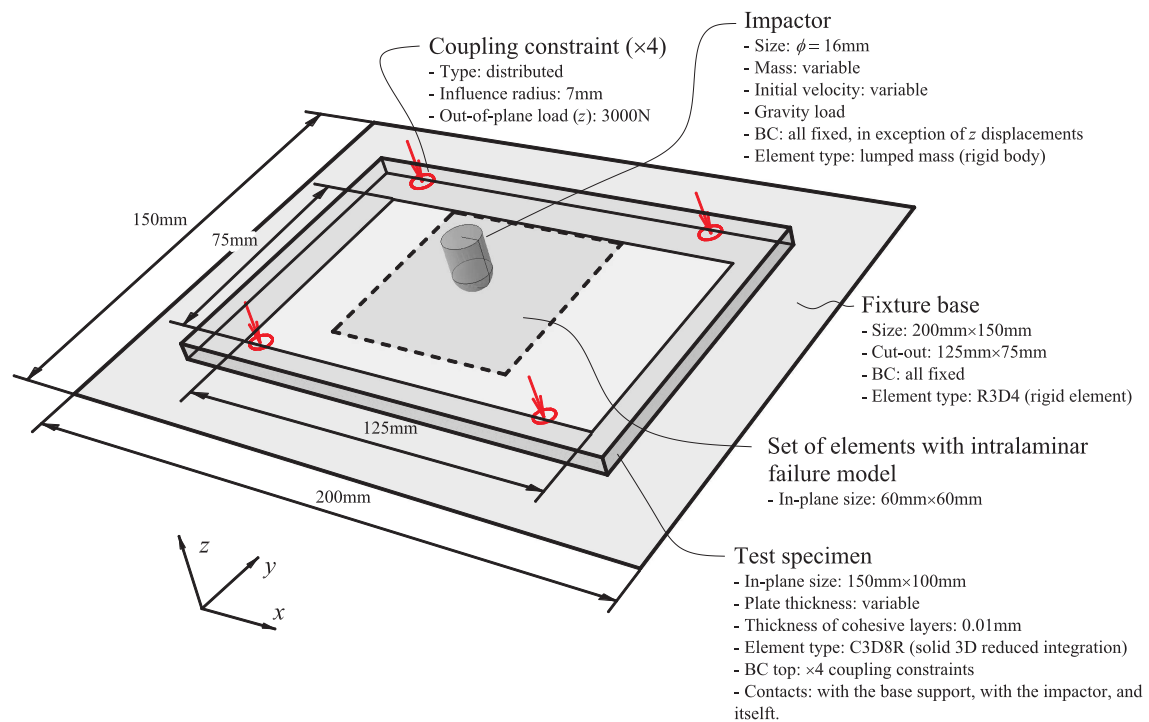


Figure 7.4: Set-up of the virtual impact tests.

The four rubber-tipped clamps which restrain the specimen over the fixture base are modeled by means of the *Distributed Coupling Constraint* capability. These constraints couple the motion of a group of nodes to the motion of a master node. Therefore, at each master node is defined an instantaneous out-of-plane load of 3000N, which is uniform distributed to the corresponding affected set of nodes located on the top plate surface. The influence radius to select the corresponding set of coupled nodes is of 7mm.

On the other hand, contact constraints are required in order to describe the contact between the impactor and the top face surface of the plate, and also the back face surface of the plate with the fixture base. The contact approach used is

the *General Contact* algorithm of Abaqus/Explicit, which defines a linear pressure-overclosure relationship between the contacting surfaces, where the contact stiffness is chosen automatically by the software, and there is not limit to the magnitude of the contact pressure that can be transmitted. In addition, the Coulomb friction model which relates the maximum allowable frictional shear stress across an interface τ_{max} to the normal contact pressure between the contacting bodies P , $\tau_{max} = \mu P$, is defined. In detail, the friction coefficient for contacts between a steel material and a composite material is considered as $\mu = 0.3$.

As it has been noted in previous section, once the finite elements of the plate are completely degraded, they are removed from the mesh in order to improve the computation efficiency. Due to this fact, new internal element faces can be subjected to contact with the impactor, or even with the neighboring elements. Therefore, contact constraints should be defined for these possible interactions.

Since in the proposed impact simulations the perforation does not occur, it is enough to consider that the impactor can take contact with the first three top surfaces of the element sets which describe the first three composite plies.

In addition, the internal faces of the elements located in the regular zone depicted in Figure 7.3 are modeled in such a way that could take contact themselves during the simulation. The friction coefficient in delaminated interfaces varies from 0.2 for $0^\circ/0^\circ$ interfaces (with sliding in the longitudinal direction), to 0.8 for $90^\circ/90^\circ$ interfaces (with sliding in the transversal direction) [163]. An average friction coefficient of 0.5 is applied between element faces, as suggested in [97].

It should be noted that any contact definition increases the required computer memory, as well as it makes worse the runtime analysis of the model, since the relative displacement between contact surfaces is checked periodically during the simulation. Therefore, the fewer contact definitions, faster the simulation will reach the solution.

CAI tests

Once the simulation of the impact test is finished, the CAI test is subsequently carried out. Therefore, the post-impact structure state should be imported and the new boundary conditions which reproduce the CAI test should be defined. In detail, the damaged plate is imported by means of the *Restart* and *Import* capabilities of

Abaqus/Explicit, and the boundary conditions are illustrated in Figure 7.5. These boundary conditions are simply modeled by constraining the corresponding degree of freedom of the nodes located at the sites pointed out.

Although the CAI test is essentially quasi-static, it will be simulated by means of the dynamic FE code Abaqus/Explicit. The reason is due to the fact that high material and geometrical non-linearities occur, yielding to severe convergence difficulties if an implicit FE code is used. Accordingly, a displacement loading is applied with sufficiently slowness at one of the short edges of the plate (see Figure 7.5), so the kinetic energy is kept despicable against the internal energy of the system.

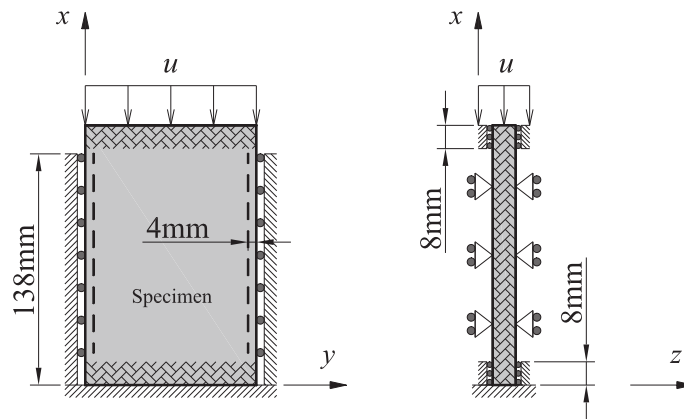


Figure 7.5: Boundary conditions of the CAI test.

7.2.4 Energy balance

The evolution of the energy variables is a valuable data to know the events that can occur during the numerical impact simulation, and then to assess if the simulation is yielding to an appropriate response. Mainly, these events are the onset and the progression of each damage mechanism that the composite material can suffer, and also, the use of the solutions considered for the proper working of the numerical models, such as the generation of artificial energy for hourglassing prevention.

For the virtual tests considered herein, the energy balance equation can be written as:

$$E_T = E_K + E_I + E_F + E_V - W_E - W_C - W_{MS} \quad (7.3)$$

where E_T is the total energy of the system, E_K is the kinetic energy, E_I is the internal energy, E_F is the frictional dissipation energy, E_V is the energy dissipated by bulk viscosity damping, W_E is the work of the external forces, W_C is the work done by contact penalties, and W_{MS} is the work done in propelling mass added in mass scaling. The internal energy can be split in the following terms:

$$E_I = E_E + E_H + E_{DC} + E_{Dm} + E_{Df} + E_{Dd} \quad (7.4)$$

where E_E is the recoverable strain energy (elastic energy), E_H is the energy generated to prevent hourglassing, and E_{DC} is energy dissipated by distortion control. The terms E_{Dm} , E_{Df} , and E_{Dd} are the energy dissipated by matrix damage, by fiber damage, and by delamination, respectively.

Most of the energy terms can be requested for the entire model or for specific element sets of the model.

7.3 Results of the virtual tests and comparison with experimental data

At following, the results of the impact test and CAI test simulations are presented and compared with the experimental data shown in Chapter 4.

The simulations have been performed using multiple processors on separate machines, i.e. cluster. Abaqus/Explicit automatically breaks up the FE model into domains and assigns each domain to a processor, so the analysis is carried out independently in each domain. Since the domains share common boundaries, the information is passed between the domains at each increment via the MPI interface mode (Message Passing Interface) [124]. At the end of the analysis, the individual files are merged automatically.

In detail, the FE models are parallelized in a cluster composed by a group of six linked computers, each one with 8GB RAM and four processors (24 CPUs). The whole runtime analysis of the impact and CAI tests has ranged between twelve and fifteen days, depending on the plate stacking sequence. The simulations are heavy due to the large number of composite plies and cohesive interfaces (each layer is modeled with an element), the small in-plane sizes of the elements, and the large

number of contact definitions. These factors yield to small time increments (of the order of 1e-9s), where each one requires fairly long time of analysis. In addition, the impact events considered are long in time (of the order of 5e-3s), so large amount of increments are required to complete the simulation.

It should be noted that not all the impact configurations tested are performed virtually, because of limitations in computer memory resources for the pre-process and analysis FE phases. Only, some cases of the ply clustering study are considered. The unresolved impact configurations are proposed as future works.

Laminate L04

Figures 7.6, 7.7 and 7.8 show the comparisons between the experimental and the numerical evolutions of the impact force of the laminate L04 for 38.6J, 28.6J and 19.3J, respectively. As can be observed, the whole profiles and the contact times are quite well predicted, whereas the damage thresholds F_d are clearly over-predicted. Moreover, in contrast with the experimental results, it is detected that the numerical values of F_d are not kept constant by changing the impact velocity.

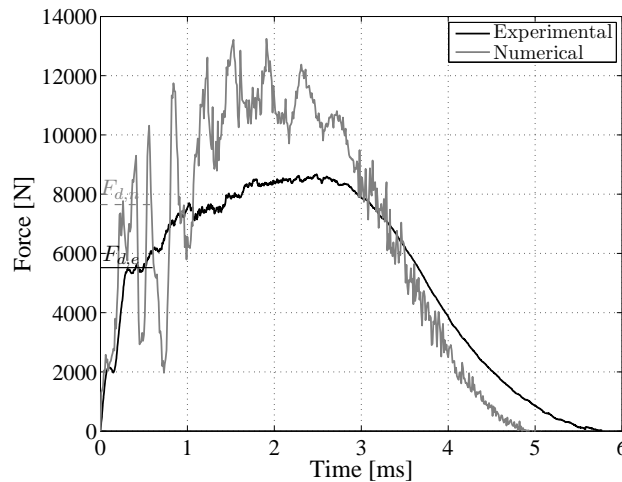


Figure 7.6: Experimental and numerical impact force histories of the laminate L04 for 38.6J.

Several differentiable simulations have been carried out in order to explain the fact that generates the over-prediction of F_d . Firstly, the mesh of the outer ply at

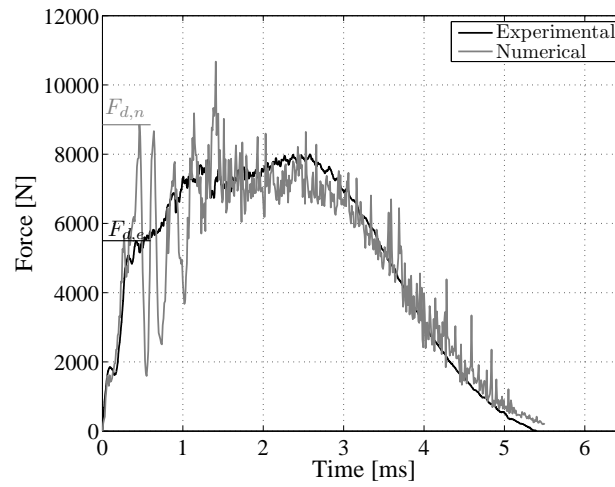


Figure 7.7: Experimental and numerical impact force histories of the laminate L04 for 29.6J.

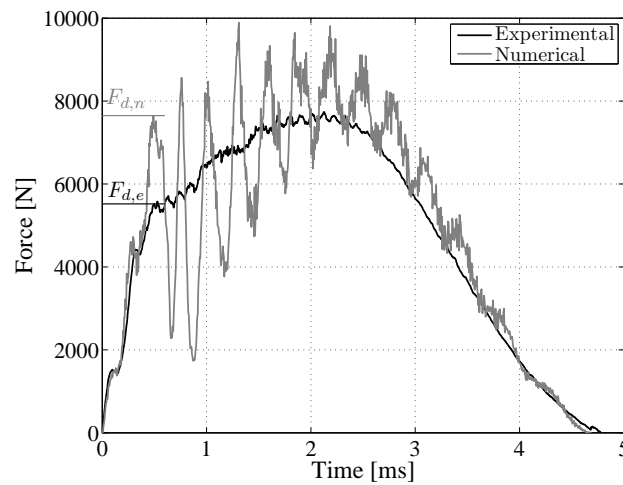


Figure 7.8: Experimental and numerical impact force histories of the laminate L04 for 19.3J.

the back face of the laminate has been refined in the through-the-thickness direction to capture better the stresses due to the flexural deformation (four elements). Secondly, the mesh of this ply has been also oriented according to the corresponding fiber orientation, so tie constraints have been used to link this ply with the whole laminate. Despite to model these modifications, no improvements have been obtained. However, it is suspected that this behavior can be attributed to an excessive

stiffness of the contact constrains defined between the surfaces of the composite plies. The pressure produced by the impactor can make that these surfaces keep contact without degrading the delamination elements, yielding to a stiffer response. Future simulations should be performed in order to improve the prediction of F_d , by using surface-based cohesive interactions which avoid to define these contact constraints.

As an illustrative example, Figure 7.9.a shows the experimental and the numerical evolution of the absorbed energy, E_a , of the laminate L04 for 19.3J. As can be observed, the numerical prediction fits well the experimental profile. The FE simulations have been modeled so the whole energy of the system can be split into the different energy components (see Equations (7.3) and (7.4)), allowing to know the role that plays each one at any moment of the impact event. Accordingly, the evolutions of the energy dissipated due to delamination (E_{Dd}) and the intralaminar damage mechanisms (E_{Dm} : matrix; E_{Df} : fiber), are plotted separately in Figure 7.9.a. It can be observed that the main dissipative mechanism is the delamination.

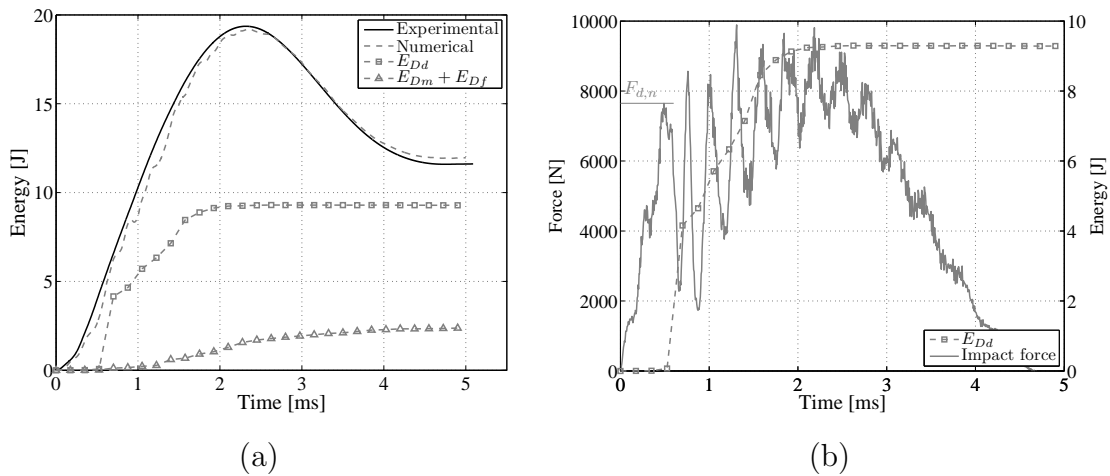


Figure 7.9: (a) Experimental and numerical evolutions of the absorbed energy (E_{Dd} : delamination; E_{Dm} : matrix; E_{Df} : fiber), and (b) numerical evolutions of the impact force and dissipated energy due to delamination (case: laminate L04 for 19.3J).

Moreover, Figure 7.9.b shows the evolutions of the impact force and the energy dissipated due to delamination. It can be observed that the drop in the impact force at the critical point F_d coincides, in time, with a quick increase of the energy dissipated by delamination. This sudden increase of the energy is the highest along

the chart. This result corroborates with the comments written in previous chapters, where it is assumed that the first drop in the impact force is mainly due to a large growth of delaminations when the structure is loaded under a low-velocity impact.

Figure 7.10 shows the predicted delamination area at two different contact times: (a) $t_i = 0.4\text{ms}$ (just before to reach F_d), and (b) $t_i = 0.8\text{ms}$ (just after the first drop of the impact force). The field variable plotted corresponds to the scalar damage variable of all the interface elements, so a translucency is applied in order to visualize all the interfaces. These projections are such as the images that can be obtained by C-scan inspections. It can be observed a large and quick increase of the delaminations between these two instants of time, as deduced previously in Figure 7.9.b.

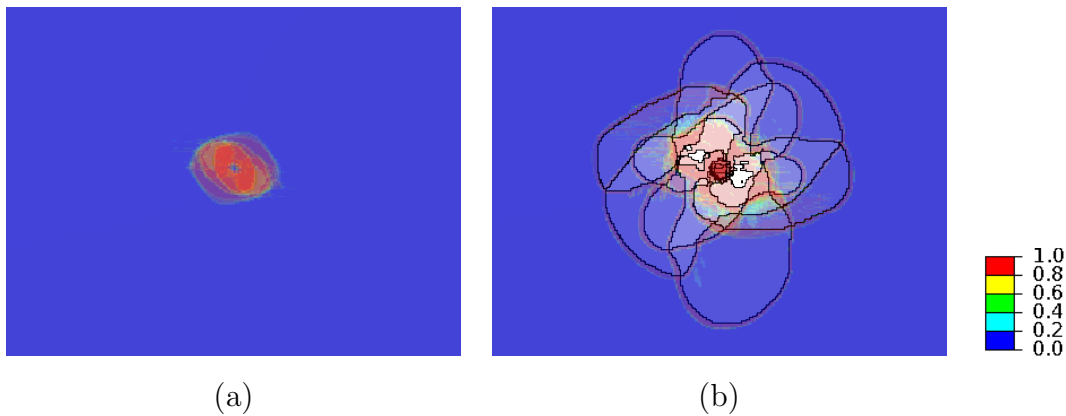


Figure 7.10: Projected delaminated area for impact times, (a) $t_i = 0.4\text{ms}$ and (b) $t_i = 0.8\text{ms}$.

According to the numerical predictions, a certain number of delaminations propagate simultaneously at the critical point F_d . Therefore, the development of analytical damage thresholds based on the assumption that a single delamination can generate a drop in the impact force history, is not fully clear.

In a similar way as the procedure used by Davies et al. [69, 85] to formulate an analytical threshold F_d based on the propagation of a single circular mid-plane delamination (F_{d1}^{stat} , see Equations (2.112) and (2.113)), a new criterion can be developed assuming that n_d^* delaminations can grow. These delaminations are counted from the back face of the plate, and generate n_d^* sub-laminates with a thickness equal to the clustering thickness h_p (see Figure 7.11). This approach is interesting for cases

which suffer the largest delaminations at the deeper interfaces of the laminate (i.e. close to the back face of the laminate), often yielding to a wide pine tree damage pattern (see Figure 2.11.a). The resulting equation deduced by means of LEFM is defined as:

$$F_{dbf}^{stat} = \pi \sqrt{\frac{8E\mathcal{G}_{IIc}}{3(1-\nu^2)}} \left(-\frac{1}{h^3} + \frac{1}{(h - n_d^* h_p)^3 + n_d^* h_p^3} \right)^{-\frac{1}{2}} \quad (7.5)$$

where \mathcal{G}_{IIc} is the fracture toughness in pure mode II, E and ν are respectively the homogenized in-plane elastic modulus and Poisson ratio of the plate, h is the plate thickness, h_p is the clustering thickness, and n_d^* is the number of delaminations considered.

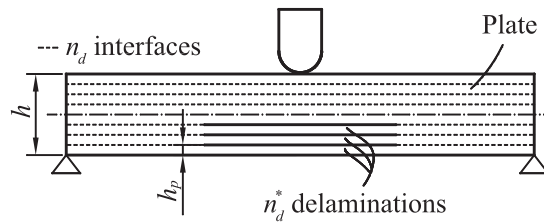


Figure 7.11: Example of back face delaminations.

The threshold F_{dbf}^{stat} does not depend on the initial crack length of the n_d^* delaminations, so it can be interpreted as a criterion for delamination onset. As can be checked, increasing the value of n_d^* , the load required to grow the delaminations decreases since the flexural stiffness of the plate is reduced. Table 7.3 summarizes the values of F_{dbf}^{stat} for laminates L02, L03, and L04, for different number of sub-laminates. The values of F_{dbf}^{stat} written in bold are the ones which are closer to the experimental values.

Figure 7.12 shows the comparisons between the numerical and the C-scan projected delamination areas at the end of the impact event of the laminate L04 for each impact energy. In a general point of view, the predictions agree with the experimental data. It should be noted that the predicted results are influenced by the in-plane mesh refinement. When a delamination reaches the rough mesh (see Figure 7.3), the growth of the delamination can be restrained because the FE discretization of the cohesive zone length is not enough.

Table 7.3: Values of F_{dbf}^{stat} to generate n_d^* sub-laminates counted from the back face of the plate (laminates L02, L03 and L04).

Laminate	Ply thickness h_p [mm]	Number of interfaces n_d	Experimental threshold load $F_{d,e}$ [kN]	Analytical threshold	
				load F_{dbf}^{stat} [kN]	
L02	0.181	30	9.94	$n_d^* = 10$	10.43
				$n_d^* = 11$	9.44
				$n_d^* = 12$	8.54
L03	0.363	14	7.60	$n_d^* = 6$	8.57
				$n_d^* = 7$	7.02
				$n_d^* = 8$	5.73
L04	0.725	6	5.50	$n_d^* = 3$	8.67
				$n_d^* = 4$	5.80
				$n_d^* = 5$	3.88

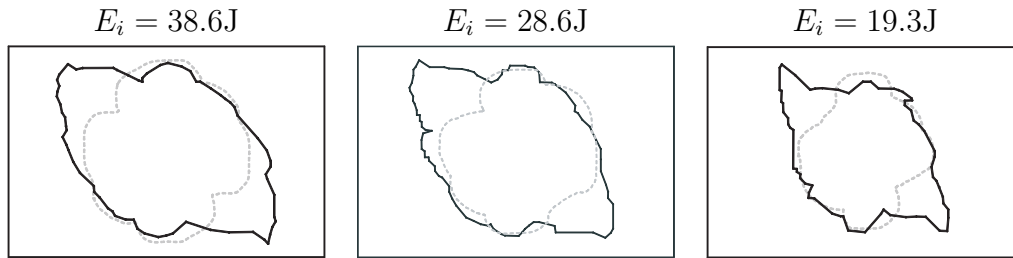


Figure 7.12: Projected delamination areas of the laminate L04 for each impact energy (experimental: black line; numerical: dashed gray line).

Figure 7.13 shows an example of through-the-thickness cut views of the plate at the impact site (case: laminate L04 for 19.3J). The variable plotted corresponds to the transverse damage variable d_2 (matrix cracking) at contact time $t_i = 2.0$ ms.

Related to the CAI tests, Table 7.4 summarizes the predictions of the post-impact residual compressive load F_{fc} and the compressive displacement at failure of the laminate L04 for each impact energy. As can be observed, the values of the residual compressive strengths are well predicted, whereas the compressive displacements at the failure point are fairly under-predicted.

Taking as an example the CAI test simulation of the laminate L04 impacted with

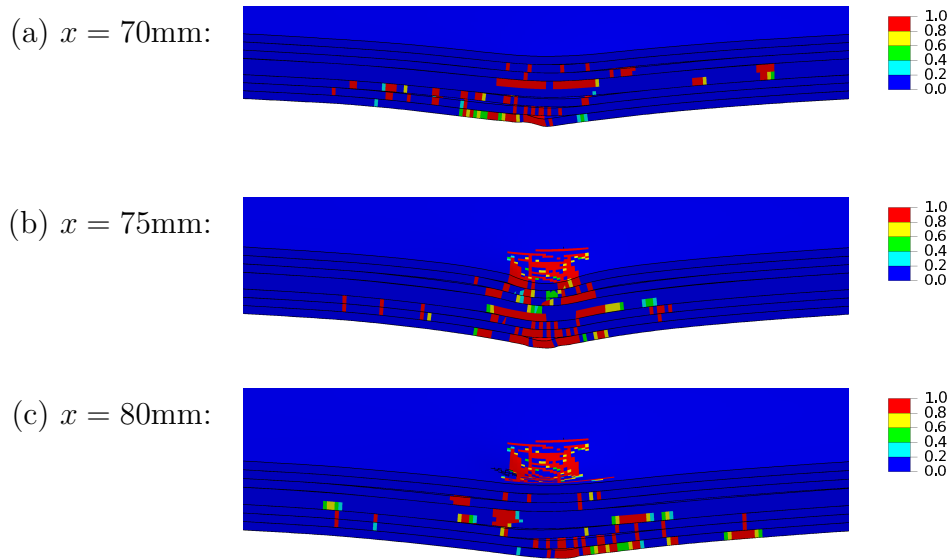


Figure 7.13: Through-the-thickness views (cut plane: $y - z$), of matrix cracking distribution at the impact site $(x, y) = (75, 50)$ mm of the laminate L04, impacted with 19.3J and at contact time $t_i = 2.0$ ms.

Table 7.4: Predictions of the post-impact residual compressive load and the compressive displacement of the laminate L04.

Impact energy [J]	Strength F_{fc} [kN]		Displacement u_{fc} [mm]	
	Experimental	Numerical	Experimental	Numerical
38.6	98	89	1.42	0.5
28.6	103	92	1.37	0.5
19.3	105	107	1.45	0.8

19.3J, in Figure 7.14 are plotted the evolutions of the dissipated energies and the compression load as a function of the compression displacement. The initial values of these energies correspond to the energies dissipated at the end of the impact test. It can be observed that practically the trend of the energies is constant until the maximum strength is reached. At this point, the energies dissipated due to the delamination and the intralaminar damage mechanisms increase. The collapse of the plate is triggered by fiber failure which, in turn, triggers matrix cracking and delamination.

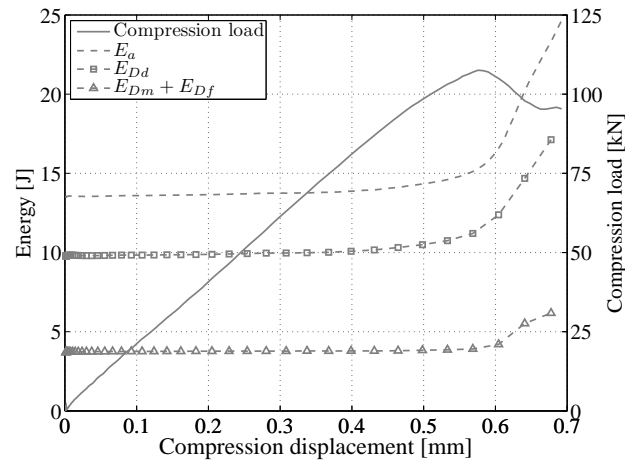


Figure 7.14: Numerical prediction of the absorbed energies (E_{Dd} : delamination; E_{Dm} : matrix; E_{Df} : fiber) and the compressive load as a function of the compression displacement, of the laminate L04 for 19.3J.

Additionally, in Figure 7.15 are shown the displacement fields at the loading axis (on top (a) and back (b) faces of the plate), and at the out-of-plane axis (also on top (c) and back (d) faces) in the instant with the maximum compressive strength. The predicted buckling mode is quite similar to the experimental results, where often a local bubble concentrated in the middle of the specimens was evidenced. According to the experimental set-up of the CAI tests, the prediction of the displacements on the top face can be compared with the lectures given by the Digital Image Correlation (DIC). Moreover, the predictions of the out-of-plane displacements at the back face can be compared with the lectures given by the LVDT transducers at the corresponding points (see Figure 3.8). For example, the maximum displacement read by the LVDT1 is 2.91mm (see Table 4.5), whereas the predicted value is 2.55mm.

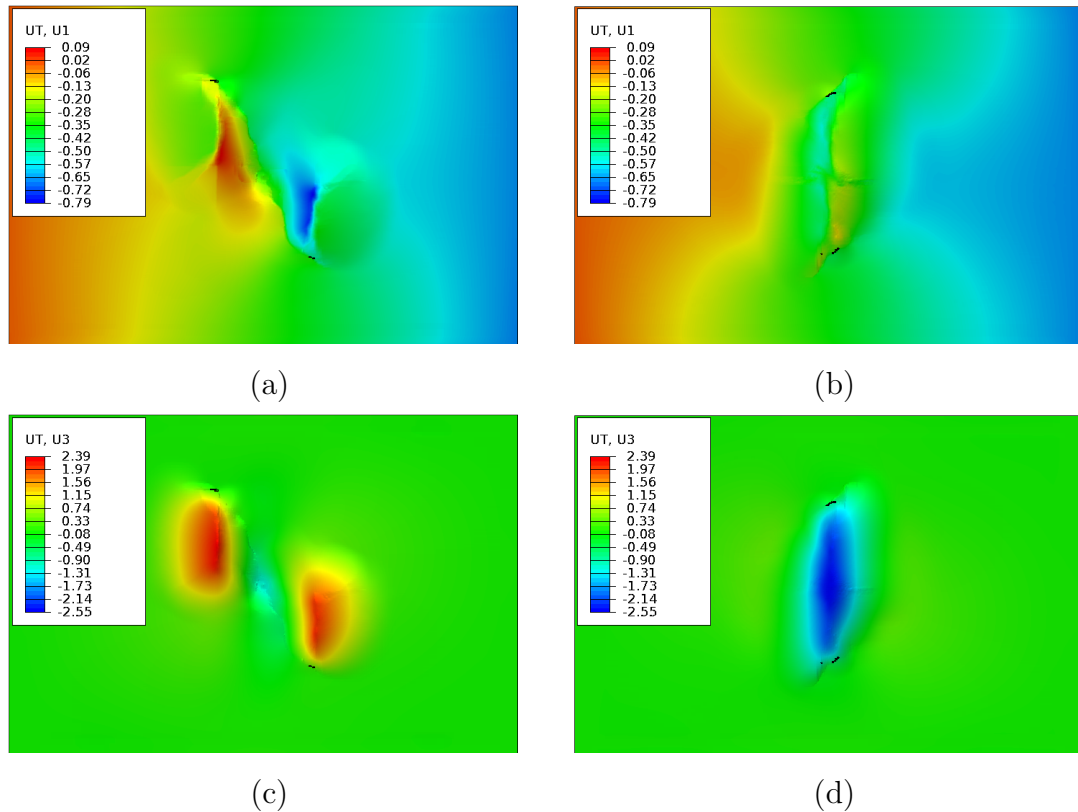


Figure 7.15: (a) Top face and (b) back face predicted displacement field at the loading axis direction; (c) top face and (d) back face out-of-plane displacement field (case: laminate L04 for 19.3J).

Laminate L03

Figures 7.16 and 7.17 show the comparisons between the experimental and the numerical evolutions of the impact force of the laminate L03 for 28.6J and 19.3J, respectively. In contrast with the simulations of the laminate L04, the whole profiles are not well predicted, whereas the contact times are still more or less in agreement with the experimental results. The damage thresholds F_d are again over-predicted, even with more offset than in the simulations of the laminate L04. This result can be related with the fact that more contact constraints are defined for laminate L03, because it has more interfaces.

On the other hand, Figure 7.18.a shows the experimental and the numerical evolutions of the absorbed energy, and the components of the dissipated energy

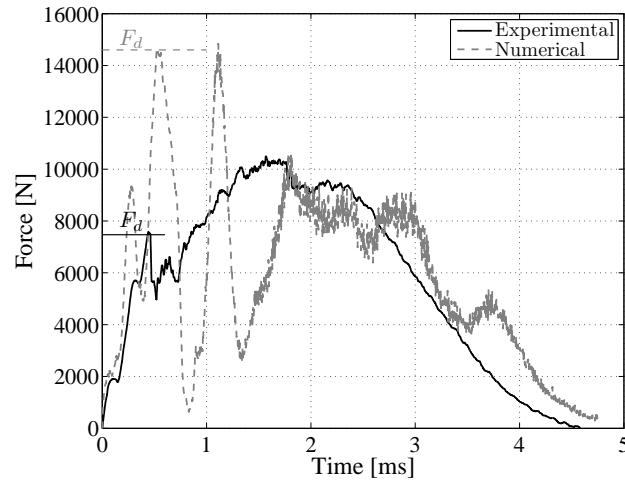


Figure 7.16: Experimental and numerical impact force histories of the laminate L03 for 29.6J.

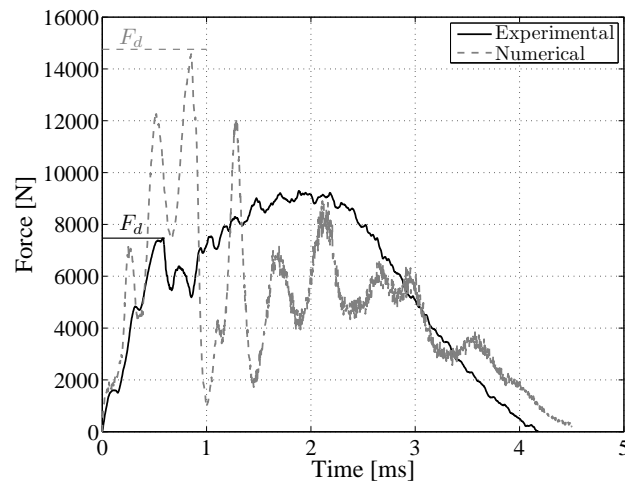


Figure 7.17: Experimental and numerical impact force histories of the laminate L03 for 19.3J.

(delamination and intralaminar damages), of the laminate L03 for 19.3J. As can be observed, the numerical result over-predicts significantly the experimental profile. In addition, Figure 7.18.b shows the evolutions of the impact force and the energy dissipated due to delamination. According to the simulations, the main dissipative mechanism in first drop of the impact force is again the delamination.

Figure 7.19 shows the comparisons between the numerical and the C-scan pro-

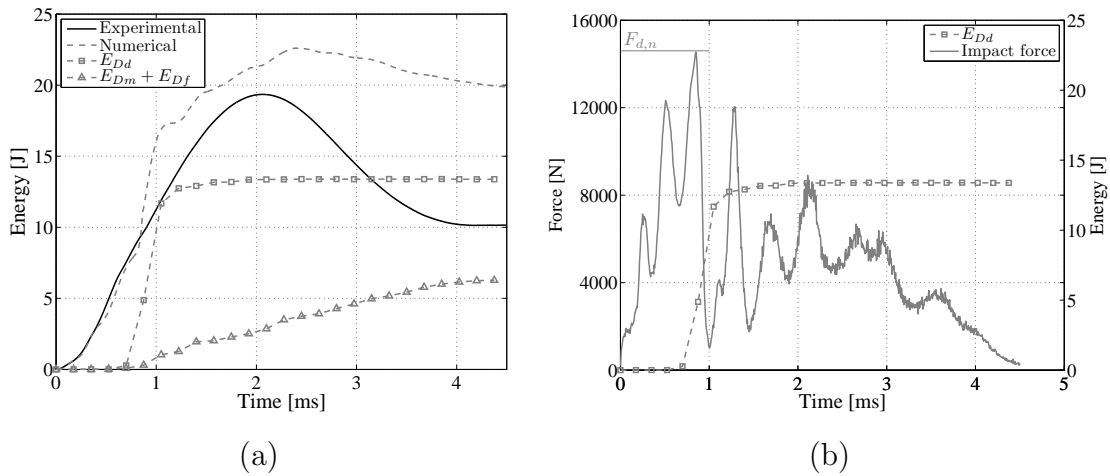


Figure 7.18: (a) Experimental and numerical evolutions of the absorbed energy (E_{Dd} : delamination; E_{Dm} : matrix; E_{Df} : fiber), and (b) numerical evolutions of the impact force and dissipated energy due to delamination (case: laminate L03 for 19.3J).

jected delamination areas at the end of the impact event of the laminate L03 for the impact energies 28.6J and 19.3J. Clearly, the sizes are over-predicted, which corroborates the result plotted previously in Figure 7.18.a.

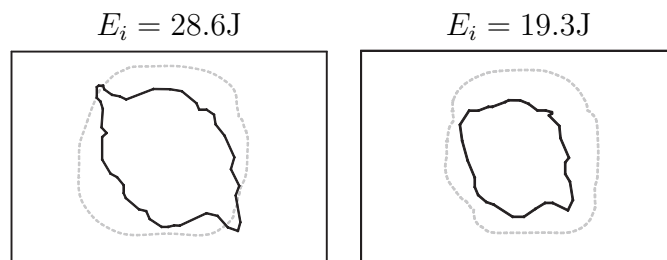


Figure 7.19: Projected delamination areas of the laminate L03 for each impact energy (experimental: black line; numerical: dashed gray line).

Obviously, since the amount of impact damage is over-predicted, the post-impact residual strength is under-predicted. The compression strengths and compression displacements obtained are summarized in Table 7.5.

Taking as an example the CAI test simulation of the laminate L03 impacted with 19.3J, in Figure 7.20 are plotted the evolutions of the dissipated energies and the

Table 7.5: Predictions of the post-impact residual compressive load and the compressive displacement of the laminate L03.

Impact energy [J]	Strength F_{fc} [kN]		Displacement u_{fc} [mm]	
	Experimental	Numerical	Experimental	Numerical
28.6	100	120	1.32	0.6
19.3	134	124	1.6	0.6

compression load as a function of the compression displacement. As occurred with laminate L04, the energies dissipated due to the delamination and the intralaminar are constant until the maximum strength is reached. On the other hand, in Figure 7.21 are shown the displacement fields at the loading axis (on top (a) and back (b) faces of the plate), and at the out-of-plane axis (also on top (c) and back (d) faces) in the instant with the maximum compressive strength. Again, a local bubble appears on the back-face of the plate.

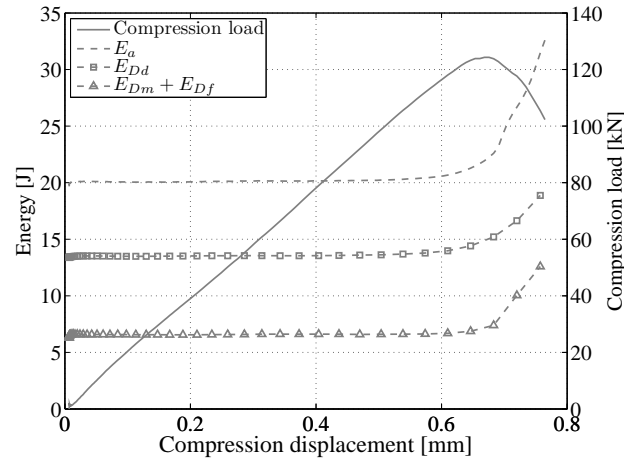


Figure 7.20: Numerical prediction of the absorbed energies (E_{Dd} : delamination; E_{Dm} : matrix; E_{Df} : fiber) and the compressive load as a function of the compression displacement, of the laminate L03 for 19.3J.

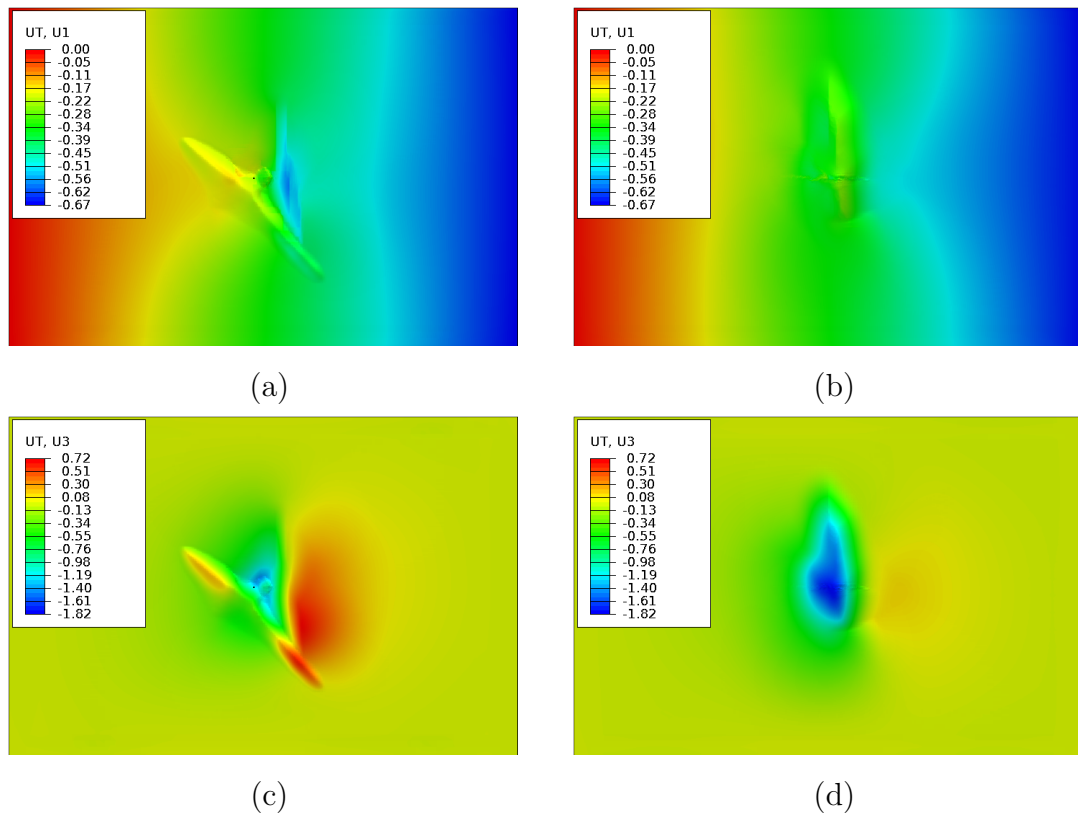


Figure 7.21: (a) Top face and (b) back face predicted displacement field at the loading axis direction; (c) top face and (d) back face out-of-plane displacement field (case: laminate L03 for 19.3J).

Chapter 8

Conclusions and future work

8.1 Conclusions

The present thesis covers a wide range of analysis of the low-velocity and large mass impact events on monolithic, flat, rectangular, polymer-based laminated composite plates with conventional stacking sequences. Keeping in mind that the main goal of this work is the prediction of the residual compressive strength of an impacted specimen coupon, a set of different tasks are performed in order to provide suitable tools to analyze the problem. In this sense, the topics which are addressed in this thesis are: the analytical description of the impact, the design and the realization of an experimental test plan, the formulation and implementation of constitutive models for the description of the composite material behavior, and the assessment of the performance of FE virtual tests where the constitutive models are used. In the following points, the main contributions and conclusions of this thesis are described.

8.1.1 Analytical impact description

Due to the simplicity of the geometry of the structure considered, the development of analytical models for the description of the impact event can be developed with sufficient accuracy. In this way, a detailed literature review of the analytical description is carried out in Chapter 2 and in the related Appendix A. The analytical models offer preliminary information for a given impact configuration, allowing the understanding of the effects of each parameter that influence the impact response.

Thus, the tools reviewed are used to acquire an initial knowledge of the problem, and also for planning the experimental test campaign.

The literature survey is focused on the models which describe the elastic response of the impact event. Different types of models are analyzed, covering the complete analytical models which fully describe the dynamic behavior of the problem, and the simplified models which describe a particular extreme impact behavior. Accordingly, the basis of any impact model, which are the contact laws and the governing equations of the plate and the impactor, are analyzed in detail. Additionally, the dimensionless frameworks which reduce suitably the number of influencing impact parameters in a more manageable dimensionless key parameters are also described. Although the analytical description performed is focused on laboratory coupons, most of the concepts reviewed can be used for other structures with more complex shapes.

The variable used to bridge the elastic stress/strain analysis and the onset of damage is the maximum impact load, which is compared with a damage threshold allowable. Damage occurs if the predicted maximum load is greater than a well-defined threshold for the corresponding dynamic response type.

Taking into account that under low-velocity impact loading the main and the most dangerous damage mechanism is the delamination, which reduces severely the residual compressive strength of the structure, the analytical damage analysis is particularized on the delamination onset. This failure mode can be detected as a first drop in the lecture of the impact force history. A new damage threshold which predicts delamination at the deepest interface of the plate is developed. It is assumed that this delamination is triggered by a vertical matrix crack located at the outer ply of the back face of the plate.

8.1.2 Experimental test plan

The sequential experimental tasks which are carried out in order to analyze laboratory coupons are: definition of the impact tests, manufacturing of the specimens, C-scan inspections for the detection of manufacturing flaws, instrumented drop-weight impact tests, dent-depth measurements, C-scan inspections to detect the BVID, and finally, instrumented CAI tests.

The selection of the impact tests is done using some of the analytical tools

previously described and taking as a reference the American Standard Test Method for drop-weight impact on laminated composite plates [59]. Modifying some of the standard parameters, three main studies are proposed: effect of the ply thickness (clustering), effect of the mismatch angles of the plies, and effect of the laminate thickness. In addition, the effect of the impact velocity, and the effect of changing the impact velocity and the impactor mass but keeping constant the impact energy, are also analyzed inside of the main proposed studies. Among the proposed studies, the most innovative is the analysis of the ply thickness effect on the impact response. For each impact study, the appearance of the first large damage is analyzed in detail. The goal of these studies is not to obtain an improved damage resistant or damage tolerant structure, rather to obtain a wide range of different experimental data that can be subsequently used to validate the numerical simulations of the impact and the CAI tests.

The main conclusions of the experimental results and their comparison with analytical models are listed below:

Effect of the impact velocity

- The threshold load, F_d , remains constant in front of changes of the impact velocity.
- Increasing the impact velocity, the slope of the elastic regime is increased, as predicted by means of the analytical impact models. Accordingly, the predicted maximum elastic impact force increases, indicating that more damage is created.
- Increasing the impact velocity, the response is extended in time because the plate develops more damage. Accordingly, the post-impact residual compressive strength is reduced.

Effect of changing the impactor mass and the velocity

- The threshold load, F_d , remains constant in front of changes of the impactor mass and velocity, but keeping constant the impact energy.
- Increasing the impactor mass, the response is more quasi-static, which means

that the response is slowed down. This behavior can also be predicted by means of the impact characterization diagram and the complete analytical impact models.

- Given a stacking sequence, the dissipated energy or the damage developed is the same between impacts with equal impact energy. In addition, the residual compressive strength remains constant under the same impact energy level. This result agrees with some of the guidelines provided by the aeronautical industry for a drop-weight impact test, where the energy is specified, and the impactor mass and the velocity can be selected freely by the engineer.

Effect of ply thickness (clustering)

- If the ply clustering is increased, under equal impact conditions the values of F_d and F_{max} are reduced.
- Increasing the ply clustering, the changes in the stiffness during the impact are more progressive and smooth when compared with laminates with thin plies. This result implies difficulties in the detection of F_d for laminates with thick plies.
- The response is elongated by increasing the ply clustering of the laminate. This result indicates that more damage develops for laminates with thick plies. Accordingly, by reducing the number of interfaces available for delamination, the resulting projected delamination area is increased. Therefore, ply clustering results in a lower damage resistance of a composite structure.
- Increasing the ply clustering, the indentation is increased.
- The free growth of the delaminations can be affected by the finite in-plane dimensions of the plates. In other words, the growth of the delaminations could be braked by the clamping system. This effect occurs basically in laminates with thick plies.
- The trend of the proposed analytical thresholds for delamination are in agreement with the experimental points for all laminate types. However, the analytical values under-predict the real values. This offset can be due to scattering

of the material properties or to the assumptions considered in the formulation of the damage threshold, e.g. strain rate effects are neglected. Further testing is required to verify these arguments, especially with critical impact energies which generate maximum impact forces similar to the damage threshold loads.

- The damage tolerance, quantified using the residual compressive load, is not affected by increasing the ply thickness, because all presented laminate types have shown similar values of compressive loads at each impact energy.

Effect of ply mismatch angle at interfaces

- The analytical prediction of F_d for the selected cross-ply laminate has been in agreement with the experimental result, although an offset also has appeared.
- The mismatch angle of the interfaces for delamination has not presented a clear effect on the damage resistance and on the damage tolerance. This result can be due to the fact that the plate thicknesses of the selected laminates for this study are slightly different.

Effect of the laminate thickness

- Increasing the laminate thickness, the response is faster and the drop in the impact force from point F_d increases. For the thinner laminate tested, the profiles of the impact force are smooth and do not present a clear first drop on the impact force. This result could mean that a sudden loss of stiffness from the point F_d does not occur, or the matrix and delamination damage that appear do not change the response of the impact, rather it is affected by progressive fiber breakage. This last argument can be related to the membrane effects.
- The predictions of the threshold load F_d for the different laminates considered have been in agreement except for the thinner laminate, i.e. L01. This result can be attributed to different causes: the membrane effects, the possibility that really the delaminations can not be detected in the force histories, or the fact that simply a sudden large delamination does not occur and rather the delaminations grow progressively.

- Increasing the laminate thickness, the damage resistance is improved since the energy dissipated is lower than for thin laminates. Likewise, the damage tolerance is improved. However, the resulting structures are heavier and more expensive.

Usefulness of the analytical impact models and analytical thresholds

- With the studies presented, it has been demonstrated that the analytical impact models for the prediction of the elastic response are a powerful tool: to define a suitable test matrix of specimens, to obtain a qualitative understanding of the effects of the governing parameters on the impact response, and to interpret the experimental results obtained.
- The analytical impact models are completed with the analytical thresholds for the prediction of the damage mechanisms that can occur in a laminated composite plate under low-velocity impact loading. For low-velocity impacts, the most critical damage is the delamination. In general, it has been shown that the damage thresholds for delamination follow the trends of the experimental results.

8.1.3 Constitutive models for FE simulations

A modified formulation and implementation of a cohesive model originally developed by Turon et al. [8–13] is presented in Chapter 5. The cohesive model accounts the onset and the propagation of the delamination in advanced composite materials, and it is formulated using a rigorous thermodynamic framework which takes into account the changes of mixed-mode loading conditions. The modifications of the original formulation are the adaptation from a cohesive surface model (stress-displacement relationship) to a continuum damage model (stress-strain relationship), and the incorporation of different penalty stiffness for either crack propagation modes I and II. The model was originally implemented in a user-written element subroutine of the implicit finite element code Abaqus/Standard [124]. In the present work, the implementation is performed using a user-written material subroutine of the explicit finite element code Abaqus/Explicit [124], allowing to use zero-thickness or non-zero-thickness cohesive elements. The model is validated by comparing the finite element

predictions with experimental data obtained in standard interlaminar fracture tests under quasi-static loading conditions.

Simple FE simulations which illustrate the well-known limitations of using a continuum damage model for capturing intra-ply matrix macro-crack paths in absence of fiber breakage are shown. Simple solutions which reduce the effect of these limitations (based on using structured meshes oriented with the corresponding ply fiber direction, and element deletion when the corresponding stiffness is degraded), are analyzed in order to know whether it can be interesting to apply them for the simulation of the drop-weight impact and the CAI tests.

8.1.4 Virtual tests: drop-weight impact and CAI

The FE models developed in Abaqus/Explicit for the simulation of the drop-weight impact and the CAI tests are described, as well as the numerical predictions obtained and their comparison with the experimental data. Due to computer and time constraints, not all the impact configurations tested experimentally are simulated. Only some cases of the ply clustering study are considered.

Prior to the FE analysis, different verifications are performed using distinct alternatives for plate modeling in order to find the most adequate in accordance with the capabilities for the FE post-processing task, the available computer equipment, and to analyze the models with an acceptable runtime. In addition, distinct FE software capabilities are checked with the aim of reaching realistic predictions and avoiding numerical problems.

In a general point of view, the comparisons with the experimental data have shown that the impact simulations reproduce better the experimental results when fewer composite plies and interfaces are modeled. However, when the number of layers increases, besides significantly increasing the computational effort, the predictions show a worse correlation with the experimental data. It is argued that this result is related with the number of contact constraints. When the number of plies is increased, the number of contact constraints increases, degrading the numerical predictions. In addition, if the numerical simulations of the impact are not predicted accurately, the results of the CAI tests will be affected by the previous errors. It is expected that using cohesive surfaces instead of defining interface elements will improve the results obtained since the definition of these contact constraints is

avoided.

The simulations presented have demonstrated the capacity of describing the phenomena that occur at any moment of the impact and the CAI tests, offering significant information which often is not possible to obtain by real tests and by the non-destructive inspections. For instance, the splitting of the whole energy of the system enables to know the role that plays each dissipative mechanism for a given configuration. Moreover, the description of the damage shape and the extension of any interface or ply, as well as the post-impact residual compressive strength of the whole structure, are also obtained. Therefore, the simulations presented confirm that the FE models, controlled by suitable constitutive models and other FE capabilities, are a powerful tool for the design of damage resistant and damage tolerant structures manufactured with composite materials and subjected to impact loading. However, more work should be performed in order to overcome the limitations and to improve the low accuracy of some of the results obtained.

For the acquisition of accurate FE results, the constitutive models require of refined meshes in order to properly account for the onset and the growth of the damage mechanisms. In the simulations presented, the finite element sizes are ranged among 20 and 500 times smaller than the whole sizes of the specimen coupons tested, so, depending on the laminate type, the models results from one to four million of elements. Therefore, large number of elements with nonlinear material behavior and other heavy computer FE definitions are needed. The whole analysis of the impact and the CAI tests of the specimen coupons have required between twelve and fifteen days, and some plate configurations have not been able to be simulated due to limitations in computer resources. Consequently, the simulation of larger structures modeled at this scale level and mesh refinement can be unaffordable or can lose interest using the common computer equipments and the current parallelization methods of the FE models. However, according to the certifying process for aeronautical structures, to model large structures at this scale level may really not be critical, since part of the response prediction have been acquired previously using a smaller but representative structure. In this sense, in a task prior to the simulation, the designer should choose a well-balanced compromise of the desired information to obtain, the scale for structure modeling, and the selection of structure parts for a more detailed modeling, but always keeping an eye on simulating in an acceptable

runtime analysis.

8.2 Future works

The following improvements are suggested for future lines of work.

8.2.1 Analytical impact description

In relation to the predictions given by the complete analytical models, a strong dependence on the contact law applied was identified. Depending on the laminate type (stacking sequence and thickness) and the contact law used, the quality of the predictions changes considerably. Indentation tests can be performed in order to know the real contact behavior for each laminate type. As a result, the range of applicability of the available contact laws can be identified. The FE simulations of these indentation tests can be performed in order to obtain additional supporting data for this type of analysis.

In addition, the stresses due to the membrane effects, which are significant when large deflections occur, should be accounted in the governing equations. In this sense, the stresses used to develop the damage threshold for matrix cracking at the back face of the plate (used as a threshold for delamination), should consider these effects. Moreover, the total stresses should be calculated using a distributed load with a contact radius smaller than the impactor tip radius, as it can be deduced by means of the Hertz contact law. These modifications must be analyzed in detail, since they can change considerably the assumptions and the corresponding predictions shown in the present work.

By means of the numerical simulations of the impact, it was demonstrated that more than one delamination propagate simultaneously at the critical point F_d . Therefore, the development of analytical damage thresholds based on the assumption that a single delamination can generate a drop in the impact force history, is not fully clear. It is necessary to study the interaction between the intra-ply matrix cracks and the delaminations which occur at different through-the-thickness planes. For example, an analysis based on simplified FE models, at which the Virtual Crack Closure Technique (VCCT) [104] is applied in order to know the energy release

rates of the considered intra-ply and delamination pre-cracks, can be performed to understand better the process.

Additionally, the perforation criterion proposed should also be calculated taking into account the membrane effects. Fiber breakage occurs preferably due to the high membrane stresses which often are superimposed on the flexural stresses when the impact behavior is quasi-statically dominated.

The review and the development of analytical tools for the elastic prediction of the impact response and for the prediction of the damage onset can be of interest for other plate configurations, such as plates with non-conventional stacking sequences (including plates with straight or curvilinear fiber orientations of the plies), or hybrid composite laminated plates with embedded metallic plies (e.g. glass fiber reinforced plastic with aluminium plies: GLARE).

8.2.2 Experimental tests

The repeatability of the CAI tests is not as good as in the impact tests. Therefore, a larger sample of CAI tests should be performed in order to support more solidly the conclusions of the damage tolerance behavior of the plates described in Chapter 4.

On the other hand, an interesting analysis would be to perform impact tests with impact energies which generate maximum impact loads similar to the experimental threshold values shown in the present work. The goal is to understand clearly the damage mechanisms that generate the first load drop, if it occurs, in the evolution of the impact force. In this sense, it is interesting to use a non-destructive inspection technique which can offer 3D views of the post-impact damage, such as X-ray computerized tomography. Accordingly, the suitability of the analytical damage thresholds can be analyzed in more detail, so new improved proposals can be developed.

8.2.3 Constitutive models for FE simulations

In the simulations carried out in the present thesis where delamination elements are applied, an engineering solution which ensures an accurate propagation under mixed-mode loading conditions is used. This solution was developed by Turon et al. [13],

and it is based on defining one of the pure mode interlaminar strengths by means of the pure mode fracture toughnesses and the remaining interlaminar strength. Alternatively, another proposed solution consists of considering a mode-dependent penalty stiffness, which can be more suitable for materials where the modification of the measured interlaminar strengths can influence the global response of the corresponding simulation. Therefore, in a similar way as it is done in Chapter 5 (for the adaptation from a cohesive surface model to a continuum damage model), different penalty stiffness for pure mode I and for pure shear mode can be used, and by defining a relationship between these stiffnesses the proper energy dissipation can be ensured [13]. However, this solution requires the re-formulation of the constitutive model, which is proposed as a future task.

Additionally, an interesting future consideration in the re-formulation of the delamination model is to couple the damage and the friction process in the shear constitutive response, such as the model proposed by Chaboche et al. [164, 165]. That is, to account the interlaminar pressure on the interlaminar shear strength, and to formulate the area under the shear constitutive law equal to the energy dissipated by the material degradation (corresponding to the shear propagation mode), and by the friction process if it occurs. This consideration will improve the results of the impact simulations, where delamination often occurs under shear and normal contact pressure conditions.

The implementation of the re-formulated delamination model should be performed by means of a user-written subroutine for the definition of a surface-based interaction (i.e. `VUINTER` [124]), because the material degradation and the friction process between the contacting surfaces are defined in the same formulation. As noted in Chapter 7, this type of implementation avoids to model delamination using additional finite elements and additional constraints which are required when non-matched meshes of the adjoining composite plies of an interface are used. Therefore, this type of implementation makes the FE pre-processing task more simple, and probably, the runtime of the analysis shorter.

Concerning the intralaminar model summarized in Chapter 6, some improvements are also suggested. The damage activation functions which define the surfaces where the elastic domain is enclosed, basically are formulated using the LaRC04 failure criteria [76, 77], by neglecting the out-of-plane stresses. These stresses should

be accounted in the corresponding functions since their effects can be significant in problems such as in out-of-plane impact loadings.

Additionally, when an unidirectional laminate is loaded in shear, a non-linear response is observed before the laminate fails by through-the-thickness transverse matrix cracking. The non-linearity results in an elastic degradation and in plastic strains when the material is unloaded. Therefore, the constitutive law for the shear components which are parallel to the fiber direction, should be formulated using a coupled plasticity and damage model, as proposed in a recent paper of Maimí et al. [166] for in-plane loading conditions. The formulation should be developed such that a 3D stress state is accounted in the corresponding activation functions for plasticity and for damage. In part, these considerations will enable to capture the permanent dent-depth which occurs in impacts on polymer-based composite structures.

On the other hand, the consideration of strain rate effects can be of interest in order to obtain an intralaminar constitutive model which deals with any impact behavior, covering from a quasi-statically dominated response to a dilatational wave controlled response. Mainly, strain rate effects should be considered in the constitutive law of the in-plane shear and transversal compression. As documented in a recent paper of Koerber et al. [167], these effects should be reflected on the corresponding elastic modulus, and on the yielding and the failure strengths. All these proposals require additional material characterization.

8.2.4 Virtual tests

It is understood that the development of reliable numerical tools for the simulation of the impact and the CAI tests depends on the suitability of the formulated constitutive models, on the implemented FE software capabilities, and on the advances in Computational Mechanics.

Implementing the proposed re-formulations of the constitutive models, it is expected that the observed deficiencies in the FE predictions will be solved, such as the prediction of the first drop in the impact force or the prediction of the impact and the CAI responses for plates with large number of plies. Moreover, the simulation of other impact configurations which are far of the quasi-static behavior can be accounted using these updated constitutive models. However, improvements of the constitutive models should be go side by side with improvements in computing

power.

The recent emerging and more accessible super-computing centers which are equipped with thousands of CPUs and so, with a high velocity of calculation in comparison with common computer equipments, open the possibility to achieve detailed and reliable simulations of large structures with an acceptable time of analysis. Obviously, the use of these type of computer equipment, should be accompanied with optimized parallelization algorithms and FE softwares. This is the expected way to perform future numerical predictions, such as the simulations of the impact configurations which were tested experimentally in the present thesis, but they are outstanding to be analyzed numerically.

Finally, other types of impact tests can be proposed for future lines of work since they are of interest for the aeronautical industry. As examples, there are the bird impacts on a leading edge of a composite wing, or the simulation of impacts on hybrid composite configurations. Accordingly, the virtual tests should be performed using new material models, such as the model which describes the behavior of the bird, or the model that describes the delamination in an interface of a metallic ply and a composite ply.

8.3 Publications

Finally, the papers published and submitted during the development of the present thesis are listed below:

- González, E.V., Maimí, P., Turon, A., Camanho, P.P., Renart, J.. Simulation of delamination by means of cohesive elements using an explicit finite element code. *Computers Materials and Continua - CMC* 2009;9(1):51-92.
- Lopes, C.S., Camanho, P.P., Gürdal, Z., Maimí, P., González, E.V.. Low-velocity impact damage on dispersed stacking sequence laminates, Part II: Numerical simulations. *Composites Science and Technology* 2009;69(7- 8):937-947.
- González, E.V., Maimí, P., Camanho, P.P., Lopes, C.S., Blanco, N.. Effects of ply clustering in laminated composite plates under low-velocity impact loading. *Composites Science and Technology* 2010 (submitted).

- Turon, A., González, E.V., Maimí, P., Camanho, P.P., Costa, J.. Reformulation of a cohesive damage model to accurately simulate delamination under mixed-mode loading in composites. *Mechanics of Materials* 2010 (submitted).

Bibliography

- [1] Going to extremes: Meeting the emerging demand for durable polymer matrix composites. Tech. Rep.; National Research Council of the National Academies. The National Academies Press; 2005.
- [2] King, D., Inderwildi, O., Carey, C.. Advanced aerospace materials: past, present and future. 2009.
- [3] MIL-HDBK-17-3F (Military Handbook). Composite Materials Handbook: Polymer Matrix Composites Materials Usage, Design, and Analysis; vol. 3. Department of Defense of USA; 2002.
- [4] Cox, B.N., Spearing, S.M., Mumm, D.R.. Practical challenges in formulating virtual tests for structural composites; vol. 10. 2008, p. 57–75.
- [5] Davies, G.A.O., Ankersen, J.. Virtual testing of realistic aerospace composite structures. *Journal of Materials Science* 2008;43(20):6586–6592.
- [6] Bailie, J.A., Ley, R.P., Pasricha, A.. A summary and review of composite laminate design guidelines. Tech. Rep. NASA, contract NAS1-19347; Northrop Grumman - Military Aircraft Systems Division; 1997.
- [7] Abrate, S.. Impact on composite structures. Cambridge, UK: Cambridge University Press; 1998.
- [8] Turon, A.. Simulation of delamination in composites under quasi-static and fatigue loading using cohesive zone models (PhD Thesis). 2006.
- [9] Turon, A., Camanho, P.P., Costa, J., Dávila, C.G.. A damage model for the simulation of delamination in advanced composites under variable-mode loading. *Mechanics of Materials* 2006;38(11):1072–1089.

- [10] Turon, A., Camanho, P.P., Dávila, C.G., Costa, J.. Decohesion element for progressive delamination using abaqus. Tech. Rep. SMAP 2005/01, DECO-UEL.v1; Department of Mechanical Engineering. University of Porto (Portugal); 2005.
- [11] Turon, A., Costa, J., Maimí, P., Trias, D., Mayugo, J.A.. A progressive damage model for unidirectional fibre-reinforced composites based on fibre fragmentation. Part I: Formulation. *Composites Science and Technology* 2005;65(13):2039–2048.
- [12] Turon, A., Dávila, C.G., Camanho, P.P., Costa, J.. An engineering solution for mesh size effects in the simulation of delamination using cohesive zone models. *Engineering Fracture Mechanics* 2005;74(10):1665–1682.
- [13] Turon, A., Camanho, P.P., Costa, J., Renart, J.. Accurate simulation of delamination growth under mixed-mode loading using cohesive elements: Definition of interlaminar strengths and elastic stiffness. *Composite Structures* 2010;92(8):1857–1864.
- [14] Maimí, P., Camanho, P.P., Mayugo, J.A., Dávila, C.G.. A continuum damage model for composite laminates: Part I Constitutive model. *Mechanics of Materials* 2007;39(10):897–908.
- [15] Maimí, P., Camanho, P.P., Mayugo, J.A., Dávila, C.G.. A continuum damage model for composite laminates: Part II Computational implementation and validation. *Mechanics of Materials* 2007;39(10):909–919.
- [16] Maimí, P., Camanho, P.P., Mayugo, J.A., Dávila, C.G.. A thermodynamically consistent damage model for advanced composites. Tech. Rep. NASA/TM-2006-214282; 2006.
- [17] Maimí, P.. Modelización constitutiva y computacional del daño y la fractura de materiales compuestos (PhD Thesis). 2006.
- [18] Christoforou, A.P.. Impact dynamics and damage in composite structures. *Composite Structures* 2001;52(2):181–188.

- [19] Christoforou, A.P., Yigit, A.S.. Characterization of impact in composite plates. *Composite Structures* 1998;43(1):15–24.
- [20] Olsson, R.. Mass criterion for wave controlled impact response of composite plates. *Composites Part A: Applied Science and Manufacturing* 2000;31(8):879–887.
- [21] Davies, G.A.O., Olsson, R.. Impact on composite structures. *The Aeronautical Journal* 2004;108(1089):541–563.
- [22] Olsson, R.. Impact response of composite laminates - a guide to closed form solutions, FFA TN 1992-33. Tech. Rep.; The Aeronautical Research Institute of Sweden, Bromma; 1993.
- [23] Olsson, R., Donadon, M.V., Falzon, B.G.. Delamination threshold load for dynamic impact on plates. *International Journal of Solids and Structures* 2006;43(10):3124–3141.
- [24] Olsson, R.. Analytical prediction of large mass impact damage in composite laminates. *Composites Part A: Applied Science and Manufacturing* 2001;32(9):1207–1215.
- [25] Olsson, R.. Closed form prediction of peak load and delamination onset under small mass impact. *Composite Structures* 2003;59(3):341–349.
- [26] Yigit, A.S., Christoforou, A.P.. Limits of asymptotic solutions in low-velocity impact of composite plates. *Composite Structures* 2007;81(4):568–574.
- [27] Christoforou, A.P., Yigit, A.S.. Effect of flexibility on low velocity impact response. *Journal of Sound and Vibration*, 1998;217(3):563–578.
- [28] Abrate, S.. Modeling of impacts on composite structures. *Composite Structures* 2001;51(2):129–138.
- [29] Lin, C., Fatt, M.S.H.. Perforation of composite plates and sandwich panels under quasi-static and projectile loading. *Journal of Composite Materials* 2006;40(20):1801–1840.

- [30] Richardson, M.O.W., Wisheart, M.J.. Review of low-velocity impact properties of composite materials. *Composites Part A: Applied Science and Manufacturing* 1996;27(12):1123–1131.
- [31] Schoeppner, G.A., Abrate, S.. Delamination threshold loads for low velocity impact on composite laminates. *Composites Part A: Applied Science and Manufacturing* 2000;31(9):903–915.
- [32] Godwin, W., Davies, G.A.O.. Impact behaviour of thermoplastic composites. *Proceedings of the International Conference Computer aided design in composite material technology*. 1988, p. 371–382.
- [33] Robinson, P., Davies, G.A.O.. Impactor mass and specimen geometry-effects in low velocity impact of laminated composites. *International Journal of Impact Engineering* 1992;12(2):189–207.
- [34] Johnson, K.L.. *Contact mechanics*. Cambridge University Press; 1985.
- [35] Olsson, R.. Impact response of orthotropic composite plates predicted from a one-parameter differential equation. *AIAA Journal* 1992;30(6):1587–1596.
- [36] Dahan, M., Zarka, J.. Elastic contact between a sphere and a semi infinite transversely isotropic body. *International Journal of Solids and Structures* 1977;13(3):229–238.
- [37] Turner, J.R.. Contact on a transversely isotropic half-space, or between two transversely isotropic bodies. *International Journal of Solids and Structures* 1980;16(5):409–419.
- [38] Wu, E., Yen, C.S.. The contact behavior between laminated composite plates and rigid spheres. *Journal of Applied Mechanics* 1994;61(1):60–66.
- [39] Chao, C.C., Tu, C.Y.. Three-dimensional contact dynamics of laminated plates: Part 1. Normal impact. *Composites Part B: Engineering* 1999;30(1):9–22.
- [40] Swanson, S.R.. Hertzian contact of orthotropic materials. *International Journal of Solids and Structures* 2004;41(7):1945–1959.

- [41] Yang, S.H., Sun, C.T.. Indentation law for composite laminates. *Composite Materials: Testing and Design (Sixth Conference)*, ASTM STP 787. ASTM Special Technical Publication; 1982, p. 425–449.
- [42] Wu, E., Shyu, K.. Response of composite laminates to contact loads and relationship to low-velocity impact. *Journal of Composite Materials* 1993;27(15):1443–1464.
- [43] Cairns, D.S.. A simple, elasto-plastic contact law for composites. *Journal of Reinforced Plastics and Composites* 1991;10(4):423–433.
- [44] Christoforou, A.P.. On the contact of a spherical indenter and a thin composite laminate. *Composite Structures* 1993;26(1-2):77–82.
- [45] Yigit, A.S., Christoforou, A.P.. On the impact of a spherical indenter and an elastic-plastic transversely isotropic half-space. *Composites Engineering* 1994;4(11):1143–1152.
- [46] Tan, T.M., Sun, C.T.. Use of statical indentation laws in the impact analysis of laminated composite plates. *Journal of Applied Mechanics* 1985;52(1):6–12.
- [47] Suemasu, H., Kerth, S., Maier, M.. Indentation of spherical head indentors on transversely isotropic composite plates. *Journal of Composite Materials* 1994;28(17):1723–1739.
- [48] Chen, P., Xiong, J., Shen, Z.. Thickness effect on the contact behavior of a composite laminate indented by a rigid sphere. *Mechanics of Materials* 2008;40(4-5):183–194.
- [49] Swanson, S.R.. Contact deformation and stress in orthotropic plates. *Composites Part A: Applied Science and Manufacturing* 2005;36(10):1421–1429.
- [50] Greszczuk, L.B.. *Damage in composite materials due to low velocity impact*. New York: John Wiley and Sons; 1982.
- [51] Crook, A.W.. A study of some impacts between metal bodies by a piezo-electric method. *Proceedings of the Royal Society of London Series A, Mathematical and Physical* 1952;212(1110):377–390.

- [52] Christoforou, A.P., Swanson, S.R.. Analysis of impact response in composite plates. *International Journal of Solids and Structures* 1991;27(2):161–170.
- [53] Yigit, A.S., Christoforou, A.P.. On the impact between a rigid sphere and a thin composite laminate supported by a rigid substrate. *Composite Structures* 1995;30(2):169–177.
- [54] Christoforou, A.P., Yigit, A.S.. Scaling of low-velocity impact response in composite structures. *Composite Structures* 2009;91(3):358–365.
- [55] Choi, I.H., Lim, C.H.. Low-velocity impact analysis of composite laminates using linearized contact law. *Composite Structures* 2004;66(1-4):125–132.
- [56] Davies, G.A.O.. *Structural Impact and Crashworthiness: Keynote lectures; vol. 1. International Conference on Structural Impact and Crashworthiness.* Elsevier Applied Science Publishers; 1984.
- [57] Morton, J.. Scaling of impact-loaded carbon-fiber composites. *AIAA Journal* 1988;26(8):989–994.
- [58] Vlot, A.. *Low Velocity Impact Loading on Fibre Reinforced Aluminium Laminates (PhD Thesis).* 1991.
- [59] ASTM D 7136/D 7136M-05. Standard Test Method for Measuring the Damage Resistance of a Fiber-Reinforced Polymer Matrix Composite to a Drop-Weight Impact Event. ASTM International. West Conshohocken PA, USA. 2005.
- [60] Fuoss, E., Straznicky, P.V., Poon, C.. Effects of stacking sequence on the impact resistance in composite laminates - Part 1: Parametric study. *Composite Structures* 1998;41(1):67–77.
- [61] Reddy, J.N.. *Theory and analysis of elastic plates and shells.* Philadelphia: Taylor and Francis; 2007.
- [62] Clough, R.W., Penzien, J.. *Dynamics of structures.* New York: McGraw-Hill; 1993.

- [63] Mittal, R.K.. A simplified analysis of the effect of transverse shear on the response of elastic plates to impact loading. *International Journal of Solids and Structures* 1987;23(8):1191–1203.
- [64] Olsson, R.. Engineering method for prediction of impact response and damage in sandwich panels. *Journal of Sandwich Structures and Materials* 2002;4(1):3–29.
- [65] Zener, C.. The intrinsic inelasticity of large plates. *Physical Review* 1941;59(8):669–673.
- [66] Swanson, S.R.. Limits of quasi-static solutions in impact of composite structures. *Composites Engineering* 1992;2(4):261–267.
- [67] Shivakumar, K.N., Elber, W., Illg, W.. Prediction of impact force and duration due to low-velocity impact on circular composite laminates. *Journal of Applied Mechanics* 1985;52(3):674–680.
- [68] Sierakowski, R.L., Newaz, G.M.. *Damage tolerance in advanced composites*. Lancaster, Pennsylvania (USA): Technomic Publishing Company, Inc.; 1995.
- [69] Davies, G.A.O., Zhang, X., Zhou, G., Watson, S.. Numerical modelling of impact damage. *Composites* 1994;25(5):342–350.
- [70] Elder, D.J., Thomson, R.S., Nguyen, M.Q., Scott, M.L.. Review of delamination predictive methods for low speed impact of composite laminates. *Composite Structures* 2004;66(1-4):677–683.
- [71] Sjoblom, P.O., Hartness, J.T., Cordell, T.M.. On low-velocity impact testing of composite materials. *Journal of Composite Materials* 1988;22(1):30–52.
- [72] Nettles, A.T.. *Basic mechanics of laminated composite plates*. Tech. Rep. NASA Reference Publication 1351; 1994.
- [73] Dávila, C.G., Camanho, P.P.. Physically based failure criteria for transverse matrix cracking. 9th Portuguese conference on fracture. Setúbal, Portugal. 2004, p. 1–8.

- [74] Camanho, P.P., Dávila, C.G., Pinho, S.T., Iannucci, L., Robinson, P.. Prediction of in situ strengths and matrix cracking in composites under transverse tension and in-plane shear. *Composites Part A: Applied Science and Manufacturing* 2006;37(2):165–176.
- [75] Dávila, C.G., Jaunky, N., Goswami, S.. Failure criteria for FRP laminates in plane stress. vol. 7. 2003, p. 5380–5390.
- [76] Pinho, S.T., Dávila, C.G., Camanho, P.P., Iannucci, L., Robinson, P.. Failure models and criteria for FRP under in-plane or three-dimensional stress states including shear non-linearity. Tech. Rep. NASA/TM-2005-213530; 2006.
- [77] Dávila, C.G., Camanho, P.P., Rose, C.A.. Failure criteria for FRP laminates. *Journal of Composite Materials* 2005;39(4):323–345.
- [78] Conway, H.D., Farnham, K.A., Ku, T.C.. The indentation of a transversely isotropic half-space by a rigid sphere. *Journal of Applied Mechanics* 1967;34:491–492.
- [79] Olsson, R., Nilsson, S.. Simplified prediction of stresses in transversely isotropic composite plates under Hertzian contact load. *Composite Structures* 2006;73(1):70–77.
- [80] Liu, D.. Impact-induced delamination - A view of bending stiffness mismatching. *Journal of Composite Materials* 1988;22(7):674–692.
- [81] Morita, H., Adachi, T., Tateishi, Y., Matsumoto, H.. Characterization of impact damage resistance of CF/PEEK and CF/toughened epoxy laminates under low and high velocity impact tests. *Journal of Reinforced Plastics and Composites* 1997;16(2):131–143.
- [82] Davies, G.A.O., Zhang, X.. Impact damage prediction in carbon composite structures. *International Journal of Impact Engineering* 1995;16(1):149–170.
- [83] Zhang, X.. Impact damage in composite aircraft structures. Experimental testing and numerical simulation. *Proceedings of the Institution of Mechanical Engineers, Part G: Journal of Aerospace Engineering* 1998;212(4):245–259.

- [84] Jackson, W.C., Poe, C.C.. Use of impact force as a scale parameter for the impact response of composites laminates. *Journal of Composites Technology and Research* 1993;15(4):282–289.
- [85] Davies, G.A.O., Robinson, P.. Predicting failure by debonding delaminations. In: *debonding/delamination of composites*, AGARD-CP-530 (Advisory Group for Aerospace Research and Development). Neuilly Sur Seine, France. 1992. 1992, p. 5–11.
- [86] Davies, G.A.O., Hitchings, D., Wang, J.. Prediction of threshold impact energy for onset of delamination in quasi-isotropic carbon/epoxy composite laminates under low-velocity impact. *Composites Science and Technology* 2000;60(1):1–7.
- [87] Suemasu, H., Majima, O.. Multiple delaminations and their severity in circular axisymmetric plates subjected to transverse loading. *Journal of Composite Materials* 1996;30(4):441–453.
- [88] Suemasu, H., Majima, O.. Multiple delaminations and their severity in non-linear circular plates subjected to concentrated loading. *Journal of Composite Materials* 1998;32(2):123–140.
- [89] Caprino, G., Lopresto, V.. On the penetration energy for fibre-reinforced plastics under low-velocity impact conditions. *Composites Science and Technology* 2001;61(1):65–73.
- [90] Sjoblom, P.. Simple design approach against low-velocity impact damage. vol. 32. 1987, p. 529–539.
- [91] Wen, H.M.. Predicting the penetration and perforation of FRP laminates struck normally by projectiles with different nose shapes. *Composite Structures* 2000;49(3):321–329.
- [92] Wen, H.M.. Penetration and perforation of thick FRP laminates. *Composites Science and Technology* 2001;61(8):1163–1172.

- [93] Hsiao, H.M., Daniel, I.M., Cordes, R.D.. Strain rate effects on the transverse compressive and shear behavior of unidirectional composites. *Journal of Composite Materials* 1999;33(17):1620–1642.
- [94] AITM1-0010. Airbus Test Method. Fibre Reinforced Plastics: Determination of Compression Strength After Impact. Blagnac Cedex, France. 2005.
- [95] BSS-7260. Boeing Specification Support Standard: Advanced Composite Compression Tests. The Boeing Company, Seattle, Washington. 1988.
- [96] NASA ST-1. Standard test for toughened resin composites. Tech. Rep. 1092; 1982.
- [97] Lopes, C.S., Camanho, P.P., Gürdal, Z., Maimí, P., González, E.V.. Low-velocity impact damage on dispersed stacking sequence laminates. Part II: Numerical simulations. *Composites Science and Technology* 2009;69(7-8):937–947.
- [98] Lopes, C.S., Seresta, O., Coquet, Y., Gürdal, Z., Camanho, P.P., Thuis, B.. Low-velocity impact damage on dispersed stacking sequence laminates. Part I: Experiments. *Composites Science and Technology* 2009;69(7-8):926–936.
- [99] ASTM D 7137/D 7137M-05. Standard Test Method for Compressive Residual Strength Properties of Damaged Polymer Matrix Composite Plates. ASTM International. West Conshohocken PA, USA. 2005.
- [100] Irwin, G.R.. Analysis of stresses and strains near the end of a crack traversing a plate. *Journal of Applied Mechanics* 1957;24(3):361–364.
- [101] Rybicki, E.F., Kanninen, M.F.. A finite element calculation of stress intensity factors by a modified crack closure integral. *Engineering Fracture Mechanics* 1977;9(4):931–938.
- [102] Raju, I.S.. Calculation of strain-energy release rates with higher order and singular finite elements. *Engineering Fracture Mechanics* 1987;28(3):251–274.
- [103] Zou, Z., Reid, S.R., Soden, P.D., Li, S.. Mode separation of energy release rate for delamination in composite laminates using sublaminates. *International Journal of Solids and Structures* 2001;38(15):2597–2613.

- [104] Krueger, R.. Virtual crack closure technique: History, approach, and applications. *Applied Mechanics Reviews* 2004;57(1-6):109–143.
- [105] Rice, J.R.. A path independent integral and the approximate analysis of strain concentration by notches and cracks. *Journal of Applied Mechanics* 1968;35:379–386.
- [106] Hellen, T.K.. On the method of virtual crack extensions. *International Journal for Numerical Methods in Engineering* 1975;9(1):187–207.
- [107] Parks, D.M.. A stiffness derivative finite element technique for determination of crack tip stress intensity factors. *International Journal of Fracture* 1974;10(4):487–502.
- [108] Griffith, A.A.. The phenomena of rupture and flow in solids. *Philosophical Transactions of the Royal Society* 1920;221:163–198.
- [109] Pagano, N.J., Pipes, R.B.. Some observations on the interlaminar strength of composite laminates. *International Journal of Mechanical Sciences* 1973;15(8):679–686.
- [110] Hashin, Z.. Failure criteria for unidirectional fiber composites. *Journal of Applied Mechanics* 1980;47(4):329–334.
- [111] Barenblatt, G.I.. The mathematical theory of equilibrium cracks in brittle fracture. *Advances in Applied Mechanics* 1962;7:55–129.
- [112] Dugdale, D.S.. Yielding of steel sheets containing slits. *Journal of the Mechanics and Physics of Solids* 1960;8(2):100–104.
- [113] Hillerborg, A., Mod er, M., Petersson, P.E.. Analysis of crack formation and crack growth in concrete by means of fracture mechanics and finite elements. *Cement and Concrete Research* 1976;6(6):773–781.
- [114] Schellekens, J.C.J., Borst, R.D.. A non-linear finite element approach for the analysis of mode-I free edge delamination in composites. *International Journal of Solids and Structures* 1993;30(9):1239–1253.

- [115] Allix, O., Ladevéze, P., Corigliano, A.. Damage analysis of interlaminar fracture specimens. *Composite Structures* 1995;31(1):61–74.
- [116] Mi, Y., Crisfield, M.A., Davies, G.A.O., Hellweg, H.B.. Progressive delamination using interface elements. *Journal of Composite Materials* 1998;32(14):1246–1272.
- [117] Alfano, G., Crisfield, M.A.. Finite element interface models for the delamination analysis of laminated composites: Mechanical and computational issues. *International Journal for Numerical Methods in Engineering* 2001;50(7):1701–1736.
- [118] Camanho, P.P., Dávila, C.G., de Moura, M.F.. Numerical simulation of mixed-mode progressive delamination in composite materials. *Journal of Composite Materials* 2003;37(16):1415–1438.
- [119] de Borst, R.. Numerical aspects of cohesive-zone models. *Engineering Fracture Mechanics* 2003;70(14):1743–1757.
- [120] Pinho, S.T., Iannucci, L., Robinson, P.. Formulation and implementation of decohesion elements in an explicit finite element code. *Composites Part A: Applied Science and Manufacturing* 2006;37(5):778–789.
- [121] Iannucci, L.. Dynamic delamination modelling using interface elements. *Computers and Structures* 2006;84(15-16):1029–1048.
- [122] Aymerich, F., Dore, F., Priolo, P.. Prediction of impact-induced delamination in cross-ply composite laminates using cohesive interface elements. *Composites Science and Technology* 2008;68(12):2383–2390.
- [123] Zhang, Y., Zhu, P., Lai, X.. Finite element analysis of low-velocity impact damage in composite laminated plates. *Materials and Design* 2006;27(6):513–519.
- [124] ABAQUS 6.8-3 User's Manual. Dassault Systemes Simulia Corp. Providence, RI, U.S.A. 2008.

- [125] Corigliano, A., Allix, O.. Some aspects of interlaminar degradation in composites. *Computer Methods in Applied Mechanics and Engineering* 2000;185(2-4):203–224.
- [126] Xu, X.P., Needleman, A.. Numerical simulations of fast crack growth in brittle solids. *Journal of the Mechanics and Physics of Solids* 1994;42(9):1397–1434.
- [127] Martha, L.F., Wawrzynek, P.A., Ingraffea, A.R.. Arbitrary crack representation using solid modeling. *Engineering with Computers* 1993;9(2):63–82.
- [128] Oliver, J.. On the discrete constitutive models induced by strong discontinuity kinematics and continuum constitutive equations. *International Journal of Solids and Structures* 2000;37(48):7207–7229.
- [129] Simo, J.C., Rifai, M.S.. Class of mixed assumed strain methods and the method of incompatible modes. *International Journal for Numerical Methods in Engineering* 1990;29(8):1595–1638.
- [130] Belytschko, T., Moës, N., Usui, S., Parimi, C.. Arbitrary discontinuities in finite elements. *International Journal for Numerical Methods in Engineering* 2001;50(4):993–1013.
- [131] Babuška, I., Melenk, J.M.. The partition of unity method. *International Journal for Numerical Methods in Engineering* 1997;40(4):727–758.
- [132] Ortiz, M., Pandolfi, A.. Finite-deformation irreversible cohesive elements for three-dimensional crack-propagation analysis. *International Journal for Numerical Methods in Engineering* 1999;44(9):1267–1282.
- [133] Jansson, N.E., Larsson, R.. Rotational interface formulation for delamination analysis of composite laminates. *Computers and Structures* 2003;81(30-31):2705–2716.
- [134] Mazars, J.. *Mechanical Damage and Fracture of Concrete Structures*. Oxford: Pergamon Press; 1982.

- [135] Simo, J.C., Ju, J.W.. Strain- and stress-based continuum damage models-I. Formulation. *International Journal of Solids and Structures* 1987;23(7):821–840.
- [136] Oliver, J., Cervera, M., Oller, S., Lubliner, J.. Isotropic damage models and smeared crack analysis of concrete. *Computer Aided Analysis and Design of Concrete Structures* 1990;2:945–958.
- [137] Benzeggagh, M.L., Kenane, M.. Measurement of mixed-mode delamination fracture toughness of unidirectional glass. *Composites Science and Technology* 1996;56(4):439–449.
- [138] Ye, L.. Role of matrix resin in delamination onset and growth in composite laminates. *Composites Science and Technology* 1988;33(4):257–277.
- [139] Bažant, Z.P., Oh, B.H.. Crack band theory for fracture of concrete. *Matériaux et Constructions* 1983;16(3):155–177.
- [140] Remmers, J.J.C., Borst, R.D., Needleman, A.. A cohesive segments method for the simulation of crack growth. *Computational Mechanics* 2003;31(1-2):69–77.
- [141] Yang, Q., Cox, B.. Cohesive models for damage evolution in laminated composites. *International Journal of Fracture* 2005;133(2):107–137.
- [142] Rice, J.R.. The mechanics of earthquake rupture. School of Physics "E. Fermi", Course 78, 1978. *Physics of the Earth's Interior*. Italian Physical Society/North Holland Publ. Co. 1980.
- [143] Prinz, R., Cao, L.. Analysis of strain-energy-release rates for unidirectional graphite/epoxy laminates with separated central plies under fatigue loading. *Proceedings of Seventh International Conference on Composite Materials: ICCM-VII*. Beijing, China. 1989, p. 1–6.
- [144] Reeder, J.R., Crews, J.H.J.. Mixed-mode bending method for delamination testing. *AIAA Journal* 1990;28(7):1270–1276.

- [145] Reeder, J.R., Crews, J.H.J.. Redesign of the mixed-mode bending delamination test to reduce nonlinear effects. *Journal of Composites Technology and Research* 1992;14(1):12–19.
- [146] Crews, J.H.J., Reeder, J.R.. Mixed-mode bending method apparatus for delamination testing. Tech. Rep. NASA TM 100662; 1998.
- [147] Kinloch, A.J., Wang, Y., Williams, J.G., Yayla, P.. The mixed-mode delamination of fibre composite materials. *Composites Science and Technology* 1993;47(3):225–237.
- [148] Carlsson, L.A., Gillespie, J.W., Pipes, R.B.. On the analysis and design of the end notched flexure (ENF) specimen for mode II testing. *Journal of Composite Materials* 1986;20(6):594–604.
- [149] Ye, L., Prinz, R., Klose, R.. Characterization of interlaminar shear fracture toughness and delamination fatigue growth of composite materials using TCT specimen. Tech. Rep. IB 131-90/15, DLR, Institute for Structural Mechanics; 1990.
- [150] König, M., Krüger, R., Kussmaul, K., Alberti, M.V., Gädke, M.. Characterizing static and fatigue interlaminar fracture behavior of a first generation graphite/epoxy composite. ASTM Special Technical Publication 1997;1242:60–81.
- [151] ASTM D 3039/D 3039M-00. Standard test method for tensile properties of polymer matrix composite materials. ASTM International. West Conshohocken PA, USA. 2000.
- [152] ASTM D 3410-87. Standard test method for compressive properties of unidirectional or cross-ply fibre-resin composites of unidirectional or cross-ply fibre-resin composites. ASTM International. West Conshohocken PA, USA. 1987.
- [153] ASTM D 3518/3518M-94. Standard test method for in-plane shear response of polymer matrix composite materials by test of a ± 45 laminate. ASTM International. West Conshohocken PA, USA. 1994.

- [154] ASTM D 5528-01. Standard test methods for mode I interlaminar fracture toughness of unidirectional fibre-reinforced polymer matrix composites. ASTM International. West Conshohocken PA, USA. 2001.
- [155] Martin, R.H., Elms, T., Bowron, S.. Characterization of mode II delamination using the 4ENF. Proceedings of the 4th European Conference on Composites: Testing and Standardization. Institute of Materials, London. 1998, p. 161–170.
- [156] Pinho, S.T., Robinson, P., Iannucci, L.. Fracture toughness of the tensile and compressive fibre failure modes in laminated composites. *Composites Science and Technology* 2006;66(13):2069–2079.
- [157] Jirásek, M.. *Advanced courses: Numerical Modeling of Deformation and Failure of Materials*. 1999.
- [158] Laš, V., Zemčík, R.. Progressive damage of unidirectional composite panels. *Journal of Composite Materials* 2008;42(1):25–44.
- [159] Paepegem, W.V., Baere, I.D., Degrieck, J.. Modelling the nonlinear shear stress-strain response of glass fibre-reinforced composites. Part I: Experimental results. *Composites Science and Technology* 2006;66(10):1455–1464.
- [160] Wisnom, M.R.. Modelling discrete failures in composites with interface elements. *Composites Part A: Applied Science and Manufacturing* 2010;41(7):795–805.
- [161] Bergan, P.G., Mollestad, E.. An automatic time-stepping algorithm for dynamic problems. *Computer Methods in Applied Mechanics and Engineering* 1985;49(3):299–318.
- [162] Olsson, R.. *Impact response and delamination of composite plates (PhD Thesis)*. 1998.
- [163] Schön, J.. Coefficient of friction of composite delamination surfaces. *Wear* 2000;237(1):77–89.
- [164] Chaboche, J.L., Girard, R., Levasseur, P.. On the interface debonding models. *International Journal of Damage Mechanics* 1997;6(3):220–257.

- [165] Chaboche, J.L., Girard, R., Schaff, A.. Numerical analysis of composite systems by using interphase/interface models. *Computational Mechanics* 1997;20(1-2):3–11.
- [166] Maimí, P., Camanho, P.P., Mayugo, J.A., Turon, A.. Matrix cracking and delamination in laminated composites. Part I: ply constitutive law, first ply failure and onset of delamination. *Composites Science and Technology* 2010; submitted for publication.
- [167] Koerber, H., Xavier, J., Camanho, P.P.. High strain rate characterisation of unidirectional carbon-epoxy IM7-8552 in transverse compression and in-plane shear using digital image correlation. *Mechanics of Materials* 2010;42(11):1004–1019.
- [168] Ochoa, O.O., Reddy, J.N.. *Finite Element Analysis of Composite Laminates*. The Netherlands: Kluwer Academic Publishers; 1992.
- [169] Kollár, L., Springer, G.S.. *Mechanics of composite structures*. Cambridge, UK: Cambridge University Press; 2003.

Appendix A

Governing equations of the plate

In the present Appendix, the development of the governing equations of rectangular, flat and monolithic laminated composite plates under general loading is described. This development is widely studied in the bibliography and basically requires a knowledge of anisotropic elasticity, to select an appropriate plate theory that accounts for desired kinematics, and a method to formulate the equations. All the developments detailed in this Appendix are extracted from references Reddy [61], Ochoa and Reddy [168], Kollár and Springer [169], and Abrate [7].

As shown in Chapter 2, the governing equations of the plate for concentrated impact loading joined with the governing equation of the impactor, a suitable contact law, and a proper approximation of the unknown variables yield to typically called *complete analytical models* of the impact event [19, 28]. In these models, the most usually plate theories used in order to develop the governing equations are the *classical laminated plate theory* and the *first-order shear deformation plate theory*. These plate theories and the corresponding governing equations are explained in detail in the present Appendix.

Therefore, equations for calculating displacements, stresses, and strains are presented. Due to the configuration of the structure considered (see Figure A.1), two Cartesian coordinate systems are used in order to describe these equations: a global coordinate system (x, y, z) attached to a fixed reference point, and a local coordinate system (x_1, x_2, x_3) aligned, at a point, with the fibers of one lamina. The stress and strain notation conventions for each coordinate system are collected in Tables A.1 and A.2, respectively.

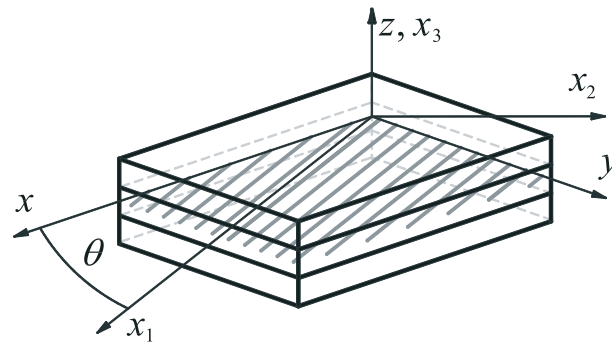


Figure A.1: Laminated composite plate and coordinate systems.

In the (x, y, z) coordinate system, the components of the displacement vector at one point are denoted by (u, v, w) , and in (x_1, x_2, x_3) the displacement components are (u_1, u_2, u_3) . The displacements of a point in the mid-plane of the plate are denoted by the subscript o .

Table A.1: Stress notations.

	Normal stresses			Shear stresses		
(x, y, z) coordinate system						
Tensorial stress	σ_{xx}	σ_{yy}	σ_{zz}	σ_{yz}	σ_{xz}	σ_{xy}
Engineering stress	σ_x	σ_y	σ_z	τ_{yz}	τ_{xz}	τ_{xy}
Contracted notation	σ_x	σ_y	σ_z	σ_q	σ_r	σ_s
(x_1, x_2, x_3) coordinate system						
Tensorial stress	σ_{11}	σ_{22}	σ_{33}	σ_{23}	σ_{13}	σ_{12}
Engineering stress	σ_1	σ_2	σ_3	τ_{23}	τ_{13}	τ_{12}
Contracted notation	σ_1	σ_2	σ_3	σ_4	σ_5	σ_6

A.1 Ingredients for the development of the equations

Before describing the classical laminated plate theory and the first-order shear deformation plate theory, the ingredients required for the development of these theories are presented in the following points.

Table A.2: Strain notations. The engineering and contracted notation shear strains are twice the tensorial shear strain.

	Normal strains			Shear strains		
<hr/> <hr/> (x, y, z) coordinate system <hr/> <hr/>						
Tensorial strain	ε_{xx}	ε_{yy}	ε_{zz}	ε_{yz}	ε_{xz}	ε_{xy}
Engineering strain	ε_x	ε_y	ε_z	γ_{yz}	γ_{xz}	γ_{xy}
Contracted notation	ε_x	ε_y	ε_z	ε_q	ε_r	ε_s
<hr/> <hr/> (x_1, x_2, x_3) coordinate system <hr/> <hr/>						
Tensorial strain	ε_{11}	ε_{22}	ε_{33}	ε_{23}	ε_{13}	ε_{12}
Engineering strain	ε_1	ε_2	ε_3	γ_{23}	γ_{13}	γ_{12}
Contracted notation	ε_1	ε_2	ε_3	ε_4	ε_5	ε_6

A.1.1 Strain-displacement relations

For full geometric nonlinear analysis, the components of the Green-Lagrange strain tensor referenced to a (x_1, x_2, x_3) Cartesian coordinate system are (sum on repeated subscript is implied):

$$\varepsilon_{ij} = \frac{1}{2} \left(\frac{\partial u_i}{\partial x_j} + \frac{\partial u_j}{\partial x_i} + \frac{\partial u_m}{\partial x_i} \frac{\partial u_m}{\partial x_j} \right); \quad i, j, m = 1, 2, 3 \quad (\text{A.1})$$

If the gradients of the displacements are so small that products of partial derivatives of u_i are negligible compared with linear derivative terms (i.e. first-order), the infinitesimal strain components are given by:

$$\varepsilon_{ij} = \frac{1}{2} \left(\frac{\partial u_i}{\partial x_j} + \frac{\partial u_j}{\partial x_i} \right); \quad i, j = 1, 2, 3 \quad (\text{A.2})$$

The plate problem that is considered here may involve moderate rotations, such as 10° - 15° [168]. Hence, the following terms associated with rotations of transverse normals are small but not negligible:

$$\left(\frac{\partial u_3}{\partial x_1} \right)^2, \left(\frac{\partial u_3}{\partial x_2} \right)^2, \frac{\partial u_3}{\partial x_1} \frac{\partial u_3}{\partial x_2} \quad (\text{A.3})$$

Using Equations (A.1) and the restriction (A.3), the called *von Kármán strain components* are obtained:

$$\begin{aligned}
\varepsilon_{11} &= \frac{\partial u_1}{\partial x_1} + \frac{1}{2} \left(\frac{\partial u_3}{\partial x_1} \right)^2 \\
\varepsilon_{22} &= \frac{\partial u_2}{\partial x_2} + \frac{1}{2} \left(\frac{\partial u_3}{\partial x_2} \right)^2 \\
\varepsilon_{33} &= \frac{\partial u_3}{\partial x_3} \\
\varepsilon_{12} &= \frac{1}{2} \left(\frac{\partial u_1}{\partial x_2} + \frac{\partial u_2}{\partial x_1} + \frac{\partial u_3}{\partial x_1} \frac{\partial u_3}{\partial x_2} \right) \\
\varepsilon_{13} &= \frac{1}{2} \left(\frac{\partial u_1}{\partial x_3} + \frac{\partial u_3}{\partial x_1} \right) \\
\varepsilon_{23} &= \frac{1}{2} \left(\frac{\partial u_2}{\partial x_3} + \frac{\partial u_3}{\partial x_2} \right)
\end{aligned} \tag{A.4}$$

A.1.2 Lamina constitutive equation

The linear relation between the stress and strain components is known as the generalized Hooke law. Taking as the reference the Cartesian coordinate system (x_1, x_2, x_3) , the Hooke law is expressed by:

$$\sigma_{ij} = c_{ijkl} \varepsilon_{kl}; \quad i, j, k, l = 1, 2, 3 \tag{A.5}$$

where c_{ijkl} is the fourth-order stiffness tensor with 81 components. The fact that the stress and strain tensors are symmetric, it allows to write:

$$c_{ijkl} = c_{jikl} = c_{ijlk} = c_{jilk} \tag{A.6}$$

which effectively reduces the number of independent components from 81 to 36. The 36 independent components can be written as a second-order stiffness tensor which allows to rewrite Equation (A.5) in contracted notation (see Tables A.1 and A.2):

$$\sigma_i = C_{ij} \varepsilon_j; \quad i, j = 1, 2, \dots, 6 \tag{A.7}$$

On the other hand, by postulating the existence of a function called strain energy density it is possible to demonstrate that the stiffness tensor is symmetric $C_{ij} = C_{ji}$. Because of this symmetry, there are only 21 independent stiffness components for anisotropic materials.

As shown in Figure A.1, the structure configuration considered in the present thesis corresponds to laminated composite plates manufactured by stacking unidirectional fiber reinforced laminae with randomly distributed fibers in their cross section. The cross section of each lamina presents isotropy which allows to model each one as a transversely isotropic material (see Figure A.2). Therefore, the constitutive equation of a lamina is defined by:

$$\begin{pmatrix} \sigma_1 \\ \sigma_2 \\ \sigma_3 \\ \sigma_4 \\ \sigma_5 \\ \sigma_6 \end{pmatrix} = \begin{bmatrix} C_{11} & C_{12} & C_{12} & 0 & 0 & 0 \\ & C_{22} & C_{23} & 0 & 0 & 0 \\ & & C_{22} & 0 & 0 & 0 \\ & & & \hat{C} & 0 & 0 \\ & sym. & & & C_{66} & 0 \\ & & & & & C_{66} \end{bmatrix} \begin{pmatrix} \varepsilon_1 \\ \varepsilon_2 \\ \varepsilon_3 \\ \varepsilon_4 \\ \varepsilon_5 \\ \varepsilon_6 \end{pmatrix} \quad (\text{A.8})$$

where $\hat{C} = (C_{22} - C_{23})/2$, and the stiffness coefficients are written as:

$$\begin{aligned} C_{11} &= \frac{(1 - \nu_{23}^2) E_1}{(1 + \nu_{23})(1 - \nu_{23} - 2\nu_{12}\nu_{21})}, & C_{12} &= \frac{\nu_{12}(1 + \nu_{23}) E_1}{(1 + \nu_{23})(1 - \nu_{23} - 2\nu_{12}\nu_{21})} \\ C_{22} &= \frac{(1 - \nu_{12}\nu_{21}) E_2}{(1 + \nu_{23})(1 - \nu_{23} - 2\nu_{12}\nu_{21})}, & C_{23} &= \frac{\nu_{23} + (\nu_{12}\nu_{21}) E_2}{(1 + \nu_{23})(1 - \nu_{23} - 2\nu_{12}\nu_{21})} \\ C_{66} &= G_{12} \end{aligned} \quad (\text{A.9})$$

Only five elastic properties are required in order to define the constitutive relation of transversely isotropic materials. These properties are the longitudinal Young modulus (i.e. along the fiber direction) E_1 , the transverse Young modulus E_2 , the in-plane shear modulus G_{12} , the major in-plane Poisson coefficient ν_{12} (or minor ν_{21}) and the transverse Poisson coefficient ν_{23} .

The stiffness matrix C_{ij} depends on the coordinate system used. For the unidirectional lamina shown in Figure A.3, the fiber orientation is rotated θ degrees respect to the global coordinate system (x, y, z) . The corresponding relationship between the stresses and strains at local and global coordinate system are defined by:

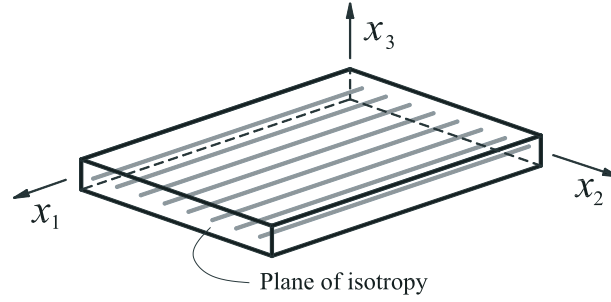


Figure A.2: Transverse isotropic lamina.

$$\begin{Bmatrix} \sigma_1 \\ \sigma_2 \\ \sigma_3 \\ \sigma_4 \\ \sigma_5 \\ \sigma_6 \end{Bmatrix} = [T] \begin{Bmatrix} \sigma_x \\ \sigma_y \\ \sigma_z \\ \sigma_q \\ \sigma_r \\ \sigma_s \end{Bmatrix}; \quad \begin{Bmatrix} \varepsilon_1 \\ \varepsilon_2 \\ \varepsilon_3 \\ \varepsilon_4 \\ \varepsilon_5 \\ \varepsilon_6 \end{Bmatrix} = [T]_\gamma \begin{Bmatrix} \varepsilon_x \\ \varepsilon_y \\ \varepsilon_z \\ \varepsilon_q \\ \varepsilon_r \\ \varepsilon_s \end{Bmatrix} \quad (\text{A.10})$$

Letting $c = \cos(\theta)$ and $s = \sin(\theta)$, the rotation matrixes $[T]$ and $[T]_\gamma$ are defined as:

$$[T] = \begin{bmatrix} c^2 & s^2 & 0 & 0 & 0 & 2cs \\ s^2 & c^2 & 0 & 0 & 0 & -2cs \\ 0 & 0 & 1 & 0 & 0 & 0 \\ 0 & 0 & 0 & c & -s & 0 \\ 0 & 0 & 0 & s & c & 0 \\ -cs & cs & 0 & 0 & 0 & c^2 - s^2 \end{bmatrix} \quad (\text{A.11})$$

$$[T]_\gamma = ([T]^{-1})^T \quad (\text{A.12})$$

The constitutive equation for an off-axis lamina defined in the global coordinate system (x, y, z) is:

$$\begin{Bmatrix} \sigma_x \\ \sigma_y \\ \sigma_z \\ \sigma_q \\ \sigma_r \\ \sigma_s \end{Bmatrix} = \underbrace{[T]^{-1}[C][T]}_{[\bar{C}]} \begin{Bmatrix} \varepsilon_x \\ \varepsilon_y \\ \varepsilon_z \\ \varepsilon_q \\ \varepsilon_r \\ \varepsilon_s \end{Bmatrix} \quad (\text{A.13})$$

where $[C]$ is the second-order stiffness tensor written in matrix form referenced to the local coordinate system (x_1, x_2, x_3) , and $[\bar{C}]$ is the stiffness tensor referenced to the global coordinate system (x, y, z) .

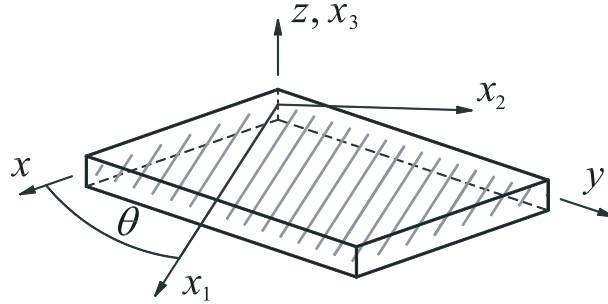


Figure A.3: Lamina coordinate systems.

A.1.3 Laminate resultants

Assuming unitary width in x and y axes, the resulting in-plane forces N_x, N_y, N_{xy} and through-the-thickness shear forces Q_x, Q_y , and in-plane moments M_x, M_y, M_{xy} of lamina p (see Figure A.4) can be calculated from equilibrium conditions as:

$$\begin{Bmatrix} N_x \\ N_y \\ N_{xy} \end{Bmatrix}_p = \int_{z_{p-1}}^{z_p} \begin{Bmatrix} \sigma_x \\ \sigma_y \\ \sigma_{xy} \end{Bmatrix}_p dz \quad (\text{A.14})$$

$$\begin{Bmatrix} Q_x \\ Q_y \end{Bmatrix}_p = \int_{z_{p-1}}^{z_p} \begin{Bmatrix} \sigma_{xz} \\ \sigma_{yz} \end{Bmatrix}_p dz \quad (\text{A.15})$$

$$\begin{Bmatrix} M_x \\ M_y \\ M_{xy} \end{Bmatrix}_p = \int_{z_{p-1}}^{z_p} \begin{Bmatrix} \sigma_x \\ \sigma_y \\ \sigma_{xy} \end{Bmatrix}_p z dz \quad (\text{A.16})$$

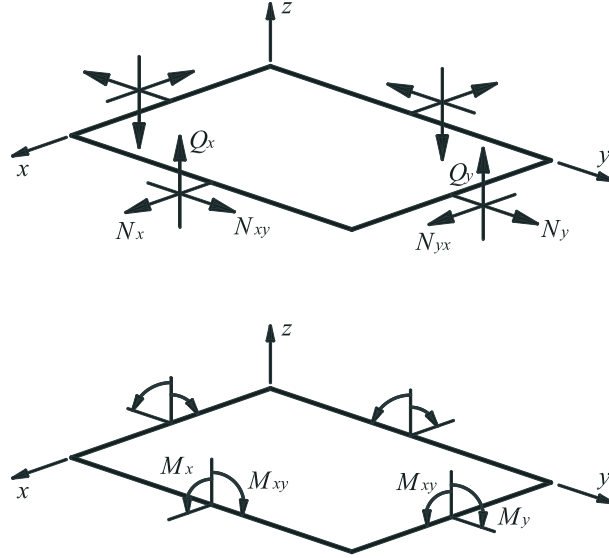


Figure A.4: Force and moment resultants on a lamina (or laminate).

where z_{p-1} and z_p are the thickness coordinates of the bottom and top of lamina p (see Figure A.5). The superposition of different laminae, with different fiber orientations or not, configures the laminate. For a laminate with N laminae, the resulting forces and moments are:

$$\begin{Bmatrix} N_x \\ N_y \\ N_{xy} \end{Bmatrix} = \int_{-h/2}^{h/2} \begin{Bmatrix} \sigma_x \\ \sigma_y \\ \sigma_{xy} \end{Bmatrix} dz = \sum_{p=1}^N \int_{z_{p-1}}^{z_p} \begin{Bmatrix} \sigma_x \\ \sigma_y \\ \sigma_{xy} \end{Bmatrix}_p dz \quad (\text{A.17})$$

$$\begin{Bmatrix} Q_x \\ Q_y \end{Bmatrix} = \int_{-h/2}^{h/2} \begin{Bmatrix} \sigma_{xz} \\ \sigma_{yz} \end{Bmatrix} dz = \sum_{p=1}^N \int_{z_{p-1}}^{z_p} \begin{Bmatrix} \sigma_{xz} \\ \sigma_{yz} \end{Bmatrix}_p dz \quad (\text{A.18})$$

$$\begin{Bmatrix} M_x \\ M_y \\ M_{xy} \end{Bmatrix} = \int_{-h/2}^{h/2} \begin{Bmatrix} \sigma_x \\ \sigma_y \\ \sigma_{xy} \end{Bmatrix} z dz = \sum_{p=1}^N \int_{z_{p-1}}^{z_p} \begin{Bmatrix} \sigma_x \\ \sigma_y \\ \sigma_{xy} \end{Bmatrix}_p z dz \quad (\text{A.19})$$

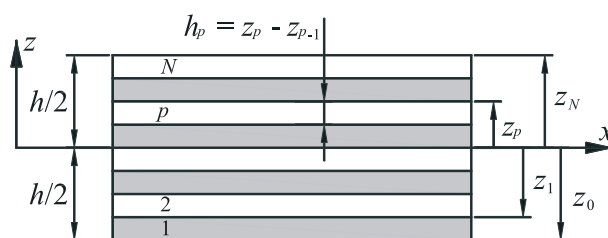


Figure A.5: Lamina location in a laminate.

A.1.4 Frameworks to develop the governing equations

The equations of motion (i.e. governing equations defined by displacement variables) of a solid body can be derived using either vector mechanics or energy principles. In vector mechanics, a representative volume element of the body is isolated with all its applied and reactive forces. Then, the vector sum of all static and dynamic forces and moments acting on the element is set to zero to obtain the equations. In methods based on energy principles, the total work done or energy stored in a body due to actual forces in moving through virtual displacements that are consistent with the essential (i.e. geometric) constraints of the body is set to zero to obtain the equations of motion. The energy approach also yields to the natural (i.e. force) boundary conditions as well as the form of the variables involved in the specification of geometric boundary conditions.

Principle of virtual displacements

The principle of virtual displacements states: *if a body is in static or dynamic equilibrium, the total virtual work done by all externally applied and internally generated forces in moving through their respective virtual displacements must be zero.* That is:

$$\delta W \equiv \delta W_I + \delta W_E = 0 \quad (\text{A.20})$$

where δW is the total virtual work of the body, δW_I and δW_E are the internal and external virtual works, respectively. The delta symbol δ is used in conjunction with virtual displacements and forces, and it is interpreted as an operator called the *variational operator*. It is used to denote a variation (or change) in a given quantity.

The external work done due to virtual displacements $\delta \mathbf{u}$ in a solid body Ω subjected to body forces \mathbf{f} per unit of mass and surface tractions \mathbf{T} per unit area of the boundary Γ_σ is given by:

$$\delta W_E = - \int_{\Omega} \rho \mathbf{f} \cdot \delta \mathbf{u} \, dv - \int_{\Gamma_\sigma} \mathbf{T} \cdot \delta \mathbf{u} \, ds \quad (\text{A.21})$$

where ρ is the density, ds denotes a surface element, dv denotes a volume element and Γ_σ denotes the portion of the boundary in which the stresses are specified. The negative sign of Equation (A.21) indicates that the work is performed on the body. The external virtual work can also be done due to virtual body forces and surface tractions, which yield to called *complementary virtual work*.

The forces applied on a deformable body cause it to deform and the body experiences internal stresses. The relative movement of the material particles in the body can be measured in terms of strains. Therefore, the work done on the body by external forces is responsible for the internal work. The internal virtual work is also called *virtual strain energy* and is expressed by:

$$\delta W_I = \delta U = \int_{\Omega} \sigma : \delta \varepsilon \, dv \quad (\text{A.22})$$

where σ is the stress tensor and $\delta \varepsilon$ is the virtual strain tensor due to the virtual displacement $\delta \mathbf{u}$.

Replacing Equations (A.21) and (A.22), the principle of virtual work written in terms of Cartesian rectangular components yields to (sum on repeated subscripts is implied):

$$\int_{\Omega} (\sigma_{ij} \delta \varepsilon_{ij} - \rho f_i \delta u_i) \, dv - \int_{\Gamma_\sigma} T_i \delta u_i \, ds = 0; \quad i, j = 1, 2, 3 \quad (\text{A.23})$$

By means of the fundamental lemma of variational calculus [61], the principle of virtual works can be expressed by differential equations called *Euler-Lagrange equations*. These equations are the usually form used to write the governing equations.

Hamilton principle

The *Hamilton principle* states that *of all possible paths that a material particle could travel from its position at time t_1 to its position at time t_2 , its actual path will be*

one for which the following integral is an extremum:

$$\int_{t_1}^{t_2} (K - W) dt \tag{A.24}$$

The difference between the kinetic and potential energies is called the *Lagrangian function*:

$$L = K - W = K - W_I - W_E \tag{A.25}$$

Thus, Hamilton principle can be expressed as:

$$\int_{t_1}^{t_2} (\delta K - \delta W_I - \delta W_E) dt = 0 \tag{A.26}$$

The kinetic energy of a continuous body Ω is given by:

$$K = \frac{1}{2} \int_{\Omega} \rho \frac{\partial \mathbf{u}}{\partial t} \cdot \frac{\partial \mathbf{u}}{\partial t} dv \tag{A.27}$$

where $\frac{\partial \mathbf{u}}{\partial t}$ denotes the velocity of the material particle.

Principle of minimum total potential energy

A special case of the principle of virtual displacements is the *principle of minimum total potential energy*. The difference between the principle of virtual displacements and the principle of minimum total potential energy is that, in the latter a constitutive law is invoked. Thus, the principle of virtual displacements is more general and it is applied to all material bodies independent of their constitutive behavior.

The sum $U + V = \Pi$ is called the *total potential energy* of the elastic body, where V is a potential equal to W_E and U is the strain energy which is equal to W_I . The principle of minimum total potential energy states that: *of all admissible displacements, those that satisfy the equilibrium equations make the total potential energy a minimum*. Thus, the principle of virtual work takes the form:

$$\partial U + \partial V \equiv \partial \Pi = 0 \tag{A.28}$$

The Euler-Lagrange equations resulting from the principle of virtual displacements are always in terms of the stresses or stress resultants, whereas those from

the principle of minimum total potential energy are in terms of the strains or displacements.

Variational methods

In general, exact solutions for the dynamic response of rectangular and flat plates with a certain boundary conditions are not available. Under these circumstances, methods known as *classical variational methods* can be applied (e.g. *Ritz method*; *Galerkin method*).

In variational methods it is seek an approximate solution to the problem in terms of adjustable parameters that are determined by substituting the assumed solution into the energy principle ($\partial W = 0$ or $\partial \Pi = 0$) that is equivalent to the governing equations of the problem. Such solution methods are called *direct methods* because the approximate solutions are obtained directly by applying the same energy principle that was used to derive the governing equations. The assumed solutions in the energy methods are in the form of a finite linear combination of undetermined parameters and appropriately chosen functions. Since the solution of a continuum problem, in general, cannot be represented by a infinite set of functions, error is introduced into the solution.

In the Ritz method, a dependent unknown displacement u is approximated by a finite linear combination U_N of the form:

$$u \approx U_N = \sum_{j=1}^N c_j \varphi_j + \varphi_0 \quad (\text{A.29})$$

where φ_0 represents the particular solution, while $\sum c_j \varphi_j$ is the homogeneous part of the solution. c_j denote undetermined parameters and φ_j are called the *approximation functions* which are appropriately selected functions of position. In order to ensure that the algebraic equations resulting from the Ritz approximation have a solution which converges to the true solution of the problem as the number of parameters N is increased, the approximation functions have to satisfy some requirements:

1. $\varphi_j (j = 1, 2, \dots, N)$ should satisfy the following three conditions:

- (a) Each φ_j is continuous, as required in the variational statement (i.e. $\delta W = 0$ or $\delta \Pi = 0$).
 - (b) Each φ_j satisfies the homogeneous form of the specified essential boundary conditions.
 - (c) The set $\{\varphi_j\}$ is linearly independent and complete.
2. φ_0 has to satisfy only the specified essential boundary conditions associated with the variational formulation since the natural boundary conditions are included in the functional Π or the statement δW ; φ_0 plays the role of the particular solution. It is necessarily equal to zero when the specified essential boundary conditions are homogeneous.

Once the approximation functions φ_0 and φ_j are selected, the parameters c_j in Equation (A.29) are determined by requiring U_N to minimize the total potential energy functional Π or satisfy the principle of virtual displacements of the problem.

For the principle of minimum total potential energy, upon substitution of the approximation $u \approx U_N$, $\Pi(U_N)$ becomes a function of c_1, c_1, \dots, c_N . Hence, minimization of the functional $\Pi(c_1, c_1, \dots, c_N)$ is reduced to the minimization of a function of several variables:

$$0 = \delta \Pi(U_N) = \sum_{j=1}^N \frac{\delta \Pi}{\delta c_j} c_j \quad \text{or} \quad \frac{\delta \Pi}{\delta c_j} = 0 \quad (\text{A.30})$$

The same procedure applies to the principle of virtual displacements. That is:

$$0 = \delta W(U_N) = \sum_{j=1}^N \frac{\delta W}{\delta c_j} c_j \quad \text{or} \quad \frac{\delta W}{\delta c_j} = 0 \quad (\text{A.31})$$

Equation (A.30) or (A.31) gives N algebraic equations in the N coefficients (c_1, c_2, \dots, c_N) ,

$$0 = \frac{\delta \Pi}{\delta c_j} = \sum_{j=1}^N R_{ij} c_j - F_i \quad \text{or} \quad \mathbf{Rc} = \mathbf{F} \quad (\text{A.32})$$

where R_{ij} and F_i are known coefficients that depend on the problem parameters (e.g. geometry, material coefficients and loads) and the approximation functions.

Equation (A.32) is then solved for c_i and substituted back into Equation (A.29) to obtain the Ritz solution with N parameters.

A.2 Plate theories and governing equations

A plate is a structural element with planform dimensions that are large compared to its thickness and is subjected to loads that cause bending deformation in addition to stretching. Because of the smallness of thickness dimension, it is often not necessary to model them using 3D elasticity equations. Simple 2D plate theories can be developed by making assumptions concerning the variation of the displacement field. Therefore, the *compatibility conditions* which provide single-valued solution of the displacements by means of the strain-displacement relations (i.e. Equations (A.1)) are not necessary since the displacements are directly assumed.

In this section only are shown the resulting governing equations for the *classical laminated plate theory* and for the *first-order shear plate theory*. These plate theories are the most easier and used in the literature in order to develop complete analytical impact models of laminated composite plates. Other more accurate plate theories can be used but are often dismissed since the development of the governing equations becomes algebraic complicated and their integration imply high computational effort without improving significantly the accuracy of the results.

A.2.1 Classical laminated plate theory

Displacement field and kinematics

The displacement field of the classical laminated plate theory is based on the *Kirchhoff-Love hypothesis*, which involve the following assumptions:

1. Straight lines perpendicular to the mid-plane (i.e. transverse normals) before deformations remain straight after deformation.
2. The transverse normals do not experience elongation (i.e. they are inextensible).
3. The transverse normals rotate such that they remain perpendicular to the mid-plane after deformation.

The first two assumptions of the hypothesis require that in-plane displacements u and v vary linearly through-the-thickness of the laminate, and the transverse displacement w is constant through-the-thickness of the laminate (see Figure A.6). That is:

$$\begin{aligned} u(x, y, z) &= u_o(x, y) + z\phi_1(x, y) \\ v(x, y, z) &= v_o(x, y) + z\phi_2(x, y) \\ w(x, y, z) &= w_o(x, y) \end{aligned} \quad (\text{A.33})$$

where u_o, v_o, w_o are the displacement components of a point on the mid-plane of the laminate, ϕ_1 is the rotation of a transverse normal about the y axis, and ϕ_2 is the rotation of a transverse normal about the x axis. The third assumption of the Kirchhoff-Love hypothesis implies that the rotations ϕ_1 and ϕ_2 are equal to:

$$\phi_1 = -\frac{\partial w_o}{\partial x}; \quad \phi_2 = -\frac{\partial w_o}{\partial y} \quad (\text{A.34})$$

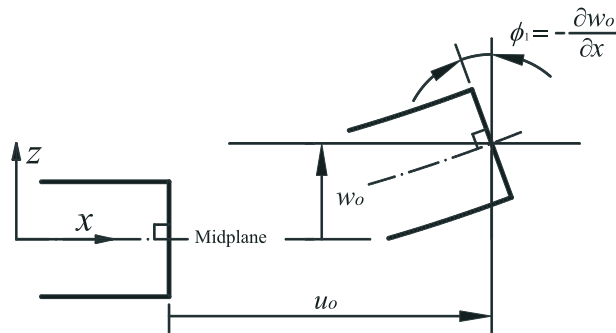


Figure A.6: Behavior of transverse section in classical plate theory.

Using the von Kármán strain-displacement relations (Equations (A.4)) referenced to the coordinate system (x, y, z) and the assumed displacement field (Equations (A.33) and (A.34)) the strain components yield to the following expressions:

$$\begin{aligned}
\varepsilon_x &\equiv \varepsilon_{xx} = \frac{\partial u}{\partial x} + \frac{1}{2} \left(\frac{\partial w}{\partial x} \right)^2 = \frac{\partial u_o}{\partial x} + \frac{1}{2} \left(\frac{\partial w_o}{\partial x} \right)^2 - z \frac{\partial^2 w_o}{\partial x^2} \\
\varepsilon_y &\equiv \varepsilon_{yy} = \frac{\partial v}{\partial y} + \frac{1}{2} \left(\frac{\partial w}{\partial y} \right)^2 = \frac{\partial v_o}{\partial y} + \frac{1}{2} \left(\frac{\partial w_o}{\partial y} \right)^2 - z \frac{\partial^2 w_o}{\partial y^2} \\
\varepsilon_z &\equiv \varepsilon_{zz} = \frac{\partial w}{\partial z} = \frac{\partial w_o}{\partial z} = 0 \\
\varepsilon_q &\equiv 2\varepsilon_{yz} = \frac{\partial v}{\partial z} + \frac{\partial w}{\partial y} = -\frac{\partial w_o}{\partial y} + \frac{\partial w_o}{\partial y} = 0 \\
\varepsilon_r &\equiv 2\varepsilon_{xz} = \frac{\partial u}{\partial z} + \frac{\partial w}{\partial x} = -\frac{\partial w_o}{\partial x} + \frac{\partial w_o}{\partial x} = 0 \\
\varepsilon_s &\equiv 2\varepsilon_{xy} = \frac{\partial u}{\partial y} + \frac{\partial v}{\partial x} + \frac{\partial w}{\partial x} \frac{\partial w}{\partial y} = \frac{\partial u_o}{\partial y} + \frac{\partial v_o}{\partial x} + \frac{\partial w_o}{\partial x} \frac{\partial w_o}{\partial y} - 2z \frac{\partial^2 w_o}{\partial x \partial y}
\end{aligned} \tag{A.35}$$

The three assumptions considered lead to the neglect of the transverse strains ε_{xz} , ε_{yz} and ε_z . Neglecting these strains leads to the omission of σ_{xz} , σ_{yz} and σ_z . Thus the classical laminated plate theory does not account for out-of-plane deformations and stresses. This implies that plates are infinitely rigid in the transverse direction, whereas in reality laminated composite plates are weaker in this direction.

Equations (A.35) can be expressed in a general form by:

$$\varepsilon_i = \varepsilon_i^o + z\kappa_i; \quad i = x, y, s \tag{A.36}$$

The strains $\varepsilon_i^o = (\varepsilon_x^o, \varepsilon_y^o, \varepsilon_s^o)$ are associated with the in-plane stretching and shearing of the mid-plane, and are called the *membrane strains*. The quantities $\kappa_i = (\kappa_x, \kappa_y, \kappa_s)$ are the curvatures which multiplied by z gives the bending strains. Equations (A.35) shows that membrane strains and curvatures for the classic laminate plate theory have the following explicit form:

$$\begin{aligned}
\varepsilon_x^o &= \frac{\partial u_o}{\partial x} + \frac{1}{2} \left(\frac{\partial w_o}{\partial x} \right)^2, & \kappa_x &= -\frac{\partial^2 w_o}{\partial x^2} \\
\varepsilon_y^o &= \frac{\partial v_o}{\partial y} + \frac{1}{2} \left(\frac{\partial w_o}{\partial y} \right)^2, & \kappa_y &= -\frac{\partial^2 w_o}{\partial y^2} \\
\varepsilon_s^o &= \frac{\partial u_o}{\partial y} + \frac{\partial v_o}{\partial x} + \frac{\partial w_o}{\partial x} \frac{\partial w_o}{\partial y}, & \kappa_s &= -2 \frac{\partial^2 w_o}{\partial x \partial y}
\end{aligned} \tag{A.37}$$

where the underlined terms are the von Kármán nonlinear strains.

Laminate resultants

The in-plane laminate forces (A.17) and moment resultants (A.19) can be expressed in function of the membrane strains and curvatures resulted in the classical laminated plate theory (Equation (A.36)) by replacing the constitutive equation of each lamina (Equation (A.13)) of the laminate (see Figure A.5), referenced to the coordinate system (x, y, z) . The in-plane resultants of the laminated plate yield to:

$$\begin{Bmatrix} N_x \\ N_y \\ N_{xy} \end{Bmatrix} = \begin{bmatrix} A_{11} & A_{12} & A_{16} \\ A_{12} & A_{22} & A_{26} \\ A_{16} & A_{26} & A_{66} \end{bmatrix} \begin{Bmatrix} \varepsilon_x^o \\ \varepsilon_y^o \\ \varepsilon_s^o \end{Bmatrix} + \begin{bmatrix} B_{11} & B_{12} & B_{16} \\ B_{12} & B_{22} & B_{26} \\ B_{16} & B_{26} & B_{66} \end{bmatrix} \begin{Bmatrix} \kappa_x \\ \kappa_y \\ \kappa_s \end{Bmatrix} \quad (\text{A.38})$$

$$\begin{Bmatrix} M_x \\ M_y \\ M_{xy} \end{Bmatrix} = \begin{bmatrix} B_{11} & B_{12} & B_{16} \\ B_{12} & B_{22} & B_{26} \\ B_{16} & B_{26} & B_{66} \end{bmatrix} \begin{Bmatrix} \varepsilon_x^o \\ \varepsilon_y^o \\ \varepsilon_s^o \end{Bmatrix} + \begin{bmatrix} D_{11} & D_{12} & D_{16} \\ D_{12} & D_{22} & D_{26} \\ D_{16} & D_{26} & D_{66} \end{bmatrix} \begin{Bmatrix} \kappa_x \\ \kappa_y \\ \kappa_s \end{Bmatrix} \quad (\text{A.39})$$

where A_{ij} denote the extensional stiffness, B_{ij} the bending-extensional coupling stiffness, and D_{ij} the bending stiffness of a laminate. They are defined by:

$$A_{ij} = \sum_{p=1}^N \bar{C}_{ij,p} (z_p - z_{p-1}); \quad i, j = 1, 2, 6 \quad (\text{A.40})$$

$$B_{ij} = \frac{1}{2} \sum_{p=1}^N \bar{C}_{ij,p} (z_p^2 - z_{p-1}^2); \quad i, j = 1, 2, 6 \quad (\text{A.41})$$

$$D_{ij} = \frac{1}{3} \sum_{p=1}^N \bar{C}_{ij,p} (z_p^3 - z_{p-1}^3); \quad i, j = 1, 2, 6 \quad (\text{A.42})$$

Governing equations

The boundary conditions considered for the test ASTM - D7136 / D7136M [59] are approximated to simply supported boundary conditions. In this case, the application of a variational method is not necessary since the assumed solutions of the displacements provided by the *Navier solutions* yield, for some laminate configurations, to the exact solution of the governing equations. Therefore, the governing equations are obtained by applying the Hamilton principle.

The virtual strain energy for classical plate theory in a solid element of the plate is done by:

$$\delta U = \int_{\Omega} (\sigma_x \delta \varepsilon_x + \sigma_y \delta \varepsilon_y + \sigma_s \delta \varepsilon_s) dv \quad (\text{A.43})$$

By replacing the assumed kinematics (Equation (A.36)) and the stress resultants of the laminate (Equations (A.17) and (A.19)), the virtual strain energy results:

$$\delta U = \int_{\Omega} (N_x \delta \varepsilon_x^o + M_x \delta \kappa_x + N_y \delta \varepsilon_y^o + M_y \delta \kappa_y + N_{xy} \delta \varepsilon_s^o + M_{xy} \delta \kappa_s) dx dy \quad (\text{A.44})$$

The virtual kinetic energy is defined by:

$$\delta K = \int_{\Omega} \int_{-h/2}^{h/2} \rho (\dot{u} \delta \dot{u} + \dot{v} \delta \dot{v} + \dot{w} \delta \dot{w}) dz dx dy \quad (\text{A.45})$$

where the superposed dot indicates first derivative respect time. By replacing the assumed displacement field (Equations (A.33)) and integrating over the plate thickness, the virtual kinetic energy yields to:

$$\begin{aligned} \delta K = \int_{\Omega} \left[-I_1 (\dot{u}_o \delta \dot{u}_o + \dot{v}_o \delta \dot{v}_o + \dot{w}_o \delta \dot{w}_o) + I_2 \left(\frac{\partial \delta \dot{w}_o}{\partial x} \dot{u}_o \right. \right. \\ \left. \left. + \frac{\partial \dot{w}_o}{\partial x} \delta \dot{u}_o + \frac{\partial \delta \dot{w}_o}{\partial y} \dot{v}_o + \frac{\partial \dot{w}_o}{\partial y} \delta \dot{v}_o \right) - I_3 \left(\frac{\partial \dot{w}_o}{\partial x} \frac{\partial \delta \dot{w}_o}{\partial x} + \frac{\partial \dot{w}_o}{\partial y} \frac{\partial \delta \dot{w}_o}{\partial y} \right) \right] dx dy \end{aligned} \quad (\text{A.46})$$

For laminates composed by plies with the same material and by considering that the center of masses is located in the laminate centerline, the inertia terms (I_1, I_2, I_3) are defined by:

$$\begin{Bmatrix} I_1 \\ I_2 \\ I_3 \end{Bmatrix} = \int_{-h/2}^{h/2} \begin{Bmatrix} 1 \\ z \\ z^2 \end{Bmatrix} \rho dz = \rho \begin{Bmatrix} h \\ 0 \\ \frac{h^3}{12} \end{Bmatrix} \quad (\text{A.47})$$

The external applied forces consist of a distributed transverse load q over the surface located at $(x, y, \frac{h}{2})$, and forces and moments due to in-plane normal stress

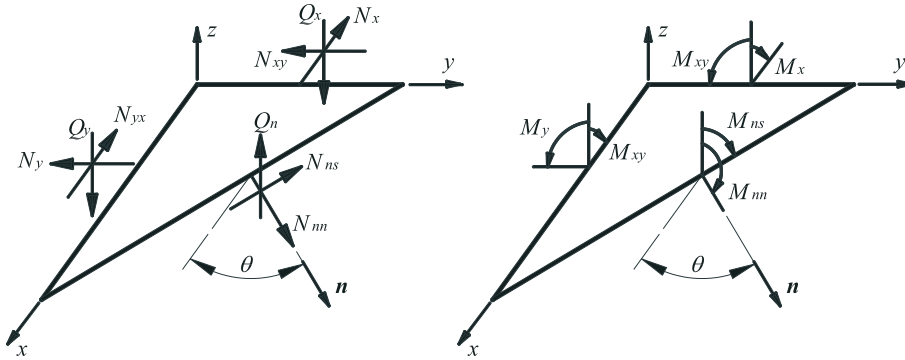


Figure A.7: Stress resultants on an arbitrary edge of a laminate.

$\hat{\sigma}_{nn}$, in-plane tangential stress $\hat{\sigma}_{ns}$, and transverse shear stress $\hat{\sigma}_{nz}$, all acting on and edge with normal $\hat{\mathbf{n}}$ (see Figure A.7).

Then, the virtual work done by the external forces is:

$$\begin{aligned} \delta V = & - \int_{\Omega} q(x, y) \delta w_o(x, y, \frac{h}{2}) dx dy \\ & - \int_{\Gamma_{\sigma}} \int_{-h/2}^{h/2} [\hat{\sigma}_{nn} \delta u_n + \hat{\sigma}_{ns} \delta u_s + \hat{\sigma}_{nz} \delta w] dz ds \end{aligned} \quad (\text{A.48})$$

The stresses $\hat{\sigma}_{nn}$, $\hat{\sigma}_{ns}$, and stress $\hat{\sigma}_{nz}$ can be expressed in force and moment resultants by:

$$\begin{aligned} \begin{Bmatrix} \hat{N}_{nn} \\ \hat{N}_{ns} \end{Bmatrix} &= \int_{-h/2}^{h/2} \begin{Bmatrix} \hat{\sigma}_{nn} \\ \hat{\sigma}_{ns} \end{Bmatrix} dz, & \begin{Bmatrix} \hat{M}_{nn} \\ \hat{M}_{ns} \end{Bmatrix} &= \int_{-h/2}^{h/2} \begin{Bmatrix} \hat{\sigma}_{nn} \\ \hat{\sigma}_{ns} \end{Bmatrix} z dz \\ \hat{Q}_n &= \int_{-h/2}^{h/2} \hat{\sigma}_{nz} dz \end{aligned} \quad (\text{A.49})$$

Applying Hamilton principle, the following Equation (A.50) defined in terms of the force and moment resultants is obtained:

$$\begin{aligned}
0 = & \int_0^T \int_{\Omega} \left[- \left(\frac{\partial N_x}{\partial x} + \frac{\partial N_{xy}}{\partial y} - I_1 \ddot{u}_o \right) \delta u_o \right. \\
& - \left(\frac{\partial N_{xy}}{\partial x} + \frac{\partial N_y}{\partial y} - I_1 \ddot{v}_o \right) \delta v_o \\
& - \left(\frac{\partial^2 M_x}{\partial x^2} + 2 \frac{\partial^2 M_{xy}}{\partial x \partial y} + \frac{\partial^2 M_y}{\partial y^2} + \mathcal{N}(u_o, v_o, w_o) \right. \\
& \left. \left. + q - I_1 \ddot{w}_o + I_3 \frac{\partial^2 \ddot{w}_o}{\partial x^2} + I_3 \frac{\partial^2 \ddot{w}_o}{\partial y^2} \right) \delta w_o \right] dx dy dt \\
& + \int_0^T \int_{\Gamma_{\sigma}} \left[\left(N_{nn} - \hat{N}_{nn} \right) \delta u_{on} + \left(N_{ns} - \hat{N}_{ns} \right) \delta u_{os} \right. \\
& \left. + \left(V_n - \hat{V}_n \right) \delta w_o - \left(M_{nn} - \hat{M}_{nn} \right) \frac{\partial \delta w_o}{\partial n} \right] ds dt
\end{aligned} \tag{A.50}$$

where $\mathcal{N}(u_o, v_o, w_o)$, V_n and \hat{V}_n are defined by:

$$\mathcal{N}(u_o, v_o, w_o) = \frac{\partial}{\partial x} \left(N_x \frac{\partial w_o}{\partial x} + N_{xy} \frac{\partial w_o}{\partial y} \right) + \frac{\partial}{\partial y} \left(N_{xy} \frac{\partial w_o}{\partial x} + N_y \frac{\partial w_o}{\partial y} \right) \tag{A.51}$$

$$\begin{aligned}
V_n \equiv & \frac{\partial M_x}{\partial x} n_x + \frac{\partial M_{xy}}{\partial y} n_x + \frac{\partial M_y}{\partial y} n_y + \frac{\partial M_{xy}}{\partial x} n_y + \frac{\partial M_{ns}}{\partial s} n_x \\
& + \mathcal{P}(u_o, v_o, w_o) + I_3 \frac{\partial \ddot{w}_o}{\partial x} n_x + I_3 \frac{\partial \ddot{w}_o}{\partial y} n_y
\end{aligned} \tag{A.52}$$

$$\hat{V}_n = \hat{Q}_n + \frac{\partial \hat{M}_{ns}}{\partial s} \tag{A.53}$$

where $\mathcal{P}(u_o, v_o, w_o)$ is defined by:

$$\mathcal{P}(u_o, v_o, w_o) = \left(N_x \frac{\partial w_o}{\partial x} + N_{xy} \frac{\partial w_o}{\partial y} \right) n_x + \left(N_{xy} \frac{\partial w_o}{\partial x} + N_y \frac{\partial w_o}{\partial y} \right) n_y \tag{A.54}$$

From Equation (A.50) the Euler-Lagrange governing equations are obtained:

$$\frac{\partial N_x}{\partial x} + \frac{\partial N_{xy}}{\partial y} = I_1 \ddot{u}_o - I_2 \frac{\partial \ddot{w}_o}{\partial x} \tag{A.55}$$

$$\frac{\partial N_{xy}}{\partial x} + \frac{\partial N_y}{\partial y} = I_1 \ddot{v}_o - I_2 \frac{\partial \ddot{w}_o}{\partial y} \tag{A.56}$$

$$\begin{aligned}
& \frac{\partial^2 M_x}{\partial x^2} + 2 \frac{\partial^2 M_{xy}}{\partial x \partial y} + \frac{\partial^2 M_y}{\partial y^2} + \mathcal{N}(u_o, v_o, w_o) + q \\
& = I_1 \ddot{w}_o + I_2 \left(\frac{\partial \ddot{u}_o}{\partial x} + \frac{\partial \ddot{v}_o}{\partial y} \right) - I_3 \left(\frac{\partial^2 \ddot{w}_o}{\partial x^2} + \frac{\partial^2 \ddot{w}_o}{\partial y^2} \right)
\end{aligned} \tag{A.57}$$

where the terms involving I_3 are called rotary (or rotatory) inertia terms, and are often omitted because it is small in comparison to the $I_1 \ddot{u}$ and $I_1 \ddot{v}$.

And the natural boundary conditions [61] are:

$$\begin{aligned}
N_{nn} - \hat{N}_{nn} &= 0, & N_{ns} - \hat{N}_{ns} &= 0 \\
M_{nn} - \hat{M}_{nn} &= 0, & V_n - \hat{V}_n &= 0
\end{aligned} \tag{A.58}$$

When transient response of a plate is of interest, it is necessary to know the initial displacement field and velocity field throughout the domain of the plate. In classical laminated plate theory, the initial conditions at time $t = 0$ for all points in Ω are:

$$\begin{aligned}
u_n &= u_n^0, & u_s &= u_s^0, & w_o &= w_o^0 \\
\dot{u}_n &= \dot{u}_n^0, & \dot{u}_s &= \dot{u}_s^0, & \dot{w}_o &= \dot{w}_o^0
\end{aligned} \tag{A.59}$$

The governing Equations (A.55-A.57) can be expressed in terms of displacements u_o, v_o, w_o by substituting Equations (A.38) and (A.39), and the resulting expressions of the strains (Equations (A.37)). Neglecting the third order derivative terms in the space, the resulting motion equations are:

$$\begin{aligned}
& \frac{\partial}{\partial x} \left[A_{11} \frac{\partial u_o}{\partial x} + A_{12} \frac{\partial v_o}{\partial y} + A_{16} \left(\frac{\partial u_o}{\partial y} + \frac{\partial v_o}{\partial x} \right) + B_{11} \left(-\frac{\partial^2 w_o}{\partial x^2} \right) + \right. \\
& B_{12} \left(-\frac{\partial^2 w_o}{\partial y^2} \right) + B_{16} \left(-2 \frac{\partial^2 w_o}{\partial x \partial y} \right) \left. \right] + \frac{\partial}{\partial y} \left[A_{16} \frac{\partial u_o}{\partial x} + A_{26} \frac{\partial v_o}{\partial y} + \right. \\
& A_{66} \left(\frac{\partial u_o}{\partial y} + \frac{\partial v_o}{\partial x} \right) + B_{16} \left(-\frac{\partial^2 w_o}{\partial x^2} \right) + B_{26} \left(-\frac{\partial^2 w_o}{\partial y^2} \right) \\
& \left. + B_{66} \left(-2 \frac{\partial^2 w_o}{\partial x \partial y} \right) \right] = I_1 \frac{\partial^2 u_o}{\partial t^2} - I_2 \frac{\partial \ddot{w}_o}{\partial x}
\end{aligned} \tag{A.60}$$

$$\begin{aligned}
& \frac{\partial}{\partial x} \left[A_{16} \frac{\partial u_o}{\partial x} + A_{26} \frac{\partial v_o}{\partial y} + A_{66} \left(\frac{\partial u_o}{\partial y} + \frac{\partial v_o}{\partial x} \right) + B_{16} \left(-\frac{\partial^2 w_o}{\partial x^2} \right) \right. \\
& + B_{26} \left(-\frac{\partial^2 w_o}{\partial y^2} \right) + B_{66} \left(-2 \frac{\partial^2 w_o}{\partial x \partial y} \right) \left. + \frac{\partial}{\partial y} \left[A_{12} \frac{\partial u_o}{\partial x} + A_{22} \frac{\partial v_o}{\partial y} \right. \right. \\
& + A_{26} \left(\frac{\partial u_o}{\partial y} + \frac{\partial v_o}{\partial x} \right) + B_{12} \left(-\frac{\partial^2 w_o}{\partial x^2} \right) + B_{22} \left(-\frac{\partial^2 w_o}{\partial y^2} \right) \\
& \left. + B_{26} \left(-2 \frac{\partial^2 w_o}{\partial x \partial y} \right) \right] = I_1 \frac{\partial^2 v_o}{\partial t^2} - I_2 \frac{\partial \ddot{w}_o}{\partial y}
\end{aligned} \tag{A.61}$$

$$\begin{aligned}
& \frac{\partial^2}{\partial x^2} \left[B_{11} \frac{\partial u_o}{\partial x} + B_{12} \frac{\partial v_o}{\partial y} + B_{16} \left(\frac{\partial u_o}{\partial y} + \frac{\partial v_o}{\partial x} \right) + D_{11} \left(-\frac{\partial^2 w_o}{\partial x^2} \right) \right. \\
& + D_{12} \left(-\frac{\partial^2 w_o}{\partial y^2} \right) + D_{16} \left(-2 \frac{\partial^2 w_o}{\partial x \partial y} \right) \left. + 2 \frac{\partial^2}{\partial x \partial y} \left[B_{16} \frac{\partial u_o}{\partial x} \right. \right. \\
& + B_{26} \frac{\partial v_o}{\partial y} + B_{66} \left(\frac{\partial u_o}{\partial y} + \frac{\partial v_o}{\partial x} \right) + D_{16} \left(-\frac{\partial^2 w_o}{\partial x^2} \right) \\
& + D_{26} \left(-\frac{\partial^2 w_o}{\partial y^2} \right) + D_{66} \left(-2 \frac{\partial^2 w_o}{\partial x \partial y} \right) \left. + \frac{\partial^2}{\partial y^2} \left[B_{12} \frac{\partial u_o}{\partial x} + B_{22} \frac{\partial v_o}{\partial y} \right. \right. \\
& + B_{26} \left(\frac{\partial u_o}{\partial y} + \frac{\partial v_o}{\partial x} \right) + D_{12} \left(-\frac{\partial^2 w_o}{\partial x^2} \right) + D_{22} \left(-\frac{\partial^2 w_o}{\partial y^2} \right) \\
& \left. + D_{26} \left(-2 \frac{\partial^2 w_o}{\partial x \partial y} \right) \right] + \mathcal{N}(u_o, v_o, w_o) + q = I_1 \frac{\partial^2 w_o}{\partial t^2} \\
& + I_2 \left(\frac{\partial \ddot{u}_o}{\partial x} + \frac{\partial \ddot{v}_o}{\partial y} \right) - I_3 \left(\frac{\partial^2 \ddot{w}_o}{\partial x^2} + \frac{\partial^2 \ddot{w}_o}{\partial y^2} \right)
\end{aligned} \tag{A.62}$$

A.2.2 First-order shear plate theory

The classical laminated plate theory is not recommended for composites that are likely to fail in transverse shear or delamination, because the transverse shears and normal stresses are not accounted for. A refinement to the classical plate theory is provided by the *first-order shear deformation plate theory* (also known as *Mindlin plate theory*). There are numerous plate theories documented in the literature (not shown here) that also include transverse shear deformations. In all these theories, the displacements are expanded as linear combinations of the thickness coordinate and undetermined functions of position in the reference surface.

Displacement field and kinematics

The assumptions of the first-order shear deformation theory are the same as in the classical laminated plate theory, with the exception of the transverse normals sections can rotate such that they can not remain perpendicular to the mid-plane after deformation. Therefore, the displacement field described for classical laminated plate theory by Equations (A.33) also can be used for first-order shear plate theory, but the rotations ϕ_1 and ϕ_2 of a transverse normals are now independent of $\partial w_o/\partial x$ and $\partial w_o/\partial y$ (see Figure A.8).

Using the von Kármán strain-displacement relations (Equations (A.4)) referenced to the coordinate system (x, y, z) and the assumed displacement field (Equations (A.33)), the strain components yield to the following expressions:

$$\begin{aligned}
 \varepsilon_x &\equiv \varepsilon_{xx} = \frac{\partial u}{\partial x} + \frac{1}{2} \left(\frac{\partial w}{\partial x} \right)^2 = \frac{\partial u_o}{\partial x} + \frac{1}{2} \left(\frac{\partial w_o}{\partial x} \right)^2 + z \frac{\partial \phi_1}{\partial x} \\
 \varepsilon_y &\equiv \varepsilon_{yy} = \frac{\partial v}{\partial y} + \frac{1}{2} \left(\frac{\partial w}{\partial y} \right)^2 = \frac{\partial v_o}{\partial y} + \frac{1}{2} \left(\frac{\partial w_o}{\partial y} \right)^2 + z \frac{\partial \phi_2}{\partial y} \\
 \varepsilon_z &\equiv \varepsilon_{zz} = \frac{\partial w}{\partial z} = \frac{\partial w_o}{\partial z} = 0 \\
 \varepsilon_q &\equiv 2\varepsilon_{yz} = \frac{\partial v}{\partial z} + \frac{\partial w}{\partial y} = \phi_2 + \frac{\partial w_o}{\partial y} \\
 \varepsilon_r &\equiv 2\varepsilon_{xz} = \frac{\partial u}{\partial z} + \frac{\partial w}{\partial x} = \phi_1 + \frac{\partial w_o}{\partial x} \\
 \varepsilon_s &\equiv 2\varepsilon_{xy} = \\
 &= \frac{\partial u}{\partial y} + \frac{\partial v}{\partial x} + \frac{\partial w}{\partial x} \frac{\partial w}{\partial y} = \frac{\partial u_o}{\partial y} + \frac{\partial v_o}{\partial x} + \frac{\partial w_o}{\partial x} \frac{\partial w_o}{\partial y} + z \left(\frac{\partial \phi_1}{\partial y} + \frac{\partial \phi_2}{\partial x} \right)
 \end{aligned} \tag{A.63}$$

As in classical laminated plate theory, Equations (A.63) can be expressed in a general form by:

$$\varepsilon_i = \varepsilon_i^o + z\kappa_i; \quad i = x, y, q, r, s \tag{A.64}$$

where the strains $\varepsilon_i^o = (\varepsilon_x^o, \varepsilon_y^o, \varepsilon_s^o)$ are the membrane strains, the quantities $\kappa_i = (\kappa_x, \kappa_y, \kappa_s)$ are the curvatures, and ε_q^o and ε_r^o are the transverse shear strains. Equations (A.63) show that membrane strains, shear strains and curvatures for the first-order shear deformation plate theory have the following explicit form:

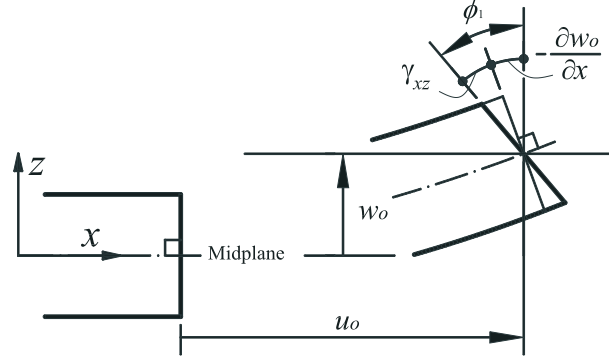


Figure A.8: Behavior of transverse section in first-order shear plate theory.

$$\begin{aligned}
 \varepsilon_x^o &= \frac{\partial u_o}{\partial x} + \frac{1}{2} \left(\frac{\partial w_o}{\partial x} \right)^2, & \kappa_x &= \frac{\partial \phi_1}{\partial x} \\
 \varepsilon_y^o &= \frac{\partial v_o}{\partial y} + \frac{1}{2} \left(\frac{\partial w_o}{\partial y} \right)^2, & \kappa_y &= \frac{\partial \phi_2}{\partial y} \\
 \varepsilon_z^o &= 0, & \kappa_z &= 0 \\
 \varepsilon_q^o &= \phi_2 + \frac{\partial w_o}{\partial y}, & \kappa_q &= 0 \\
 \varepsilon_r^o &= \phi_1 + \frac{\partial w_o}{\partial x}, & \kappa_r &= 0 \\
 \varepsilon_s^o &= \frac{\partial u_o}{\partial y} + \frac{\partial v_o}{\partial x} + \frac{\partial w_o}{\partial x} \frac{\partial w_o}{\partial y}, & \kappa_s &= \frac{\partial \phi_1}{\partial y} + \frac{\partial \phi_2}{\partial x}
 \end{aligned} \tag{A.65}$$

where the underlined terms are the von Kármán nonlinear strains.

Laminate resultants

The in-plane laminate forces (A.17) and moment resultants (A.19) expressed in function of the membrane strains and curvatures resulted in the first-order shear deformation plate theory (Equation (A.64)) yield to the same expressions obtained for classical laminated plate theory (Equations (A.38) and (A.39)). However, the transverse shear resultants have also to be defined. Replacing the strains of Equation (A.64) in the transverse shear forces (A.18) by using the constitutive equation of each lamina of the laminate referenced to the coordinate system (x, y, z) (Equation (A.13)), the shear forces result:

$$\begin{Bmatrix} Q_y \\ Q_x \end{Bmatrix} = \begin{bmatrix} A_{44} & A_{45} \\ A_{45} & A_{55} \end{bmatrix} \begin{Bmatrix} \varepsilon_q^o \\ \varepsilon_r^o \end{Bmatrix} \quad (\text{A.66})$$

The transverse shear stiffness A_{ij} are defined by:

$$A_{ij} = K_{ij} \sum_{p=1}^N \bar{C}_{ij,p} (z_p - z_{p-1}); \quad i, j = 4, 5 \quad (\text{A.67})$$

where K_{ij} are the dimensionless shear correction factors. Modeling transverse shear strains and stresses to be constant through the thickness results in the transverse shear energy being too large when compared to that coming from a more realistic parabolic distribution. In addition, equilibrium is not satisfied at the surfaces. Therefore, the shear correction factors are used so that the constant distribution of transverse shear strains and stresses has the same strain energy as the parabolic distribution. Normally, K_{ij} are taken as an isotropic material (i.e. 5/6).

Governing equations

The virtual strain energy for first-order shear deformation plate theory in a solid element of the plate is done by:

$$\delta U = \int_{\Omega} (\sigma_x \delta \varepsilon_x + \sigma_y \delta \varepsilon_y + \sigma_s \delta \varepsilon_s + \sigma_q \delta \varepsilon_q + \sigma_r \delta \varepsilon_r) dv \quad (\text{A.68})$$

By replacing the assumed kinematics (Equation (A.64)) and the stress resultants of the laminate (Equations (A.17), (A.18) and (A.19)), the virtual strain energy results:

$$\begin{aligned} \delta U = \int_{\Omega} & (N_x \delta \varepsilon_x^o + M_x \delta \kappa_x + N_y \delta \varepsilon_y^o + M_y \delta \kappa_y + N_{xy} \delta \varepsilon_s^o \\ & + M_{xy} \delta \kappa_s + Q_x \delta \varepsilon_r^o + Q_y \delta \varepsilon_q^o) dx dy \end{aligned} \quad (\text{A.69})$$

The virtual kinetic energy was previously defined by Equation (A.45). By replacing in the assumed displacement field which coincides with that of classical laminated plate theory (Equations (A.33)) and integrating over the plate thickness, the virtual kinetic energy yields to:

$$\begin{aligned} \delta K = \int_{\Omega} \left[-I_1 (\dot{u}_o \delta \dot{u}_o + \dot{v}_o \delta \dot{v}_o + \dot{w}_o \delta \dot{w}_o) - I_2 \left(\dot{\phi}_1 \delta \dot{u}_o \right. \right. \\ \left. \left. + \dot{\phi}_2 \delta \dot{v}_o + \delta \dot{\phi}_1 \dot{u}_o + \delta \dot{\phi}_2 \dot{v}_o \right) - I_3 \left(\dot{\phi}_1 \delta \dot{\phi}_1 + \dot{\phi}_2 \delta \dot{\phi}_2 \right) \right] dx dy \end{aligned} \quad (\text{A.70})$$

where the inertia terms (I_1, I_2, I_3) were defined by Equation (A.47).

The virtual work done by the external forces was previously defined by Equation (A.48).

Applying Hamilton principle, the principle yields to the following equation defined in terms of the force and moment resultants:

$$\begin{aligned} 0 = \int_0^T \int_{\Omega} \left[- \left(\frac{\partial N_x}{\partial x} + \frac{\partial N_{xy}}{\partial y} - I_1 \ddot{u}_o - I_2 \ddot{\phi}_1 \right) \delta u_o \right. \\ - \left(\frac{\partial N_{xy}}{\partial x} + \frac{\partial N_y}{\partial y} - I_1 \ddot{v}_o - I_2 \ddot{\phi}_2 \right) \delta v_o \\ - \left(\frac{\partial M_x}{\partial x} + \frac{\partial M_{xy}}{\partial y} - Q_x - I_3 \ddot{\phi}_1 - I_2 \ddot{u}_o \right) \delta \phi_1 \\ - \left(\frac{\partial M_{xy}}{\partial x} + \frac{\partial M_y}{\partial y} - Q_y - I_3 \ddot{\phi}_2 - I_2 \ddot{v}_o \right) \delta \phi_2 \\ \left. - \left(\frac{\partial Q_x}{\partial x} + \frac{\partial Q_y}{\partial y} + \mathcal{N}(u_o, v_o, w_o) + q - I_1 \ddot{w}_o \right) \delta w_o \right] dx dy \\ + \int_0^T \int_{\Gamma_{\sigma}} \left[\left(N_{nn} - \hat{N}_{nn} \right) \delta u_{on} + \left(N_{ns} - \hat{N}_{ns} \right) \delta u_{os} \right. \\ \left. + \left(Q_n - \hat{Q}_n \right) \delta w_o + \left(M_{nn} - \hat{M}_{nn} \right) \delta \phi_n + \left(M_{ns} - \hat{M}_{ns} \right) \delta \phi_s \right] ds dt \end{aligned} \quad (\text{A.71})$$

where $\mathcal{N}(u_o, v_o, w_o)$ was previously defined by Equation (A.51). The boundary expressions were arrived by expressing ϕ_1 and ϕ_2 in terms of the normal and tangential rotations (ϕ_n, ϕ_s):

$$\phi_1 = n_x \phi_n - n_y \phi_s, \quad \phi_2 = n_y \phi_n + n_x \phi_s \quad (\text{A.72})$$

From Equation (A.71) the Euler-Lagrange governing equations are obtained:

$$\frac{\partial N_x}{\partial x} + \frac{\partial N_{xy}}{\partial y} = I_1 \frac{\partial^2 u_o}{\partial t^2} + I_2 \frac{\partial^2 \phi_1}{\partial t^2} \quad (\text{A.73})$$

$$\frac{\partial N_{xy}}{\partial x} + \frac{\partial N_y}{\partial y} = I_1 \frac{\partial^2 v_o}{\partial t^2} + I_2 \frac{\partial^2 \phi_2}{\partial t^2} \quad (\text{A.74})$$

$$\frac{\partial Q_x}{\partial x} + \frac{\partial Q_y}{\partial y} + \mathcal{N}(u_o, v_o, w_o) + q = I_1 \frac{\partial^2 w_o}{\partial t^2} \quad (\text{A.75})$$

$$\frac{\partial M_x}{\partial x} + \frac{\partial M_{xy}}{\partial y} - Q_x = I_3 \frac{\partial^2 \phi_1}{\partial t^2} + I_2 \frac{\partial^2 u_o}{\partial t^2} \quad (\text{A.76})$$

$$\frac{\partial M_{xy}}{\partial x} + \frac{\partial M_y}{\partial y} - Q_y = I_3 \frac{\partial^2 \phi_2}{\partial t^2} + I_2 \frac{\partial^2 v_o}{\partial t^2} \quad (\text{A.77})$$

And the natural boundary conditions [61] are:

$$\begin{aligned} N_{nn} - \hat{N}_{nn} &= 0, & N_{ns} - \hat{N}_{ns} &= 0, & Q_n - \hat{Q}_n &= 0 \\ M_{nn} - \hat{M}_{nn} &= 0, & M_{ns} - \hat{M}_{ns} &= 0 \end{aligned} \quad (\text{A.78})$$

where $Q_n \equiv Q_x n_x + Q_y n_y + \mathcal{P}(u_o, v_o, w_o)$. The term $\mathcal{P}(u_o, v_o, w_o)$ was previously defined in Equation (A.54).

The initial conditions of the theory involve specifying the values of the displacements and their first derivatives with respect to time at $t = 0$ for all points in Ω :

$$\begin{aligned} u_n &= u_n^0, & u_s &= u_s^0, & w_o &= w_o^0, & \phi_n &= \phi_n^0, & \phi_s &= \phi_s^0 \\ \dot{u}_n &= \dot{u}_n^0, & \dot{u}_s &= \dot{u}_s^0, & \dot{w}_o &= \dot{w}_o^0, & \dot{\phi}_n &= \dot{\phi}_n^0, & \dot{\phi}_s &= \dot{\phi}_s^0 \end{aligned} \quad (\text{A.79})$$

The governing Equations (A.73-A.77) can be expressed in terms of displacements (u_o, v_o, w_o) and rotations (ϕ_1, ϕ_2) by substituting Equations (A.38), (A.39) and (A.66), and the resulting expressions of the strains (A.65). Neglecting the third order derivative terms in the space, the resulting motion equations are:

$$\begin{aligned} & \frac{\partial}{\partial x} \left[A_{11} \frac{\partial u_o}{\partial x} + A_{12} \frac{\partial v_o}{\partial y} + A_{16} \left(\frac{\partial u_o}{\partial y} + \frac{\partial v_o}{\partial x} \right) + B_{11} \frac{\partial \phi_1}{\partial x} \right. \\ & \left. + B_{12} \frac{\partial \phi_2}{\partial y} + B_{16} \left(\frac{\partial \phi_1}{\partial y} + \frac{\partial \phi_2}{\partial x} \right) \right] + \frac{\partial}{\partial y} \left[A_{16} \frac{\partial u_o}{\partial x} + A_{26} \frac{\partial v_o}{\partial y} \right. \\ & \left. + A_{66} \left(\frac{\partial u_o}{\partial y} + \frac{\partial v_o}{\partial x} \right) + B_{16} \frac{\partial \phi_1}{\partial x} + B_{26} \frac{\partial \phi_2}{\partial y} + B_{66} \left(\frac{\partial \phi_1}{\partial y} + \frac{\partial \phi_2}{\partial x} \right) \right] \\ & = I_1 \frac{\partial^2 u_o}{\partial t^2} + I_2 \frac{\partial^2 \phi_1}{\partial t^2} \end{aligned} \quad (\text{A.80})$$

$$\begin{aligned}
& \frac{\partial}{\partial x} \left[A_{16} \frac{\partial u_o}{\partial x} + A_{26} \frac{\partial v_o}{\partial y} + A_{66} \left(\frac{\partial u_o}{\partial y} + \frac{\partial v_o}{\partial x} \right) + B_{16} \frac{\partial \phi_1}{\partial x} \right. \\
& \left. + B_{26} \left(\frac{\partial \phi_2}{\partial y} \right) + B_{66} \left(\frac{\partial \phi_1}{\partial y} + \frac{\partial \phi_2}{\partial x} \right) \right] + \frac{\partial}{\partial y} \left[A_{12} \frac{\partial u_o}{\partial x} + A_{22} \frac{\partial v_o}{\partial y} \right. \\
& \left. + A_{26} \left(\frac{\partial u_o}{\partial y} + \frac{\partial v_o}{\partial x} \right) + B_{12} \frac{\partial \phi_1}{\partial x} + B_{22} \frac{\partial \phi_2}{\partial y} + B_{26} \left(\frac{\partial \phi_1}{\partial y} + \frac{\partial \phi_2}{\partial x} \right) \right] \\
& = I_1 \frac{\partial^2 v_o}{\partial t^2} + I_2 \frac{\partial^2 \phi_2}{\partial t^2}
\end{aligned} \tag{A.81}$$

$$\begin{aligned}
& \frac{\partial}{\partial x} \left[A_{45} \left(\frac{\partial w_o}{\partial y} + \phi_2 \right) + A_{55} \left(\frac{\partial w_o}{\partial x} + \phi_1 \right) \right] \\
& + \frac{\partial}{\partial y} \left[A_{44} \left(\frac{\partial w_o}{\partial y} + \phi_2 \right) + A_{45} \left(\frac{\partial w_o}{\partial x} + \phi_1 \right) \right] \\
& + \mathcal{N}(u_o, v_o, w_o) + q = I_1 \frac{\partial^2 w_o}{\partial t^2}
\end{aligned} \tag{A.82}$$

$$\begin{aligned}
& \frac{\partial}{\partial x} \left[B_{11} \frac{\partial u_o}{\partial x} + B_{12} \frac{\partial v_o}{\partial y} + B_{16} \left(\frac{\partial u_o}{\partial y} + \frac{\partial v_o}{\partial x} \right) + D_{11} \frac{\partial \phi_1}{\partial x} \right. \\
& \left. + D_{12} \left(\frac{\partial \phi_2}{\partial y} \right) + D_{16} \left(\frac{\partial \phi_1}{\partial y} + \frac{\partial \phi_2}{\partial x} \right) \right] + \frac{\partial}{\partial y} \left[B_{16} \frac{\partial u_o}{\partial x} + B_{26} \frac{\partial v_o}{\partial y} \right. \\
& \left. + B_{66} \left(\frac{\partial u_o}{\partial y} + \frac{\partial v_o}{\partial x} \right) + D_{16} \frac{\partial \phi_1}{\partial x} + D_{26} \frac{\partial \phi_2}{\partial y} + D_{66} \left(\frac{\partial \phi_1}{\partial y} + \frac{\partial \phi_2}{\partial x} \right) \right] \\
& - \left[A_{45} \left(\frac{\partial w_o}{\partial y} + \phi_2 \right) + A_{55} \left(\frac{\partial w_o}{\partial x} + \phi_1 \right) \right] = I_3 \frac{\partial^2 \phi_1}{\partial t^2} + I_2 \frac{\partial^2 u_o}{\partial t^2}
\end{aligned} \tag{A.83}$$

$$\begin{aligned}
& \frac{\partial}{\partial x} \left[B_{16} \frac{\partial u_o}{\partial x} + B_{26} \frac{\partial v_o}{\partial y} + B_{66} \left(\frac{\partial u_o}{\partial y} + \frac{\partial v_o}{\partial x} \right) + D_{16} \frac{\partial \phi_1}{\partial x} \right. \\
& \left. + D_{26} \left(\frac{\partial \phi_2}{\partial y} \right) + D_{66} \left(\frac{\partial \phi_1}{\partial y} + \frac{\partial \phi_2}{\partial x} \right) \right] + \frac{\partial}{\partial y} \left[B_{12} \frac{\partial u_o}{\partial x} + B_{22} \frac{\partial v_o}{\partial y} \right. \\
& \left. + B_{26} \left(\frac{\partial u_o}{\partial y} + \frac{\partial v_o}{\partial x} \right) + D_{12} \frac{\partial \phi_1}{\partial x} + D_{22} \frac{\partial \phi_2}{\partial y} + D_{26} \left(\frac{\partial \phi_1}{\partial y} + \frac{\partial \phi_2}{\partial x} \right) \right] \\
& - \left[A_{44} \left(\frac{\partial w_o}{\partial y} + \phi_2 \right) + A_{45} \left(\frac{\partial w_o}{\partial x} + \phi_1 \right) \right] = I_3 \frac{\partial^2 \phi_2}{\partial t^2} + I_2 \frac{\partial^2 v_o}{\partial t^2}
\end{aligned} \tag{A.84}$$